CHARLES UNIVERSITY IN PRAGUE
FACULTY OF MATHEMATICS AND PHYSICS

DEPARTMENT OF ELECTRONICS
AND VACUUM PHYSICS

UNIVERSITY OF RENNES 1
STRUCTURE AND PROPERTIES OF MATTER

EXPERIMENTAL ASTROCHEMISTRY
U.M.R. PALMS N° 6627 DU CNRS

UNIVERSITÉ DE
RENNES 1

DOCTORAL THESIS

EXPERIMENTAL STUDY OF ELECTRON-ION RECOMBINATION USING STORAGE RING AND AFTERGLOW TECHNIQUES

BY

OLDŘICH NOVOTNÝ

SUPERVISORS:

DOC. RNDR. JURAJ GLOSÍK, DRSC.

PROF. J. BRIAN A. MITCHELL

STUDY BRANCH:

PHYSICS OF PLASMAS
AND IONIZED MEDIA

SCIENCE OF MATTER

PRAGUE, DECEMBER 2005

The work described in this thesis has been performed at:

Department of Electronics and Vacuum Physics
Faculty of Mathematics and Physiscs
Charles University in Prague
V Holešovičkách 2
182 00, Praha 8
Czech Republic

Group of Experimental Astrochemistry
PALMS
University of Rennes 1
Campus de Beaulieu, Bât 11C
Avenue du Général Leclerc
35042 RENNES Cédex
France

Institute for Storage Ring Facilities
University of Aarhus
Ny Munkegade, bygn. 520
DK-8000 Aarhus C
Denmark

The author of this thesis was during his PhD. study further trained at:

Department of Physics
Stockholm University
AlbaNova
S-106 91 Stockholm
Sweden

Institut of Physics
Świętokrzyska Academy
ul. Świętokrzyska 15
25-406 Kielce
Poland

Physics is like sex:
sure, it may give some practical results,
but that's not why we do it.

Richard P. Feynman

Acknowledgments

During my time as a PhD student I have enjoyed the help, support and company of a great number of people and would like to thank them all at this point.

First of all I would like to express my gratitude to both my supervisors. To Prof. Juraj Glosík who has shown me the admirable world of experimental physics and who has guided me with his constructive criticism through the intrigues of scientific work. I will always consider his group in Prague as my "home laboratory". I thank also Prof. J. Brian A. Mitchell who has supervised my study in Rennes. He has helped me to be better acquainted with the complicated domain of dissociative recombination and the no less complicated domain of French bureaucracy. I thank him also for his unflagging optimism and for correcting the language of this work.

I am also very grateful to other mentors who I have met during my study. It was very instructive to work with Dr. Bertrand Rowe who shared with me some of his great ideas. I am also greatly indebted to Prof. Jacek Semaniak who was my first foreign teacher and who with patience and indulgence of my language skills introduced me to storage ring techniques. I thank also Prof. Mats Larsson for giving me the opportunity to work in his group and for his trust in my skills when I was a trainee in a new subject.

There are plenty of other people for whom I am appreciative, not only for their professional help but also for their personal support with my integration into the new environment. I consider many of them to be not only colleagues but also my friends, who definitely do not correspond to the boring scientific cliché that the average human being has in mind. So if you recognized yourself in this description, you are sincerely acknowledged for the good times we have spent together and for what I have learned from you.

Děkuji i mým rodičům a partnerce Hance za jejich dlouhodobou duševní podporu a zejména shovívavost k mé časté nepřítomnosti.

THESIS OBJECTIVES AND OUTLINE

In this thesis the author presents his work performed during almost four years of doctoral studies. The *Dissociative Recombination* (*DR*) of several different simple or more complex ions with electrons has been experimentally investigated using various techniques. The main parameters studied were recombination rate coefficients or cross-sections for particular reactions but in some cases branching ratios for dissociative channels have also been obtained. The work consisted not only of measurement and data analysis but also of rebuilding or design and development of new experimental techniques, data acquisition systems and data analysis procedures.

The diversity of the experimental techniques and reactions studied is described in separate chapters. The description provided for each problem that has been undertaken, includes the aims and motivation for that study together with the experimental method, the results and a discussion.

In **chapter 1** a basic overview of electron-ion interactions is given where the stress is placed on recombination processes. A short overview describes the history of the investigation of *DR* and then basic principles of currently known pathways for *DR* are explained.

Chapter 2 covers descriptions of all the experimental techniques and data analysis procedures used or developed for obtaining results presented in the subsequent chapters. The *Flowing Afterglow Langmuir Probe with Variable Temperature* (*FALP–VT*) which have been substantially rebuilt and then used for the measurement in He-Ar-H_2 and He-Ar-D_2 plasmas is described first. The measurements and results obtained with this apparatus are described in chapter 3. The second technique is the *Flowing Afterglow with Photo-Ions* (*FlAPI*) which was newly developed for the measurement of the recombination of large polyatomic ions with electrons. The results of these measurements on PAH ions are presented in chapter 4. The next technique widely employed in this thesis is the *Aarhus STorage RIng, Denmark* (*ASTRID*). This storage ring have been used for cross-section and branching ratio measurements of several ions described in chapters 5 and 6. The *CRYRING* storage ring is also mentioned as some measurements were performed in cooperation with this facility.

Chapter 3 first briefly summarizes the motivation and current status of recombination studies of H_3^+ and D_3^+ ions. The new measurement is then introduced including the discussion of ion-formation processes. The results of measurements in an afterglow plasma over a very broad range of reactant number densities is presented and values obtained are extensively discussed.

Chapter 4 includes a brief introduction of PAHs, PAH ions, their recombination and astrochemisty. Then follows the description of a unique measurement of recombination rates for several PAH ions using a newly developed technique.

Chapter 5 describes measurements and results for the recombination of two rare gas hydride ions, ArH^+ and NeH^+ supplemented with a short general foreword on rare gas hydride ions.

Finally **chapter 6** presents measurements of recombination cross-sections and branching ratios for CF^+ and CF_3^+, the ions commonly found in CF_4 industrial plasmas.

ACRONYMS

AISA	Advanced Integrated Stationary Afterglow
ASTRID	Aarhus STorage RIng Denmark
CID	Collision Induced Dissociation
CRDS	Cavity Ring-Down Spectroscopy
CRESU	Cinétique de Réaction en Ecoulement Supersonique Uniforme
CRYRING	CRYogenic ion source RING
DE	Dissociative Excitation
DIB	Diffuse Interstellar Bands
DR	Dissociative Recombination
EEDF	Electron Energy Distribution Function
FALP-MS	Flowing Afterglow with Langmuir Probe and Mass Spectrometer
FALP-VT	Flowing Afterglow with Langmuir Probe – Variable Temperature
F$_l$API	Flowing Afterglow with Photo-Ions
HPFA	High Pressure Flowing Afterglow
ISM	InterStellar Medium
KER	Kinetic Energy Release
LP	Langmuir Probe
MCA	Multi-Channel Analyser
MCP	Multi-Channel Plates
MCS	Multi-Channel Scaler
MQDT	Multi-channel Quantum Defect Theory
PAH	Polycyclic Aromatic Hydrocarbons

QMS	Quadrupole Mass Spectrometer
RGA	Residual Gas Analysis
SBD	Surface Barrier Detector
sccm	standard cubic centimeter per minute, $1\,\mathrm{Pa\,m^3 s^{-1}} = 592$ sccm
slpm	standard liter per minute, 1 slpm = 1000 sccm
SIFT-VT	Selected Ion Flow Tube - Variable Temperature
SVD	Singular Value Decomposition
UHV	Ultra-High Vacuum
UIB	Unidentified Infra-red Bands

CONTENTS

DISSOCIATIVE RECOMBINATION

1.1 Electron-ion interactions

Interactions of electrons and ions are some of the most important processes in plasmas and as plasma is the most common state of matter in space [1], electron-ion interactions are highly interesting for many research fields.

Omitting elastic interactions, the incident electron is not only a provider of kinetic energy, but when captured by the target particle, a new atom or molecule with significantly changed configuration of internal states is formed. The "complex" so produced is very often highly excited[1] and can be stabilized by different processes. The following list summarizes several electron-ion interactions taking place in processes studied in this thesis. AB^+ represents an atomic or polyatomic ion.

Elastic interaction:
An essentially mechanical collision without change of the internal state of the target ion.

Inelastic collision - excitation:
The incident electron excites (or de-excites) the target ion but is not itself captured. The energy transfer is represented by a change of kinetic energy E_K.

$$AB^+ + e^- \longrightarrow (AB^+)^* + e^- \pm E_k \tag{1.1}$$
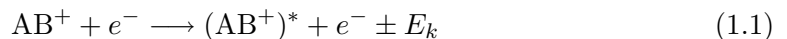
Autoionization:
The incident electron is captured by forming an excited neutral particle. However, this can autoionize back to the original state by emitting the electron. Autoionization is usually competing with other processes such as recombination (see next processes below).

$$AB^+ + e^- \rightleftharpoons AB^* \tag{1.2}$$

Radiative recombination:
The energy is stored in internal excitations of the neutral particle (ro-vibrational excitations) and is released later by photon emission.

$$AB^+ + e^- \rightleftharpoons AB^* \longrightarrow AB + h\nu \tag{1.3}$$

---
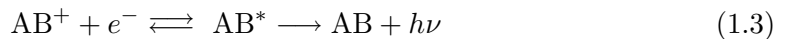
[1]The maximum energy stored in additional excitation is equal to the ionization energy needed for forming the ion from the neutral (recombination energy) plus the kinetic energy of incident electron.

For small molecular ions, this process is usually less probable and the overall rate is much slower than other recombination pathways. As it is the only possibility of recombination for atomic ions without involving a third particle, the recombination of atomic ions is a very slow process. In the case of large polyatomic ions, however, the recombination energy can be easily stored in many ro-vibrational states and thus the product does not need to dissociate.

Dissociative recombination (DR):

The excess of internal energy is converted into kinetic energy of the nuclei and the particle dissociates into two or more neutral products. For polyatomic ions, there are often several dissociative channels with different products.

$$AB^+ + e^- \rightleftharpoons AB^* \longrightarrow A + B + E_k \tag{1.4}$$
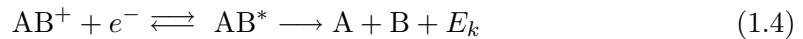
More detailed descriptions of DR are given in sections 1.2 and 1.3.

Three-body recombination:

In the case of a long-lived neutral complex AB^*, the stabilization may be provided by a third particle CD. The internal energy of AB^* is shared with CD, where AB^* can, but does not need to dissociate. This process is more effective with polyatomic CDs as those have more degrees of freedom for storing the energy but on the other hand in some cases, an electron can play the role of the third particle. Efficiency also increases with the concentration of CD, thus three-body recombination is important in high-density plasmas.

$$AB^+ + e^- + CD \rightleftharpoons AB^* + CD \longrightarrow \begin{cases} A + B + CD^* \\ AB + CD^* \\ A + B + CD + E_k \end{cases} \tag{1.5}$$
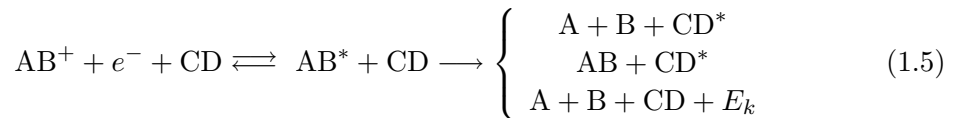
Dissociative excitation (DE):

Dissociation into charged products is usually less probable than DR. Dissociative excitation occurs directly or via neutral intermediate state. The distribution of charge between products depends upon the internal configuration of AB^*.

$$AB^+ + e^- \begin{cases} \rightleftharpoons AB^* \longrightarrow \\ \longrightarrow \end{cases} \begin{cases} A^+ + B + e^- \\ A + B^+ + e^- \end{cases} \tag{1.6}$$
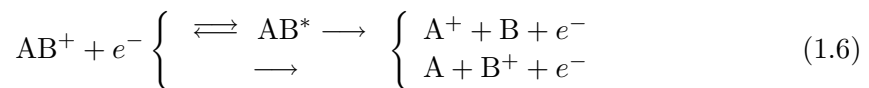
Dissociative ionization:

In this dissociative process, both products are positively charged. This pathway is open at high energies, when the incident electron can doubly-ionize the target ion.

$$AB^+ + e^- \longrightarrow A^+ + B^+ + 2e^- \tag{1.7}$$
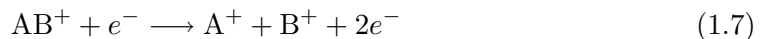
Resonant ion-pair formation (RIP):

In this reaction, an intermediate state AB^+ may interfere with another state producing a pair of positive and negative ions. This process was observed e.g. for H_3^+ [2].

$$AB^+ + e^- \rightleftharpoons AB^* \longrightarrow \begin{cases} A^+ + B^- \\ A^- + B^+ \end{cases} \tag{1.8}$$
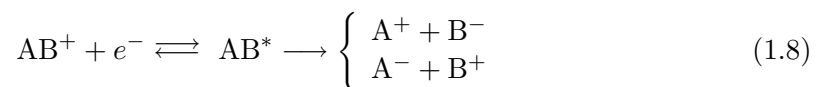
This thesis describes mostly experiments on recombination, especially dissociative recombination. For a more detailed description of the last three "more exotic" processes in the list see ref. [3].

1.2   Historical overview on Dissociative Recombination

Dissociative recombination (DR) was first introduced by *Kaplan* [4] in 1931 soon after the discovery of the Earth's ionosphere in order to explain spectroscopic observations of oxygen emissions from the nightglow and the aurora. The discussion [5] evoked from this hypothesis considered the DR with electrons as too slow a process to be responsible for the expected high rates ($\alpha > 10^{-8}$cm^{3}s^{-1}) derived from *Appletons's* radio waves experiment [6] and ion-ion recombination was proposed as a more probable process for explaining this hypothesis.

The common belief of the slow DR of ions with electrons originated from two incorrect formulations: Firstly, due to the mass mismatch, a light electron was not expected to break the massive ion, and secondly, the non-crossing rule requires that potential curves of the same symmetry in the adiabatic representation[2] do not cross [7]. Thus a repulsive neutral state could not cross the ion state because it would have to cross an infinite number of Rydberg states[3] having the ion state as a series limit. It is now understood, however, that if the repulsive state (see eg. fig. 1.1) is a diabatic state (nuclei change their distance during dissociation) that the non-crossing rule is no more applicable.

Those two obstacles were overcome and *Bates* in late 1940's proposed the first mechanism of DR [8], today known as the **Direct process** for DR. Bates and Massey also re-established DR as an important process for electron removal in the ionosphere [9]. The first detailed calculation based upon the direct mechanism was performed by *Bardsley* [10]. In order to explain the energy dependence seen in shock tube experiments on rare gas ions [11], he proposed an alternative process involving Rydberg states into DR [12], today known as the **Indirect process** of DR. Further progress and unification in DR theory came from O'Malley [13, 14], who demonstrated with resonance scattering theory that electronic transitions to Rydberg states of the molecule can also interrupt the direct DR mechanism.

The DR of HeH$^+$ with electrons was first studied by *Yousif and Mitchell* [15] in 1989 and a surprising result was found: Despite a lack of a suitable curve crossing through which the direct mechanism could proceed [16] the recombination of HeH$^+$ exhibits a substantial recombination cross-section at low collision energies. This observation has been confirmed by a series of measurements [17–23]. *Guberman* [24] and *Sarpal et al.* [25] assumed, that a nona-diabatic coupling exists between the ion's ground state and a neutral repulsive state lying below the ionic ground state, and this coupling arises from terms normally neglected in the Born-Oppenheimer approximation[4]. This process is known as the **Tunneling process** and was observed also for other ions such as H$_3^+$ and NeH$^+$ (see sections 3 and 5.4 respectively).

The behavior, however, of the HeH$^+$ cross-section at high energies (above 10 eV) was still not explained. The observed broad peaks [20] were theoretically studied by *Orel and co-workers* [27, 29] who suggested another dissociation pathway involving electron capture into Rydberg states lying below an excited ion state. This is often referrred to as Resonant DR.

---

[2]The solution of Schrödinger equation applying the Born-Oppenheimer approximation[4]. Heavy nuclei are considered as essentially stationary in comparison to fast electrons.

[3]Highly excited electronic states (high n). An electron in such a state is weakly bound to the atom/molecule.

[4]Due to their mass mismatch, the Hamiltonian for electrons and nuclei may be separated. Electronic wave-functions are then solved independently for fixed nuclei positions [26].
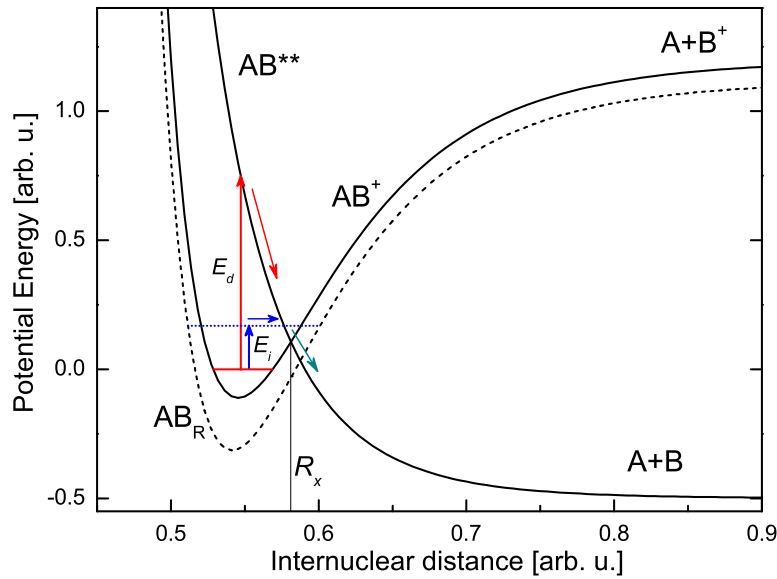
Figure 1.1: Crossing mode: direct and indirect mechanisms of DR.

1.3 Mechanisms of dissociative recombination

Although a perfect description of the DR process valid for any ion can be given only by
a full quantum mechanical analysis, it is instructive, nevertheless, to describe the process via
a number of two-dimensional mechanisms.

1.3.1 The crossing mode of DR

Figure 1.1 shows the potential curve for an ion AB^+ in its ground state. The origin of
the potential energy is fixed at the vibrational ground state $AB^+(v = 0)$. In the so-called
direct (or resonant) mechanism, the incident electron of energy E_d excites an electron of the
ion core and is itself captured into a doubly-excited repulsive state AB^{**}, which crosses the
initial ionic state. The system can either autoionize to the original or to an excited ion state
releasing the electron, or be stabilized by the system converting its potential energy into the
kinetic energy of dissociated atoms or molecules. Autoionization is possible up to the point
where the internuclear distance reaches a value R_x : the crossing of the ion ground state and
the neutral dissociative state. Although the doubly excited repulsive curve can be treated as
a resonance state, it can be accessed over a wide range of E_d since it is repulsive and since the
system can start from a range of R values, defined by the nuclear wavefunction. The cross
section σ arising from the direct mechanism has an E^{-1} energy dependence, where E is the
collision energy of the interacting particles [30].

The *Indirect mechanism* for DR proceeds via an intermediate step: The incident electron
of energy E_i is first captured by vibronic coupling into a vibrationally excited neutral Rydberg
state $AB_R(n)$ lying below the ion state AB^+. The Rydberg state is then predissociated by
the neutral AB^{**} repulsive state. An observable demonstration of the indirect process is the
presence of narrow peaks in the plot of σ vs E at energies for each n.

O'Malley [13] enlarged the description of the previous two mechanisms taking into account
interference between them. In the direct process, the AB^{**} state, during its dissociation, may
be captured into several intersecting Rydberg states $AB_R(v, n)$, while in the indirect process,
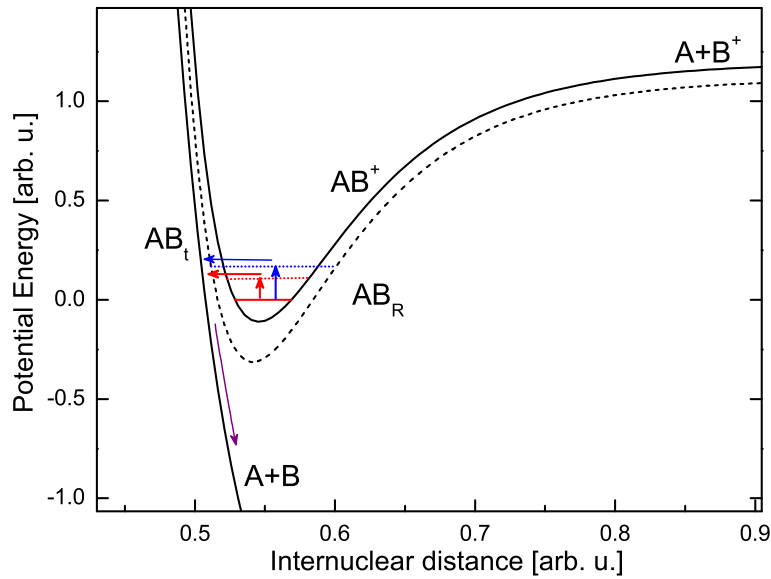
Figure 1.2: Tunnelling mechanism of DR.

the predissociating AB** state can autoionize before reaching the crossing point. Those interferences lead to narrow peaks and dips in the measured cross-section. These pathways are summarized in following schema:

$$
AB^+ + e^- \begin{cases} \xrightarrow{e} & AB^{**} \longrightarrow A + B \\ & e \uparrow\downarrow \\ \xrightarrow{\Delta v} & AB_R \\ & (n,v) \end{cases} \tag{1.9}
$$
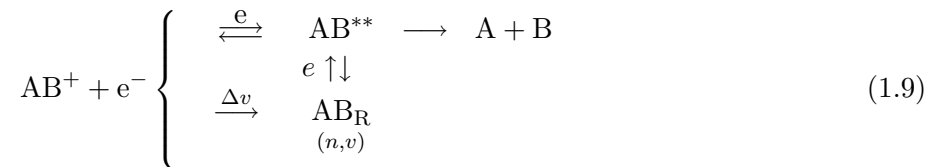
where e represents electronic transitions and Δv vibrational transitions.

1.3.2 Tunnelling mechanism for DR

Even with the lack of curve crossings the cross-section for DR has been seen experimentally in a number of instances, (HeH^+, NeH^+, H_3^+) to reach high values at low energies. The presence of a dissociative state AB_t near the ionic state AB^+ (see figure 1.2) can provide sufficient overlap for DR to proceed. This non-adiabatic coupling (wave-mixing) leads to the so-called *tunneling mechanism* for DR. As with the crossing mode, the tunnelling mechanism can be direct or indirect in the case where a Rydberg state AB_R plays an intermediate role. Due to the crossing of many Rydberg states between AB^+ and AB_t, the process displays significant sharp resonances in the cross-section.

1.3.3 Other pathways for DR

There are several more complicated pathways for DR combining the previously mentioned processes. An interesting one is an indirect process, where the intermediate neutral Rydberg state AB_R does not lie below the original ionic state AB^+, but has the excited ion state $(AB^+)^*$ as it's limit (see figure 1.3). The molecule is then predissociated by the same repulsive state AB^{**} which gives rise to the direct process. This pathway proceeds at higher energies
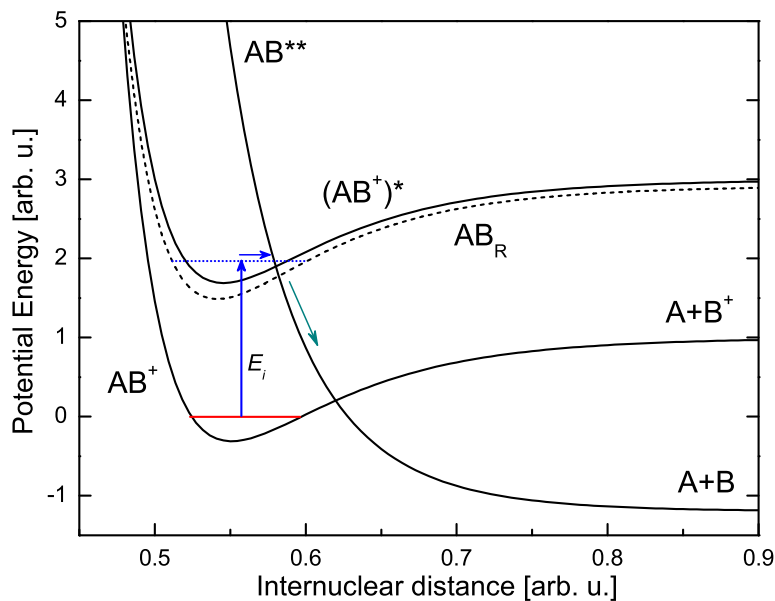
Figure 1.3: Other pathways of DR

than the previously described indirect process and so gives rise to peaks in the cross section at higher energies. Such process have been identified in the recombination of HeH^+, NeH^+ and CF^+.

1.3.4 Cluster ion recombination

Cluster ions are large polyatomic species held together by weak bonds. Their recombination cannot be easily explained using the previously introduced pathways for DR. Almost all cluster ions display significantly higher recombination rate coefficients, however, than "normal" polyatomic molecules at similar masses and so the recombination process must be different.

Bates [31,32] has shown that cluster ions can be separated into two groups. The first family are dimers such as $N_2 \cdot N_2^+$, $O_2 \cdot O_2^+$, etc. These clusters are bound by electron delocalization forces and have low dissociation energies. The products of their dissociative recombination are in highly excited Rydberg states and so many dissociative channels are available at similar energies. In addition, to ensure large overlap between wavefunctions of the ion and neutral states, the gradient of the curves of the repulsive dissociating states should be very low. These two facts make the recombination a fast process, sometimes called *super-dissociative recombination* [33].

The second group of cluster ions are structures such as $(H_2O)_n \cdot H_3O^+$, $(NH_3)_n \cdot NH_4^+$, etc., where the bond is formed by proton bridges. Deep potential wells are typical for these type of bonds and there is not usually an excess of energy to dissociate into electronically excited products. The fast recombination proceeds via electron capture by the proton which, being neutralized, releases the cluster and thus the recombination energy is provided. This kind of neutralization involves a single electron transition, while normally a double-electron transition is required for DR. As single-electron transitions are much more probable, recombination rates for this type of clusters display high recombination rates. A nice overview on the DR of clusters is given in ref. [34].

EXPERIMENTAL TECHNIQUES

2.1 Introduction

Dissociative recombination (DR), the main subject of this thesis, has been investigated using several experimental techniques. In this section, first a basic overview is given, while following sections describes specific equipment and procedures in detail.

Two main groups of methods are used for studying DR processes. The difference lies in the form of the results so obtained and in the interaction environment.

The first group of experiments are called *swarm experiments* or *multi-collisional experiments* and the quantitative result is given directly as a *thermal rate coefficient $\alpha(T)$*. In these techniques, ionized particles are driven by an inert buffer-gas, while the concentration of these particles is several orders of magnitude lower than the concentration of neutral gas. Many collisions induce a state of thermodynamic equilibrium between the neutral gas and the ionized particles. Velocities and excited states of the particles correspond, therefore, to a equilibrium distribution function and may be, in a first approximation, described by the temperature of the buffer gas T.

An excellent environment for swarm experiments is the *plasma afterglow*, where a plasma is created in the plasma source and then decays in time while the concentration of charge densities or product densities is monitored. The study of DR processes for a selected reaction requires a good understanding of the plasma formation mechanisms together with all the elementary processes in the plasma, e.g. diffusion, ion-molecule reactions and of course recombination. Typical experimental configurations are the *stationary afterglow*, where the afterglow begins after switching off the plasma source, and the *flowing afterglow*, where the plasma flows out of the plasma source and the afterglow appears. Many modifications have been developed[1], e.g. *Selected Ion Flow Tube* (SIFT) [35], *Advanced Integrated Stationary Afterglow* (AISA) [36], *High Pressure Flowing Afterglow* (HPFA) [37], *Flowing Afterglow with Langmuir Probe and movable Mass Spectrometer* (FALP–MS) [38], etc.

In this thesis, two modifications of the flowing afterglow are described: in section 2.2 the *Flowing Afterglow Langmuir Probe with Variable Temperature* (FALP–VT) and in section 2.3 the *Flowing Afterglow with Photo Ions* (FlAPI).

In the second basic group of experiments, called *beam experiments*, two beams of mono-energetic particles interact and thus the result is given directly as a *cross–section $\sigma(v)$* that depends on the collision velocity v (often converted to collision energy), which is varied by

---

[1]Not all versions have been employed for DR investigation.

changing the relative velocity of the interacting beams.

It is desirable to compare results from *swarm* and *beam* experiments. The rate coefficient α can be calculated from $\sigma(v)$ as

$$\alpha(f(v)) = \langle \sigma v \rangle = \int_0^\infty f(v)\sigma(v)v\mathrm{d}v, \qquad (2.1)$$

where v is the relative velocity of the interacting particles, $\langle \, \rangle$ indicates averaging in velocity space and $f(v)$ is the appropriate velocity distribution function (in the case of thermal rate coefficients, a Maxwellian distribution is used). The determination of cross-sections over a wide range of energies is required, however, for correct conversion of σ to α and obtaining values at low collision energies may be complicated due to the spread of particle velocities in the beams. The inverse process, the calculation of $\sigma(v)$ from α is mathematically possible by deconvolution, but practically unfeasible due to the very low precision of such a procedure.

The mass selection of particles in beams and in some cases also the mass and energy identification of products make beam techniques very useful for recombination studies. Several configurations of experiments have been developed. First the *crossed beams* [39,40] technique was been used, with two perpendicular particle beams interacting in a small region. Later the *merged beams* [41, 42] technique was developed with both beams overlapping on a common axis and propagating in the same direction. The advantage of such a configuration is the much higher product yield due to the long interaction region and above all, the possibility of measurement at interaction energies close to 0 eV.

Heavy ion *Storage rings* were originally developed for collecting and storing rare high-energy ions for particle physics experiments. In these devices, charged particles are confined in a vacuum chamber by means of magnetic and/or electric fields and move in a closed loop. Combination with the merged electron-ion beams technique has proved to be a very successful methods of studying recombination reactions: usually a beam of ions is stored in the ring and a beam of electrons is merged with the ion beam over a limited region. The long storage time in these machines allows ion beam cooling by interactions with a cold electron beam to occur, since the ions are usually stored for several seconds before the actual measurement commences. The electron beam that provides the ion cooling can also be used as a target, where the interaction energy may be varied by changing the electron velocity. In this way the dependence of the cross-section on interaction energy is obtained. Part of this study is based on measurements using the *Arhus STorage RIng Denmark* (*ASTRID*) and the *CRYogenic storage RING* (*CRYRING*). More detailed descriptions of these apparatuses is given in sections 2.4 and 2.5.

Apart from the already described techniques, several other techniques have been used for recombination including *ion traps* [43, 44], *shock tubes* [11] and *flames* [45] but since these techniques were not used in this work, they will not be discussed here.

2.2 The *FALP–VT*

In the 1960's *Ferguson and coworkers* [46] developed the *Flowing Afterglow* (FA) apparatus. This technique is based on the principle of a chemical reactor (see figure 2.1): the carrier gas (buffer gas) flows through the ion source (typically a microwave cavity) and the plasma thus created is then carried along the flowtube by the action of the buffer gas and decays in time. At some point, downstream, a reactant gas is injected into the afterglow. Primary and product ions are monitored by the mass spectrometer (normally a QMS) located at the end of the flowtube. This basic version of the FA is suitable for studying ion-molecule reactions.

The FA technique was significantly extended in 1971 [47] when a movable Langmuir probe was used for electron density measurements along the flowtube. Measurements at different distances from the plasma source are equivalent to measurements at different times after plasma decay initiation[2]. Thus the spatial scale parallel to the flowtube axis is transformed into the time scale. Moreover, absolute values of number densities of charged particles can be determined and thus rates for elementary processes as e.g. recombination can be measured. This modification, called the *Flowing Afterglow with Langmuir Probe* (FALP), was extensively used and developed by *D Smith, N. G. Adams and coworkers* [48].

The FALP technique has been used for measurements of rate coefficients for a great number of reactions, mainly electron-ion recombination, ion-ion recombination, ion-molecule reactions and electron attachment. Several specialized modifications have been created, e.g. such as a version with movable mass spectrometer *FALP–MS* [38] or with ions created by photoionization (see section 2.3).

Technical arrangements and constraints for given measurements with the Langmuir probe require typical working pressures in FALP apparatuses of ~ 100 Pa. For some reactions, however, (especially three-body processes), higher working pressures are required. For this reason, a special modification to the FALP apparatus was developed at the Faculty of Mathematics and Physics, Charles University, Prague: The *High Pressure Flowing Afterglow*[3] (HPFA). In this version, a nozzle is used at the end of the flowtube and so higher pressures have been reached (~ 1000 Pa). This version of the apparatus was built for the study of hydrogen and deuterium plasmas, and especially the recombination of H_3^+, D_3^+, H_5^+ and D_5^+ ions with electrons. Results of this work are published in ref. [49].

---

[2]If the plasma flow velocity v is constant along the flowtube, then the time to reach a distance z from the source is $t = z/v$.

[3]The author of this thesis participated in the rebuilding of the *HPFA* using UHV technology during his master's thesis study.
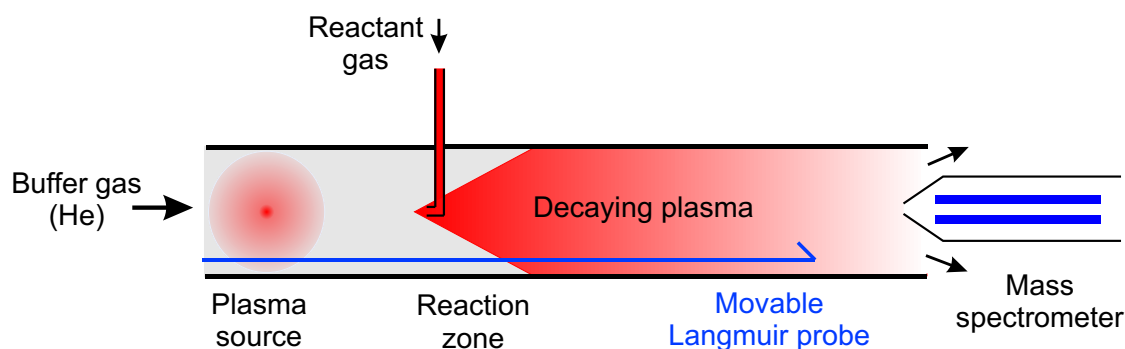

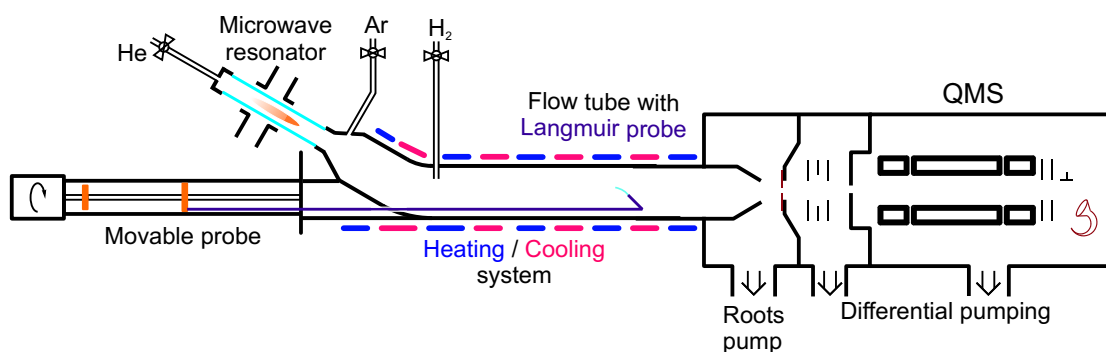Figure 2.1: The basic principle of the FA and FALP techniques.

Figure 2.2: The schematic of the *FALP-VT* apparatus – September 2005.

Further study of this topic required a measurement at lower densities of the hydrogen/deuterium reactant gas where values of the recombination rate coefficient α were expected to be below the lower measurable limit of the apparatus: 10^{-7} cm^{3}s^{-1}. In addition, it was proposed to perform experiments at low temperatures, down to 130 K, with a good temperature control and stability. For these reasons, a new FALP fulfilling these new requirements has been designed and built. A more detailed description of the motivation for this advance is described in chapter 3.

2.2.1 Description of the apparatus

The schematic of this new apparatus, called the *Flowing Afterglow with Langmuir Probe – Variable Temperature* (*FALP–VT*), is shown in figure 2.2. Helium, as a buffer gas, flows through the glass discharge tube (12 mm in diameter), where the plasma is formed in a microwave discharge (2.45 GHz, 25 Watt). Ions are than driven by the buffer gas into the flowtube, where reactants can be introduced at several injection points located at different distances downstream of the plasma source. The end of the flowtube is equipped with a nozzle, which regulates the working pressure and the velocity of the flow to the required levels[4]. The buffer gas is pumped by a large Roots pump (1000 m^3/hr).

The concentration of electrons in the flowtube is measured by a movable Langmuir probe over a distance range of 0–35 cm from the first reactant inlet. The radial position of the probe is always held in the center of the tube. The probe itself is made from a tungsten wire, 14 μm in diameter and $\sim$ 7 mm long. A more detailed description of Langmuir theory restrictions and of the data analysis of Langmuir characteristics is given in appendix B.

The apparatus is equipped with a Quadrupole Mass Spectrometer (QMS) placed on-axis of the flowtube behind the output nozzle. For the proper operation of channeltron detector, the pressure in the chamber of the QMS has to be maintained below 5×10^{-4} Pa. To get reasonable yield in the measured QMS spectra, however, a sufficient number of ions have to be transported from the high pressure section of the apparatus. This is guaranteed by a differentially pumped ion-optics system placed between the main chamber and the QMS chamber. The ion optics array consists of 5 electrostatic lenses maintained at different potentials. Both, the QMS chamber and the ion optics chamber, are pumped by turbomolecular pumps (210 and 53 l/hr respectively). The QMS is not used directly for obtaining the recombination rate coefficient, but is intended for studying the ion composition at the end of the flowtube.

---

[4]During the experiments described here, a nozzle of 4.5 mm in diameter has been used, maintaining the pressure at 1650 Pa at a temperature of 300 K and a flow rate of the buffer gas of 5900 sccm.

Figure 2.3: The vacuum schematic of the FALP-VT apparatus.

He

Ar

reactant

Pn2
Ion pump
B1
Pr
Pn1
QMS
Pr2

Pfeiffer
TMU 261

Ve2

Pn3

Pfeiffer
TMU 261

Ve1

Pr1

B2

Reservoir

R

Reactant

Roots pump

Pr4

Pr3

Pr5

Cryosorption
pump

He

Pr2

Rotary pump

Rotary pump

Rotary pump

Rotary pump

Kryopump

Flowmeter/controller

Needle, on/off, electric valve
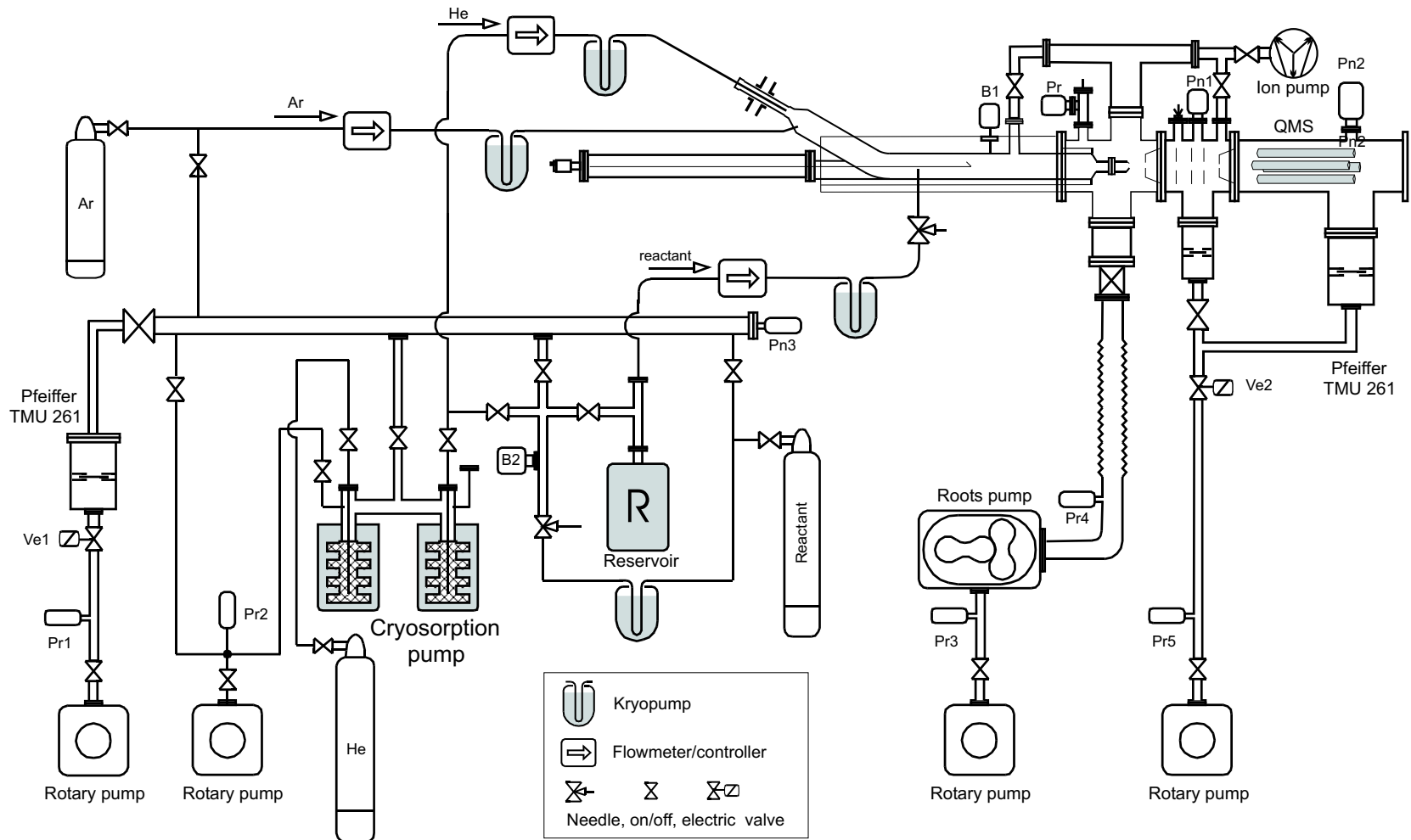
The complete vacuum schematic of the *FALP–VT* apparatus, including the system for regulation, cleaning and injection of reactant gases, is given in figure 2.3. All gases are cleaned in condensate traps prior injection into the main chamber. Helium, as the major carrier of impuritiesis cleaned in 2 zeolite traps, cooled by liquid nitrogen. Flow rates of introduced gases are controlled and measured by flow-controllers or by needle valves and flow-meters. In some cases a very low amount of reactant gas has to be introduced; even lower than the minimal flow rate controllable mechanically by a system of needles or flow-controllers. Than the reactant gas is first mixed in the reservoir with helium at known ratio and than the mixture is introduced at a controllable flow rate into the chamber. The whole "injection system" can be pumped independently by a turbomolecular pump. The pressure is measured at several points along the apparatus. Membrane manometers are used for absolute measurements of high pressures in the flowtube and in the reactant reservoir, while low pressures in the main chamber and in the injection system during the cleaning stage are measured by Penning manometers. Pirani gauges are employed in sections between the primary and secondary pumps.

Up to this point, the sub-systems just described, did not differ significantly from the *HPFA* version of the apparatus. In the following paragraphs, however, the main advantages of the new *FALP–VT* are highlighted in detail:

Decrease of the lower limit of the measurable recombination rate

The lower limit of the measurable recombination rate coefficient in the FALP apparatus is given mainly by the ratio of recombination losses to other losses. At too low ratios, the recombination is indistinguishable from other processes and the recombination rate coefficient cannot be obtained. In the approximation represented in equation 2.7, the ratio is given by

$$R = \frac{\alpha n}{k[B] + D_a/\Lambda^2},$$
(2.2)

where α is the recombination rate coefficient, n the plasma concentration, k the rate of ion-molecule reactions, $[B]$ the concentration of neutral impurities, D_a the coefficient of ambipolar diffusion and Λ the characteristic diffusion length. For a detailed description of particular parameters and terms see section 2.2.3.

Obviously k and α are fixed parameters. The initial plasma concentration in the discharge tube usually does not exceed a maximum value of $n_0 \approx 10^{11}$ cm^{-3} and in the flowtube (several centimeters downstream), of $n_0 \approx 10^{10}$ cm^{-3}. This value cannot be significantly increased while preserving reasonable dimensions and costs of the experiment. Losses by ion-molecule reactions, however, can be suppressed by minimizing $[B]$. This is ensured by cleaning the chamber and introduced gases as described above and in section 2.2.4.

The main increase in R can be gained by changing the diffusion term D_a/Λ^2. Λ is proportional to the flowtube diameter. We changed, therefore, the internal diameter of the new flowtube in the *FALP–VT* to $d = 50$ mm (from $d = 17$ mm at *HPFA*). The diffusion coefficient D_a is proportional to the pressure p as $D_a \propto 1/p$. Thus in the experiments presented here, we maintained the working pressure at ~ 1600 Pa, in comparison to 1000 Pa in the *HPFA* (both values for T=300 K). The flow rate of buffer gas ~ 6000 sccm was not changed and the pressure increase is caused by the use of a different nozzle of smaller diameter (4.5 mm), at the end of the flowtube. The original value of plasma velocity $v \approx 80$ m/s of course decreased to $v \approx 4.9$ m/s (both at $T = 300$ K). Changes of p and D increased R at least 10×.
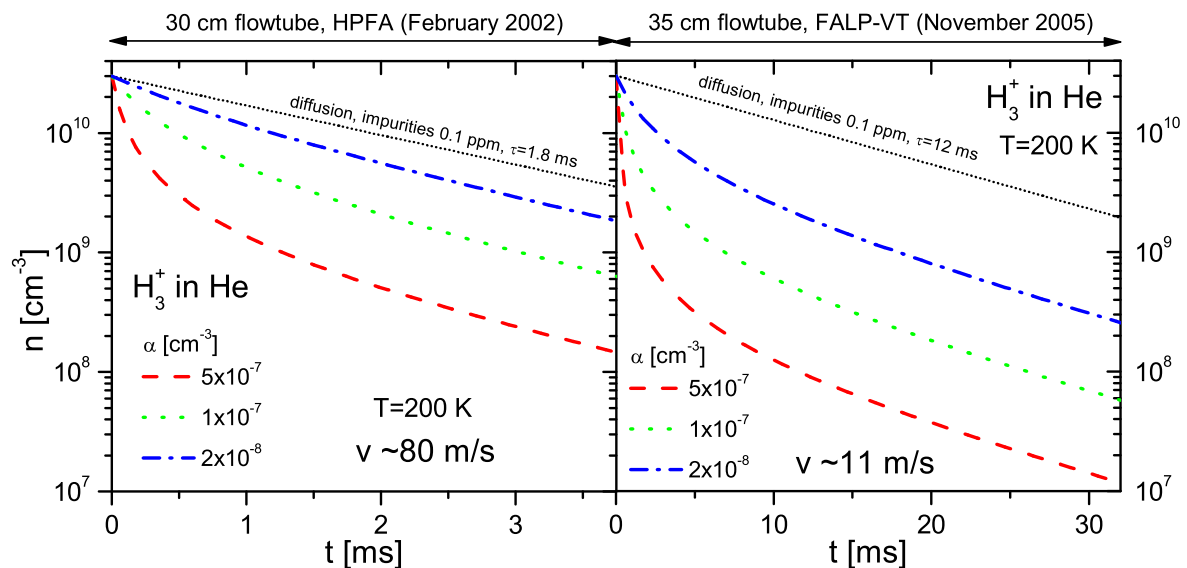
Figure 2.4: A comparison of losses due to recombination and diffusion in the *HPFA* apparatus (left panel) and in the new *FALP-VT* apparatus (right panel). The simple model includes losses by recombination, ambipolar diffusion and by ion-molecule reactions at typical conditions. For details see section 2.2.3, particularly equation 2.9. Diffusion losses are calculated from mobility of H_3^+ in He gas at temperature $T = 200$ K and pressure $p = 1100$ Pa.

There are two interpretations for this improvement: Firstly, the diffusion decreased in comparison to recombination. This is valid in the time scale of the experiment. The physical length of the flowtube remained, however, almost the same while the plasma velocity v significantly decreased. Thus it is clearer to work in the spatial scale $x = tv$ where e.g. the diffusion term is $D_a/\Lambda^2 v$ and is proportional to

$$\frac{D_a}{\Lambda^2 v} \propto \frac{D_{a0}\, p_0}{p\, d^2 v} \propto \frac{D_{a0}\, p_0}{p V/t} \propto \frac{1}{Q}, \tag{2.3}$$

where D_{a0} is the coefficient of ambipolar diffusion at pressure p_0, V is the volume and Q the flow rate of buffer gas. As the flow rate Q was not changed, it is obvious that in the spatial scale the diffusion losses remained constant and recombination losses increased. In figure 2.4 the model comparing diffusion and recombination losses in the *HPFA* and the *FALP–VT* apparatuses is shown. This simple model assumes the immediate formation of studied ions. A more detailed model including the plasma formation stage is presented in section 3.2.

Temperature control

The *FALP–VT* is both heated and cooled during different stages of the experimental procedure. In the preparation phase, the whole vacuum chamber including the injection system is heated up to 90 °C to evaporate and pump out impurities condensed on the walls of the vacuum system. It is desirable to heat all parts approximately to the same temperature to avoid re-condensation of "hot" molecules in colder parts of the chamber. The heating is provided by "heating bands" and "heating wires" twisted around vacuum components.

The measurement of the recombination rate coefficient can be performed at different temperatures. In principle, the heating system could also be employed for measurements at higher temperatures. The topic under study require sub-thermal temperatures, however, and thus the main chamber was cooled during the measurement to temperatures in the range 130–300 K. It was already proved at the *HPFA* apparatus that a very short distance is necessary for cooling the gas flowing through the flowtube down to the temperature of the wall – typically a distance corresponding to the diameter of the tube [50]. Thus it is not necessary to pre-cool the plasma in a special section prior to the reaction zone, but the only cooled part is the flowtube itself. The tube is surrounded by two layers of shielding; the first is filled with a cooling medium and the second with an insulating material. For the lowest temperatures, liquid nitrogen is directly poured into the reservoir surrounding the flowtube. For intermediate temperatures, cooled ethanol is applied as a cooling medium, where a thin copper tube lying in the liquid is flushed by liquid nitrogen. In this configuration, the temperature can be maintained within 5 K range during the whole measurement stage of the experiment ($\sim$ 3 hours). The temperature of the flowtube wall is monitored at two different places by means of thermocouples.

Vacuum maintenance

The new *FALP–VT* apparatus was built using UHV technology. The limit of pressure in the main chamber is $\sim 10^{-5}$ Pa and $\sim 10^{-6}$ Pa in the QMS chamber respectively[5]. The apparatus has been recently equipped with a sputter-ion pump which can maintain the main chamber at a low pressure ($\sim 10^{-4}$ Pa) for long time periods.

The next improvement in this domain was reached by controlling important pumping devices with a "safety system". Valves separating the turbomolecular pumps and the primary pumps are now electrically controlled and are automatically closed in the following cases:

- The main power is switched off.

- The power to the primary pump is switched off.

- The turbomolecular pump is overloaded – the rotating frequency decreases below some level, which covers also the case of a sudden high pressure in the chamber.

At the same time, turbomolecular pumps and the heating system are also switched off. The heating system is exclusively switched off when the water that cools the turbomolecular pumps no longer flows through the cooling loop. With this system, the apparatus could be operated safely without human control, which is a great advantage e.g. for pumping during nights. The security system is contained in a new central power control system box.

2.2.2 Data acquisition

Electron density

The electron density is measured by a movable Langmuir probe. The basic principle lies in the measurement of the voltage-current (I-V) characteristics of the plasma, where one electrode is the vacuum chamber and the second electrode is the Langmuir probe. The

---

[5]It is normally possible to get a much lower pressure in the UHV apparatus, but it should be noted here, that the *FALP–VT* cannot be baked (max. used heating is 90 ˚C) and that the apparatus is operated in a high-pressure mode during the experiment, which interrupts the pumping procedure.

voltage is set typically from -1 to $+5$ V, while the measured current ranges from 10^{-9} to 10^{-3} A in a single Langmuir characteristic. Measurement of such low currents in so broad a range requires advanced measurement methods. The measurement itself is performed using a picoammeter/voltage source *Keithley^{TM} 6487* that fulfills the requirements for the current range and precision. Great attention is paid to noise suppression, especially by avoiding loops in wires at the ground potential and to electrostatic shielding of sensitive parts of the measurement system.

The measurement tool is digitally controlled from the PC while acquired values are first stored to obtain the complete Langmuir characteristic and then analyzed in an independent software module. The measurement of each point of the Langmuir characteristic is performed in steps: the probe is first cleaned[6]., then the required voltage is set and the current is acquired over several periods of the power line frequency to get an average value and exclude any influence of noise synchronized with this frequency. An example of the probe characteristic is given in appendix B, figure B.1.

The probe is moved along the flowtube between measurements of a particular probe characteristic. The motion is provided by a step motor, where digital controll of the probe movement and the current measurement is integrated in one software module developed using *LabView^{TM}* software.

The duration of the measurement has been significantly decreased in comparison to experiments at the *HPFA* apparatus. The main reason for this is an automated probe movement and faster operation of the new software control module.

Other quantities

Apart from the Langmuir probe, the apparatus is equipped with several other measurement tools such as pressure gauges, flow-meters and flow-controllers, and a temperature-meter. Measured quantities are acquired directly in digital form or by means of the A/D PC card and then displayed in an integrated window. All values are also saved together with every Langmuir characteristic.

The QMS is controlled digitally and QMS spectra are acquired by means of commercial software. Potentials of particular electrostatic lenses in the ion optics are set with an D/A PC card. The data acquisition schematic is shown in figure 2.5.

2.2.3 Data analysis

The data analysis is separated into two steps. The first phase is the on-line analysis producing the decay of electron concentration vs position of the probe: Each file containing data of the Langmuir characteristic is automatically analyzed employing the theory described in appendix B. The measured electron concentration $[e^-]$ and other analyzed plasma parameters[7] are saved in one file together with values acquired from other Langmuir characteristics measured at different distances. The actual plot of $[e^-]$ vs position of the Langmuir probe z is always displayed on the screen to inform the operator and thus give him a chance to change the parameters of further measurements, e.g. the length of the probe movement step.

In the second phase, the decays of $[e^-]$ vs z are then analyzed independently, thus obtaining the recombination rate coefficient for different physical conditions. The position of

---

[6]The probe cleaning is provided by ion bombardment when the probe potential is set to -80 V for ~ 100 ms
[7]E.g. electron temperature, plasma potential, floating potential, etc., see appendix B.
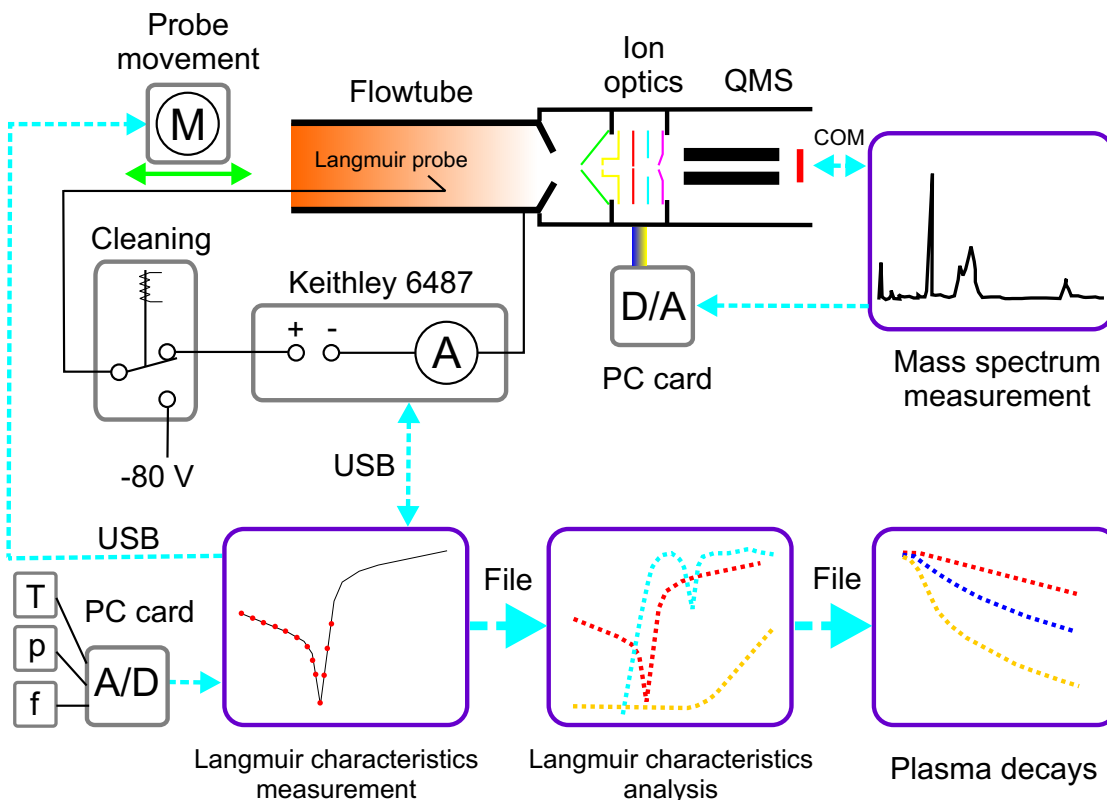
Figure 2.5: The data acquisition schematic and data analysis procedure in the FALP-VT apparatus. Black full lines shows analog signals while dashed lines the digital communication. a detailed description is given in sections 2.2.2 and 2.2.3.

the probe z is first transformed to the time scale applying the conversion formula

$$t = \frac{z}{v_0} \frac{p}{p_0} \frac{T_0}{T} \frac{Q_0}{Q}, \tag{2.4}$$

where v_0 is the plasma flow velocity measured in the center of the flowtube at a pressure p_0, temperature T_0 and flow rate of the buffer gas Q_0. p, T and Q are actual physical conditions. More details concerning the necessity of direct v measurement is given in section 2.2.4.

The time evolution of concentration of the studied ion $[A^+]$ in time is described in a general form by following balance equation:

$$\frac{d[A^+]}{dt} = - \underbrace{\alpha \, [e^-][A^+]}_{\text{recombination}} - \underbrace{k[A^+][B]}_{\substack{\text{ion}-\text{molecule} \\ \text{reactions}}} - \underbrace{D_a \, \Delta[A^+]}_{\substack{\text{ambipolar} \\ \text{diffusion}}} \tag{2.5}$$

saying, that ions $[A^+]$ are removed in recombination with electrons at rate α, in ion molecule reaction with $[B]$ (usually impurities) and by ambipolar diffusion[8] to the walls at a rate coefficient D_a. In the FALP apparatus, the dominance of one ion type in the reaction zone is required. This ensures, together with the quasi-neutrality of the plasma, that the electron concentration is equal to the concentration of the studied ion: $[A^+] = [e^-] = n$.

---

[8] The ambipolar diffusion occurs in the case of high plasma density, where diffusion of both electrons and ions is driven by the electrical field of the space charge and proceeds at the same rate [51, 64].

The plasma concentration n is a function of time and position. Recombination losses and ion-molecule reaction losses do not depend on position. Diffusion, however, depends significantly on the chamber geometry. In an infinitely long cylinder (good approximation for the flowtube) a Bessel distribution of n as a function of radial distance r from the center of the flowtube is established. After relaxation, the distribution decays to the so-called *0 diffusion mode* where $n(r)$ is an 0-Bessel function with maximum at $r = 0$ [51]. In the FALP, the concentration n is always measured at $r = 0$. Thus the measured decay in time (or in z, see relation 2.4) due to diffusion is simplified to

$$\frac{dn}{dt} = -\frac{D_a}{\Lambda^2}\, n.$$ (2.6)

The equation 2.5 can be then rewritten as

$$\frac{dn}{dt} = -\alpha\, n^2 - k\, n[B] - \frac{D_a}{\Lambda^2}\, n.$$ (2.7)

Here Λ is the characteristic diffusion length depending purely on the flowtube geometry[9]. After final simplification, we obtain

$$\frac{dn}{dt} = -\alpha\, n^2 - n/\tau$$ (2.8)

taking notice that the term $1/\tau = k\,[B] + D_a/\Lambda^2$ is a constant. It could be seen, that diffusion losses and losses due to ion-molecule reactions can be combined in the same term and thus have the same behavior. In the case of $\alpha = 0$, the solution of equation 2.8 gives an exponential decay of $[A^+]$ in time characterized by τ. On the other hand, when $1/\tau = 0$, the decay displays a hyperbolic behavior[10]. Usually both processes are included, however, and thus the general solution has to be used to describe the observed concentration decay:

$$n(t) = \frac{n_0}{\alpha\, \tau\, n_0(\exp t/\tau - 1) + \exp t/\tau}$$ (2.9)

Here n_0 is an initial concentration at $t = 0$.

Measured data $n(t)$ are fitted with equation 2.9 where n_0, α and τ are examined parameters. Thus the result is not only the desired recombination rate coefficient, but also a parameter describing "exponential" losses. This is often applied to estimate the amount of impurities $[B]$ as the diffusion part can be easily estimated from tabulated values. For examples of decay curves see e.g. figure 3.13.

2.2.4 Experimental procedure

The experimental work at the *FALP–VT* apparatus can be divided into preparation and measurement stage. During the preparation phase the Roots pump is disconnected and the main chamber is pumped only with the turbomolecular pump. Several other valves are opened to connect different parts of the chamber via shorter and broader junctions with higher conductance and thus provide higher pumping rate. At the same time, the vacuum

---

[9]For an infinitely long cylinder $\Lambda = R/J_0$, where R is the diameter of the cylinder and J_0 is a 0 Bessel coefficient $J_0 \doteq 2.4$.

[10]The solution of equation 2.8 for $\alpha\, n \gg 1/\tau$ is: $1/n = 1/n_0 + \alpha t$. Thus data plotted as $1/n$ vs t gives a linear trend with slope α. Such a solution is often used as a first approximation to the rate coefficient and in case of negligible "exponential losses" can be also used for the final result.

chamber is heated to make the desorption of impurities from walls more effective. The gas injection system is also prepared in the same way. Zeolite pumps are periodicaly flushed by helium.

The duration of the cleaning stage depends on the previous level of purity. Between experiments, the cleaning takes usually one day. After opening and closing the chamber, however, more than one week is necessary to clean the system.

On the experimental day, the chamber is pumped and heated for 2–3 hours. The apparatus is then separated into the high-pressure part pumped by a Roots pump (flowtube) and the low-pressure parts pumped by turbomolecular pumps (ion optics and QMS chamber) by closing corresponding valves. Helium is introduced and after reaching the required pressure, the discharge is ignited. The flowtube is slowly cooled with cold ethanol or liquid nitrogen down to the required temperature, while the walls of the flowtube are further cleaned by energetic ions and metastable neutrals in excited states. The evolution of the plasma composition is also checked with the QMS, while spectra for both positive and negative ions can be acquired. The measurement of recombination starts usually within 1 hour after switching off the heating system.

A first measurement is always performed in an helium-argon plasma. As Ar^+ recombines extremely slowly, the observed decay should behave exponentially in time and corresponds only to diffusion and losses due to ion-molecule reactions. The decay time is compared with expected values for pure diffusion. A measurement of the recombination of the ion under study is then performed under different physical conditions. Usually varied parameters are the concentration of reactant gas, temperature of the flowtube and the pressure of the buffer gas.

Flow velocity

The flow of neutral gas in a viscous environment in a cylindrical tube should display a parabolic velocity distribution in the radial direction. In reality, at the wall, the velocity gradient is much higher and "slipping" can be observed. Thus it could be complicated to calculate the flow velocity in the center of the flowtube just from the flow rate of the buffer gas and the pressure. Moreover, electrical fields in the plasma due to gradients in the plasma concentration and the sheath layer around the walls causes deviations in the velocity distribution in the plasma with respect to the velocity distribution in the buffer gas. It is thus that the plasma flow velocity can differ from the buffer gas velocity. Therefore the "time-of-flight" method is applied to determine the plasma flow velocity experimentally. The plasma concentration is pulsed by changing the power in the microwave source. The time of arrival of the pulse t is registered with the Langmuir probe at different distances z from the plasma source. The velocity can then be easily obtained from the slope of the plot of z vs t.

Langmuir probe calibration

As discussed in appendix B, the Langmuir probe has to be calibrated, especially when used at high pressures as in the case of the *FALP–VT*. The calibration is performed by measurement of the recombination rate coefficient for O_2^+ with electrons. The rate coefficient is well known over a wide range of temperatures and pressures [55]:

$$\alpha(O_2^+) = 2.0 \times 10^{-7}(300/T^{0.65}) \text{ cm}^3\text{s}^{-1}. \tag{2.10}$$

From the ratio of the tabulated value and the measured value, a correction factor is obtained which is then applied to multiply the measured electron density values or could be used to directly correct the final rate coefficients.

2.2.5 *FALP-VT* evolution

In the above sections, the latest version of the *FALP–VT* apparatus (as of November 2005) has been described. The development was not always straightforward, however, and one less successful version was tested. The evolution of the apparatus from *HPFA* (February 2002), through the *FALP-VT-prototype* (March 2005) to the latest *FALP–VT* (November 2005) is shown in figure 2.6. The version *FALP-VT-prototype* already had the flowtube of 5 cm in diameter, but the connection link between the discharge tube and the flowtube was only 1.7 cm in diameter and the transition between them was not gradual due to the mechanical construction of the probe movement system. As a result, the measured flow velocity was not constant along the whole flowtube and an additional correction for this effect had to be applied to the measured data. The corrected electron density decays measured in a pure argon plasma also displayed a different behavior than the expected decay due to diffusion only. A reason for this effect has been suggested: the inconsistency in the flow direction at the beginning of the flowtube. If the main stream does not flow through the center of the tube, then the Langmuir probe does not measure the maximal electron density as is usual in the case of uniform flow. We did not succeeded in suppressing this effect either by numerical correction of the data nor by mechanical correction of the flow direction using a spacer inserted into the critical section.

This inconsistency was not important for measurements of recombination rate coefficients greater than $\sim 1 \times 10^{-7}$ cm^{3}s^{-1} as it was negligible in respect to the fast decay due to recombination[11]. The *FALP-VT-prototype* have been used for investigation of D$_3^+$ and D$_5^+$ recombination (chapter 3, especially section 3.4). For slower reactions, however, it was impossible to reach a valid result. Thus a new flowtube with a gradual transition of diameters and with less sharp bending has been designed and this version have been used for the presented measurement on H$_3^+$ (chapter 3, especially section 3.5).

---

[11]Strictly speaking, the lower limit of measurable recombination rate coefficient is also given by the duration of ion formation. During long ion formation stage the electron density decreases and the parasitic effect is then more important in respect to recombination losses.
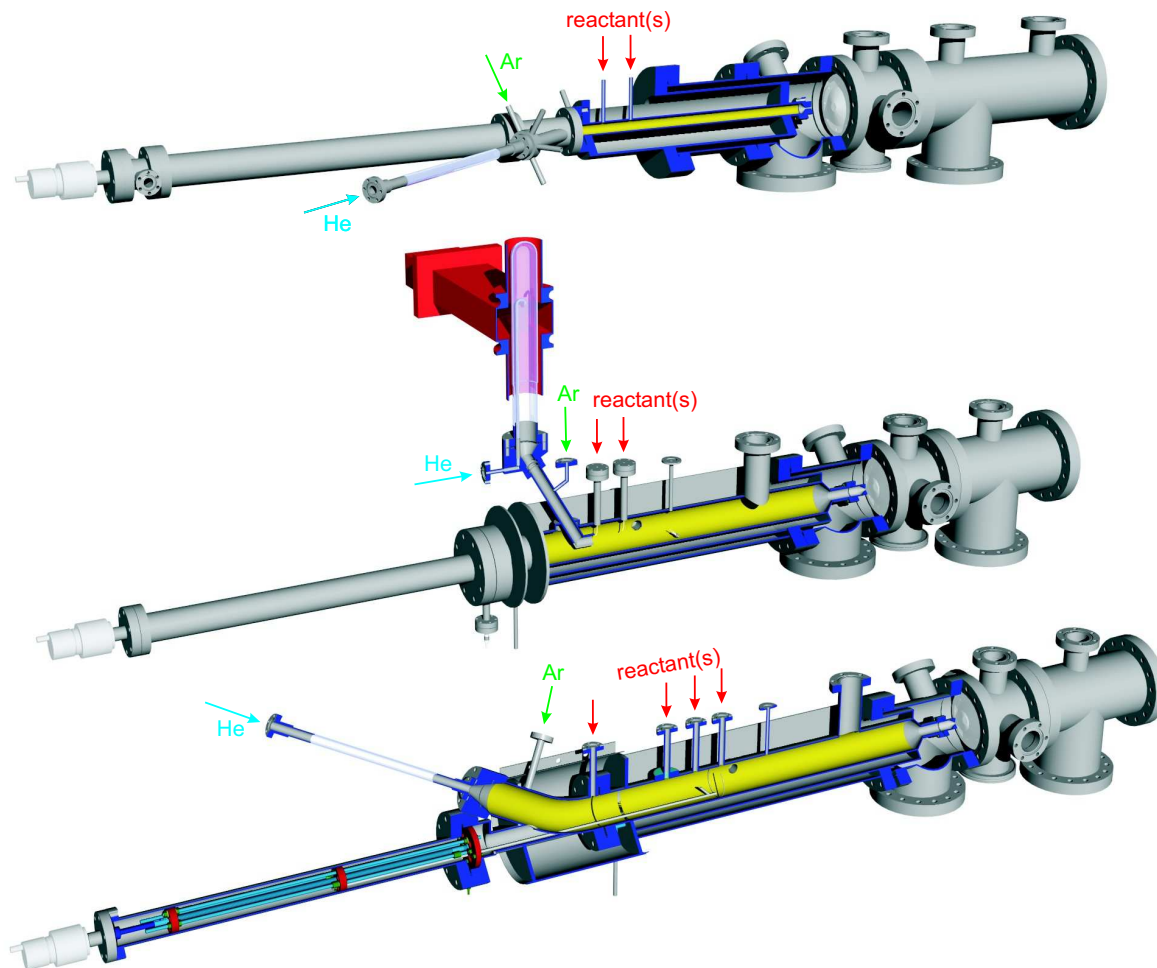
Figure 2.6: Main chambers of FALP apparatuses described in section 2.2. The buffer gas flows from the left (glass discharge tube) to the right. Chambers are opened to show the internal arrangement. Blue faces indicate the section, yellow faces highlight the flowtube. Fully right part (not open) are chambers of the ion optics and of the QMS. All chambers were designed directly in 3D. **Top:** The *HPFA* apparatus (February 2002). Flowtube diameter: 17 mm. **Middle:** The *FALP-VT-prototype* apparatus (March 2005). Flowtube diameter: 50 mm. Vertical orientation of the discharge tube significantly simplified the cooling procedure. However, two bends on the tube between the discharge and the flowtube decreased the initial electron density and a step transition at the beginning of the flowtube affected the laminarity of the flow and thus made the analysis impossible for low recombination rate coefficients. **Bottom:** The *FALP–VT* apparatus (November 2005). Flowtube diameter: 50 mm. Number of diameter changes and the total bend angle have been minimized to 30°. After a simple rebuilding, the apparatus will be also prepared for spectroscopic measurements along the flowtube.
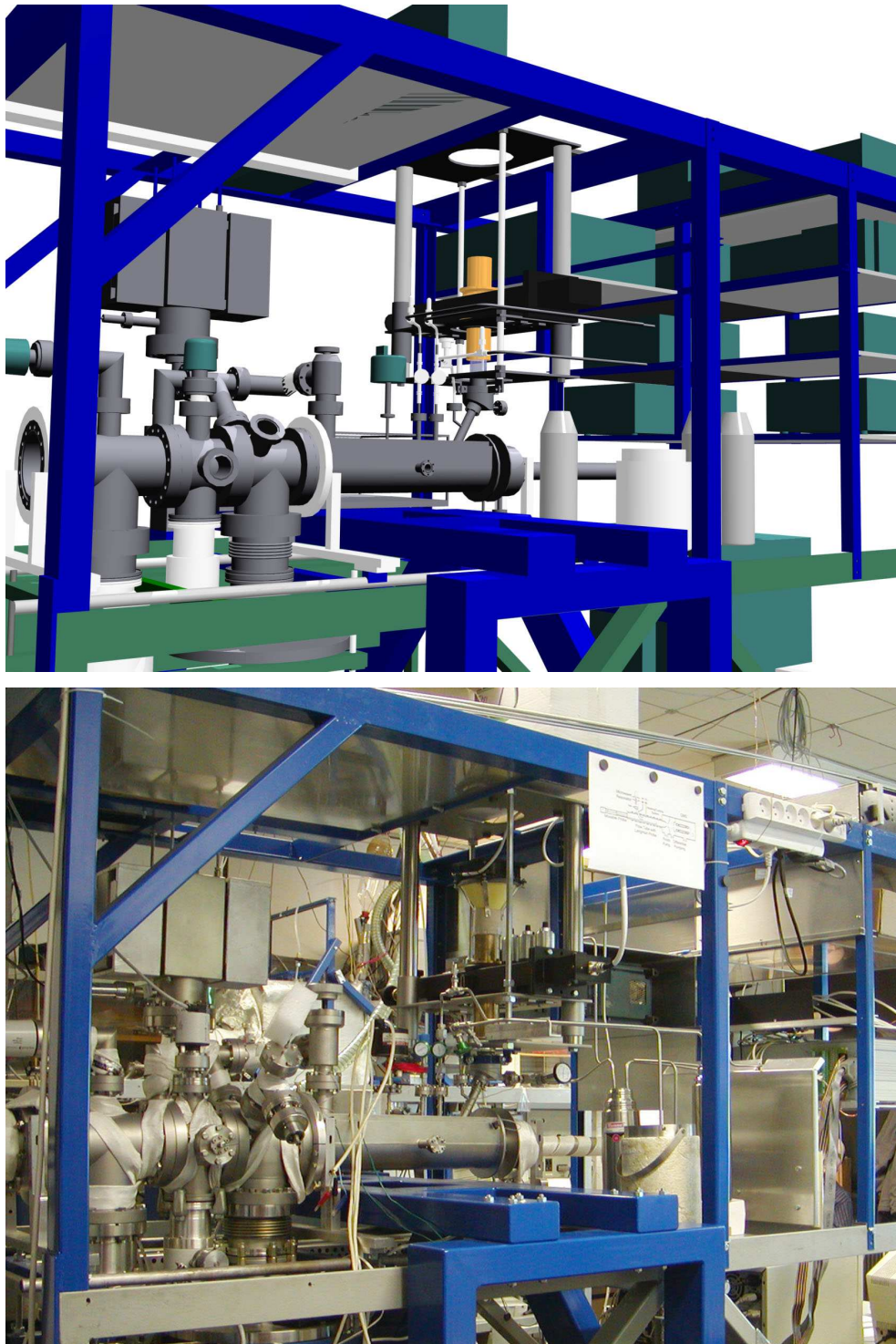
Figure 2.7: The apparatus *FALP-VT-prototype* in January 2004. Top panel: the whole chamber and also surrounding systems have been designed in 3D. The precise design significantly compressed the building stage. Bottom: Photograph of the constructed apparatus.

2.3 The *FlAPI*

The *FlAPI (Flowing Afterglow with Photo-Ions)* is a new technique designed and operated at the University of Rennes I. The need for the development of this method arose from limitations of the *FALP–MS (Flowing Afterglow with Langmuir Probe and Mass Spectrometer)* method [38] when applied to the measurement of the recombination of large polyatomic ions such as PAHs (*Polycyclic Aromatic Hydrocarbons*) with electrons. Before finishing this thesis, PAHs were the only species studied with the *FlAPI* and in the following text, PAHs are used as a general example of large polyatomic molecules.

In the *FALP–MS*, the ions to be studied are produced via charge-transfer reactions of neutral PAHs with precursor ions (usually He^+ and Ar^+). Production of PAH cations in this way is not very effective and thus a high concentration of neutral PAHs is required. However, effects due to electron attachment to PAHs, producing negative PAH anions and pollution of the Langmuir probe by condensed PAHs, significantly decrease the precision of the measurement. In the *FlAPI*, an alternative process for ion production requiring lower concentration of neutral PAHs has been used and thus this unique technique is much more adapted for the study of PAH recombination. For further discussion on the motivation of the *FlAPI* development and on PAH recombination, see section 4.1.

2.3.1 Description of the apparatus

The *FlAPI* apparatus (see figure 2.8) is based on the frame of the *FALP–MS* apparatus and it is possible to switch between both techniques without mechanical changes to the chamber. The apparatus is equipped with two main measurement tools, the Langmuir probe and the Quadrupole Mass Spectrometer (QMS), both movable along the axis of the main chamber. An afterglow is formed in a helium buffer gas, introduced into a cylindrical glass tube (40 mm in diameter) surrounded by a microwave cavity operating at 2.45 GHz. The main chamber is pumped by a Roots pump (4000 m^3h^{-1}), while the chamber of the QMS is differentially pumped by the turbomolecular pump reaching the limit pressure of $< 10^{-4}$ Pa. All experiments presented in this work have been performed at a pressure of 100 Pa in the main chamber and the buffer gas flow rate $\sim$ 20 slpm. Such a pressure corresponds to a helium density of 2.6×10^{16} cm^{-3} fulfilling preconditions for Langmuir probe measurements (see appendix B for details on Langmuir probe measurements).
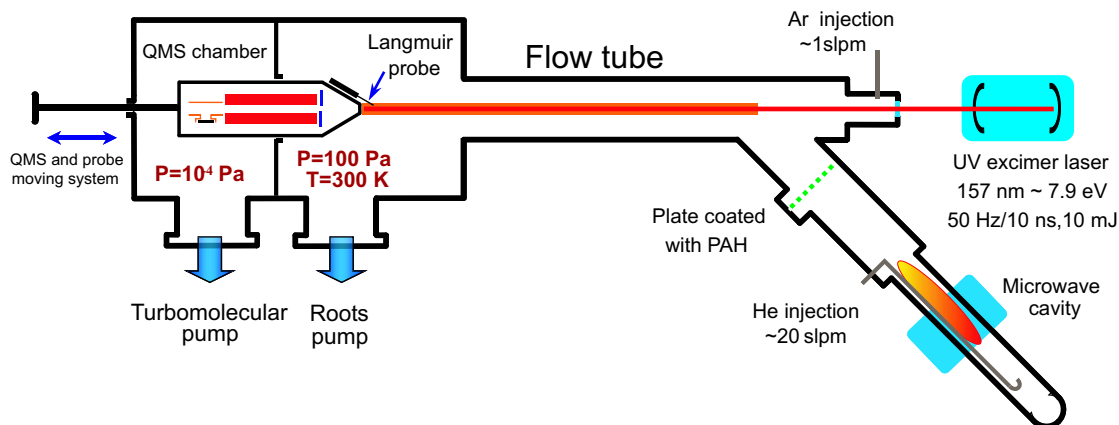
Figure 2.8: The FlAPI apparatus.
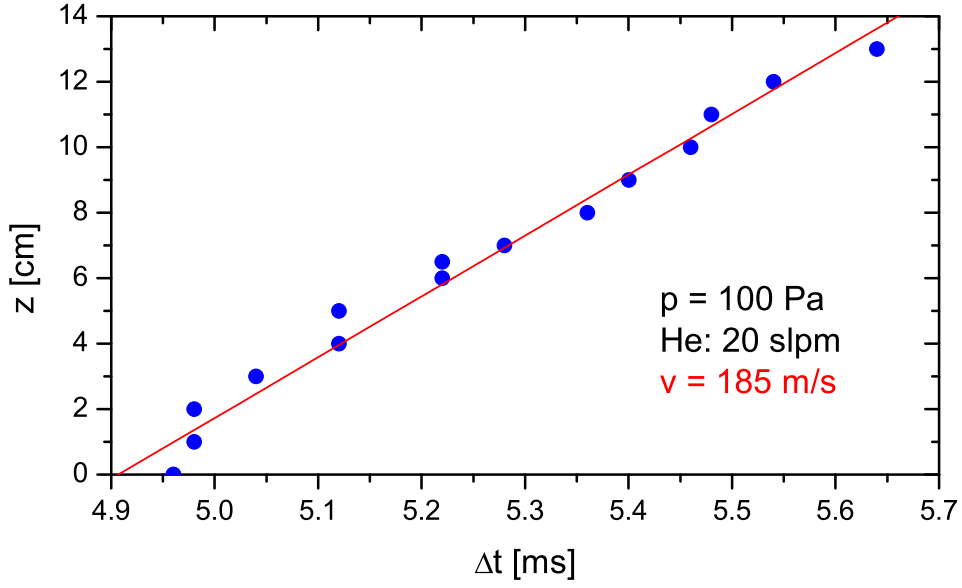
Figure 2.9: An example of buffer-gas flow velocity determination at pressure 100 Pa and He flow rate 20 slpm. The electron density was converted to pulses by modulating the power in the microwave resonator. The velocity has been determined from the time difference Δt between the pulse generation and its arrival at the Langmuir probe over the actual position of the Langmuir probe z. In the figure data are plotted reciprocally giving v directly as a slope of the linear fit.

Under these conditions, the velocity of the flow derived from time of flight measurements (figure 2.9) was $v = 185 \pm 15$ m/s. Defining the "reaction zone" as the zone that can be scanned by the movable Langmuir probe, and this being 14 cm long, the hydrodynamic measuring time was ~ 0.75 ms.

The afterglow plasma contains neutral ground state helium atoms He, metastable excited state helium atoms $He^M(2^3S)$ and helium ions He^+ and He_2^+. Argon is introduced downstream at a second entry port at about 1 slpm to remove He^M atoms[12] by Penning ionization [52]:

$$He^M + Ar \longrightarrow He + Ar^+ + e^- \qquad\qquad k_1 = 7 \times 10^{-11} \text{ cm}^3\text{s}^{-1} \qquad (2.11)$$

It also reacts via ion-molecule reactions (charge-transfer) with helium ions [53]

$$He^+ + Ar \longrightarrow He + Ar^+ \qquad\qquad k_2 < 10^{-13} \text{ cm}^3\text{s}^{-1} \qquad (2.12)$$

$$He_2^+ + Ar \longrightarrow 2He + Ar^+ \qquad\qquad k_3 = 2.1 \times 10^{-10} \text{ cm}^3\text{s}^{-1} \qquad (2.13)$$

and thus a plasma containing both He^+ and Ar^+ ions is produced. Argon is introduced near the MgF_2 laser entry window and is also employed as a counterflow protecting the window from pollution.

The apparatus is equipped by another entry port for the reactant gas at the beginning of the reaction zone. In the *FlAPI* mode, this port is used only for introducing oxygen for calibration of the Langmuir probe (see section 2.3.2). There is no direct gas phase injection

---

[12]Metastable atoms He^M may release their internal energy and ionize the reactant gas in the reaction zone at an uncontrollable rate, thus making the data-analysis impossible.

of PAHs into the afterglow. PAHs are dissolved in acetone, and the solution is deposited on both sides of a stainless steel plate with a total surface area of ~ 100 cm^2. The solvent spontaneously evaporates, leaving the plate coated with a solid PAH powder. The plate is then mounted into the *FlAPI* tube downstream of the discharge where PAHs evaporate at room temperature and react by ion-molecule reactions with the rare gas ions of the afterglow or are ionized by the excimer laser beam oriented along the axis of the flow-tube. Preliminary experiments have shown that the PAH cations present in the flow are not formed by surface sputtering by energetic He$^+$ or He$_2^+$ ions: When the support, coated with PAHs is frozen down to liquid nitrogen temperature, the mass spectrometric measurement has shown that PAH cations are no longer produced. PAHs in a liquid state or solid PAHs with too high vapour pressure (the layer on the metal plate is evaporated too quickly) can be evaporated in an external reservoir flushed by helium gas and then injected in a controlled amount by the inlet replacing the plate. It should be noted here, that in both cases, the amount of PAHs introduced into the chamber is much lower than the amount required for using the *FALP–MS* technique[13].

All introduced gases can be cleaned in condensate or sorption traps to remove impurities, mainly H$_2$O, in order to decrease the influence of ion-molecule reactions in the measurement zone. For details on the vacuum schematic of the *FlAPI* apparatus, see figure 2.10.

2.3.2 Electron density and temperature

The initial electron density can be varied by adjusting the position of the microwave discharge with respect to the buffer gas entry port in a range of $10^8 - 3 \times 10^{10}$ cm^{-3}. The electron density is measured in the reaction zone by a movable heated Langmuir probe [54], 19 mm long and 25 μm in diameter (see appendix B for details on the measurement procedure). An example of such a measurement is given in figure 2.11, where a slight exponential decay can be observed. The decay time $\tau_e \sim$2 ms does not depend on the presence of PAHs in the flow, and the decay process is attributed to ambipolar diffusion and ion-molecule reactions[14].

We have learned from previous experiments that when PAHs are present in the afterglow, the measured electron density can shift due to progressive pollution of the probe which can change the effective probe diameter and cause so-called "surface effect"[15]. To take into account this eventual shift and to control the probe state, a probe calibration is performed immediately after the recombination rate measurement, and under the same conditions. This is done by measuring the kinetics of the dissociative recombination of O$_2^+$ with electrons[16], and the value for this rate coefficient is compared to the well documented value $\alpha(300$ K$) = 2.0 \times 10^{-7}$ cm^{3}s^{-1} [55] to obtain a correction factor. The measured value never differed from the literature value by more than a factor of two. We can then directly scale the PAH$^+$ recombination rate coefficient by this calibration factor, as the electron density is proportional to the measured rate coefficient (see the data analysis section 2.3.4 and an example in figure 4.2).

In our experimental conditions, the momentum transfer during He-electron collisions is such that the time needed for the electron temperature to differ from the room temperature

---

[13]There are not enough neutral PAHs to convert a significant amount of Ar$^+$ and He$^+$ ions to PAH cations.

[14]Mainly H$_2$O reacts rapidly with Ar$^+$ and He$^+$ ions producing H$_3$O$^+$, which recombines immediately. The charge loss rate is then limited by H$_3$O$^+$ formation and ambipolar diffusion, where both processes behave as an exponential decay in time.

[15]This effect is mainly caused by low conductivity of sticked layer of "impurities".

[16]The basic FALP technique is used for measuring only the electron density decay in time.

Figure 2.10: The vacuum schematic of the *FIAPI* apparatus.
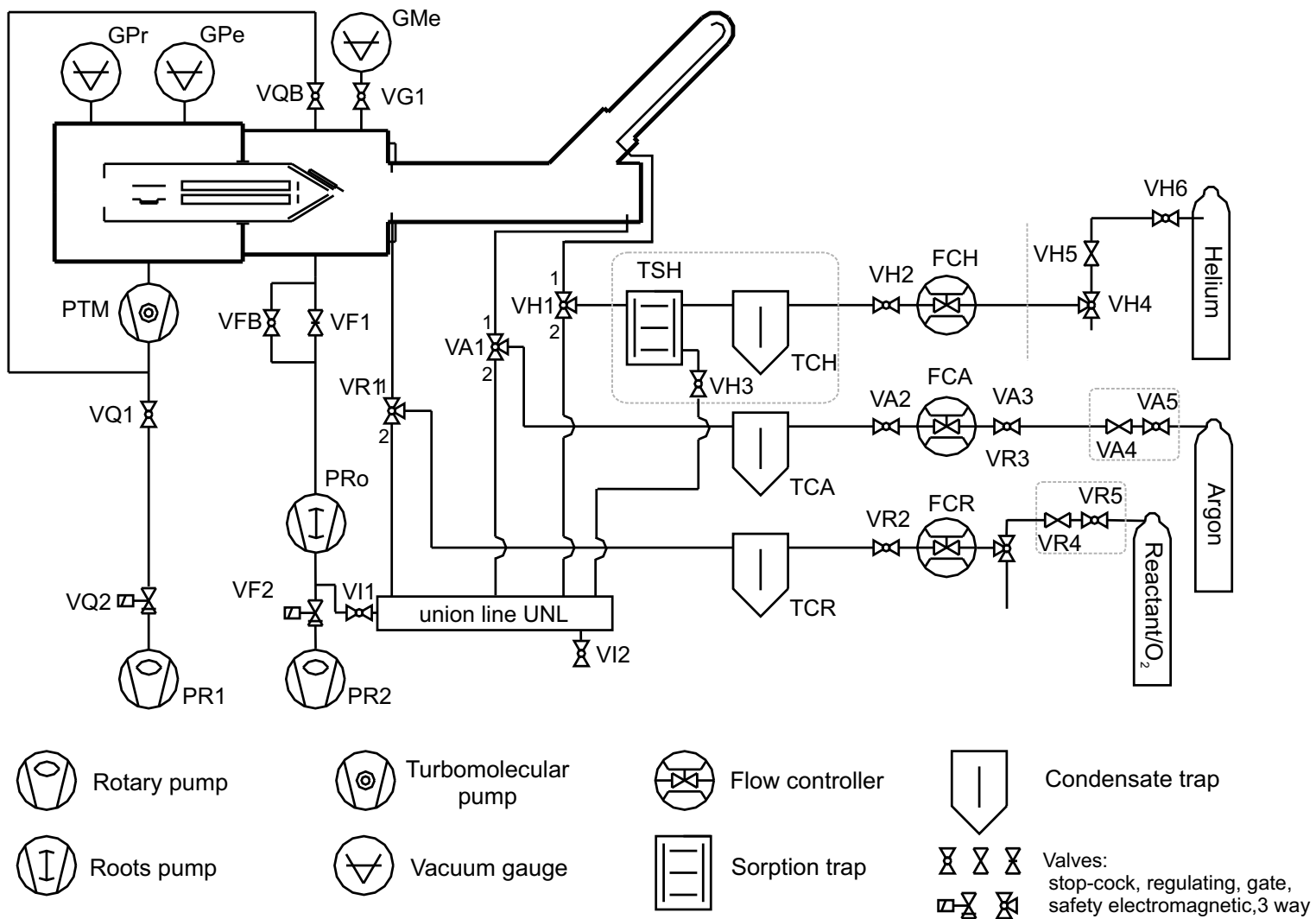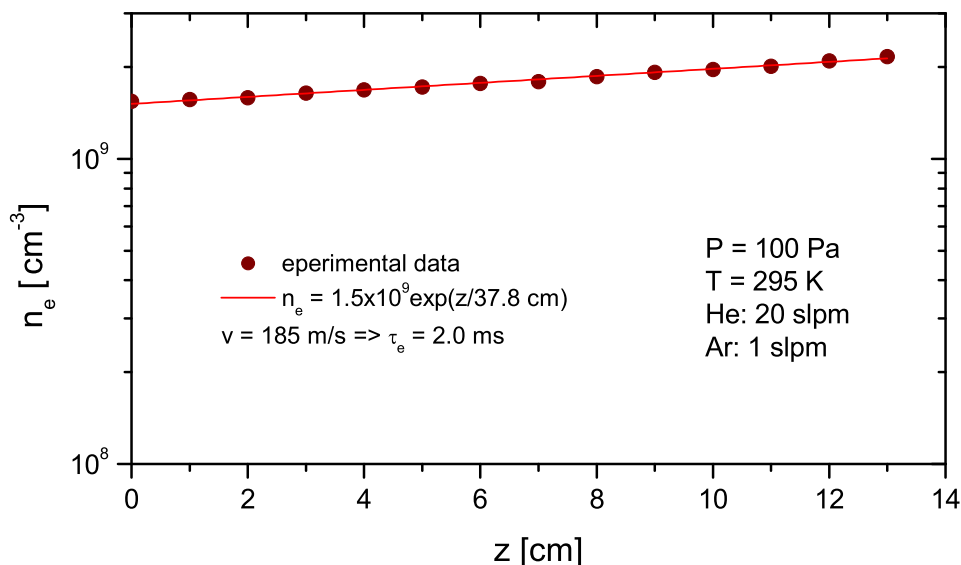
Figure 2.11: An example of the electron density measurement by the movable Langmuir probe. Electron density n_e is plotted versus probe position z, where $z = 0$ corresponds to the position at the end of the flowtube, farthest from the microwave cavity. The plasma than "flows" from the right to the left and n_e decays in time.

by no more than 1% is estimated to be about 100 μs [56]. Relaxation through momentum transfer by electron-electron collisions is even faster. The electrons are thus thermalized to the temperature of the flow at about 10 cm downstream of the cavity. As the reaction zone is situated about 1m downstream, the post-discharge flow is thermalized at 300 K.

2.3.3   Ion formation

As already mentioned, in the *FlAPI* method, photo-ionization is used for producing PAH$^+$ ions. Charge transfer reactions between Ar$^+$, He$^+$ and neutral PAHs take place as well, however, and is also included in the physical model used for the data-analysis. Any qualitative formulations in this section are related to the experiments on anthracene ions ($C_{14}H_{10}^+$, mass 178 amu), as anthracene have been used in most test measurements during the development and testing of the *FlAPI* technique.

Charge transfer

When the laser is off, the concentration of PAH$^+$ in the flow reaches a steady state, as their formation by ion-molecule reactions is compensated by their destruction by recombination. This can be checked by mass spectrometry where the PAH$^+$ density can be evaluated from the relative peaks heights to be about 1% of the total ion density (see figure 2.12), thus ranging from 10^6 to 5×10^7 cm^{-3} according to the initial electron density.

The reactions of anthracene with He$^+$ and Ar$^+$ have been found to proceed at the Langevin rate[17] and by analogy, we assume that the reactions of other PAHs with the same ions are

---

[17]Langevin capture theory [57] allows one to calculate the rate for ion molecule reactions as $k_L = 2\pi q \sqrt{\frac{\alpha}{\mu}}$, where q is the ion charge (esu units, elementary charge $= 4.8 \times 10^{-10}$), α is the polarizability volume of the
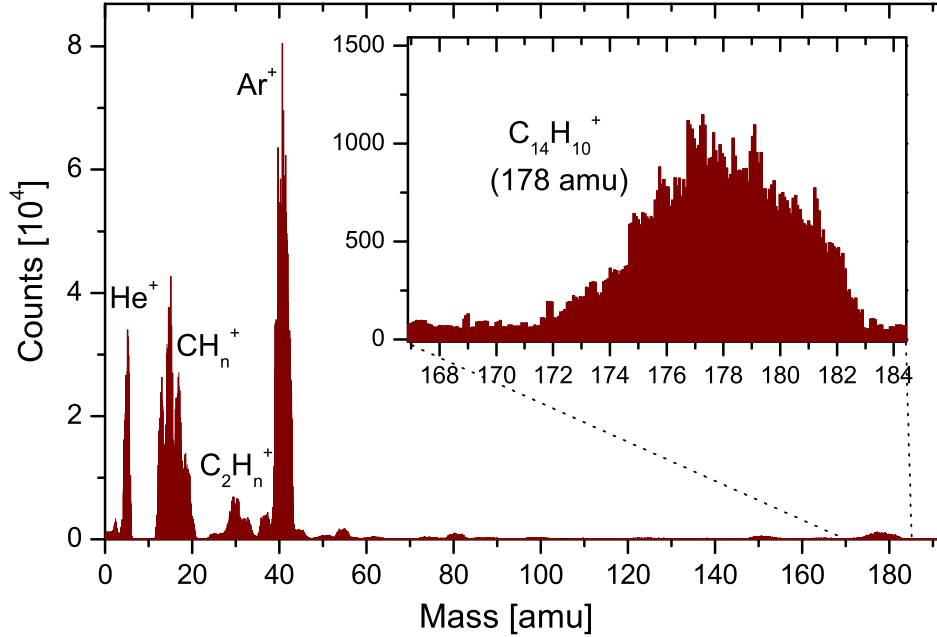
Figure 2.12: An example of the mass spectrum measured with laser switched off and microwave discharge switched on. The plate has been coated by anthracene $C_{14}H_{10}$ (178 amu). The electron density n_e have been set to $\sim 10^{10}$ cm^{-3}. The spectrum displays ions produced by ion molecule reactions with impurities, (mainly water H_2O and hydrocarbons), in addition to Ar$^+$, He$^+$ and PAH$^+$. The broadening of the peak corresponding to anthracene ions is due to low resolution of employed QMS.

fast also. The neutral PAH density can then be calculated from the steady state, estimating the recombination rate to be about 10^{-6} cm^{3}s^{-1}. Such a density (see the estimated plasma composition before the laser shot in table 2.1) is low enough to ensure that the conversion of gas phase neutral PAHs into ions is not complete within the hydrodynamic time of the experiment, leaving most (99%) of the gaseous PAHs, neutral.

	[He]	[Ar]	[PAH]	[e$^-$]	[PAH$^+$]
Density [cm^{-3}]	2.6×10^{16}	10^{15}	$< 5 \times 10^{10}$	$3 \times 10^8 - 5 \times 10^9$	$10^6 - 5 \times 10^7$

Table 2.1: The plasma composition in the *FlAPI* apparatus before the laser shot.

Photo-ionization

An F$_2$ excimer laser (Excistar M-100, Tuilaser) operating at 157 nm (the beam propagating along the flow) is used to produce the ions to be studied. The ions can be formed only if the

---

neutral molecule (cm^3) and μ is the reduced mass of the system (g). Using the polarizability for anthracene $\alpha = 2.5 \times 10^{-23}$ cm^3 [58] we obtain the following rate coefficients for reactions of anthracene neutrals with He$^+$ and Ar$^+$ respectively: $k_{He+} = 6 \times 10^{-9}$ cm^{3}s^{-1}, $k_{Ar+} = 2 \times 10^{-9}$ cm^{3}s^{-1}. For details see ref. [59].

vertical ionization potential[18] of the neutral parent of the cation is less than the equivalent laser energy 7.87 eV. While we choose ions with ionization energies very close to the energy of the excimer laser (see table 4.1), we minimize the energy, which can be stored in excited states of PAH$^+$, or which can be used for breaking the molecule. Before finishing this thesis we were not able to measure full mass spectra in synchronization with the laser shots and so directly observe the production of ionized fragments. However, a good estimation may be performed based on QMS spectra measured without the laser: As the ionization potentials of both He and Ar are much higher[19] than the energy of the laser used, He$^+$ and Ar$^+$ may produce PAH$^+$ in ion-molecule reactions with neutral PAHs (as discussed above). Measured QMS spectra (figure 2.12) do not display heavy fragments corresponding to the removal of a whole benzene ring or even of particular C atoms. On the other hand, the broad peak observed in the low resolution spectrum around the mass of the parent PAH may also include dehydrogenation. This effect should not appear, however, in the case of photoionization as quite a high energy is needed for removing the hydrogen atom from the PAH molecule[20]. Peaks corresponding to CH_n^+ and $C_2H_n^+$ do not have to originate from the dissociation of PAH$^+$, but may be formed by deposition of condensed and transformed hydrocarbons from the surface of the chamber. Moreover, the data analysis remains valid even if other ions are formed by the laser shot or other processes.

The plasma is optically thin for the laser beam used: The laser pulse duration is 10 ns, and its energy is 10 mJ per pulse. This energy is high enough to ensure that the decay of photon density along the flow-tube is negligible and immediately after the laser shot, a column of PAH cations is formed, whose density is constant along the flow-tube. The photon density decay length was estimated to be $1/(\sigma\,[\mathrm{PAH}]) > 7 \times 10^9$ m, as the photoionization cross-section σ for anthracene is lower than 1.5×10^{-17} cm^2 at 157 nm [62].

The laser shot produces the same amount of photoelectrons and PAH cations. Over the time ranges used for data analysis, the density of these additional electrons is verified to be negligible compared to the electron density that prevails without photo-ionization. Langmuir probe measurement synchronized with the laser shot, performed with "laser on" but without the microwave discharge yields an estimation of the photo-electron density lower than 10^8 cm^{-3}. In addition, no variation of the electron density decay is noticed (with the microwave discharge on), when the photo-ions are created, as should be the case for a fast recombination reaction with a high density of reactants. The estimation of [PAH$^+$] using an estimated concentration of neutral PAHs (see table 2.1) and the photo-ionization cross-section (see the paragraph above) gives a value lower than 10^{10} cm^{-3}. This value is an upper limit for the following reasons:

- The value of [PAH] is an upper limit.

- The energy of 1 laser pulse may be lower than the value of 10 mJ used in the estimation (this value is normally not reached).

---

[18]The vertical ionization energy is the minimal energy required for ionization without changing the distance of atoms in the molecule. This is typical for fast processes such as photoionization. On the other hand the adiabatic ionization energy is the difference between potentials of ground states of neutral molecule and of produced ion and is thus usually lower than the vertical ionization energy.

[19]$E_i(\mathrm{He}) = 24.6$ eV, $E_i(\mathrm{Ar}) = 15.8$ eV.

[20]The C–H bond dissociation energy for PAH molecules was estimated from indirect experimental evidence by *Léger et al* [60] as $E_{CH} = 4.5$ eV. For the C–C bond, the value is even higher $E_{CC} = 8$ eV. *Fujiwara et al* [61] calculated dissociation energies of C–H bond for 13 PAH cations with number of carbon atoms lower than 40. In all cases the value is $E_{CH} = 4.65 \pm 0.04$ eV.
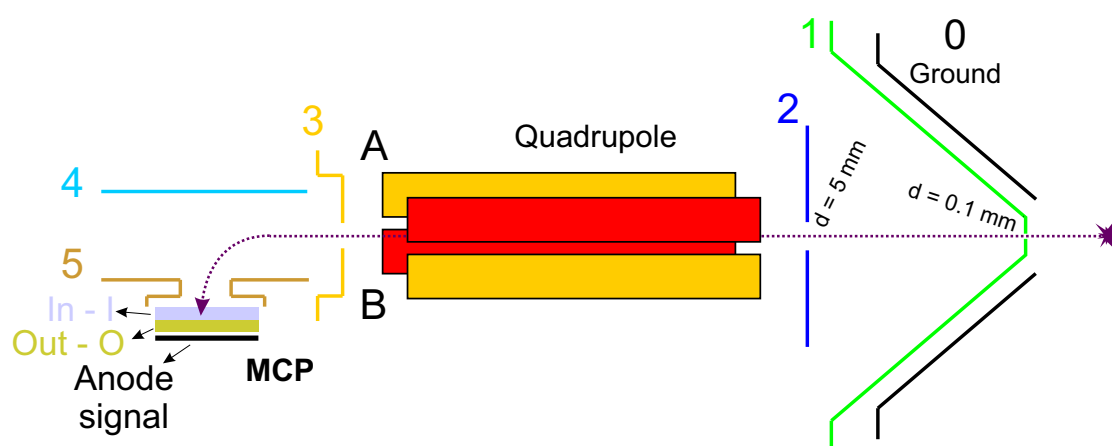
Figure 2.13: Basic schematic of the Quadrupole Mass Spectrometer used in the *FlAPI* apparatus. Electrostatic lenses are numbered 0 - 5, where lens 0 is at ground potential to avoid the influence of electrical fields on the plasma and Langmuir probe, lenses 1, 2 and 3 are employed as focusing lenses and 4 and 5 deflect ions to the MCP detector. Two pairs of rods A and B form the quadrupole, where A and B are at high voltage – high frequency potential allowing transmission of ions of selected mass and charge only [63]. The aperture in lens 1 is the only "junction" for gas-phase particles between the main chamber and the chamber of QMS.

- The entrance window may cause a loss of a significant proportion of photons.

- The geometrical cross-sectional area of the laser beam used in the estimation (and declared by the laser manufacturer, 4×7 mm) seems to be lower, that the real cross-sectional area observed during laser alignment.

The arguments listed above can decrease the maximum value of [PAH$^+$] by more than 10-times. Moreover, this value is calculated as an initial value in the center of the flowtube and a numerical model, including diffusion[21] and recombination, shows that within 0.2 ms after the laser shot, the value of the electron density reaches the level seen before firing the laser. This time corresponds to the value of the relaxation time t_1 used in the data-analysis (see section 2.3.4).

PAH$^+$ density measurement

The PAH ions are mass-selected[22] by the QMS (see figure 2.13) and detected by a Multi-Channel Plate (MCP) detector. The PAH$^+$ population is monitored in time at a fixed position at the end of the reaction zone. Signals from events detected by the MCP are pre-amplified, amplified and are registered by a Multi Channel Scaler (MCS) card driven by a personal computer. Both the laser shot and the MCS recording are triggered by the same pulse at a frequency of 50 Hz.

---

[21]In this case a full description of the diffusion in the cylindrical tube is used including all decay modes: $d[e^-]/dt = -D_a \Delta[e^-]$.

[22]Mass fluctuations during the measurement, resolution and calibration of the QMS limits the precision of mass selection to ± 1 amu. Thus dehydrogenated ions cannot be easily separated from ions with the full number of hydrogen atoms.

The delay between two successive recordings is thus much larger than the hydrodynamic time of ion flight through the reaction zone, and the recorded time dependence of PAH^+ density is linked to its decay along the flow. Moreover, the 50 Hz measurement frequency guarantees simple removal of noise synchronized with the power-line frequency. To obtain a signal due to the photo-ions only, two MCS spectra are measured, with the laser switched off and with the laser switched on. Required data are calculated as a simple subtraction of both spectra[23]. Data from several laser shots are accumulated to improve the signal/noise ratio. The measurement schematic is presented in figure 2.14.

The noise observed in the MCS spectra consists of several components:

1. The level of "white noise" does not depend on the time or the number of counts in a particular channel.

2. The noise synchronized with 50 Hz arises from the power line and loops on the ground line. The measurement triggered at 50 Hz allows one to find the region within one period (20 ms) with a constant and minimal level of such noise. Mentioned noise components have been minimized by reducing the length of cables between the MCP detector and the preamplifier. Finally, the preamplifier has been placed in a small chamber cooled by a flowing gas at atmospheric pressure, located inside the vacuum chamber of the QMS.

3. This noise component is not synchronized with any frequency and appears unpredictably as a noise burst in the MCS spectra. Such events are normally much shorter than the data accumulation time and it was possible to remove this component numerically as described in section 2.3.5.

2.3.4 Data analysis

PAH^+ kinetics before the laser shot

The PAH^+ ions produced without involving the photo-ionization undergo several processes in the afterglow and their concentration $[PAH^+]_0$ follows this balance equation:

$$
\begin{aligned}
\frac{d[PAH^+]_0}{dt} &= \left(k_{L1}[Ar^+] + k_{L2}[He^+]\right)[PAH] \\
&\quad -k_d[PAH][PAH^+]_0 - \frac{D_a}{\Lambda^2}[PAH^+]_0 - \alpha[PAH^+]_0[e^-]_0
\end{aligned}
\tag{2.14}
$$

where PAH^+ production is provided by ion-molecule reactions of Ar^+ and He^+ with PAHs at rates[24] k_{L1} and k_{L2}. The PAH^+ destruction is represented by ion-molecule reactions with neutrals[25] at rate k_d, by recombination with electrons at rate α, and by ambipolar

---

[23]The background signal measured with the "laser off" consists of the noise and of events arising from PAH^+ formed by charge transfer. The laser is actually not off during the "laser off" measurement. Instead a mechanical shutter blocks the laser beam and thus both measurements are performed at the same external conditions including possible electrical noise coming from the laser device.

[24]$k_{L1} = 2 \times 10^{-9}$ cm^{3}s^{-1} and $k_{L2} = 6 \times 10^{-9}$ cm^{3}s^{-1} have been calculated as Langevin rates based on the procedure described in section 2.3.3

[25]Neutrals here represent mainly the PAH itself, but PAH^+ may react also with PAH fragments and other neutral molecules.

diffusion[26], where D_a is the coefficient of ambipolar diffusion and Λ a characteristic diffusion length. As was discussed in section 2.3.3 and verified by QMS measurements along the reaction zone, the concentration of PAH$^+$ formed by ion-molecule reactions reaches a steady state: $d[\text{PAH}^+]_0/dt = 0$.

The total concentration of electrons (denoted as $[e^-]_0$) produced in both the microwave discharge and by Penning ionization of He^M, decays by diffusion and recombination. As electron-ion recombination rates for the most abundant ions Ar$^+$ and He$^+$ are slow, the decay in time displays an exponential behavior (see figure 2.11) corresponding to diffusion losses only. The electron attachment influence is excluded as no difference in electron densities measured with and without the presence of PAHs in the chamber has been observed and moreover no distortion of the Langmuir probe characteristic has been noticed.

PAH$^+$ kinetics after the laser shot

At $t = 0$ (the time of triggering the laser), additional PAH$^+$ are created together with photoelectrons by photo-ionization. The concentration of photoelectrons is much smaller than the electron density measured without the laser, and so the total electron density remains very close to $[e^-]_0$.

The kinetics of all PAH$^+$ are now described by the equation similar to eq. 2.14 but $[\text{PAH}^+]_0$ is replaced by the total PAH$^+$ concentration $[\text{PAH}^+] = [\text{PAH}^+]_0 + [\text{PAH}^+]_{\text{PI}}$, where $[\text{PAH}^+]_{\text{PI}}$ is the concentration of photo-ions only:

$$
\begin{aligned}
\frac{d[\text{PAH}^+]}{dt} =\ & \left(k_{L1}[\text{Ar}^+] + k_{L2}[\text{He}^+] \right) [\text{PAH}] \\
& -k_d[\text{PAH}][\text{PAH}^+] - \frac{D_a}{\Lambda^2}[\text{PAH}^+] - \alpha[\text{PAH}^+][e^-]_0
\end{aligned}
\tag{2.15}
$$

Taking into account the steady state that prevails before t = 0, we subtract all terms included in equation 2.14:

$$
\frac{d[\text{PAH}^+]_{\text{PI}}}{dt} = -k_d[\text{PAH}][\text{PAH}^+]_{\text{PI}} - \frac{D_a}{\Lambda^2}[\text{PAH}^+]_{\text{PI}} - \alpha[\text{PAH}^+]_{\text{PI}}[e^-]_0
\tag{2.16}
$$

Equation 2.16 is used in the frame of a Lagrange description, which consist of describing the decay of the ions contained in an elementary cell flowing downstream with the buffer-gas. The cell is at $t = 0$ at a distance $z_1 = vt_1$ from the QMS. For a schematic description, see figure 2.14.

Equation 2.16 can be integrated between the time of the laser shot ($t = 0$) and the time of arrival at the QMS ($t = t_1$):

$$
\ln \frac{[\text{PAH}^+]_{\text{PI},t=t_1}}{[\text{PAH}^+]_{\text{PI},t=0}} = -\frac{\alpha}{v} \int_0^{z_1} [e^-]_0 \, dz - \left(\frac{D_a}{\Lambda^2} + k_d[\text{PAH}] \right) (t_1 - 0)
\tag{2.17}
$$

where time integration over $[e^-]$ is interpreted as integration in position from $z = z_1$ to $z = 0$ ($z = 0$ is at the QMS position).

---

[26] For simple explanation of the ambipolar diffusion process see section 2.2.3. Here the expression of zero-mode ambipolar diffusion is used as it is the main diffusion channel in the cylindrical configuration of the flowtube.
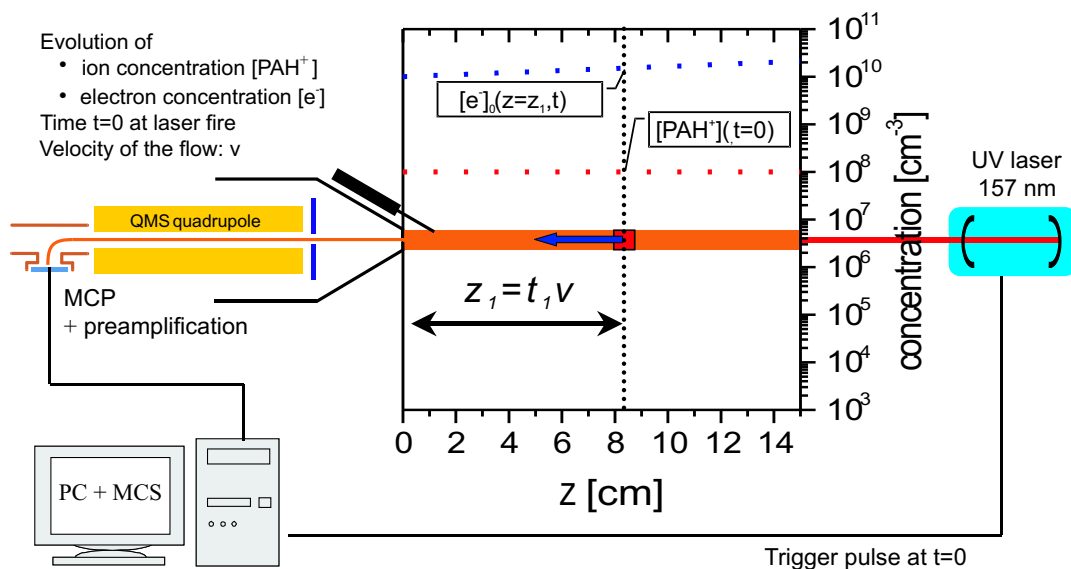
Figure 2.14: The FlAPI: Principle of the data analysis. The laser beam creates a column of ion density $[PAH^+]$ which is constant along the flowtube at time $t = 0$. In the data analysis the description of an elementary cell of PAH^+ flowing with the buffer gas is used (Lagrange description). Note that the electron density $[e^-]_0$ is much higher than $[PAH^+]$ and so recombination of those species can not affect the $[e^-]_0$ decay significantly.

As it may be complicated to measure the actual photo-ion density at $t = 0$, we write equation 2.17 for another elementary cell with initial distance $z_2 = vt_2$ from the QMS, where the term $[PAH^+]_{PI,t=0}$ is identical[27]. After subtraction of both equations we obtain:

$$\ln \frac{[PAH^+]_{PI,t=t_2}}{[PAH^+]_{PI,t=t_1}} = -\frac{\alpha}{v} \int_{z_1}^{z_2} [e^-]_0 \, dz - \left(\frac{D_a}{\Lambda^2} + k_d[PAH] \right) (t_2 - t_1) \qquad (2.18)$$

Obtaining the recombination rate constant

To simplify the text hereafter, the term $[PAH^+]$ replaces the term $[PAH^+]_{PI}$ and only PAH photo-ions are discussed.

The validity of equation 2.18 may be not fulfilled for t_1 close to 0 due to the presence of higher diffusion modes shortly after the laser pulse and due to laser scattering on the QMS entrance lens which may produce a non-homogeneous concentration of $[PAH^+]$ close to the QMS. The initial electron density $[e^-]_0$ may also be affected in the case of a too high initial $[PAH^+]$. Therefore we analyze the data after a relaxation time t_1. A typical value of t_1 is 0.25 ms. Time t_2 is usually chosen as long as possible and is limited by the increasing statistical error of $[PAH^+]$ at long times.

The rate coefficient α can be obtained in several ways using equation 2.18. If the losses by diffusion and ion-molecule reactions are small in comparison to recombination losses, we can neglect the second term on the right hand side. The data are then plotted as $\ln([PAH^+]_{t_2}/[PAH^+]_{t_1})$ vs $\int_{z_1}^{z_2} [e^-]_0 \, dz$ with variable limits t_1 or t_2. The plot so obtained is a straight line whose slope is α/v.

---

[27]This says that concentration of photo-ions immediately after the laser shot is constant along the flowtube, as was already discussed in section 2.3.3.

The next method, which was also used in our first paper on *FlAPI* [65], is to fix time limits t_1 and t_2 and to measure several decays of the cation density $[\text{PAH}^+](t)$ and electron density $[e^-](z)$, the variable being the initial electron density, which can be varied by setting the microwave cavity at different positions with respect to the buffer gas input nozzle. The second term in equation 2.18 is then a constant for all measurements and will not affect the slope of $\ln([\text{PAH}^+]_{t_2}/[\text{PAH}^+]_{t_1})$ vs $\int_{z_1}^{z_2}[e^-]_0\,dz$. However, this type of analysis uses only 2 points from each ion density decay (at times t_1 and t_2) and the result may depend significantly on the right choice of these time limits, e.g. if t_2 is chosen too high giving high statistical error to the result.

Another method of data analysis has been found later: equation 2.18 is divided by term $(t_2 - t_1)$ obtaining the form:

$$\ln \frac{[\text{PAH}^+]_{\text{PI},t=t_2}}{[\text{PAH}^+]_{\text{PI},t=t_1}} \Big/ (t_2 - t_1) = -\frac{\alpha}{v} \int_{z_1}^{z_2} [e^-]_0\,dz \,/\, (t_2 - t_1) - \left(\frac{D_a}{\Lambda^2} + k_d[\text{PAH}]\right). \qquad (2.19)$$

The term $(\frac{D_a}{\Lambda^2} + k_d[\text{PAH}])$ is then always a constant and cannot affect the slope. In principle, it is now possible to use the data from only one measurement with a fixed initial electron density and plot the $\ln([\text{PAH}^+]_{t_2}/[\text{PAH}^+]_{t_1})\,/\,(t_2 - t_1)$ vs $\int_{z_1}^{z_2}[e^-]_0\,dz\,/\,(t_2 - t_1)$ varying the time limits t_1 or t_2 and the slope of such a plot should give again α/v. However, the electron density $[e^-]_0$ is almost constant along the scanned zone (see figure 2.11) and the integration over the interval from z_1 to z_2 divided by $(t_2 - t_1)$ gives also almost a constant value. Thus it is better to use again more decays measured for different initial electron densities, while time limits can be different for particular measurements. In this work the latter method is used for analyzing all measured data.

It should be noted that the mass spectrometric measurements do not need to be absolute measurements.

2.3.5 Data processing

As already discussed in section 2.3.3, several types of noise appear in the data measured by the MCS. The noise component mentioned as 3rd appears unpredictably and suddenly in quick "noise bursts". To be able to remove this component, a special procedure of data measurement has been implemented. Data measured for one initial electron density are not accumulated in one single datafile, but in several datafiles (typically 20). The accumulation time of one datafile should be much larger than the duration of the "noise burst", but shorter than typical time intervals of their occurrences. As the "sudden noise" appears usually only in a minor number of datafiles, it is possible to identify those files by comparing the mean value of counts and the number of counts in particular files.

Electron density values are obtained from Langmuir probe characteristics following the standard Langmuir theory. This says, that in the saturated part of the probe characteristics, the second power of the measured current over voltage set on the probe is proportional to the electron concentration. For details see appendix B.

The processing of measured data consists of severals steps, which have been implemented in a set of program scripts written in $Matlab^{TM}$, forming the data analysis system with a wide possibilities of user settings, but once set, with minimal requirements on user intervention. A quick overview of the numerical treatment is given in this section.
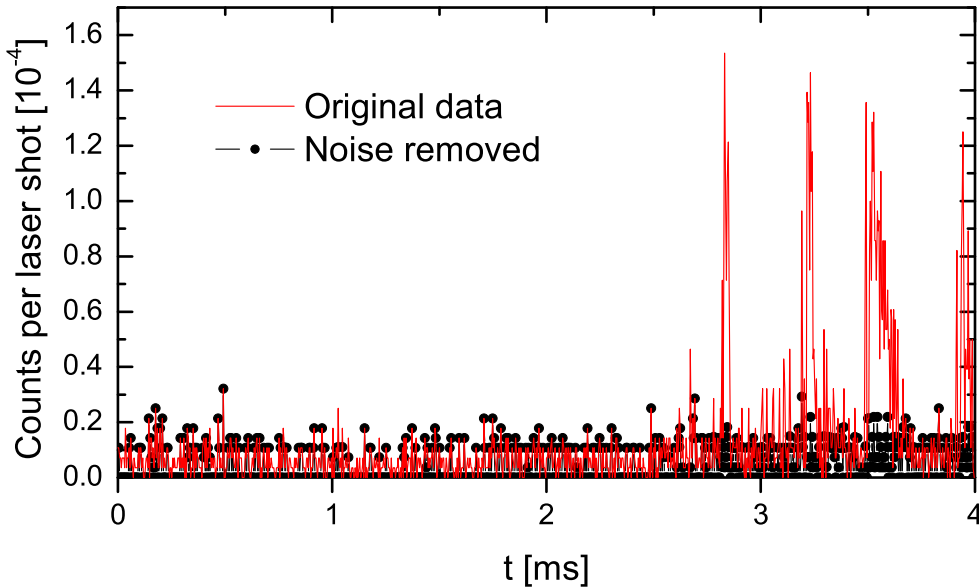
Figure 2.15: An example of the noise removal procedure. The line shows an original MCS spectrum measured with the laser off, while points represent data after removing the noise. The bulk of the noise is succesfully removed without affecting the shape of the background signal.

First a set of program scripts is applied on every data measurement set:

1. **Removing the "noise bursts":** As discussed at the beginning of this subsection, the data measured by the MCP detector are stored in several files. The first data processing step analyzes those files and searches for the presence of "sudden noise". Time channels (typical dwell time is 4μs) are analyzed separately. The average value of the number of counts is calculated from all datafiles except the one currently tested. The obtained value is then compared with the number of counts in the non-used file. If the difference exceeds some level, the data from this file are not used in this particular channel. The limit level is set as multiple statistical errors. The script is applied separately on the "laser on" and "laser off" data files. An example of the result of described procedure is shown in figure 2.15.

2. **Noise level estimation:** In this step the level of white noise is estimated for further error analysis. On the flat part of the MCS spectrum (e.g. after 2.5 ms in figure 2.16) the standard deviation of the average value is calculated. After subtraction of the statistical error (calculated as the square root of the number of counts in one channel) arising from the counting procedure, the level of white noise is obtained. Then the white noise error is added to the statistical error calculated for particular channels. The error thus obtained is probably not the total error, but is certainly much closer to the total error value than the statistical error alone.
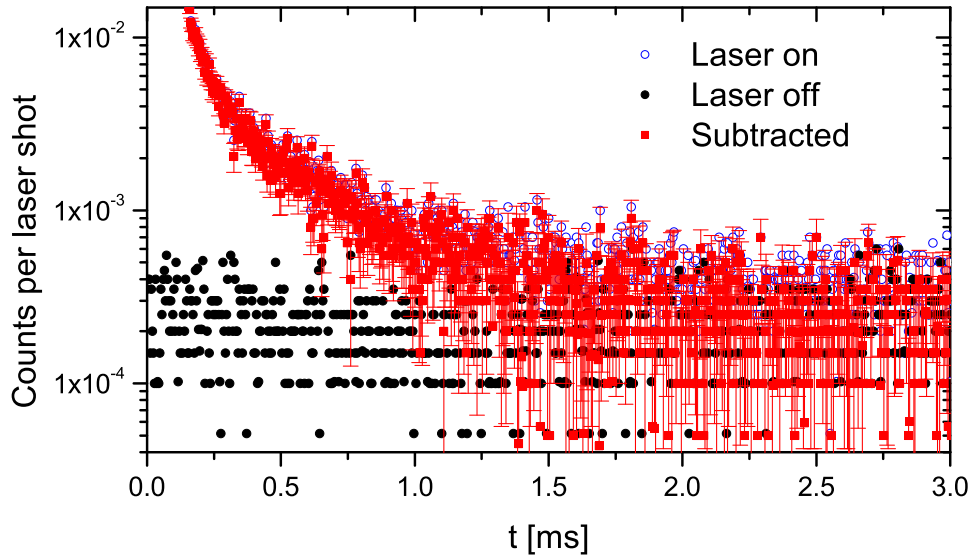
Figure 2.16: A typical MCS spectrum (dwell time 4 μs, 20 000 laser shots) measured with anthracene after application of the the first 3 data processing steps: removing the "sudden noise", noise level estimation and background subtraction. The number of counts is normalized to 1 laser shot. Error bars are plotted only for subtracted data.

3. **Background subtraction:** Now the data measured with the "laser off" are subtracted from data measured with the "laser on" as background yielding only events arising from photo-ions. Appropriate calculation of errors is then applied. An example of data subtraction is given in figure 2.16.

4. **Electron density analysis:** As we know that the electron density decreases exponentially in space (see an example in figure 2.11), we fit the electron density decay by an exponential function and then only an amplitude and decay time need be used for numerical integration. For fitting the data, the χ^2 minimization method is used [66].

As the Langmuir probe is not located at the same position as the MCP detector and as the ion velocity inside the QMS is almost unpredictable, it is not possible to use a simple relation $z = vt$ for converting the time of arrival at the QMS t and the probe position z. For that an additional measurement of "time (distance)" of both measurement tools is performed: The apparatus is operated under normal conditions but with the microwave discharge off. The column of photo-ions and photo-electrons flows towards both measurement tools and in both cases it is easy to identify the end of the column as a measured ion density or as the current measured by the Langmuir probe. The position of this edge in time with respect to the trigger pulse gives the "time (distance)". This is also an alternative method for velocity measurement, when the time of arrival of the edge is measured at several positions of the probe.

Errors of output values (amplitude and the decay time) are based on the fitting error, velocity error and "time delay" error.

5. Final analysis - single measurement: The last script calculates expressions

$$y = \ln([\text{PAH}^+]_{t_2}/[\text{PAH}^+]_{t_1})/(t_2 - t_1) \tag{2.20}$$

and

$$x = -\frac{1}{v}\int_{z_1}^{z_2}[e^-]_0\, dz\,/\,(t_2 - t_1) \tag{2.21}$$

for all points in the selected time range. The time range is selected manually, where the minimum value is limited by inhomogeneous PAH^+ production close to the QMS nose cone and the maximum value by the statistical error, as already discussed in section 2.3.4. The integration limit t_1 or z_1 respectively is fixed as a reference point while the t_2 and z_2 scans all points in the selected time range. As the wrong selection of the reference point may affect all calculated points, it is profitable to chose the reference point inside the scanned time range[28]. The amplitude of the reference point is obtained by fitting several points around the selected time with an exponential function. It is obvious, that for t_2 close to t_1 calculated values of x and y diverge as well as their errors.

In principle it is possible to obtain the rate coefficient α already from one analyzed set of data as the slope of the plot y vs x, but the precision significantly increases when the data from all data sets measured with different initial electron densities are combined. Errors of both x and y are calculated. An example of this data processing calculation is given in figure 2.17.

In the last phase, the results calculated independently for all data sets are merged and the recombination rate coefficient is obtained. All calculated values are plotted in one single plot as y vs x and fitted by the χ^2 minimization method with error weighting. If the final χ^2 value is much higher than the value predicted by the χ^2 distribution, the error in α is increased. A similar "trick" is described in detail in appendix C.1. For examples of analysed data, see section 4.2.

---

[28]The reference point at the edge of the selected interval is more probably affected by a wrong selection of time range limits. Of course, the integration limit t_2 scans also over points close to the time limits, but the number of such points is minor in comparison to the total number of calculated points.
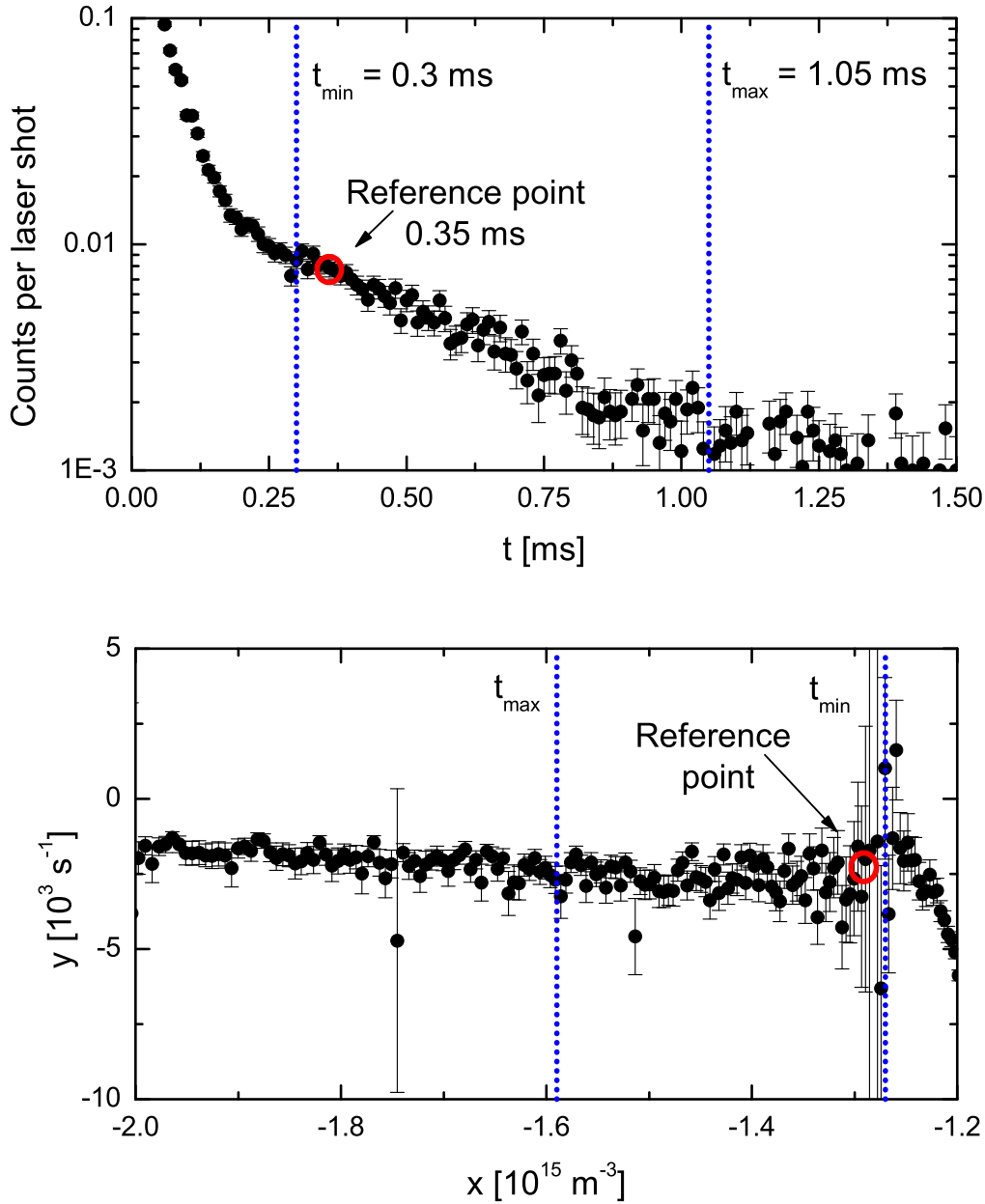
Figure 2.17: An example of the final analysis on a single data set measured with acenaptha-lene. **Upper panel:** The decay of ion density in time measured by the QMS. t_{min} and t_{max} limit the region used for the analysis. Data at shorter times may be affected by laser scatter-ing and non-zero diffusion mode (see the text) and data at longer times have low precision. The fixed reference point is selected inside this range. **Lower panel:** The plot of y vs x (as denoted in equations 2.21 and 2.20) with marked limits of scanned time range and the reference point. It is obvious, that the data precision does not allow one to obtain the rate coefficient α from just one data set.

2.4 The *ASTRID* heavy-ion storage ring

2.4.1 Basic overview

The *ASTRID (Aarhus STorage RIng Denmark)* storage ring, located at the Department of Physics and Astronomy at the University of Aarhus, Denmark, is a dual-purpose storage ring, capable of storing both positive and negative heavy-ions and electrons. In this thesis, only experiments with positive ions interacting with electrons are presented. A brief description of *ASTRID* is given here but for more details see e.g. [67–69].

The apparatus can be divided into four parts:

- ion sources

- mass selector and injection system

- electron cooler

- detection stations

The accelerator is equipped with several ion sources, but in the experiments presented in this thesis, only the electron impact ion source was used (see section 2.4.7).

After extraction, the ions are pre-accelerated to an energy of ∼150 kV, mass-selected by separator magnet and then injected into the storage ring. The ring itself has a 10 by 10 meter square geometry with two 45 ° bending magnets in each of four corners. The straight sections are equipped with quadrupole magnets for focusing purposes and correction dipole magnets for final beam positioning. Figure 2.18 presents a schematic diagram of the storage ring.

After injection into the ring, ions are further accelerated by means of a radio-frequency acceleration system to the final storage energy, which is usually a few MeV. The maximum storage energy is limited by the magnetic rigidity of the bending magnets and for *ASTRID* can be calculated as

$$E_{\max} = 931.5 \left[\sqrt{M_{ion}^2 + 0.3858Q^2} - M_{ion} \right] \text{ MeV}, \qquad (2.22)$$

where M_{ion} is the ion mass in *amu*, and Q is the charge of the ion in q (simply 1 in case of singly charged ions).

The electron target for recombination experiments at *ASTRID* is provided by an *electron cooler* device, which is mounted in one of the straight sections of the storage ring (see figure 2.19). The electron cooler produces a beam of essentially mono-energetic electrons that is merged with the ions in a 0.95 m long interaction region. By ensuring, that the electrons are cold (that they have a narrow velocity spread in comparison to the ions), the continuously replaced electrons will also act as a heat reservoir for the ion beam. This process, called *phase-space cooling* [70], diminishes the velocity spread of the ions and reduces the beam radius. The limiting factor in the cooling process is the electron-velocity spread in the electron cooler.

The first dipole magnet downstream of the electron cooler, acts as a separator, distinguishing the primary beam particles with their original charge and mass from the particles arising from the ion-electron and ion-background interactions. The ions, that do not interact continue circulating in the ring, while the particles with changed charge or mass are deflected by the magnet. Neutrals produced in this straight section of the ring, follow a straight line
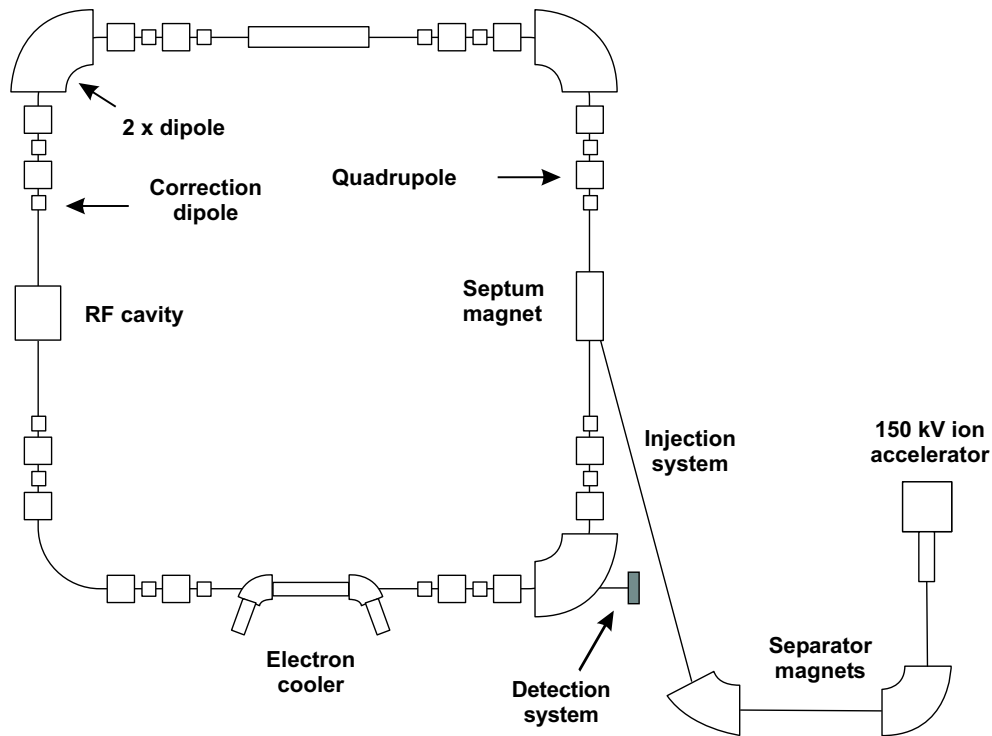
Figure 2.18: Schematic diagram of the *ASTRID* heavy-ion storage ring. Ions are injected in the right hand side of the ring, circulating counter-clockwise. The electron target (electron cooler) is shown in the bottom of the figure, and after the dipole magnet following the electron target, a neutral particle detector is shown.

path (called the "0° arm") and enter the detector section equipped with an energy sensitive *Surface Barrier Detector (SBD)*.

One injection cycle, which includes the production of ions, the transport to the injection point, injection of the ions, acceleration and storing them for several seconds during beam cooling and data acquisition, is repeated many times to decrease the statistical error of obtained data. The duration of one cycle is limited by the beam lifetime, which is determined by collisions with the residual gas in the vacuum system. The mean pressure is maintained in the 10^{-11} mBar region, and this results in typical beam lifetimes[29] of between 1 and 5 seconds. Thus for a beam of ions with a permanent dipole moment, the storage time is sufficiently long to vibrationally cool these ions through radiative emission and they can reach the zero vibrational level prior to data acquisition [71]. This is not necessarily the case for rotationally excited states, and indeed recent studies have indicated that the ions studied in storage ring experiments are often rotationally excited to energies higher than expected at a temperature of 300 K [72].

---

[29]As a lifetime is taken τ in an exponential decay $N = N_0 \exp(-t/\tau)$.
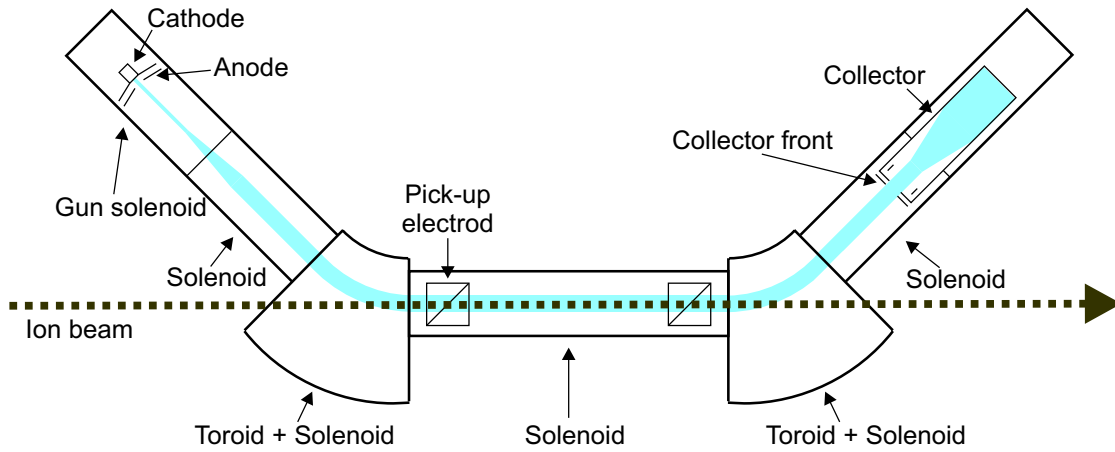
Figure 2.19: Schematic diagram of the electron cooler at *ASTRID*. The electrons travel from the cathode in the upper left part of the figure down to the interaction region between the two toroids, and finally up to the collector in the upper right part of the figure.

2.4.2 The electron cooler

The electron gun produces electrons by thermionic emission from a BaO coated tungsten cathode heated to T_{cath}= 1200 K. Electrons velocities are then described by a three-dimensional Maxwellian distribution:

$$f(\mathbf{v}_e) = \left(\frac{m_e}{2\pi k T_{cath}}\right)^{3/2} e^{-m_e v_e^2/2kT_{cath}}, \qquad (2.23)$$

where m_e and v_e are the electron mass and velocity respectively, and k is the Boltzmann constant. Electrons are then accelerated from the negative acceleration voltage V_{acc} of the cathode towards the grounded anode grid and in the next step, adiabatically expanded in the non-homogenous magnetic field of the solenoid. Acceleration of electrons with an initial longitudinal temperature T_{cath} to an energy E_0, causes a kinematic compression [73] of the velocity spread corresponding to the temperature $T_{||}$:

$$kT_{||} = \frac{(kT_{cath})^2}{4E_0} \qquad (2.24)$$

Since there is no acceleration in the transverse direction, the transverse temperature $T_\perp$ is not affected. The transverse temperature may be reduced, however, by expanding the electron beam adiabatically. At *ASTRID*, this is provided by guiding the electron beam through a solenoid where the magnetic field strength is slowly reduced without changing the magnetic flux through the electron cyclotron orbit [74, 75]. As a result of this, the transverse temperature is decreased by a factor $f_a = B_{gun}/B_{solenoid}$ (where B_{gun} and $B_{solenoid}$ are the initial and final magnetic fields respectively), which for the experiments presented here was equal to 4.5. The longitudinal temperature increases slightly during this procedure. There are also other contributions to the energy distribution due by electron-electron interactions (*transverse-longitudinal Boerch effect* and *longitudinal-longitudinal relaxation*). For a detailed description, see ref. [69, 76].

The final electron velocity spread is anisotropic and can be described by the following Maxwell-Boltzmann distribution:

$$f(\mathbf{v}_e) = \frac{m_e}{2\pi k T_\perp} \sqrt{\frac{m_e}{2\pi k T_\parallel}} \; e^{-m_e v_\perp^2/2kT_\perp} \; e^{-m_e v_\parallel^2/2kT_\parallel}, \qquad (2.25)$$

where $v_\parallel$ and $v_\perp$ are longitudinal and transverse velocities in the frame moving with the mean electron velocity. Temperatures are defined by the Maxwell distribution of the mean energy corresponding to the described velocity spread. After acceleration and adiabatic expansion at *ASTRID*, the energy spreads are $kT_\perp \approx 22$ meV and $kT_\parallel = (1.0\pm0.5)$ meV.

2.4.3 The energy scale

The interaction energy of the electrons and ions does not depend on the absolute velocities of the interaction partners but only on their relative velocity. It is therefore convenient to work in the center of mass (CM) frame of reference. Here, the interaction energy E_{CM} is defined as

$$E_{CM} = \frac{1}{2}\mu(v_e - v_i)^2, \qquad (2.26)$$

where μ is the reduced mass of the electron and the ion. v_e and v_i are electron and ion velocities respectively. Since the mass of the electron m_e is much lower than that of the ion m_i, the reduced mass of the electron-ion system is approximated by the mass of the electron $\mu \simeq m_e$.

During the cooling process, the electron and ion velocities are equal and this velocity is the called *cooling velocity* $v_{cool} = v_i = v_e$. During the experiments, the ion velocity v_i is held constant and the electron velocity v_e is varied by changing the electron cooler cathode voltage V_{acc} corresponding to a given electron energy in the laboratory frame E_{lab} (see Eq. 2.29 below). Equation 2.26 can then be expressed using only electron energies:

$$E_{CM} = \left(\sqrt{E_{lab}} - \sqrt{E_{cool}} \right)^2, \qquad (2.27)$$

where E_{cool} determined as

$$E_{cool} = \frac{1}{2}m_e v_{cool}^2 = \frac{m_e}{m_i}E_i \qquad (2.28)$$

is the cooling energy.

The electrons emitted from the electron gun are not accelerated exactly from the cathode potential to the ground potential, because the potential difference is reduced by the electron beam space charge potential. The overall effect is that the electron energy is reduced in the following way:

$$E_{lab} = q \left(V_{acc} - K \frac{I_e}{\sqrt{E_{lab}}} \right), \qquad (2.29)$$

where second term in brackets represents a *space charge correction*. Here q is the elementary charge, I_e the electron current in the beam and K is the space charge constant dependent purely on the geometrical parameters of the chamber. Equation 2.29 is expressed in implicit form and has to be solved iteratively. For a detailed description see ref. [69].

2.4.4 Experimental procedures

Experiments are performed by producing, storing and accelerating the ions, merging them with electrons of a particular relative energy and extracting the rate coefficients from the measured number of reactants and products. In short, the number of reactants is obtained through measurements of electron and ion currents, while the number of products is counted from the SBD detector positioned after the bending magnet downstream of the interaction region. Neutral fragments created in the electron cooler will pass through the magnet undeflected and when the fragments impact upon the detector they will result in a signal proportional to their kinetic energy. The time resolution of the SBD detector is low in comparison to the difference of particular fragment arrival times and thus only one event representing the total energy of all fragments is recorded. Fragments produced by dissociative recombination are thus displayed as a single peak at the full beam energy. In processes such as dissociative excitation where both neutral and charged fragments are produced, the charged fragments are deflected by the magnet and thus do not reach the detector and so peaks at fractions of the the full beam energy are registered. An example of the pulse-height spectrum measured for CF_3^+ is given in figure 6.1.

Before the measurement itself, the beam optimization is performed for the purpose of obtaining a good overlap between the electron and ion beams. The ion beam is initially positioned visually using the neutral fragment signal on an imaging detector placed in place of the SBD detector for this purpose. Final optimization is done performed by optimizing the signal-to-noise ratio of the SBD detector.

To distinguish between neutral fragments created by interaction of the ion and electron beams and those created in collisions of the ion beam with the residual gas (the background signal), the electron beam is chopped by alternating the electron gun anode voltage between ground and -3 kV. The background signal is highly dependent on the residual gas pressure in the storage ring, and a chopping frequency (typically 20–40 Hz) is thus chosen to be faster than the response time of the vacuum system. The data acquisition system of *ASTRID* divides the measurement into a number of *samples* that again contains a number of chopper periods (see figure 2.20).

In some cases the signal rate is too high and dead-time[30] and pile-up[31] effects take place. These can be easily detected by examining the spectrum of the SBD detector on the oscilloscope. The ion beam intensity is then decreased in order to avoid these effects. The final data analysis enables the removal of the most problematic data at the beginning of the measurement period (highest ion beam intensity).

In case of a low ion current (below ~ 300 nA), the *current transformer* used for the ion current measurement [77] fails and an alternative method has to be used: the signal from a set of capacitive pick-up electrodes is fed into a spectrum-analyzer which monitors the input at the revolution frequency of the ions, thus providing a measure of the number of ions in the ring. This signal was previously calibrated to a known ion current. To be exact, the calibration beam needs to have the same shape of ion bunches, which is not always guaranteed. We thus estimate the uncertainty of this technique to be higher than 30%. For details see ref. [69]. Since the ion current value is indirectly proportional to the measured rate

---

[30]The time period after recording of an event within which the recording electronics is not able to register the next event.

[31]Multiple events arriving within a short time comparable with the duration of one event (electronic pulse) that appear as one event but with a higher energy.
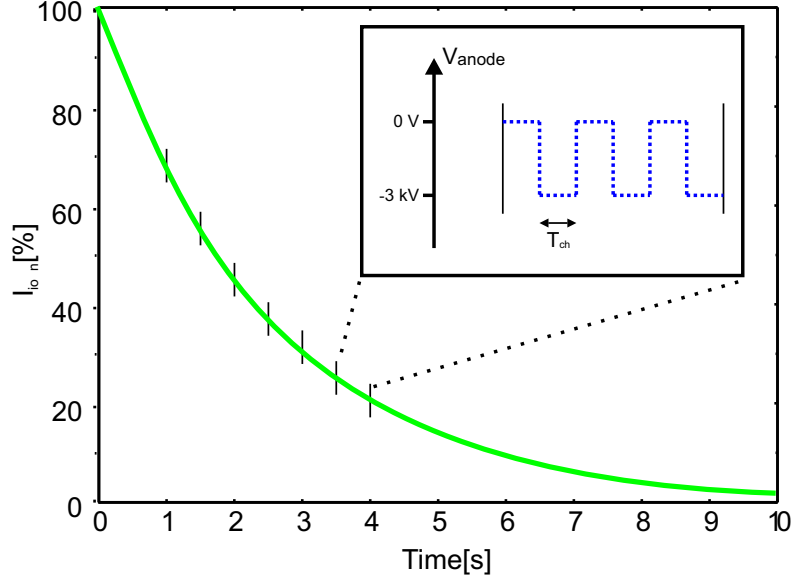
Figure 2.20: Schematic diagram of the timing of a recombination experiment. The graph shows the ion beam intensity (ion current) as a function of time. $Time = 0$ is set to the end of the cooling stage. An example shows the measurement divided into 6 samples with 3 chopper periods each.

coefficient (see section 2.4.5), this measurement is crucial for the precision of the experiment.

2.4.5 The rate coefficient

The rate coefficient for the process under examination can be written in terms of the measurable quantities as:

$$\langle \sigma \, v \rangle = \frac{N_s - N_b f}{N_{ion}} \frac{v_i}{n_e L} \quad , \tag{2.30}$$

where v is the relative velocity of the electrons and ions, σ the cross-section, v_i the ion velocity, n_e the electron density in the interaction region and L the length of the interaction region. N_s and N_b are the rates of neutrals recorded with the electron beam switched on and off, respectively. Since N_s and N_b are not recorded simultaneously, the factor $f = \exp(T_{ch}/\tau)$ is inserted to correct for the exponential decay of the ion beam in time[32]. N_{ion} is the rate of ions through the electron cooler and can be calculated from the ion beam current measured by the current transformer. By using the cathode of radius r_0 and expansion factor f_a (defined in section 2.4.2) the electron density can be expressed as:

$$n_e = \frac{I_e}{\pi q \, f_a \, r_0^2} \sqrt{\frac{m_e}{2E_{lab}}} \tag{2.31}$$

and ion velocity simply as

$$v_i = \sqrt{\frac{2E_i}{m_i}}. \tag{2.32}$$

---

[32] $1/(2T_{ch})$ is the chopping frequency and τ is the ion beam lifetime.

A relative rate coefficient is obtained as a function of the interaction energy by removing all constants and quantities that are held constant during the measurement, from equation 2.30 (e.g. E_i). Moreover N_{ion} can be replaced with the rate of neutrals produced by collisions with the residual gas which is proportional to ion beam intensity. The absolute rate coefficient is then evaluated at a single collision energy, and this is used to put the relative rate coefficient on an absolute scale.

The measurement of the rate coefficient as a function of energy consists of several injection cycles. At each cycle, one rate coefficient value at a fixed relative energy is measured. The electron energy is changed between cycles until the required energy range is covered.

When extracting the cross-section σ from a measured rate coefficient $\langle \sigma\, v \rangle$, the electron and ion velocity distribution must be considered. Since $m_e \ll m_i$, the spread in relative energies is dominated by the electron energy distribution described by Eq. 2.23. The rate coefficient is then the velocity-weighted cross-section averaged over the electron velocity distribution:

$$\langle \sigma\, v \rangle = \int \sigma\, v(v) f(\mathbf{v}) d\mathbf{v} \tag{2.33}$$

In most cases however, a good approximation to the relative velocity v is the simple difference of the electron and ion beam velocities $v_i - v_e$ (see Eq. 2.26). Thus the rate coefficient is obtained by dividing

$$\sigma = \frac{\langle \sigma\, v \rangle}{|v_i - v_e|} = \frac{\langle \sigma\, v \rangle}{\sqrt{2E_{CM}/m_e}}. \tag{2.34}$$

Significant deviations from the true cross-section will occur only for energies lower than $kT_\perp$, where the finite energy resolution of the electron beam is of importance.

The relative electron-ion velocities in the toroid regions, where the beams are merged and separated, are different from the velocities inside the interaction region. The relative energy defined by equation 2.27 is thus valid for the central part of the interaction region only and in the toroid regions a range of higher energies are encountered. This produces a small *toroidal correction* to the recombination coefficients that we measure. All data presented in this thesis have been corrected for this effect using an iterative procedure [78, 79].

It is desirable to produce results in a form applicable to models of chemical kinetics where particles usually have some velocity distribution. The thermal rate coefficient may be calculated using equation 2.1. In case of an isotropic Maxwellian velocity distribution described by a temperature T, the following formula is obtained:

$$\alpha(T) = \frac{8\pi m_e}{2\pi m_e kT} = \int_0^\infty E_{CM}\, \sigma(E_{CM})\, e^{-E_{CM}/kT}\, dE_{CM}. \tag{2.35}$$

2.4.6 Branching ratios

More information on the dissociation processes can be obtained by measuring the probability of formation of each of the fragmentation channels. Let us study the recombination of a sample molecular ion ABC^+. It's dissociative recombination may have several dissociation pathways, but not all of them are energetically allowed. A calculation of the reaction energy release (see appendix C.2) identifies possibly open channels, as they have positive energy releases, usually transformed into the kinetic energy (KER) of the products. It should be noted here, that a positive KER does not guarantee the availability of a given channel as the energy excess may be stored in internal states and may lead to autoionization.

To simplify the example, let us assume only 3 open dissociative channels:

$$ABC^+ + e^- \longrightarrow \begin{cases} A + B + C & (\alpha) \\ AB + C & (\beta) \\ A + BC & (\gamma) \end{cases} \qquad (2.36)$$
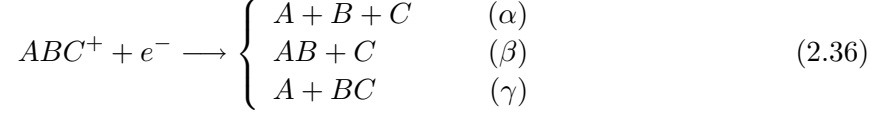
The fragments reach the detector at the same time and the integration time of the SBD detector is long in comparison to differences in arrival times of particular fragments. The dissociation event thus appears in the pulse height spectrum as a single peak at the full ion beam energy.

To differentiate between the fragments, a grid of known transmission T is inserted in front of the detector. Some fragments are then stopped with the probability $(1-T)$ and several peaks corresponding to all combinations of fragment masses appear in the pulse height spectrum. In the example case, we obtain peak areas N_X for the following fragment combinations: $N_{A\&B\&C}$, $N_{A\&B}$, $N_{A\&C}$, $N_{B\&C}$, N_A, N_B and N_C.

Now we formulate a set of equations connecting the number of counts in particular peaks and the number of dissociation events for each fragmentation channel $(M_\alpha, M_\beta, M_\gamma)$. Let us first derive only a single equation for $N_{A\&B}$ as an example, paying attention to the contribution of particular fragmentation channels. The signal appears at energy of $A\&B$ in the following cases:

- Channel α: The fragment C is stopped with probability $(1-T)$ but the other two reach the detector with probability T^2

- Channel β: The fragment C is stopped with probability $(1-T)$ but AB reach the detector with probability T

- Channel γ: Does not contribute to this peak.

Thus the equation is:

$$N_{A\&B} \;=\; M_\alpha \times T^2(1-T) \;+\; M_\beta \times T(1-T) \;+\; M_\gamma \times 0 \qquad (2.37)$$

Such an equation is derived for each measured peak. The final set of equation can be written in matrix form as

$$\begin{pmatrix} N_{A\&B\&C} \\ N_{A\&B} \\ N_{A\&C} \\ N_{B\&C} \\ N_A \\ N_B \\ N_C \end{pmatrix} = \begin{pmatrix} T^3 & T^2 & T^2 \\ T^2(1-T) & T(1-T) & 0 \\ T^2(1-T) & 0 & 0) \\ T^2(1-T) & 0 & T(1-T) \\ T(1-T)^2 & 0 & T(1-T) \\ T(1-T)^2 & 0 & 0 \\ T(1-T)^2 & T(1-T) & 0 \end{pmatrix} \times \begin{pmatrix} M_\alpha \\ M_\beta \\ M_\gamma \end{pmatrix} \qquad (2.38)$$

The set of equations may be degenerate as some fragments have identical mass. Usually, the set of equations is overdetermined – the number of equations (peaks) is higher than the number of parameters (M_X). Moreover, at *ASTRID*, two grids with different transmissions can be used and the number of equations is thus doubled. A proper solution of such a system of equations, putting stress on the correct treatment of errors, requires advanced solution methods as e.g. a *Singular Value Decomposition* (SVD). For details on the mathematical procedure used, see appendix C.1.

The branching fractions b_i are deduced from the number of dissociation events M_i by normalization to the total number of events:

$$b_i = \frac{M_i}{\sum_j M_j} \qquad (2.39)$$

As the collisions with residual gas produce additional signals in the pulse height spectrum, the background should be first subtracted. In a similar fashion as in the rate coefficient measurement, the electron beam is chopped on and off and two separate spectra are obtained. The pure signal is then obtained by a simple subtraction.

2.4.7 Ion source

The *ASTRID* apparatus is equipped with several ion sources. For the results of this thesis however, only an *electron impact source* has been used.

K. O. Nielsen developed this type of source in the 1950's [80]. The source consists of a heated filament placed in a discharge chamber surrounded by a solenoid, which provides an axial magnetic field. The filament has a negative voltage relative to the chamber walls, and thermally emitted electrons are thus accelerated from the filament, and under the combined influence of the electric and magnetic fields, the result is, oscillating electrons that cause ionization in the ambient gas. The source is suitable for the production of ions from both gas and solid source material. The limiting criterion for long-term use of this source is the lifetime of the filament.

2.5 The *CRYRING* heavy-ion storage ring

Storage ring experiments presented in this thesis were performed mainly at the *ASTRID* storage ring. As some results were also obtained from the data synthesized from both *ASTRID* and *CRYRING* storage rings, a brief description of the *CRYRING* apparatus and the corresponding data analysis is given in this section.

The *CRYogenic storage RING* (*CRYRING*) is the ion storage facility at the Manne Siegbahn Laboratory, which is run by Stockholm University, Sweden [3, 81]. The *CRYRING* is a nearly circular machine, with a circumference estimated at 51.63 m. It is composed of twelve adjacent straight sections, delimited by twelve bending dipole magnets (see figure 2.21).

We shall list the main differences in comparison to the *ASTRID* apparatus having a context for this study:

Electron energy resolution: At *CRYRING* an advanced model of the electron cooler with a superconducting solenoid is used. The decreasing magnetic field ($B_{max} \sim 5$ Tesla) and the electron acceleration, push electron beam temperatures down to $kT_\perp \approx 2$ meV and $kT_{||} = 0.1$ meV and thus the energy resolution is $\sim 10\times$ better than at *ASTRID* (see section 2.4.2).

Cross-section measurement: Instead of fixing the electron beam energy during one injection cycle and changing it in steps between injections, as is done at *ASTRID* (see section 2.4.4), the electron energy at *CRYRING* is ramped continuously in the requested energy range during each cycle (see fig. 2.22). The ion beam intensity is monitored by means of an additional scintillation detector, which acquires the level of the background signal arising from ion beam interactions with the residual gas. For detailed explanation see e.g. ref. [3].
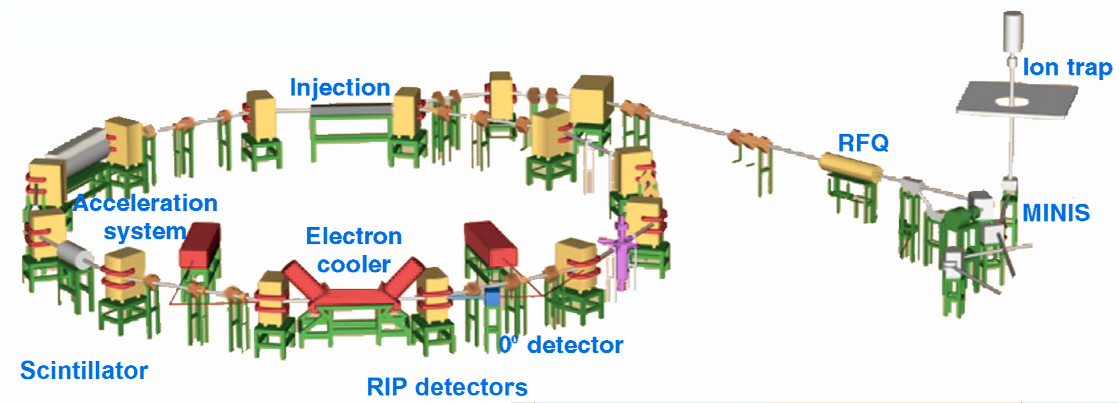
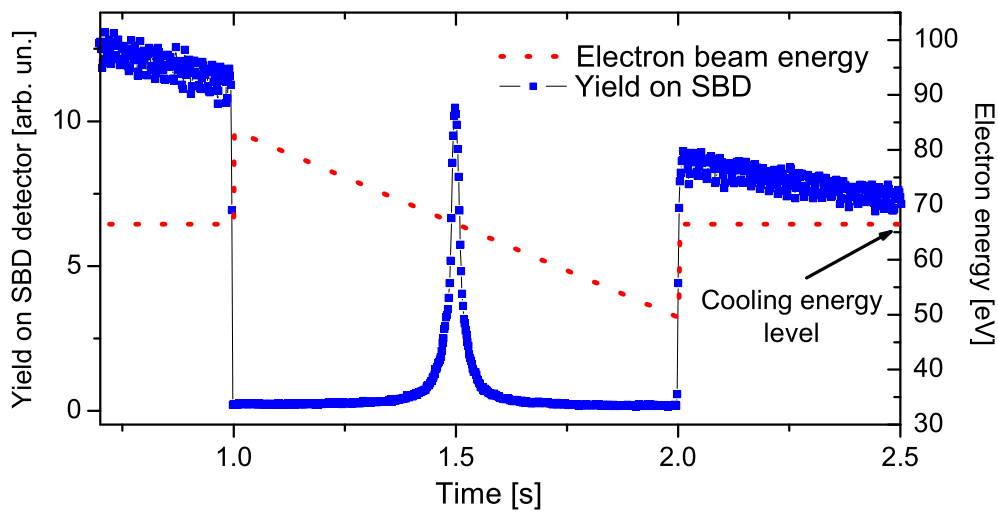Figure 2.21: An overview of the *CRYRING* ion storage ring.

Figure 2.22: The cross-section measurement principle at the *CRYRING* apparatus. An example of the electron beam energy vs time is plotted in the same time region as the count rate acquired on the SBD detector in "0° arm".

DISSOCIATIVE RECOMBINATION
OF
HYDROGEN AND DEUTERIUM IONS

3.1 Enigma of H_3^+

H_3^+ was discovered by *J. J. Thomson* in 1911 [82,83] when using a prototype mass spectrometer he identified an ion with a mass/charge ratio equal to 3. Thomson first hesitated to assign this observation to H_3^+ and instead discussed the species X_3^+ in his papers[1]. In 1916 *Dempster* readily accepted H_3^+ and correctly demonstrated the predominance of H_3^+ over H_2^+ and H^+ in hydrogen plasmas [85]. In 1925 [86], H_3^+ formation was first suggested to proceed via following reaction:

$$H_2 + H_2^+ \rightarrow H_3^+ + H. \tag{3.1}$$

This reaction is highly exothermic (1.7 eV), has no activation barrier [87] and proceeds at a high rate $k = 2 \times 10^{-9}$ cm^{3}s^{-1} [88]. The properties of reaction 3.1 and the widespread abundance of H_2 in ISM led *Martin et al.* in 1961 to postulate that H_3^+ could be present in interstellar space [89]. In 1973 it was suggested independently by Watson and by Herbst and Klemperer that H_3^+ could initiate many ion-molecule reactions which would lead to the formation of many molecules observed by radio and microwave astronomy in dense interstellar clouds [90,91]. Due to relatively low proton affinity of H_2 (4.5 eV), H_3^+ plays a role of universal proton donor via the reaction

$$H_3^+ + X \rightarrow HX^+ + H_2, \tag{3.2}$$

where X can be any atom or molecule with a proton affinity higher than H_3^+ (almost any atom or molecule). Figure 3.1 shows astrochemical models of dense and diffuse interstellar clouds.

For the spectroscopic identification of H_3^+ in the interstellar medium (ISM), it was necessary first to know it's spectrum. H_3^+ has no stable electronically excited state and calculation of its state structure is complicated due to it's non-classical configuration[2]. Thus the spectrum

---

[1]In his bibliography, however, [84] Thomson is already speaking about H_3^+: "...one of the first things discovered by the photographic method was the existence of H_3^+ ..."

[2] In 1935 *Coulson* first predicted the nature of H_3^+ to be an equilateral triangle with a bond length of 0.85 Å, quite close to the modern, computer calculated value of 0.87 Å [92]. An overview on later calculations of H_3^+ structure is given in [93].

was experimentally identified relatively late by Oka in 1981 [94]. The first extraterrestrial identification of H_3^+ was performed in 1989 through emission spectroscopy of the atmosphere of Jupiter [95, 96]. Later on [97] H_3^+ was recognized also in the atmospheres of Saturn and Uranus. In 1996 *Geballe and Oka* identified H_3^+ in dense interstellar clouds [98], where it's amount agrees with astrochemical models [99, 100]. In these clouds, H_3^+ is destroyed by ion-molecule reactions with known rates. The discovery of H_3^+ in diffuse interstellar clouds in 1998 by *McCall et al.* [101] was unexpected. Here the main destruction channel for H_3^+ is DR with electrons. At that time, the generally applied value of the recombination rate $\alpha = 1.1 \times (300/T)^{0.65} \times 10^{-7}$ cm^{3}s^{-1} [20] predicated the concentration of H_3^+ at least $10\times$ lower than the observed abundance. This discrepancy could be eliminated by decreasing the recombination rate coefficient α or by increasing the cosmic ionization rate ζ in the reaction

$$H_2 \xrightarrow{\zeta} H_2^+ + e^-, \tag{3.3}$$

which is the limiting factor for H_3^+ formation rate. More detailed discussions of this astrochemical puzzle is given e.g. in [102].

Many of the molecular species detected in dense interstellar clouds contain the rare isotopes of some elements (D, ^{13}C, ^{18}O, etc.). What at first sight was surprising is that the abundance ratios of some molecules containing the rare and the common isotopes are in some cases orders-of-magnitude greater than those expected from their solar-terrestrial isotopic ratios. It is now understood that this enrichment is mainly due to the phenomenon of "isotope fractionation" through gas-phase ion-molecule reactions [105]. Let's set $X =$HD in reaction 3.2:

$$H_3^+ + HD \rightarrow H_2D^+ + H_2. \tag{3.4}$$

This reaction has a forward preference, because the reverse reaction is endothermic by $\sim$ 19 meV. This process could be repeated and in a sequence of reactions with HD also HD_2^+ or D_3^+ can be obtained [106].

The laboratory determination of the H_3^+ and D_3^+ DR rates is controversial, as reviewed eg. by Oka [99], Larsson [107], Plasil [108] and Johnsen [109]. The very first measurement was performed by *Biondi and Brown* in 1949 [110], and this was followed by many further experiments using several different techniques. The results are summarized in figure 3.2 and in tables 3.1 and 3.2.

There are obviously two main groups of values: the first group of results (around 2×10^{-7} cm^{3}s^{-1}) were obtained by several experimental techniques including storage rings and flowing afterglows. The second group located around 2×10^{-8} cm^{3}s^{-1} were obtained by afterglow techniques and once also by single pass merged beams. The first value was for a long time taken as the "correct value" for astrochemical models. It should be noted, however, that values in the first group decreased during the last 30 years by more than $3\times$. On the other hand, theoretically calculated values of DR rate of H_3^+ continuously approach the experimental values and, especially during last 5 years, undergo a very steep evolution (see [146–150] and references therein). A very similar behavior is seen for measured and calculated values of the DR rate coefficient for D_3^+, where absolute values are usually a factor of $\sim 1/2$ lower than those for H_3^+.

As is described above, an extreme effort has been put into the solution of the discrepancy between particular measured values of the rate coefficient, theoretical values and values predicted by astrochemical models. The problem is still not, however, clearly solved and is still referred to as *The Enigma of H_3^+* .
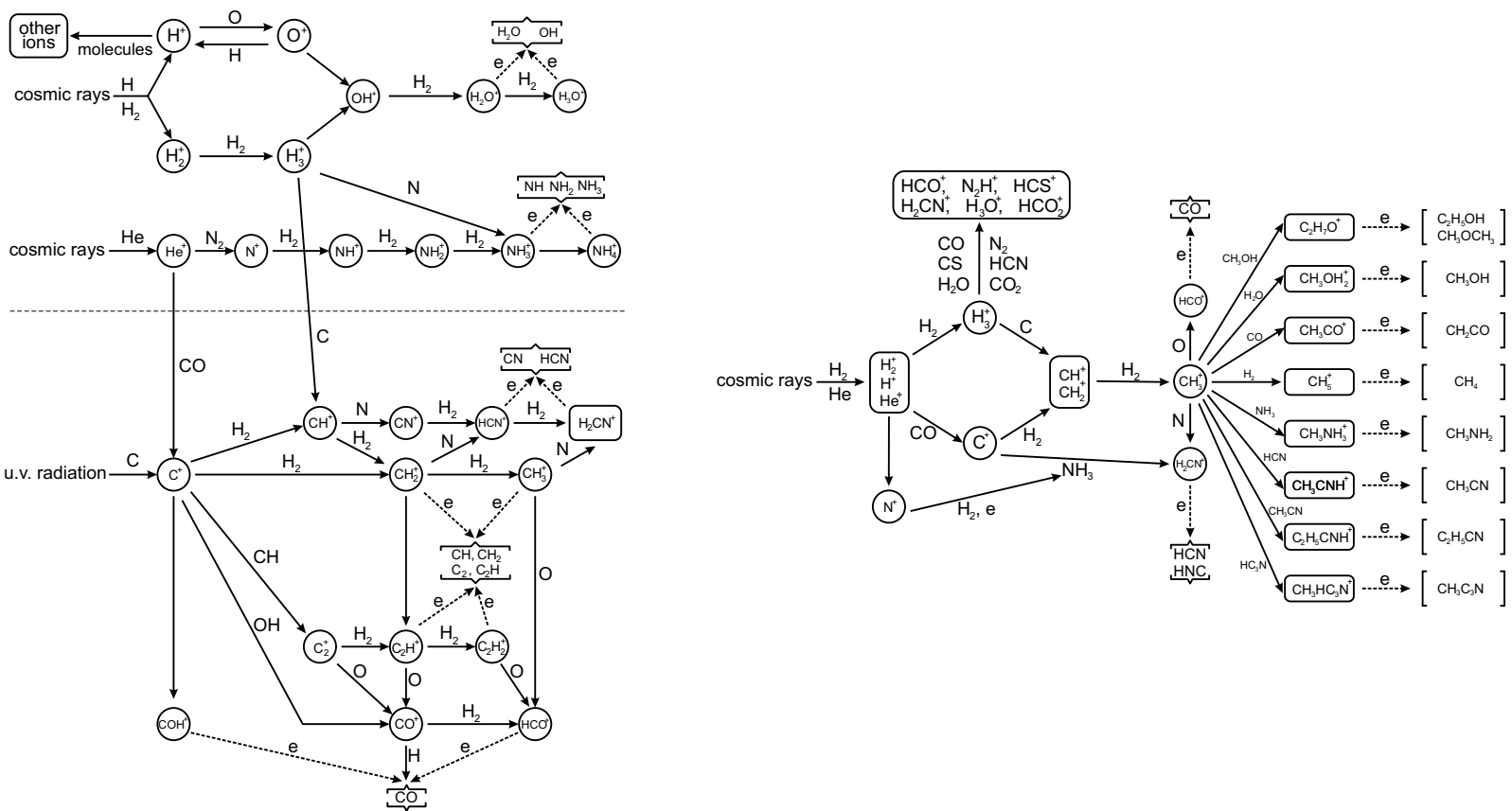
Figure 3.1: Diagram of reactions proceeding in diffuse (left panel) and dense (right panel) interstellar clouds [103]. Figure is reprinted from [104].

α [10^{-7} cm^{3}s^{-1}]	Method	Year	Comment	Reference
25	SA/μw	1949		Biondi [110]
20 and 60	SA/μw	1951	at 1 and 7 Torr of H_2	Richardson [115]
3 and 25	SA/μw	1951	at 3 and 30 Torr of H_2	Varnerin [116]
< 0.3	SA/μw	1955		Persson [117]
2.3	SA	1973	300 K	Leu [118]
2.5	inclin. beam	1974		Peart [39]
2.1	merged beams	1977		Auerbach [41]
1.5	ion trap	1978		Mathur [119]
2.1	merged beams	1979		McGowan [120]
≤ 0.2	FALP	1984		Adams [121]
1.5	SA	1984		Mac Donald [122]
≤ 0.0001	FALP	1987	estimation	Adams [123]
0.2	merged beams	1988	$\nu = 0$	Hus [124]
1.8	IR spectr.	1990	$\nu = 0$	Amano [125]
1.5	IR spectr.	1990	$\nu \leq 2$	Amano [125]
1.1	FALP-MS	1991	$\nu = 0$	Canosa [126]
1.5	FALP-MS	1991	300 K, $\nu \leq 2$	Canosa [126]
1.1	FALP-MS	1992	650 K, $\nu = 0$	Canosa [127]
1.5	FALP-MS	1992	300 K, $\nu \leq 2$	Canosa [127]
0.1 to 0.2	FALP	1993	$\nu = 0$	Smith [128, 129]
1.15	storage ring	1994		Sundström [20, 130]
< 2	IR laser. spectr.	1994		Fehér [131]
1.4 to 2	FALP	1995	$0.01 - 0.1$ Torr H_2	Gougousi [132]
0.78	FALP-MS	1998		Laubé [133]
0.7	storage ring	1999		Tanabe [134]
0.7	storage ring	1999		Schneider [135]
0.4 to 1.4	*AISA*	2000	dependent on [H_2]	Kudrna [136]
0.13 to 1.4	*AISA*	2000	dependent on [H_2]	Glosik [137]
1	storage ring	2001		Jehnsen [138]
0.04 to 1.4	*AISA*	2001	dependent on [H_2]	Glosik [111]
1.15	SA	2002	H_2 pressure 1.5 Pa	Mosbach [139]
0.03 to 1.4	*AISA*	2002	dependent on [H_2]	Plasil [108]
0.68	storage ring	2003	$T_{rot} \sim 30$ K	McCall [140, 141]
1.6	CRDS	2004	$\nu = 0$, [H_2] $\approx 5 \times 10^{14}$ cm^{-3}	Macko [142]
0.1 to 1.4	*AISA-VT*	2004	dependent on [H_2]	Glosik [143]

Table 3.1: An overview of the experimental values of DR rates for H_3^+. In the case of known temperature dependence, the rate is transformed to $T = 300$ K. In some cases it was possible to distinguish particular vibrational states ν. Data are plotted in figure 3.2.
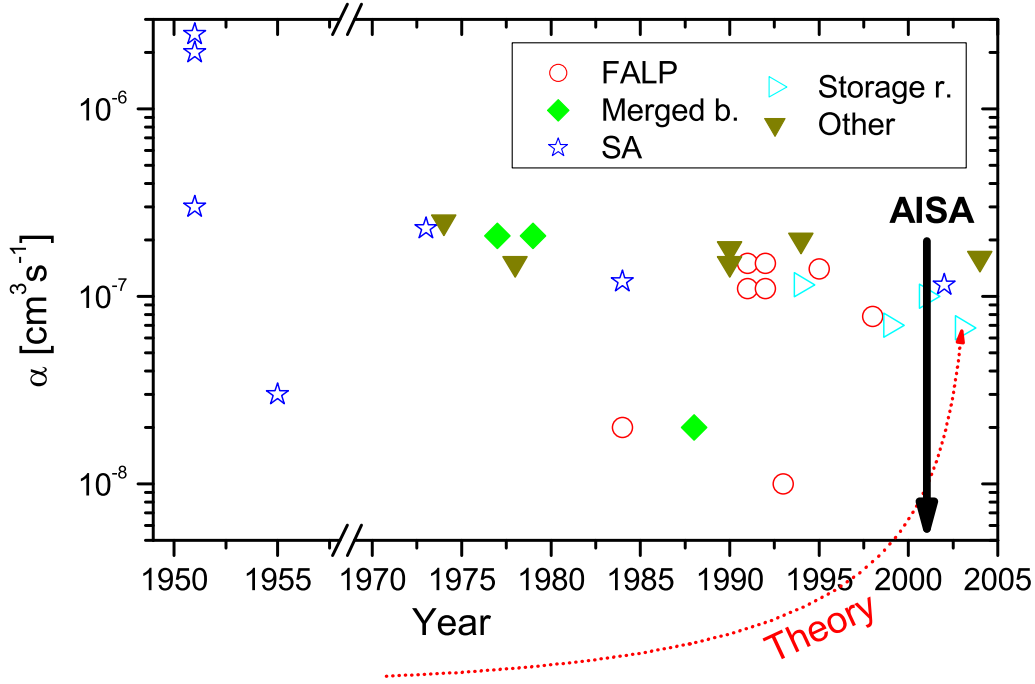
Figure 3.2: An overview of the experimental values for DR rate coefficient of H$_3^+$. Data are listed in table 3.1. The dotted line shows the evolution of theoretically calculated values.

The problem of H$_3^+$ and D$_3^+$ recombination has been investigated in our *Laboratory for elementary processes in plasmas*[3] using several experimental techniques. The measurement with the *Advanced Integrated Stationary Afterglow* (*AISA*) apparatus has shown a surprising dependence of the measured recombination rate coefficient on the partial pressure of hydrogen used as a reactant gas [108, 111, 114, 136, 137]. Such an observation (see figure 3.3) gives rise to the question whether the *DR* of H$_3^+$ rate in the ISM shouldn't be taken as the limit value of *AISA* measurement for [H$_2$] $\rightarrow$ 0: ($\alpha \leq 3 \times 10^{-9}$ cm^{3}s^{-1}). Such a result would be in direct contrast with recent measurements at storage rings: $\alpha(300\text{K}) = 6.8 \times 10^{-8}$ cm^{3}s^{-1} [141].

---

[3]Department of Electronics and Vacuum Physics, Faculty of Mathematics and Physics, Charles University, Prague, Czech Republic

$\alpha[10^{-7}$ cm^{3}s^{-1}]	Method	Year	Comment	Reference
< 0.2	FALP	1984	95 and 300 K	Adams [121]
0.8 and 0.2	FALP	1993	$\nu > 0$ and $\nu = 0$, 300 K	Smith [128]
0.75 to 1.4	FALP	1995	small dependence on [D$_2$]	Gougousi [132]
0.27	storage ring	1997		Larsson [144]
0.27	storage ring	1998		Le Padellec [145]
0.67	FALP-MS	1998	0.5 Torr of He, 300 K	Laube [133]
0.06 to 0.7	*AISA*	2002	dependent on [D$_2$]	Poterya [112]

Table 3.2: An overview of the experimental values of DR rates for D$_3^+$. In the case of known temperature dependence the rate is transformed to $T = 300$ K.
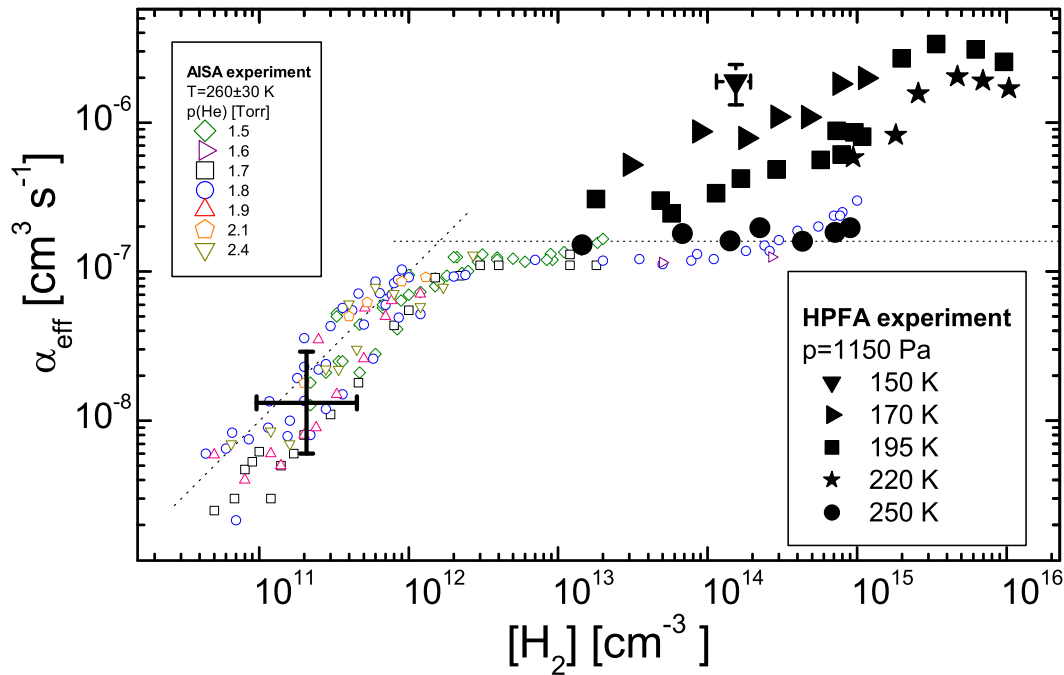
Figure 3.3: The effective recombination rate coefficient α_{eff} obtained on the *AISA* and the *HPFA* apparatuses. For $[H_2] \leq 10^{14}$ cm^{-3} α_{eff} represents the recombination rate for H_3^+. Above this limit, the effective rate is affected by the formation and consequent recombination of H_5^+. The main aim of measurements on the *FALP–VT* apparatus presented in this thesis was the confirmation and further investigation of the behavior of α_{eff} for $[H_2] \leq 2 \times 10^{12}$ cm^{-3}. For more details see [49, 50, 108] and section 3.3. The figure is reprinted from [50].

Further experiments have been performed on the *High Pressure Flowing Afterglow* (*HPFA*) apparatus [49, 50, 113]. In this configuration (see also section 2.2) we concentrated on measurements at higher number densities of H_2, where the H_5^+ ion plays an important role. In the range of $[H_2]$ overlapping with the *AISA* experiment the recombination rate α_{eff} agrees very well in both experiments, although the measurement principle, the plasma formation process and the buffer gas pressure are substantially different. This experiment has clearly shown that the decrease of α_{eff} for $[H_2] < 2 \times 10^{12}$ cm^{-3} observed with the *AISA* is not caused by the formation of H_5^+. Figure 3.3 displays merged results from experiments on the *HPFA* and *AISA* apparatuses.

The measurement on the *AISA* apparatus have also been performed for D_3^+ [112, 114] where a similar behavior of the recombination rate coefficient as for H_3^+ has been observed[4]. The *AISA* apparatus was later improved allowing measurements at variable temperatures (*VT-AISA*) [143]. The low value, however, of α_{eff} (at $[H_2] \to 0$) was confirmed and this experiment still noticeably stand out among values obtained at storage ring experiments.

One of the arguments against the conclusiveness of results obtained on the *AISA* apparatus was the indirect measurement of the absolute ion concentration. The absolute value is determined from the electron concentration measured by the Langmuir probe. In the *AISA* experiment the majority of the H_3^+ ions are expected to be in their ground vibrational state.

---

[4]The dependence α_{eff} ($[D_2]$) has a similar shape but absolute values of the recombination rate coefficients are approximately a factor of 2 lower than α_{eff} ($[H_2]$).

This assumption is based on a calculation taking into account collisions with the helium buffer gas. In subsequent experiments, *Cavity Ring-Down Spectroscopy* (CRDS) [151, 152] has been employed for the direct determination of the absolute ion concentration $[H_3^+(\nu = 0)]$ (the apparatus called *Test-Tube*). First results performed at $[H_2] > 5 \times 10^{13}$ cm^{-3} [142] are in very good agreement with results obtained at both the *AISA* and *HPFA* apparates (see figure 3.15). The measurement at lower $[H_2$] has not yet been performed due to technical problems.

In this chapter, two recent experiments are presented. A new study on D_3^+ and D_5^+ performed on the *FALP-VT-prototype* apparatus is described in section 3.4. This measurement concentrated on the investigation of the possible D_5^+ influence on results obtained on the *AISA* apparatus [112]. This experiment follows a similar measurement on H_3^+/H_5^+ performed previously using the *HPFA* [49].

In section 3.5, a new measurement on H_3^+ performed on the *FALP–VT* is presented. The experiment concentrated on a re-investigation of α_{eff} for $[H_2] < 2 \times 10^{12}$ cm^{-3}, it is the region where a very unexpectedly low α_{eff} was found with *AISA*. Using the flowing afterglow technique would exclude arguments on a complicated H_3^+ formation in the stationary afterglow, where the discharge is ignited in a mixture of all gases including hydrogen and thus many more reactions may occur during the relaxation of the plasma before the ion to be studied reaches dominance in the chamber. In addition the working pressure in the *FALP–VT* (1600 Pa) is almost $5\times$ higher than in *AISA* and thus the possible influence of this parameter can be also investigated (or excluded).

The plasma formation and several preparatory measurements are similar for both experiments (with hydrogen and deuterium as reactant gas) and therefore are jointly described in separate sections.

3.2   Plasma formation

In the *FALP–VT*, the reacting gases are injected separately: helium as a buffer gas flows through the discharge tube where He$^+$ ions and He* metastable excited atoms[5] are formed. In subsequent reactions He$^+$ is transformed to He$_2^+$ but the long-lived He* can survive and later release it's energy in the reaction zone at an uncontrollable rate. In order to remove metastables, argon is introduced via the second entry port at a flow rate, $< 0.1\%$ of the He flow rate. He* are removed by Penning ionization and also all He$_2^+$ are transformed to Ar$^+$. The hydrogen (similar reaction scheme valid also for deuterium) is introduced via the next inlet. In the case of H_2 the main channel for H_3^+ formation proceeds via the reaction sequence:

$$\mathrm{Ar}^+ \xrightarrow{\mathrm{H_2}} (\mathrm{ArH}^+ \text{ or } \mathrm{H_2^+}) \xrightarrow{\mathrm{H_2}} \mathrm{H_3^+}. \tag{3.5}$$
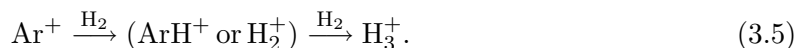
At high H_2 concentrations, H_5^+ is also formed via the association reaction

$$\mathrm{H_3^+} + \mathrm{H_2} + \mathrm{He} \longrightarrow \mathrm{H_5^+} + \mathrm{He}. \tag{3.6}$$
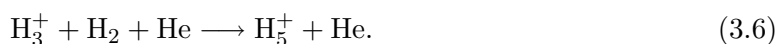
In order to fulfill the data analysis constraints of the FALP technique, dominance of the desired ion in the reaction zone (see section 2.2.3) is required. The QMS in our configuration can measure the plasma composition only at a fixed position at the end of the flowtube and

---

[5]In a discharge in pure He, He$^+$ ions and the metastable atoms He(2^{1}S) and He(2^{3}S) are produced. More energetic He(2^{1}S) are rapidly converted [153] in super-elastic collisions with electrons to He(2^{3}S). The relatively long lived He(2^{3}S) metastables represent an additional source of ionisation in the early afterglow.

No.	Reaction	Rate coefficient	Reference
		$[\mathrm{s}^{-1}]$, $[\mathrm{cm}^3\mathrm{s}^{-1}]$, $[\mathrm{cm}^6\mathrm{s}^{-1}]$	
1	$\mathrm{He}^+ + \mathrm{He} + \mathrm{He} \longrightarrow \mathrm{He}_2^+ + \mathrm{He}$	1×10^{-31}	[53]
2	$\mathrm{He}^+ + e^- \longrightarrow \mathrm{He}$	1×10^{-12}	[154, 155]
3	$\mathrm{He}^M + \mathrm{He}^M \longrightarrow \mathrm{He}^+ + \mathrm{He} + e^-$	5×10^{-9}	[156]
4	$\mathrm{He}_2^+ + e^- \longrightarrow 2\mathrm{He}$	$< 3 \times 10^{-10}$	[157]
5	$\mathrm{He}^M + \mathrm{He}^M \longrightarrow \mathrm{He}_2^+ + e^-$	5×10^{-9}	[158]
6	$\mathrm{He}^+ + \mathrm{Ar} \longrightarrow \mathrm{Ar}^+ + \mathrm{He}$	1×10^{-13}	[53]
7	$\mathrm{He}^M + \mathrm{Ar} \longrightarrow \mathrm{Ar}^+ + \mathrm{He} + e^-$	7×10^{-11}	[159]
8	$\mathrm{He}_2^+ + \mathrm{Ar} \longrightarrow \mathrm{Ar}^+ + 2\mathrm{He}$	2×10^{-10}	[53]
9	$\mathrm{Ar}^+ + \mathrm{Ar} + \mathrm{He} \longrightarrow \mathrm{Ar}_2^+ + \mathrm{He}$	1.3×10^{-31}	[160]
10	$\mathrm{Ar}_2^+ + e^- \longrightarrow 2\mathrm{Ar}$	8×10^{-7}	[161]
11	$\mathrm{Ar}^+ + \mathrm{H}_2 \longrightarrow \mathrm{ArH}^+ + \mathrm{H}$	8×10^{-10}	[162]
12	$\mathrm{Ar}^+ + \mathrm{H}_2 \longrightarrow \mathrm{Ar} + \mathrm{H}_2^+$	1×10^{-10}	[162]
13	$\mathrm{H}_2^+ + \mathrm{Ar} \longrightarrow \mathrm{ArH}^+ + \mathrm{H}$	2.3×10^{-9}	[88]
14	$\mathrm{H}_2^+ + \mathrm{H}_2 \longrightarrow \mathrm{H}_3^+ + \mathrm{H}$	2.1×10^{-9}	[88]
15	$\mathrm{ArH}^+ + \mathrm{H}_2 \longrightarrow \mathrm{H}_3^+ + \mathrm{Ar}$	1.5×10^{-9}	[163]
16	$\mathrm{H}_3^+ + \mathrm{H}_2 + \mathrm{He} \longrightarrow \mathrm{H}_5^+ + \mathrm{He}$	$< 1 \times 10^{-29}$	[164]
17	$\mathrm{H}_5^+ + \mathrm{He} \longrightarrow \mathrm{H}_3^+ + \mathrm{H}_2 + \mathrm{He}$	$< 1 \times 10^{-13}$	estim. [49]
18	$\mathrm{H}_3^+ + \mathrm{H}_2 + \mathrm{H}_2 \longrightarrow \mathrm{H}_5^+ + \mathrm{H}_2$	4.6×10^{-30}	[165]
19	$\mathrm{H}_3^+ + e^- \longrightarrow products$	$f([\mathrm{H}_2])$	this work, [49]
20	$\mathrm{H}_5^+ + e^- \longrightarrow products$	2.5×10^{-6}	[49]
21	He^+	34	[166]
22	He_2^+	53	[166]
23	Ar^+	72	[166]
24	Ar_2^+	72	estim. [166]
25	ArH^+	67	[166]
26	H_3^+	110	[166]
27	H_5^+	110	estim. [166]

Table 3.3: Basic reactions which take place in the $\mathrm{H}_3^+/\mathrm{H}_5^+$ experiment. Reactions 1–5 proceed in the section downstream from the microwave discharge. Reactions 6–10 represent conversion of the helium plasma to an argon plasma after injection of argon. Reactions 11–20 represent the formation and destruction of H_3^+. Rows 21–27 represent ambipolar diffusion of particular ions. The displayed rate coefficients are recalculated to $T = 250$ K (for the cases of known temperature dependence). Diffusion rates are displayed for $P = 1600$ Pa, $T = 250$ K, 5 cm diameter of the flowtube and flow velocity 5.1 m/s. References for reactions 17, 24 and 27 have been used for the estimation of the displayed rate coefficient value. Results of the numerical model of chemical kinetics in the *FALP–VT* using reactions in this table are presented in figure 3.4. Products of reactions 19 and 20 can be a combination of H atoms and H_2 molecules. H recombines on the walls to form H_2 and is returned to the system.

No.	Reaction $[\mathrm{cm^3s^{-1}}]$, $[\mathrm{cm^6s^{-1}}$, [s]	Rate coefficient	Reference
28	$\mathrm{Ar^+ + D_2 \longrightarrow ArD^+ + D}$	7.5×10^{-10}	[167]
29	$\mathrm{Ar^+ + D_2 \longrightarrow Ar + D_2^+}$	react. 28 is dominant	
30	$\mathrm{D_2^+ + Ar \longrightarrow ArD^+ + D}$	1.5×10^{-9}	[167]
31	$\mathrm{D_2^+ + D_2 \longrightarrow D_3^+ + D}$	1.6×10^{-9}	[167]
32	$\mathrm{ArD^+ + D_2 \longrightarrow D_3^+ + Ar}$	6×10^{-10}	[167]

Table 3.4: Additional reactions which take place in the $\mathrm{D_3^+/D_5^+}$ experiment. Listed reactions replace reactions 11–15 in table 3.3 in the case of deuterium as reactant gas.

therefore we developed a model of plasma formation so as to have a good control over the chemical kinetics in the reaction zone.

The kinetics of $\mathrm{H_3^+}$ formation is well understood and has been described several times, e.g. in [108, 111, 112, 128, 129, 137]. Tables 3.3 and 3.4 summarize the reactions involved in the experiments with $\mathrm{H_2}$ and $\mathrm{D_2}$ reactant gas respectively. An example of results from the numerical model of chemical kinetics[6] in the flowtube in the case of $\mathrm{H_2}$ as reactant gas is given in figure 3.4 where particular panels represent different concentrations $[\mathrm{H_2}]$. Numerical models help to find the right experimental conditions where the ion or ions to be studied are in the majority in the reaction zone.

Ions in the reaction zone (after injection of a reactant) are expected to be in their ground vibrational state. This assumption is supported by the high probability of deexcitation in collisions with the helium buffer gas [108,128]. For the same reason, we expect an equilibrium between the plasma and the neutral gas and thus also identical temperatures of ions, electrons and neutral gas. The electron temperature measurement by the Langmuir probe confirmed this assumption.

3.3 Preparatory measurements

Several preparatory measurements have been performed before both experiments with hydrogen and deuterium respectively.

3.3.1 Plasma velocity

In order to transform the position of the Langmuir probe to the reaction time, it is necessary to measure the plasma flow velocity in the flowtube (see section 2.2.4). Prior to performing the experiment with hydrogen, the velocity was measured at temperatures of 200 K, 250 K and 300 K and at several buffer gas flow rates. The values obtained, can in most cases be expressed by the following relation:

$$v(Q, T, p) = (5.2 \pm 0.3) \times 10^{-3} \times Q \times T / p \ [\mathrm{m/s}], \tag{3.7}$$

where Q is the buffer gas flow rate in sccm, T, the temperature in K and p, the pressure of the buffer gas in Pa. For typical experimental conditions, the flow velocity was ~ 5.1 m/s.

---

[6]The model solves a set of differential equations constructed from chemical reactions. In the case of chemical kinetics, such a set of equations is characterized by huge differences in amplitudes of particular terms. Such equations are called *stiff* and special numerical procedures have to be applied. For details see eg. [168].
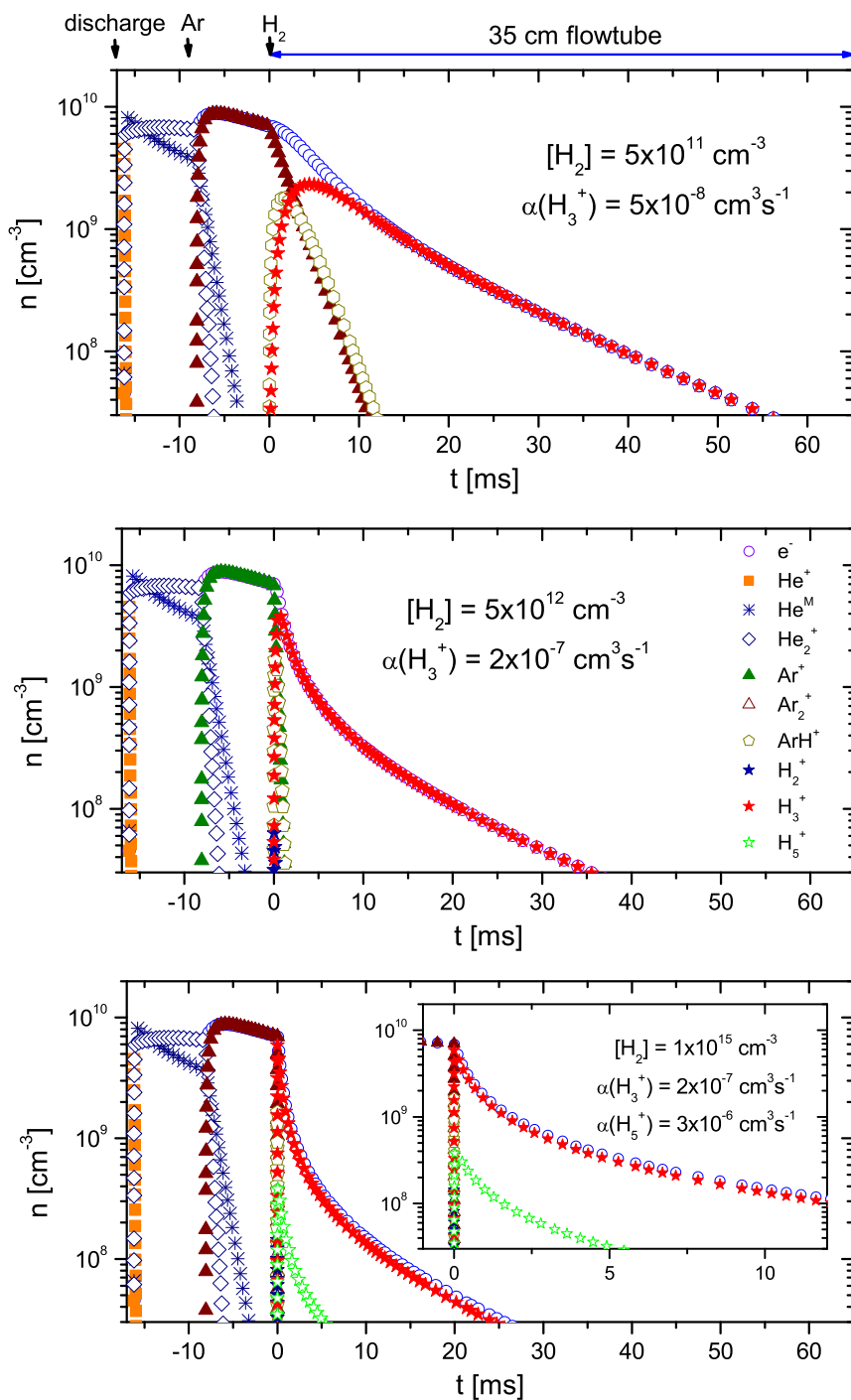
Figure 3.4: Numerical model of chemical kinetics in the *FALP–VT* for hydrogen as reactant gas based on reactions listed in table 3.3. Initial conditions: $T = 250$ K, $P = 1600$ Pa, flowtube diameter 5 cm, flow velocity 5.1 m/s, He flow rate 6500 sccm ($\sim 5 \times 10^{17}$ cm^{-3}), Ar flow rate 0.2 sccm ($\sim 1.2 \times 10^{13}$ cm^{-3}), initial electron concentration $[e^-] = 1 \times 10^{10}$ cm^{-3}. Particular panels show the behavior at three different initial concentrations of reactant gas H_2 where the recombination rate coefficient is varied according to [49] and [143]. The model of plasma formation for the D_3^+/D_5^+ experiment (section 3.4) looks very similar, the main difference being "faster" diffusion with respect to recombination due to different plasma velocity and pressure (see section 2.2.5 for more details).

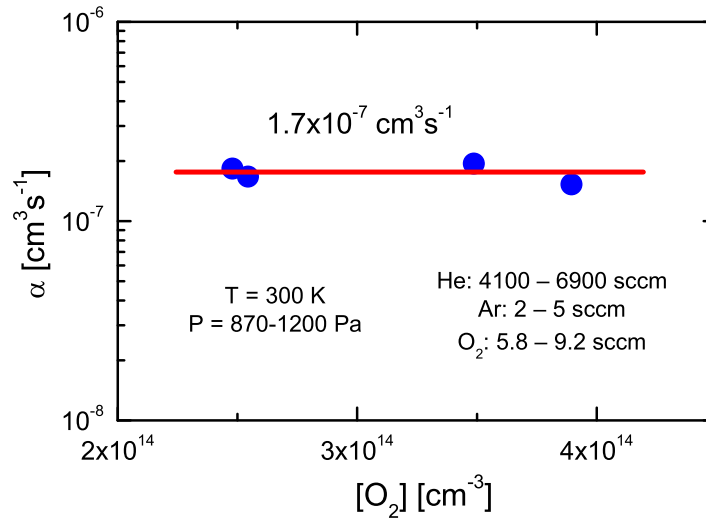Figure 3.5: Calibration of the Langmuir Probe before the experiment with deuterium as reactant gas: The recombination rate coefficient for O_2^+ ions with electrons was measured at several pressures and flow rates of O_2 (see description in the plot). The measured result corresponds well with the expected value $\alpha = 2 \times 10^{-7}(300/T)^{0.65}$ cm^{3}s^{-1} (see appendix B) and the calibration factor 1.17 ± 0.10 differs only slightly from 1.

Deviations from expression 3.7 have been observed only at $T = 200$ K for $z < 6$ cm. Such behavior can be explained by a variation of the radial velocity distribution at the beginning of the flowtube due to the bending region between the discharge tube and the flowtube. All results presented in section 3.5, however, were obtained at 250 K where such an effect was negligible; lower than the precision of the velocity measurement (maximum 10%).

Plasma velocity measurements in previous versions of the apparatus, the *FALP–VT-prototype* (used for experiment with deuterium, section 3.4) displayed the same dependence on T, Q and p, but due to different nozzles at the end of the flowtube, the amplitude was different giving $v \approx 8.5$ m/s under typical measurement conditions. The velocity deviation at the beginning of the flowtube was, however, much stronger due to the sharper bending between discharge tube and the flowtube (see section 2.2.5 for more details). This was also one of the main reasons why this version of the *FALP–VT* could not be used for the determination of very slow recombination rates in combination with a long formation time for H_3^+/D_3^+, at $[H_2] < 2 \times 10^{12}$ cm^{-3} (similarly for $[D_2]$). as the data fitting is very sensitive to any perturbative effects.

3.3.2 Calibration of Langmuir probe

Calibration of the Langmuir probe (see section 2.2.4 and appendix B) was performed by measuring the rate coefficient for the recombination of O_2^+ with electrons at temperatures $T = 250$ K and $T = 300$ K and at several concentrations of O_2 reactant gas. A numerical model for O_2^+ formation and destruction was developed so as to find the right concentration of reactant gas O_2. The negligible influence of O_4^+ formation and its recombination were taken as a limiting condition. Calibration factors obtained before the experiment with hydrogen and deuterium were 1.0 ± 0.1 and 1.17 ± 0.10 respectively. This slight difference can be easily explained e.g. by a non-precise velocity measurement as the velocity value is proportional to the final calibration factor. As the same plasma velocity was used for all data measured

in one experiment the calibration procedure removes any possible effect of error arising from this measurement. All data shown in this chapter are thus corrected. Figure 3.5 shows results of the calibration procedure performed prior to the experiment with deuterium.

3.3.3 Estimation of gas purity

Although all gases used in the experiments are cleaned in cold traps prior to use and the apparatus is heated for long periods before the experiment begins (see section 2.2.1 for more details), some impurities[7] may remain in the chamber and may possibly affect the ion formation. The amount of impurities in the apparatus can be estimated in a first approximation from the decay of the electron concentration with He and Ar as the only introduced gases, i.e. in a Ar^+ dominated plasma. As Ar^+ recombines very slowly, the observed decay is caused only due to diffusion and losses by reactions with impurities followed by fast recombination. The balance equation 2.7 can be then simplified to

$$\frac{dn}{dt} = -n/\tau_D - n/\tau_R, \tag{3.8}$$

where τ_D represents diffusion losses and τ_R losses in the following sequence of reactions:

$$Ar^+ + B \quad \xrightarrow{k_R} \quad B^+ + Ar, \tag{3.9}$$

$$B^+ + e^- \quad \xrightarrow{\alpha_R} \quad \text{neutral products}, \tag{3.10}$$

where B represents the impurity molecule. The limiting process under our conditions is reaction 3.9, where k_r can be estimated e.g. for $B = H_2O$: $k_R(B) \approx 2.0 \times 10^{-9}$ cm^3s^{-1} [169]. The Ar^+ decay can then be expressed as

$$[Ar^+] = [Ar^+]_0 \exp\left(-t\,k_R[B] - t\frac{D_a}{\Lambda^2}\right) = [Ar^+]_0 \exp\left(-\frac{t}{\tau_R} - \frac{t}{\tau_D}\right) \tag{3.11}$$

$$\Rightarrow \frac{1}{\tau_R} = k_R[B] \Rightarrow [B] = \frac{1}{k_R\tau_R},$$

where for the total measured decay time τ

$$\frac{1}{\tau} = \frac{1}{\tau_R} + \frac{1}{\tau_D}. \tag{3.12}$$

τ_D is calculated from the mobility of Ar^+ in He using the Einstein equation and therefore τ_R can be extracted from the decay characterized by τ. Figure 3.6 (left panel) shows a typical electron density decay in an argon plasma. The value of $\tau_R = 115$ ms obtained from this gives the first approximation to the concentration of impurities: $[B] \approx 4 \times 10^9$ cm^{-3} which for $p = 1600$ Pa and $T = 250$ K represents ~ 0.01 ppm of the total concentration. This purity demonstrates the efficiency of the cold traps because the purity of the helium used was 10 ppm. The right panel of figure 3.6 shows the QMS spectrum measured in an argon plasma at the end of the flowtube, approximately 120 ms downstream of the reactant gas injection port for ($t = 0$, $z = 0$). The composition of the plasma shows a small portion of ions formed from impurities (H_2O^+, H_3O^+, N_2^+, N_2H^+). A relatively high H_3^+ concentration is formed from H_2 which can penetrate into the flowtube due to leakage in the valve on the reactant gas line or can be delivered as an impurity with the helium, because H_2 is not removed in zeolite traps cooled with liquid nitrogen. Such a concentration of H_3^+ corresponds to ~ 0.01 sccm of a mixture $He:H_2$ (100:1) or to 0.015 ppm of H_2 in helium. A detailed discussion of the possible influence of "ion impurities" on the study of H_3^+ is given in section 3.5.2.

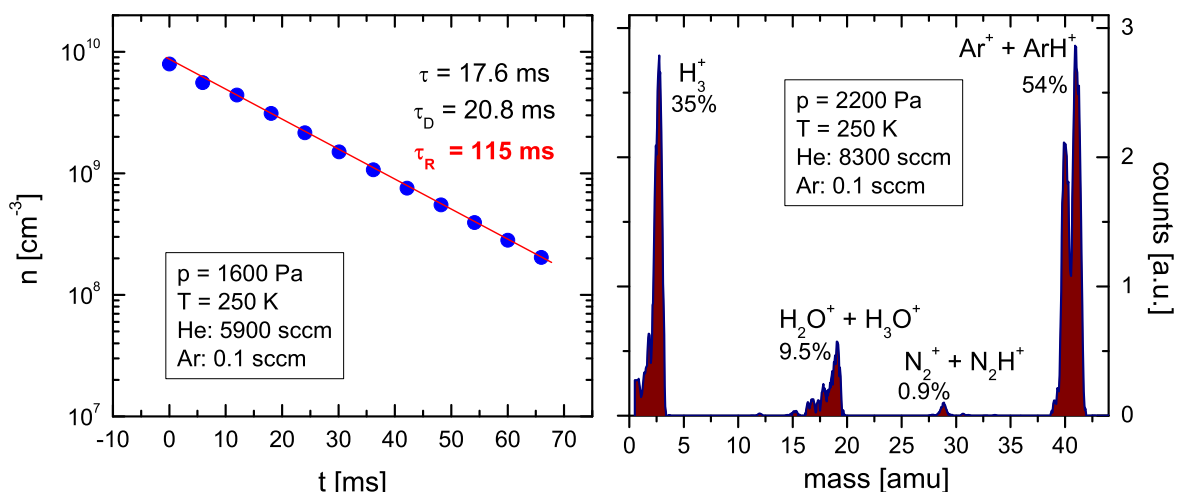[7]Unwanted species as water, air gases, hydrocarbons...

Figure 3.6: Estimation of the amount of impurities. **Left panel:** The electron concentration decay measured in an argon plasma. The curve displays pure exponential behavior and corresponds to losses by diffusion and reactions with impurities. In a first approximation, the observed decay corresponds to ~ 0.01 ppm of water of the total concentration. **Right panel:** The QMS spectrum measured in an argon plasma at a distance $z = 600$ mm ($t = 120$ ms) downstream of the injection port of the reactant gas. The plasma composition displays a small portion of ions formed via reaction with impurities. H_3^+ is formed in reactions with H_2 which can be included in helium as an impurity or can penetrate through the valve on the reactant gas line. The amount of H_2 is estimated in the text.

3.4 D_3^+, D_5^+

A measurement with deuterium as a reactant gas was performed in 2004 using the *FALP-VT-prototype* apparatus (see section 2.2.5). This study followed a similar measurement with H_2 on the older *HPFA* apparatus [49]. The main goal was to investigate the dependence of the measured effective recombination rate coefficient α_{eff} on the number density of reactant gas $[D_2]$ and on the temperature. The range of reactant concentrations was chosen to have an overlap with a similar measurement on the *AISA* apparatus [112] and to extend it to higher values where the formation of D_5^+ was expected. Technical problems (described in section 2.2.5) did not allow us, however, to investigate an interesting region below $[D_2] < 10^{12}$ cm^{-3} where the decrease of the rate coefficient was observed in *AISA*. Later, after technical improvement of the apparatus, this region was investigated with H_2 as a reactant gas and this measurement is described in section 3.5.

3.4.1 Data analysis

If D_3^+ ions are the dominant ions in the decaying plasma, the determination of the rate coefficient is straightforward and follows the standard procedure used at FALPs described in section 2.2.3. In the *FALP–VT* at a relatively low temperature and at high pressures of He and D_2, the formation of cluster ions D_5^+ via a three-body association reaction and their destruction by collision induced dissociation (CID) in collisions with He atoms [170,171] can

play an essential role. In such cases we have to consider the reaction scheme:

$$D_3^+ + D_2 + He \underset{k_{-3}}{\overset{k_3}{\longleftrightarrow}} D_5^+ + He \tag{3.13}$$

where k_3 is the rate coefficient of the three-body association (the forward process) and k_{-3} the binary rate coefficient of the CID (the reverse process). At the same time both ions recombine with electrons:

$$D_3^+ + e^- \overset{\alpha_3}{\longrightarrow} \text{ products}, \tag{3.14}$$

$$D_5^+ + e^- \overset{\alpha_5}{\longrightarrow} \text{ products}. \tag{3.15}$$
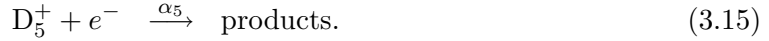
Here, α_3 and α_5 are the respective recombination rate coefficients. When considering processes 3.13–3.15 and diffusion losses, the balance equation for electrons is

$$\frac{dn}{dt} = -\alpha_3 n[D_3^+] - \alpha_5 n[D_5^+] - n/\tau, \tag{3.16}$$

where $n = n_e = [D_3^+] + [D_5^+]$ is the electron concentration and τ characterizes losses by ambipolar diffusion and losses by ion-molecule reactions (for details see equation 2.8). If we introduce the ratio $R = [D_5^+]/[D_3^+]$, equation 3.16 can be rewritten as

$$\frac{dn}{dt} = -(\alpha_3 + R\alpha_5)\frac{n^2}{1+R} - n/\tau = -\alpha_{\text{eff}}\, n^2 - n/\tau, \tag{3.17}$$

where $\alpha_{\text{eff}} = (\alpha_3 + R\alpha_5)/(1+R)$ is the effective recombination rate coefficient.

The equilibrium described by equation 3.13 is not violated by recombination losses only in the case where rates of recombination losses are negligible in comparison to the rate of "exchange" between D_3^+ and D_5^+. Such a condition can be also expressed by comparison of typical time constants for particular processes: The rate k_3 is taken to be similar to that for the comparable reaction in hydrogen (see table 3.3, reaction 16): $k_3 < 10^{-29}$ cm^{6}s^{-1}. For typical working conditions $p = 1200$ Pa, $T = 200$ K ([He] $\approx 4 \times 10^{17}$ cm^{-3}) and [D$_2$] $= 10^{15}$ cm^{-3} the time constant for association (forward reaction) is $\tau_{as} = 1/(k_3[D_2][He]) \approx 0.25$ ms. For higher [D$_2$] the τ_{as} is even shorter, while for lower [D$_2$] the D_3^+ dominates in the flowtube and the standard data analysis procedure can be applied. The "time constant" for recombination of D_3^+ is $\tau_{\alpha 3} = 1/(\alpha_3[e^-]) \approx 2.5$ ms when using values $\alpha_3 \approx 2 \times 10^{-7}$ cm^{3}s^{-1} and $[e^-] \approx 2 \times 10^9$ cm^{-3}. For the reverse process, it is necessary to estimate the rate k_{-3} for the CID. This can be calculated from the equilibrium constant defined as $K_C = k_3/k_{-3}$ taken e.g. from [174]: $K_C(200\text{ K}) = 2 \times 10^{-16}$ cm^3 $\Rightarrow k_{-3} = k_3/K_C \approx 5 \times 10^{-14}$ cm^{3}s^{-1}. The time constant is then $\tau_{CID} = 1/(k_{-3}[He]) \approx 40$ µs. For recombination of D_5^+: $\tau_{\alpha 5} = 1/(\alpha_5[e^-]) \approx 170$ µs for $\alpha_5 \approx 3 \times 10^{-6}$ cm^{3}s^{-1}. Obviously $\tau_{\alpha 3} \gg \tau_{as}$ and recombination of D_3^+ will not affect the equilibrium. For the reverse process $\tau_{\alpha 5} > \tau_{CID}$ but the ratio $4.5\times$ is not too high to fully neglect the effect of recombination. However, for the basic analysis we assumed to have equilibrium conditions between D_3^+ and D_5^+ in the flowtube and the possible effect of recombination at different temperatures is discussed in the section on results 3.4.2. This assumption of equilibrium was also verified by the kinetic model (see comparable model for hydrogen in figure 3.4, lower panel).

When conditions for equilibrium between D_3^+ and D_5^+ are fulfilled, the ratio $R = [D_5^+]/[D_3^+]$ remains constant along the flowtube and can be rewritten as

$$R = \frac{[D_5^+]}{[D_3^+]} = \frac{k_3[D_2]}{k_{-3}} = K_C[D_2], \tag{3.18}$$

where K_C is the equilibrium constant given by temperature and by an entropy and an enthalpy change in the reaction 3.13 (the vant Hoff equation [172,173]). The formula for α_{eff} can be rewritten as

$$\alpha_{\text{eff}} = (\alpha_3 + \alpha_5 K_C[D_2]) \frac{1}{1 + K_C[D_2]}. \tag{3.19}$$

This formula shows the influence of $[D_2]$ on the measured effective recombination rate coefficient in a $D_3^+/D_5^+/e^-$ plasma. For $K_C[D_2] \ll 1$ (the so called "low pressure limit") equation 3.19 collapses to

$$\alpha_{\text{eff}} = \alpha_3 + \alpha_5 K_C[D_2] \tag{3.20}$$

and in the limit case

$$\lim_{[D_2] \to 0} \alpha_{\text{eff}} = \alpha_3. \tag{3.21}$$

On the other hand, for high densities where $K_C[D_2] \gg 1$ (the so called "high pressure limit") the limit is $\alpha_{\text{eff}} = \alpha_5$. This conclusion is obvious: for low $[D_2]$ the formation of D_5^+ is negligible and recombination of D_3^+ is dominant. For high $[D_2]$ D_3^+ is transformed to D_5^+ and the recombination of D_5^+ dominates. The described procedure can be, in analogy, applied to higher clusters D_{2n+1}^+ which can be created at even higher concentrations $[D_2]$ and $[He]$.

3.4.2 Results

We have measured the decay of a plasma in a $He/Ar/D_2$ mixture at several temperatures ranging from 130 K up to 300 K. The deuterium number density was changed systematically from 2×10^{12} to 2×10^{15} cm^{-3}. This large variation allowed us to cover plasmas dominated by the recombination of D_3^+ ions and by the recombination of a mixture of D_3^+ and D_5^+. Due to technical limitations[8] we did not measure at very high $[D_2]$ to reach the dominance of D_5^+. The total pressure was maintained at 900–1200 Pa (~ 6000 sccm) and a partial pressure of argon at ~ 0.2 Pa (~ 1.1 sccm). Figure 3.7 displays an example of the Langmuir probe evolution along the flowtube and the appropriate square root of measured current fitted to obtain the electron concentration (the so called *i-square* method, see appendix B). Figure 3.8 shows an example of electron density decays measured at 190 K. It is obvious, that the decay of the plasma depends on the deuterium number density.

The effective recombination rate coefficients obtained at four different temperatures are plotted in figure 3.9. Detailed analysis of the expected rate coefficients in reaction 3.13 has shown that at the lowest temperature $T = 130$ K, destruction of D_5^+ by CID starts to be comparable, or slower than destruction by recombination. In that case the equilibrium between D_3^+ and D_5^+ is not established and formula 3.19 is not applicable. The following discussion is thus valid only for temperatures 300 K, 260 K and 190 K.

We assume that H_5^+ and D_5^+ have similar recombination rate coefficients $\alpha_5 = 3 \times 10^{-6}$ cm^{3}s^{-1} and that these do not change substantially with temperature (for the temperatures used ; the assumption is based on our measurement [49]). Using this value we can fit the data for particular temperatures with the function 3.19 to obtain $\alpha_3(T)$ and $K_C(T)$. Obtained values of α_3 are included in figure 3.9 and it can be seen that they are in good agreement with data measured at similar temperatures in the *AISA* experiment. Values of K_C follows here: $K_C(300 \text{ K}) = (1.8 \pm 0.3) \times 10^{-17}$ cm^3, $K_C(260 \text{ K}) = (5.8 \pm 0.5) \times 10^{-17}$ cm^3, $K_C(190 \text{ K}) = (3.8 \pm 2.0) \times 10^{-16}$ cm^3.

---

[8]The flow rate required for reaching the D_5^+ dominance region is higher than 10 sccm and such consumption of deuterium gas would be very expensive.
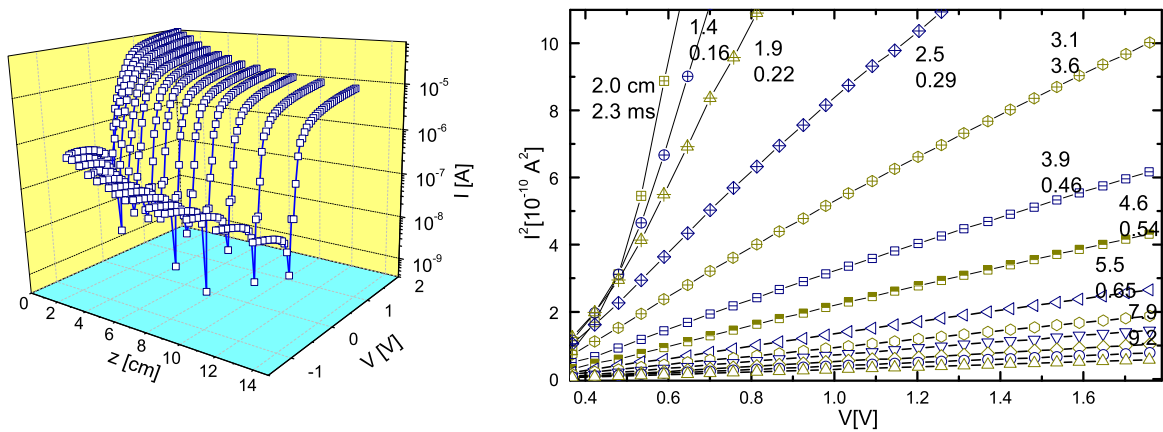
Figure 3.7: **Left panel:** The evolution of the probe characteristic along the flow tube for $p = 1200$ Pa, $T = 190$ K, $[D_2] = 10^{15}$ cm^{-3}. The probe potential is measured with respect to the potential of the metal body of the flow tube. For details on Langmuir probe measurements, see appendix B. **Right panel:** Examples of I^2 versus probe potential corresponding to the probe characteristic evolution in the plot in the left panel. The slopes of the linear portions of the plots provide the electron number densities. The numbers indicate the position along the flow tube (z) and the corresponding time (appropriate to flow velocity 8.5 m/s) in cm and ms respectively.

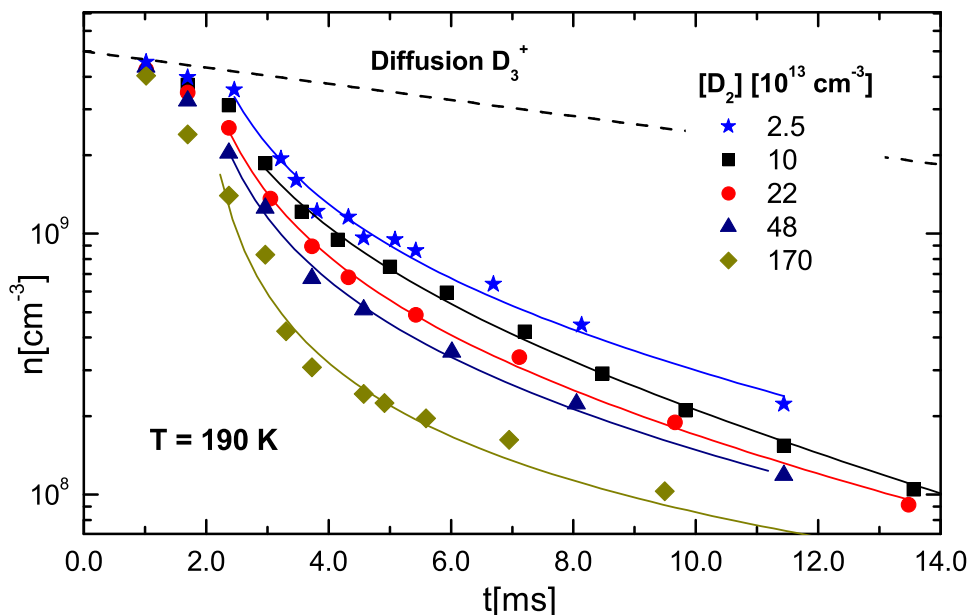Figure 3.8: The decay of a plasma containing a mixture of D_3^+ and D_5^+ ions at 190 K and helium pressure ~ 1000 Pa. The curves were measured at several deuterium number densities. The dashed line indicates the expected diffusion losses of D_3^+ in a He buffer gas and solid lines represent fits to the individual data sets.
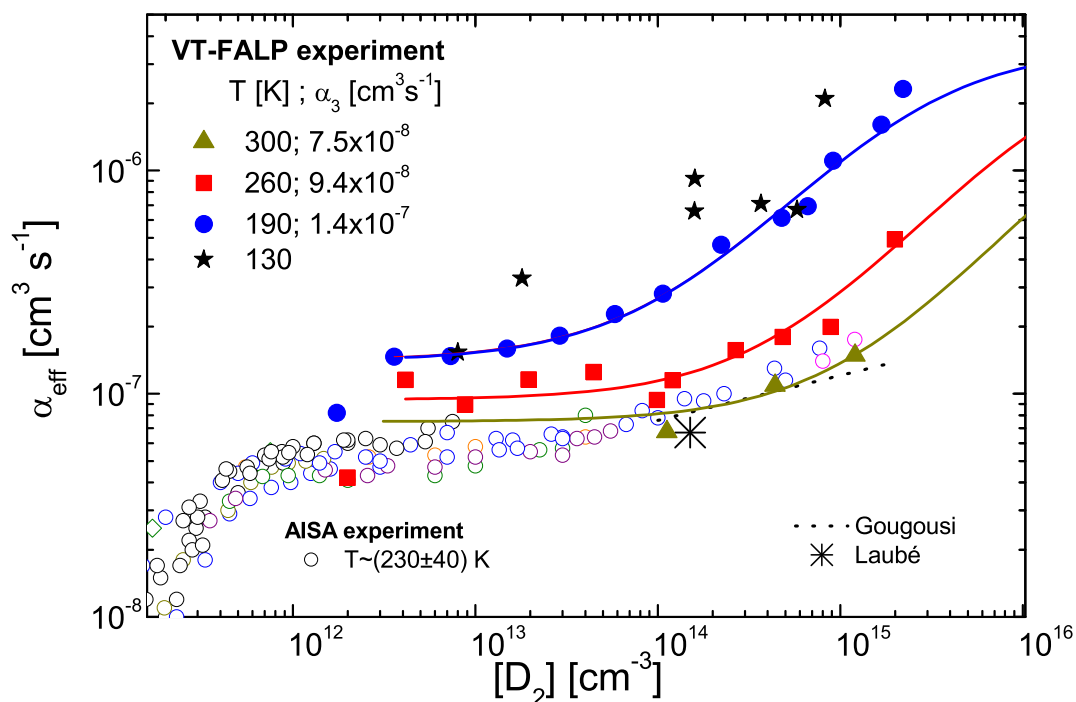
Figure 3.9: The effective recombination rate coefficients α_{eff} measured over a very broad range of hydrogen number densities in *AISA* (open symbols) and in the *FALP–VT* (closed symbols) in a He-Ar-D_2 plasma mixture. The measurements on *AISA* were carried out at the temperature (230 ± 40) K. Data are compared also with [132, 133].

Figure 3.10 shows the Van't Hoff graph of the acquired $K_C(T)$ together with thermodynamic data measured by *Hiraoka and Mori* [174] and with similar data obtained for equilibrium between H_3^+ and H_5^+.

It can be seen, that previous measurements of K_C [174–177] show almost the same values for both the hydrogen and deuterium case. Our data (this study for deuterium and [49] for hydrogen) displays also almost the same values, however, they differ from previously mentioned measurements. This deviation is due to the influence of recombination losses on the equilibrium between D_3^+ and D_5^+ (and similarly between H_3^+ and H_5^+). Below equation 3.17 it was shown that for $T \sim 200$ K the influence of recombination can be neglected. However, for lower temperatures the rate of CID k_{-3} (see equation 3.13) exponentially decreases and therefore the lifetime of D_5^+ increases and can be removed by recombination. It means that the experimental equilibrium constant K_C^{exp} obtained from the fit using equation 3.19 is lower than the real K_C without the influence of recombination. On the other hand, the rate of the association reaction k_3 decreases at higher temperatures. Similarly, increasing the lifetime of D_3^+ increases the effect of recombination of D_3^+ and therefore K_C^{exp} obtained from the fit is higher than the real K_C. This is in good agreement with our observation.

The aim of this work was to study the influence of the formation of D_5^+ in a $D_3^+/D_5^+/e^-$ plasma and to define the regions of partial pressures and temperatures where the formation of D_5^+ cannot be neglected in the afterglow of a deuterium containing plasma. The study confirms that the pressure dependence of α_{eff} at $[D_2] < 5 \times 10^{13}$ cm^{-3} observed in the *AISA* experiment is not due to the formation of D_5^+.
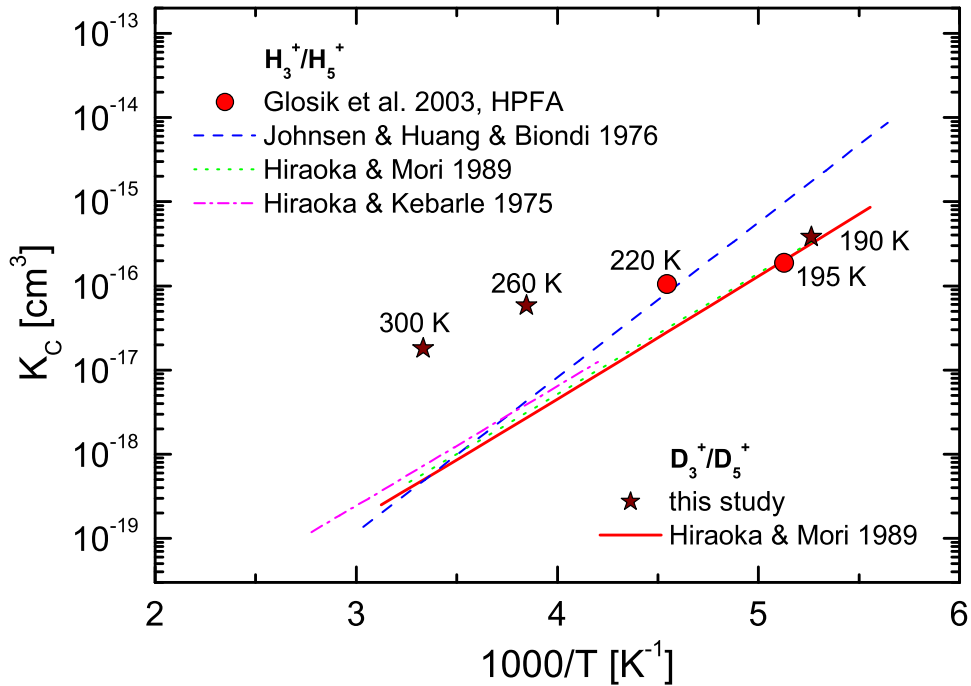
Figure 3.10: The Van't Hoff graph of the equilibrium constant $K_C(T)$ for the reaction $D_3^+ + D_2 \longleftrightarrow D_5^+$. The present data are compared with our previous measurement with hydrogen (HPFA apparatus, [49]) and with $K_C(T)$ based on thermodynamic data obtained in specialized measurements: *Hiraoka & Mori* [174] for deuterium and *Hiraoka & Mori* [175], *Johnsen & Huang & Biondi* [176] and *Hiraoka & Kebarle* [177] for hydrogen. The discrepancy between our measurement in the flowing afterglow and other studies is discussed in the text. In the cases [174, 175, 177] the $K_C(T)$ was calculated from thermodynamic data according to the Van't Hoff equation: $\ln K_C^o = -\frac{\Delta H^o}{RT} + \frac{\Delta S^o}{R}$ where K_C^o is the dimensionless equilibrium constant calculated as $K_C^o = K_C\, n^o$ and n^o, the number density at $p = 1$ Bar and temperature T. ΔH^o is the change of enthalpy and ΔS^o, the change of entropy in the reaction at standard conditions.

3.5 H_3^+

Measurements with hydrogen as reactant gas were performed in 2005 using the second improved version of the *FALP–VT* apparatus (the version described in section 2.2). The main goal was to re-investigate the dependence of the measured effective recombination rate coefficient α_{eff} on the number density of the reactant gas $[H_2]$ (and if possible also on temperature) in similar ranges of $[H_2]$ as in *AISA* experiments [108, 143]. The study also extends previous measurement with the *HPFA* apparatus [49] performed at higher $[H_2]$ which concentrated on the possible influence of H_5^+.

3.5.1 Data analysis

The numerical modeling of H_3^+ formation presented in section 3.2 has shown that the transformation of Ar^+ to H_3^+ (see table 3.3) can proceed along a considerable part of the flowtube, especially with a very low concentration of reactant - H_2. In that case there is a risk that the standard fitting procedure (see section 2.2.3, especially equation 2.9) would be applied also in the "ion formation region" where the H_3^+ is not yet dominant. For this reason, an advanced data analysis procedure have been developed.

The balance equation for plasma concentration $n = [e^-] = \sum_i [A_i^+]$, where A_i^+ represents all ion types in the studied zone, was derived in section 2.2.3:

$$\frac{dn}{dt} = -\alpha\, n^2 - n/\tau. \tag{3.22}$$

In the "ion formation zone", the ions mainly present are H_3^+, Ar^+ and ArH^+. As Ar^+ and ArH^+ recombine very slowly with electrons [178] the only electron loss process in the term αn^2 is recombination with H_3^+. The concentration $[H_3^+]$ is linked with the electron concentration as $[H_3^+] = \xi(z)\, n$, where $\xi(z)$ is a factor describing the ratio of H_3^+ and total ion concentration. Obviously $\xi \leq 1$ and ξ increases with z (or t respectively) as H_3^+ reaches majority in the plasma. Then the balance equation can be rewritten as

$$\frac{dn}{dt} = -\alpha\, \xi(t)\, n^2 - n/\tau. \tag{3.23}$$

Simple integration gives

$$\ln\left[\frac{n(t_b)}{n(t_a)}\right] + (t_b - t_a)/\tau = -\alpha \int_{t_a}^{t_b} \xi(t)\, n(t)\, dt, \tag{3.24}$$

where t_a and t_b are integration limits and τ is expected to be constant with t.

If $\xi(t) = 1$ then a plot of $\{\ln[n(t_b)/n(t_a)] + (t_b - t_a)/\tau\}$ vs $\int_{t_a}^{t_b} n(t)\, dt$ with one of the integration limits as a variable should give a straight line with slope $-\alpha$. This is ensured only if the correct value of the constant τ is used, otherwise the graph is curved. The correct value of τ is determined by minimizing the χ^2 of the linear fit[9] where τ is the varied parameter.

The analysis requires further discussion when $\xi(t) \neq 0$. Let's define $\epsilon(t) = 1 - \xi(t)$. Then the balance equation can be written as

$$\ln\left[\frac{n(t_b)}{n(t_a)}\right] + (t_b - t_a)/\tau = -\alpha \int_{t_a}^{t_b} n(t)\, dt + \alpha \int_{t_a}^{t_b} \epsilon(t)\, n(t)\, dt. \tag{3.25}$$

---

[9]Minimization of the sum of the least squares of differences between the data and the fit.
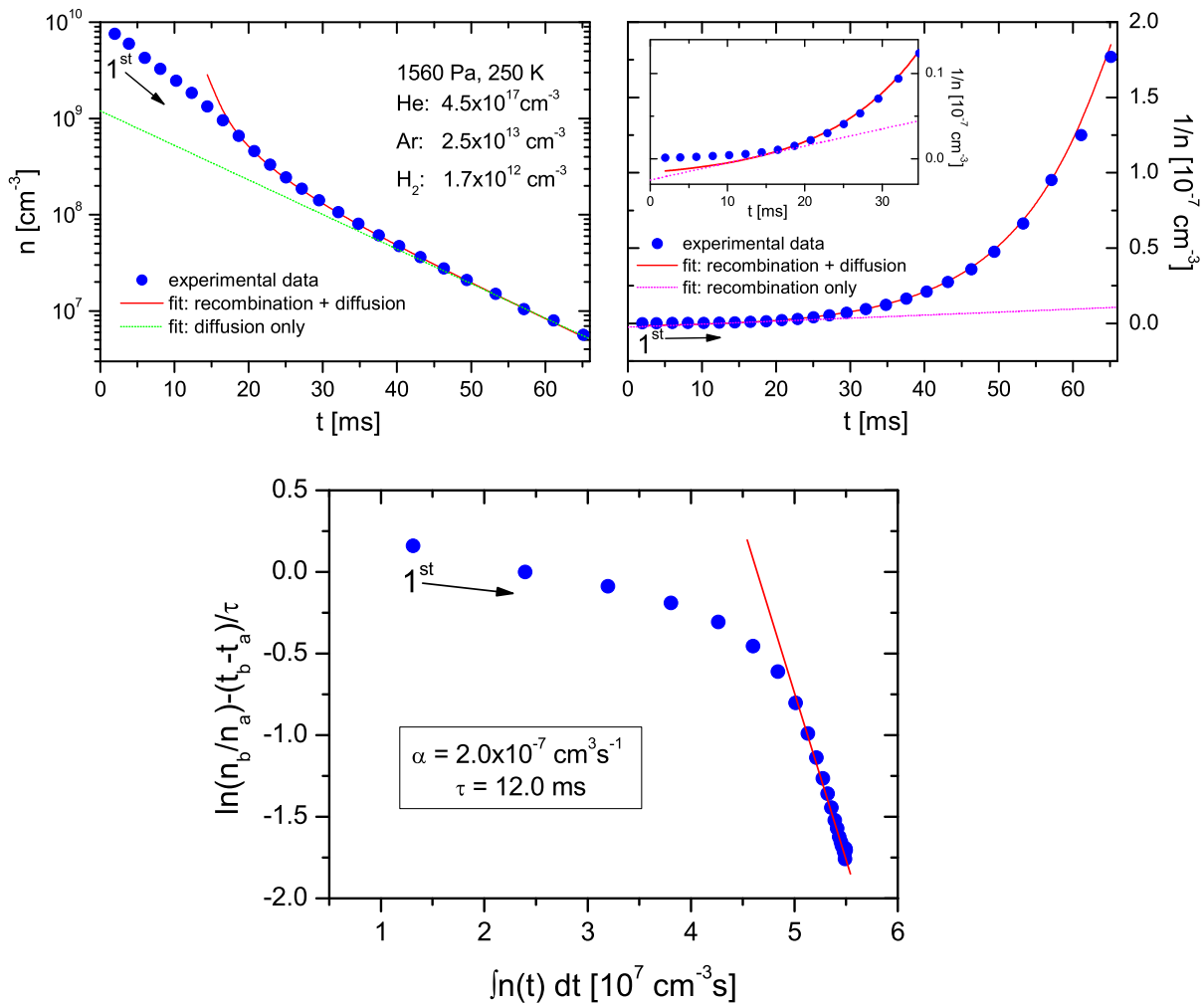
Figure 3.11: An example of the data analysis applied for the determination of the recombination rate coefficient from the measured electron density decay. Mark "1st" and arrows in all graphs show the order of data points. **Top left panel:** The measured electron density decay. Full and dotted lines show model decays via recombination and diffusion based on parameters determined by the advanced data analysis. **Top right panel:** The graph $1/n$ vs t determined from the same dataset. This projection is often used for the determination of α as it displays a linear dependence in cases of negligible diffusion (see footnote 10 on page 17). It is obvious that for our data such an analysis cannot be applied as diffusion significantly affects the decay curve. Moreover the "ion formation zone" is hidden in this projection. **Bottom panel:** The plot of $\{\ln[n(t_b)/n(t_a)] + (t_b - t_a)/\tau\}$ vs $\int_{t_a}^{t_b} n(t)\,dt$ based on the data in the left panel. The data on the left correspond to low t. The "ion formation zone" can be easily distinguished as it deviates from the linear fit to the rest of the data. τ was determined by χ^2 minimization of the linear fit to the data out of the "ion formation zone". α and τ so obtained are displayed in the figure.

Let $t_a = 0$ be a fixed parameter and t_b the variable parameter scanning over all data points starting from t_a. Then the second integral term $\int_{t_a}^{t_b} \epsilon(t)\, n(t)\, dt$ increases with increasing t_b as long as $\epsilon(t) > 0$. For higher t_b the H$_3^+$ attain dominance, $\xi = 1 \Rightarrow \epsilon = 0$ and thus the integral does not increase. In another words, the second integral term does not differ for t_b scanning over the zone with H$_3^+$ dominant and acts only as a constant. Then a plot of $\ln\left[n(t_b)/n(t_a)\right] + (t_b - t_a)/\tau$ vs $\int_{t_a}^{t_b} n(t)\, dt$ is again a straight line with α as slope. The data measured in the "ion formation zone" can be easily distinguished as they deviate from the linear fit. A different t_a than 0 only results in a different constant shift in the y-axis. τ is determined in the same way as for $\xi = 1$.

The y-axis term $\left\{\ln\left[n(t_b)/n(t_a)\right] + (t_b - t_a)/\tau\right\}$ can be also interpreted as the normalization of data to $n(t_a)$ and subtraction of diffusion losses. The remaining part yields extracted recombination losses.

The advantages of this data analysis in comparison to the standard fitting of $n(t)$ by equation 2.9 are:

- Linear fitting is easier and more precise than direct fitting by a nonlinear equation 2.9 with 3 fitted parameters (n_0, α, τ).

- The "ion formation zone" is visually more distinguishable, especially for very low α.

- The diffusion (τ) can be easily determined also from short decays where $n(t)$ does not decrease sufficiently so that recombination is negligible with respect to diffusion (long time t).

An example of a measured electron density decay, applied data analysis and additional interpretation graphs are given in figures 3.11 and 3.12.

3.5.2   Results

We have measured the electron density decay in an afterglow with a He/Ar/H$_2$ mixture. The temperature was set to $T = 250$ K as this temperature was found to be low enough for maintaining high purity in the system, but also high enough to preserve easily stable measurement conditions and to exclude the variation of velocity at the beginning of the flowtube (observed in the velocity measurement, see section 3.3.1). The hydrogen number density was changed systematically from 2×10^{11} to 10^{15} cm^{-3}. The low concentration [H$_2$] $< 10^{13}$ cm^{-3} was reached by mixing H$_2$ with He in the ratio 1:100. We did not measure at higher [H$_2$] as this region was already investigated with the *HPFA* apparatus [49]. The total pressure was maintained at 1500-1600 Pa (~ 5900 sccm of He) and the partial pressure of argon at ~ 0.03 Pa (~ 0.1 sccm). Figure 3.13 shows examples of electron density decays. The chosen datasets cover the whole range of [H$_2$] used. All datasets have been analyzed according to the procedure described in section 3.5.1. τ was found to be almost constant (ranging from 11.7 to 12.9 ms) for all [H$_2$]. The expected characteristic time for exponential losses due to diffusion only is $\tau_D = 13.8$ ms under our experimental conditions. The decay time due to reactions with impurities are then in range $\tau_R = (80 - 190)$ ms where values are distributed independently of the actual flow rate of H$_2$. These values are in good agreement with $\tau_R = 115$ ms obtained from the decay in an argon plasma (see section 3.3.3). This confirms that the reactant injection line is not the main source of impurities.
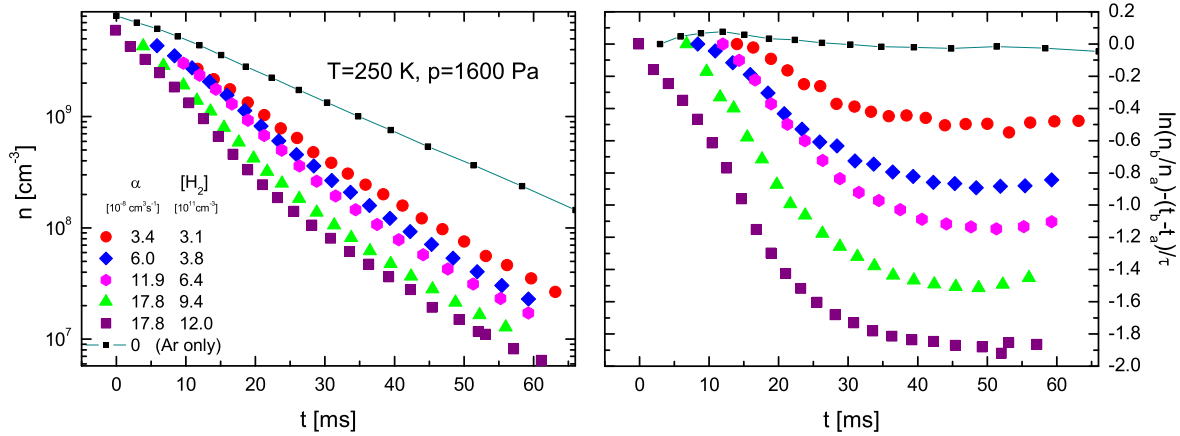
Figure 3.12: The interpretation of the data analysis described in section 3.5.1. **Left panel:** Examples of electron density decays in the *FALP–VT* for several [H_2]. Datasets are taken from figure 3.13. **Right panel:** The same data as in the left panel with the y-axis converted to $\{\ln[n(t_b)/n(t_a)] + (t_b - t_a)/\tau\}$. In this projection, data are normalized to $n(t_a)$ and diffusion losses are subtracted. The remaining part displays the extracted recombination losses, where horizontal parts shows the dominance of diffusion. The different vertical offset of these horizontal parts is caused by differing influences of the "ion formation zone" and by different recombination rates, (see explanation in the text). Obtaining α and τ requires transformation of the x-axis to $\int_{t_a}^{t_b} n(t)\,dt$, see figure 3.11.

The length of the "ion formation zone" $t_f(i)$ was determined for each dataset "i" from the fitting procedure[10] and the right panel of figure 3.13 shows decays with time scales shifted by $-t_f(i)$. In this projection, one can clearly see the evolution of the recombination rate coefficient α_{eff} dependence on [H_2]: The diffusion part of the decay is constant (straight lines in the semi-log scale) while the recombination causes "bending" of the decays (again in the semi-log scale). It can be seen, that the recombination rate increases with increasing [H_2].

Values of $t_f(i)$ range from 10 to 17 ms while values calculated in the ion formation model (see section 3.2) do not exceed 12 ms for our experimental conditions[11]. The model however does not include the effect of mixing the reactant with the plasma. The reactant is injected through the nozzle placed at $z = 0$ and oriented upstream. The mixing, however, is not finished at $z = 0$. Usually the length needed for sufficient mixing is comparable to the diameter of the flowtube. In our case it is 50 mm corresponding to $t \approx 10$ ms. The mixing can also be affected by the flow rate of the reactant mixture as the "jet" streaming from the nozzle reaches different distances depending upon the velocity of the reactant in the nozzle (flow rate).

The measured rate coefficients α_{eff} are summarized in figure 3.14. Different symbols represent different data sets where all conditions except [H_2] were fixed at the same value in all cases. All datasets display the same behavior.

There are two easily distinguishable parts: The region with [H_2] $> 10^{12}$ cm^{-3} displays an almost constant recombination rate $\alpha_{\text{eff}} = 1.85 \times 10^{-7}$ cm^{3}s^{-1}. The slight increase of α_{eff} for

---

[10]The end of the "ion formation zone" is defined in this case as the last point deviating from the linear fit to the graph $\ln[n(t_b)/n(t_a)] + (t_b - t_a)/\tau$ vs $\int_{t_a}^{t_b} n(t)\,dt$ by more than $\sim 10\%$.

[11]The "ion formation zone" was defined in the model as the region where [H_3^+] $< 0.9\,[e^-]$
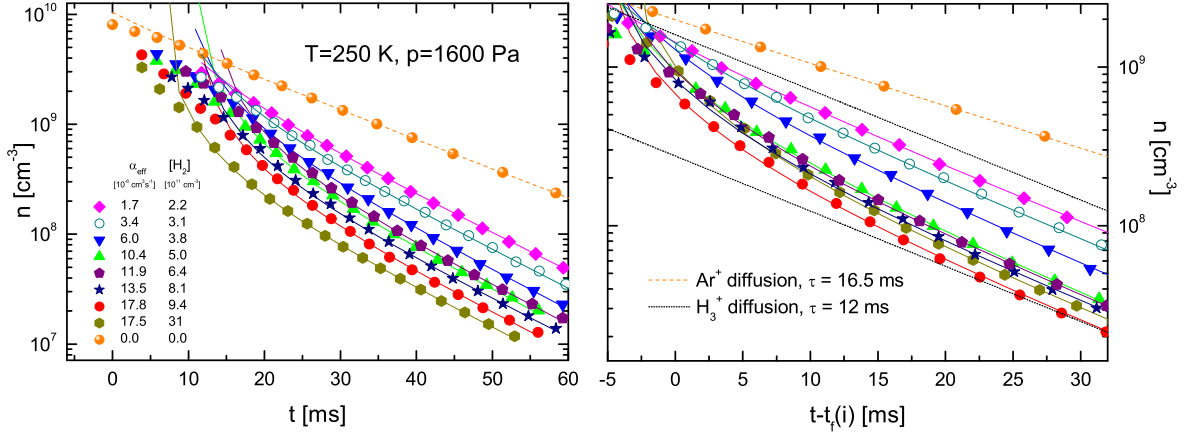
Figure 3.13: **Left panel:** A selection of electron density decays measured in a He-Ar-H_2 mixture at $T = 250$ K for several concentrations of reactant $[H_2]$. Included are the values of α_{eff} obtained from the data analysis described in section 3.5.1. **Right panel**: The same datasets as in the left panel but the time scale of particular decays is shifted by $-t_f(i)$, where $t_f(i)$ is the "length of the ion formation zone" derived for each dataset i. Here data for $t > 0$ are measured in a plasma with H_3^+ dominant and the dependence of α_{eff} on $[H_2]$ can be clearly seen.

$[H_2] > 10^{14}$ cm^{-3} is caused by the influence of the formation of H_5^+. This effect was previously studied in the *HPFA* apparatus [49]. At low concentrations of hydrogen $[H_2] < 10^{12}$ cm^{-3}, α_{eff} displays a steep evolution with α_{eff} increasing with $[H_2]$. The lowest measured value was $\alpha_{\mathrm{eff}}([H_2] = 1.5 \times 10^{11}$ cm$^{-3}) \approx 1.5 \times 10^{-8}$ cm^{3}s^{-1}.

Vertical error bars displayed in the graph represent the estimation of the total error of α_{eff} including the error arising from calibration of the Langmuir probe, the velocity measurement and fluctuations of Q, p and T. Larger error bars for very low and very high $[H_2]$ follow from the data analysis. At low $[H_2]$ (low α_{eff}) the effect of recombination is less distinguishable from diffusion and thus the fitting error increases. On the other hand, at the highest $[H_2]$, the electron concentration decreases significantly during the mixing of the reactant with the buffer gas. The data analysis is then applied at low electron concentrations where, again, the recombination is less distinguishable from diffusion losses.

Horizontal error bars include possible uncertainties due to the mixing of H_2 with He and deviations between the measured flow rate of the reactant gas at the flowmeter and the real flow rate into the chamber. This discrepancy can be caused e.g. by equilibration of the flow rate at the flowmeter and at the regulation valve as there is a ~ 70 cm long tube (~ 10 cm^3) between these two points including the cold trap. The error decreases with increasing $[H_2]$.

Figure 3.15 merges results of several afterglow experiments with H_2 as reactant. The data were selected to display only measurements performed at temperatures close to $T = 250$ K. It can be seen that the results obtained with the *FALP–VT* are in very good agreement with those obtained with the *HPFA* apparatus. As already discussed above, the formation of H_5^+ does not affect α_{eff} for $[H_2] < 10^{14}$ cm^{-3}. For higher $[H_2]$ the behavior of α_{eff} can be described by equation 3.19 rewritten for H_2 instead of D_2.
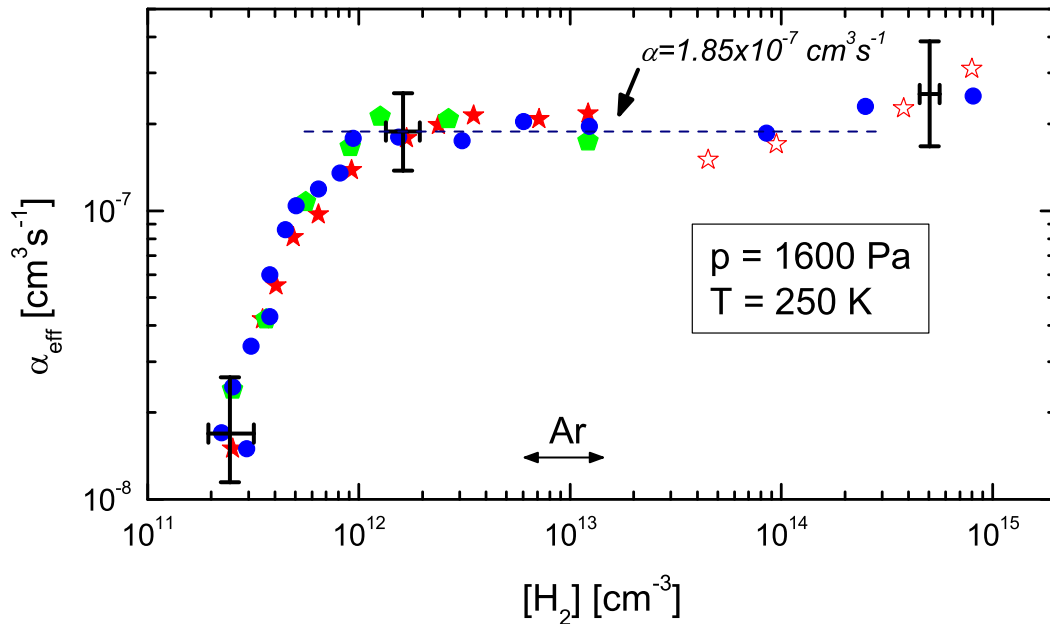
Figure 3.14: Rate coefficients measured with the *FALP–VT* apparatus for the recombination of H_3^+ with electrons (α_{eff}) in a decaying plasma as a function of H_2 addition. Particular symbols shows datasets measured on different experimental days. The dependence of α_{eff} on $[H_2]$ is discussed in the text.

α_{eff} obtained in both versions of the *AISA* apparatus in the region $3 \times 10^{11} < [H_2] < 10^{15}$ cm^{-3} are seen to be lower, by a factor of ~ 1.8. This difference is not too large if one takes into account the typical accuracy of the measurement in afterglow experiments. Nevertheless the higher values of α_{eff} in the *FALP–VT* can be explained by the possible influence of helium pressure on the recombination process as the working pressure is the main difference between the *AISA* and *FALP–VT* apparatuses (up to $8\times$ higher in the *FALP–VT*). The possible influence of collisions with helium (the rate is proportional to pressure) is discussed below. Other processes which may cause an increase of the observed α_{eff} is the influence of impurity ions. The model of chemical kinetics including reactions with impurities has shown that at concentrations of H_2O estimated in section 3.3.3, the concentration of H_3O^+ and H_2O^+ may reach 5×10^6 cm^{-3}. This concentration is relatively low in comparison to $[H_3^+]$ but a fast conversion of H_3^+ to H_3O^+ and subsequent fast recombination of H_3O^+ ($\alpha = 6 \times 10^{-7}$ cm^{3}s^{-1}) may increase the observed α_{eff} by a factor of up to 1.4. Nevertheless this effect is "one-directional", it always increases the measured α_{eff} and it cannot explain a steep evolution of α_{eff} at low $[H_2]$ if the recombination rate coefficient of H_3^+ was independent of $[H_2]$.

The measured values of α_{eff} are also in good agreement with a recent measurement using the *Test-Tube* apparatus with CRDS as the diagnostics method. As CRDS is a state selective method, it would be possible to discuss the possible difference if it could be said that vibrationally excited H_3^+ occurs in these experiments. The spread of data points in the *Test-Tube* results does not allow us, however, to make any conclusions from this point of view.
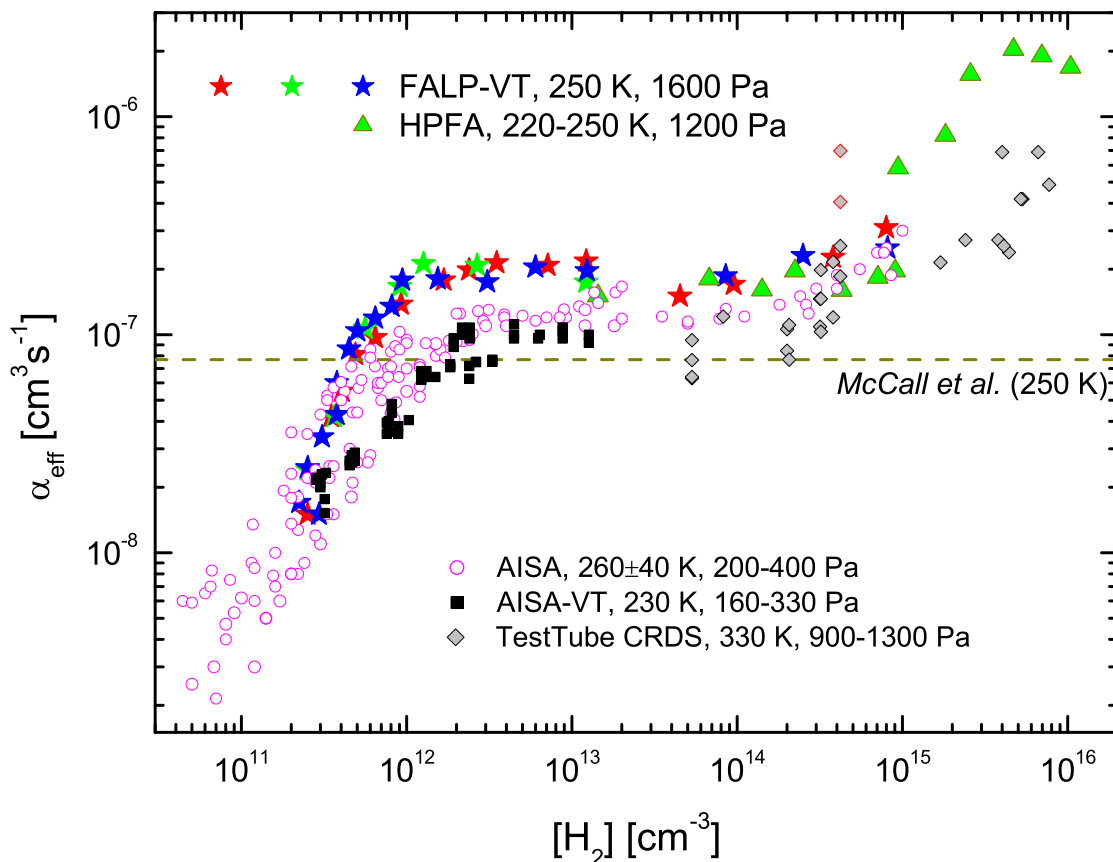
Figure 3.15: Effective recombination rate coefficients α_{eff} measured over a very broad range of hydrogen number densities in several different afterglow experiments: *FALP–VT* [this work] (particular colors of data points shows only different measurement days), *AISA* [108, 111], *AISA-VT* [143], *HPFA* [49] and *Test-Tube* [142]. Data are also compared with the results of *McCall et al.* [140, 141]. See the text for the comparison and the interpretation of particular regions.

In figure 3.16 examples are shown of decay curves obtained in the *AISA, HPFA, Test-Tube* and *FALP–VT* apparatuses measured at similar [H_2]. In this log-log, plot we can see the range of plasma densities and time-scales used in the experiments. We can see that the measured α_{eff} is independent of initial plasma density and of the time of formation of the H_3^+ dominated plasma. (See figure caption for more information).

The measurement with the *FALP–VT* apparatus can be treated as a clear confirmation of the previous measurements on the *AISA* apparatus and mainly of the steep evolution of α_{eff} at low [H_2] (see figure 3.15). The flowing afterglow principle of the recent measurement excluded the possible complications concerning ion formation in *AISA*, and the possible influence of the dissociation of H_2 to hydrogen atoms in the discharge. Such a loss of molecular hydrogen could prolong the formation of H_3^+ resulting in the observation of a lower α_{eff}. In the *FALP–VT*, the reactant port is downstream from the discharge, H_2 is introduced into a relaxed plasma and there are no species with internal energy high enough to dissociate the H_2 or to form negative ions.
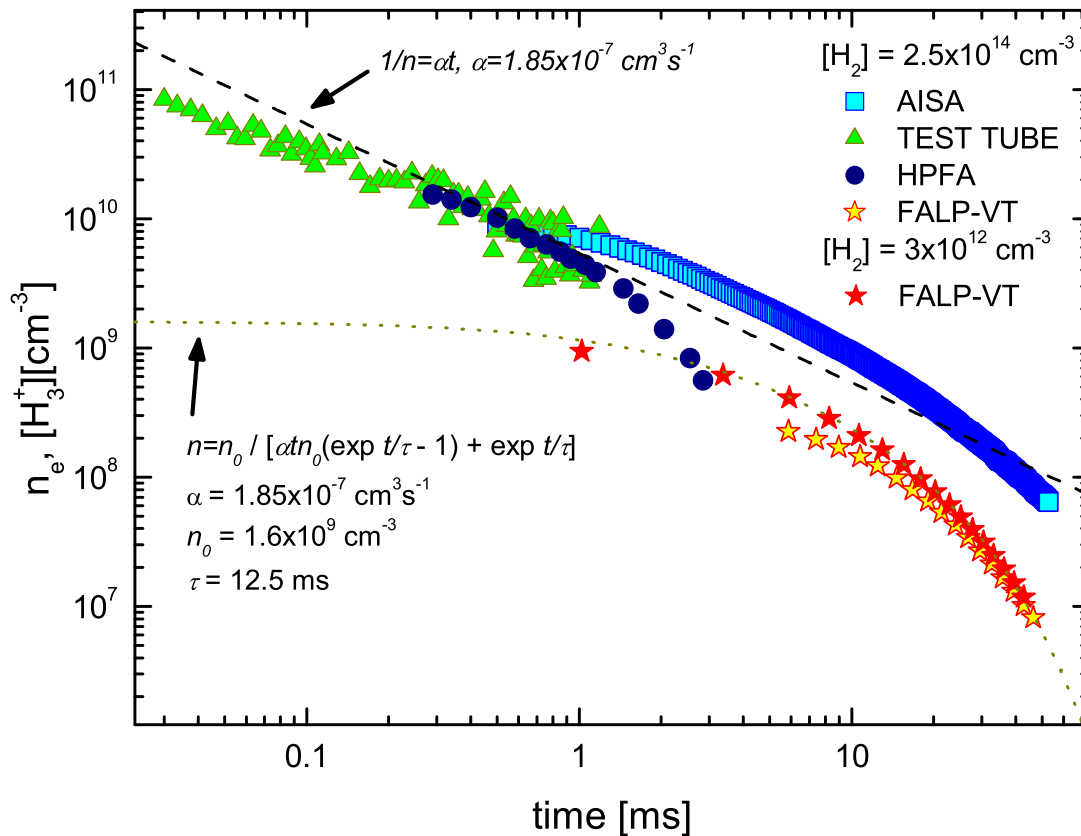
Figure 3.16: Log-log plots of decay curves as obtained in four different experiments *AISA*, *HPFA*, *Test-Tube* and *FALP–VT* (two different conditions). From each experiment one decay measured at $[H_2] \approx 2.5 \times 10^{14}$ cm^{-3} was chosen and for the *FALP–VT*, another decay at $[H_2] = 3 \times 10^{12}$ cm^{-3} is also displayed. The figure demonstrates a very broad range of measurement times and concentrations of H_3^+ used in the particular experiments while the measured α_{eff} remains almost constant for a given $[H_2]$. The dashed line indicates the decay of a recombination dominated plasma with $\alpha_{\text{eff}} = 1.85 \times 10^{-7}$ cm^{3}s^{-1}. In the *FALP–VT*, the ion formation for $[H_2] > 1 \times 10^{13}$ cm^{-3} proceeds quickly (at short distance) and the initial electron density decreases significantly during the mixing of the reactant gas with the plasma. The analyzed range of the decay, therefore, is already highly affected by diffusion. The dotted line indicates the decay including diffusion and recombination losses at a given n_0.

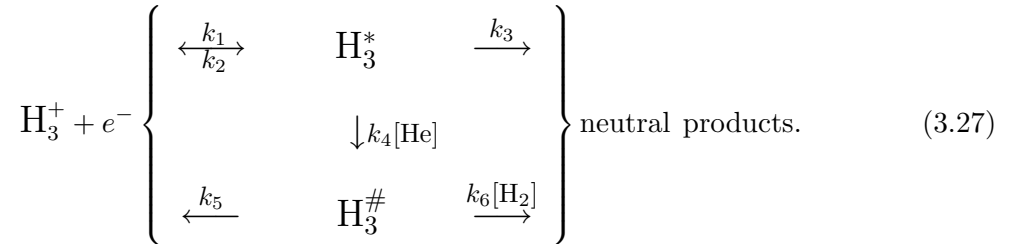Nowadays the generally accepted value of the DR rate coefficient for H_3^+ is taken from the recent measurement of *McCall et al.* [140, 141] performed at the heavy ion storage ring *CRYRING*. The resulting thermal rate coefficient for $T = 250$ K is $\alpha_{DR} = 7.7 \times 10^{-8}$ cm^{3}s^{-1}. As this experiment is performed without interactions with H_2 one would expect that α_{DR} can be obtained as

$$\alpha_{DR} \stackrel{?}{=} \lim_{[H_2] \to 0} \alpha_{\text{eff}} \left([H_2]\right). \tag{3.26}$$

Such an "extrapolation" is clearly not valid as already at $[H_2] = 2 \times 10^{11}$ cm^{-3}, the α_{eff} decreases down to 1.5×10^{-8} cm^{3}s^{-1}. The limit value from the *AISA* experiments is even lower.

The observed difference can be explained simply, that in both types of experiments (afterglow and beam experiments) the different experimental conditions affect the studied process in a different way. In storage ring experiments, the recombination process is not affected by collisions with the surrounding gas. The pressure of the residual gas is very low ($\sim 10^{-9}$ Pa $\Rightarrow$ $\sim 2.5 \times 10^5$ cm^{-3}), and at high beam energies, even a single collision with the molecule of residual gas would dissociate the colliding molecules and such events are not included in the data analysis for obtaining the α_{DR}. Hence the H_3^+ recombination products taken into account in the data analysis do not undergo collisions during the time of flight between the recombination region and the detector[12]. On the other hand, in the *FALP–VT* at a pressure of ~ 1600 Pa ($\sim 4 \times 10^{17}$ cm^{-3}), the collision rate is several orders higher and low-energy collisions can affect the recombination process itself.

For explaining the difference between α_{eff} and α_{DR} we suggest the following simplifying scheme:

$$H_3^+ + e^- \begin{cases} \xleftarrow{k_1}{\xrightarrow{k_2}} & H_3^* & \xrightarrow{k_3} \\ & \downarrow k_4[\text{He}] & \\ \xleftarrow{k_5} & H_3^\# & \xrightarrow{k_6[\text{H}_2]} \end{cases} \text{neutral products.} \tag{3.27}$$

In a collisionless environment, the recombination of H_3^+ with e^- proceeds via an intermediate doubly excited state or states (H_3^*) which can autoionize back to H_3^+ and e^- or dissociate to neutral products (see section 1.3 for details on pathways of DR). Such a process is a subset of the scheme 3.27:

$$H_3^+ + e^- \xleftarrow{k_1}{\xrightarrow{k_2}} H_3^* \xrightarrow{k_3} \text{neutral products}, \tag{3.28}$$

where k_1 is the rate for the forward process of H_3^* formation, k_2 the rate of autoionization and k_3 the rate of dissociation. The total DR recombination rate coefficient is then

$$\alpha_{DR} = k_1 \frac{k_3}{k_2 + k_3}. \tag{3.29}$$

The upper limit to the lifetime of H_3^* can be estimated from the measurement at *CRYRING* [141] where during the study of the branching ratios, the majority of products were dissociated[13]. The lifetime of H_3^* (in the machine) has to be shorter, therefore, than the time-of-flight from the electron cooler to the detector $t < 50$ ns (see the estimation in the footnote 12.).

---

[12]The time of flight can be calculated from the distance of the detector and the center of the electron cooler ($z \approx 1.5$ m) and from the velocity of the ion beam ($v = 2.78 \times 10^7$ m/s): $t = z/v \approx 50$ ns.

[13]With the grid in front of the detector most of the events yielded H and 2H. See section 2.4.6 for a description of the branching ratio analysis.

This lifetime of H_3^*, however, can be much longer than the typical time between collisions with He in the *FALP–VT*. Let's define the "collision" as the event when the state of H_3^* is changed to another state $H_3^\#$ in the reaction

$$H_3^* + He \xrightarrow{k_4} H_3^\# + He. \tag{3.30}$$

The rate k_4 for such events can be estimated e.g. from the typical electron attachment rate at low T ($\sim 10^{-6}$ cm^{3}s^{-1}) because the electron in the H_3^* is in a highly excited state and can be treated as almost a free, slowly moving electron. The mean time between collisions of He and H_3^* under typical experimental conditions in the *FALP–VT* is then

$$t > \frac{1}{k_4[He]} \approx \frac{1}{10^{-6} \times 5 \times 10^{17}} \approx 2 \times 10^{-3} \text{ ns.} \tag{3.31}$$

Although values of both the lifetime of H_3^* and the time between collisions in the *FALP–VT* are only rough estimations, the difference of 5 orders of magnitude provides a wide range of real lifetimes for H_3^* when collisions with He may affect the recombination process: H_3^* can be transformed in collision with He to another neutral excited state $H_3^\#$ at a rate of $k_4[He]$. The dissociation of the so-formed $H_3^\#$ would be enhanced by collisions with H_2 (at the rate $k_6[H_2]$) as molecular hydrogen can absorb the recombination energy. Therefore the total recombination rate coefficient would be dependent upon the concentration of H_2. For low concentrations of H_2 the $H_3^\#$ "dissociates" back to H_3^+ and e^- at the rate k_6 (this process can be e.g. autoionization or can be enhanced by another collisions with He).

The described reaction scheme may explain the considerable deviations between the *DR* rate coefficients for H_3^+ measured at storage rings and in afterglow experiments. Confirmation of this hypothesis requires however, detailed theoretical calculations, where the key parameter to be calculated is the lifetime of H_3^*. Will the enigma of H_3^+ be then finally solved? Probably not, as new problems concerning the *DR* of H_3^+ have recently been investigated, and in particular the influence of *ortho* and *para* states of H_3^+ on its recombination rate [179].

RECOMBINATION OF POLYCYCLIC AROMATIC HYDROCARBON IONS

4.1 Introduction

Polycyclic Aromatic Hydrocarbons (PAHs) are organic compounds that contain two or more aromatic rings[1]. They can take many isomeric forms and are made up of carbon and hydrogen atoms, although variants on the basic form may include other species such as nitrogen, oxygen, sulfur, halogen atoms, etc. (see sample PAHs in figure 4.1).

PAHs in their neutral or ionic forms are believed to be the most ubiquitous organic compounds in the universe. They are important species in combustion and soot formation [180–182] and through various transport processes are distributed as contaminants in all terrestrial environments: They are found e.g. in sediments [183, 184], in air [185] as direct products of combustion, e.g. diesel exhaust [182] or cigarette smoke [186], and also in food [187]. Some PAHs were identified as mutagens and carcinogens (e.g. benzo-α-pyrene) and many others demonstrate toxic characteristics [188, 189]. PAHs are, therefore, the focus of great attention by the scientific community due to their negative impact on human health.

PAHs have been also detected in extraterrestrial media such as meteorites [191, 192] and interplanetary dust particles. The most important astrophysical context of PAHs nowadays, however, is their identification in the gas phase interstellar medium (ISM) and possible relevance to the origin of life. Although no specific PAH has been identified, the presence of PAHs in the ISM is based on spectroscopic observation of emission bands at 3.28, 6.2, 7.7, 8.6, 11.3 and 12.7 μm [193]. To fulfill constraints given by spectroscopic observations it is necessary to find carbon-rich species stable enough to survive in extremely harsh environments [194]. In the mid-1980's, it was first proposed that these widespread emission features, formerly called *Unidentified Infra-Red Bands* (UIRB), might be diagnostics of gas phase PAHs [195, 196]. Calculations show unexpectedly high concentrations of PAHs in a variety of space objects,

---

[1] Aromatic hydrocarbons were so named due to their generally intense smell, long before their molecular structure was understood. From a chemical point of view, an aromatic hydrocarbon is a cyclic compound where all the atoms in the ring(s) are sp^2 having a free p orbital to provide a pipeline or "conduit" in which π electrons can travel thus being distributed throughout the molecule. This is referred to as a delocalized π electron system.
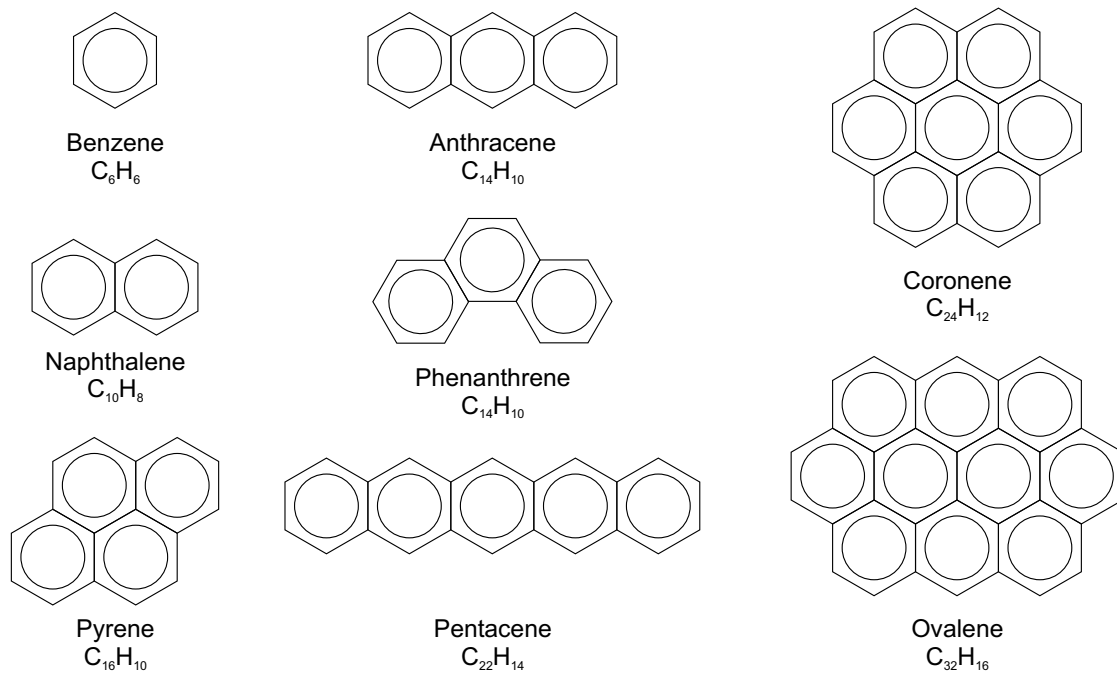
Figure 4.1: Molecular structure of benzene and and several polycyclic aromatic hydrocarbons. Pyrene, coronene and ovalene are compact (pericondensed) PAHs which are thought to be more resistant to the UV field than noncompact (catacondensed) PAHs such as phenanthrene or pentacene.

such as H II regions[2], post-AGB stars[3], planetary nebulae, galaxies and the diffuse interstellar medium. The molecules of PAH family are as abundant as the most abundant simple polyatomic molecule NH_3 ($10^{-6} - 10^{-7}$ with respect to hydrogen concentration, or 10% of all carbon atoms in the universe, see e.g. [195, 196]). It is interesting to note here, that those calculations are based only on spectroscopic observations and do not predict specific carriers (PAHs) of the infrared bands.

Soon after neutral PAHs were proposed as carriers of UIRB, PAH cations and radicals were nominated to explain the next long-standing astrophysical enigma: The *Diffuse Interstellar Bands* (DIB) [197,198]. The DIBs, discovered by *Heger* in 1921 [199], are absorption features arising in the near infrared to visible spectrum if the observed light passes through the diffuse interstellar cloud[4]. Several solid-state mechanisms have been proposed to explain the DIBs (see an overview in [200] and references therein), but observed spectra were never reproduced at a satisfactory level following those hypotheses. On the other hand, the PAH hypothesis is supported by recent laboratory measurements of PAH absorption spectra, by models of chemistry in diffuse interstellar clouds [201, 202] and by the following arguments:

- PAHs are abundant in the ISM as shown by infrared spectroscopy (see the paragraph above and [203]).

---

[2]Areas in space which are luminous with the emission spectrum of ionized hydrogen are called H II regions. A characteristic visible color from such emission is red light at 656 nm associated with the $n = 3$ to $n = 2$ transition which is called H-alpha.

[3]The star-life stage between the Asymptotic Giant Branch (AGB) star and the planetary nebulae.

[4]Diffuse clouds are almost invisible interstellar clouds of very low density ($10 - 10^3$ cm^{-3}), which allow most photons to pass through them.

- The large PAHs survive UV irradiation [204].

- The rotational structure of the DIBs [205] is consistent with large molecular species.

It should be emphasized, however, that still no particular PAH or PAH$^+$ have been identified and the current consensus on the UIB and DIB is that their carriers are large organic gas-phase species.

The crucial parameter for modeling the DIBs and UIRBs is the ionization state of the PAHs [206, 207]. Several models of the PAH charge state in the ISM have been developed [202, 204, 206, 208–213] involving the following processes: photo-ionization, *electron-ion recombination*, electron attachment and photo-detachment.

It was shown that the concentration of PAH anions increases significantly with ISM density and PAH mass, which is due to high electron attachment rates, higher electron concentrations and lack of energetic photons. PAH anions thus dominate in dense interstellar clouds[5].

On the other hand, in less dense diffuse clouds (source of DIBs) photo-detachment and photo-ionization prevail and PAH cations are the most abundant form of PAHs. Electron-ion recombination is the main neutralization channel [214] and the recombination rate coefficient of PAHs is an important parameter for any model of PAH charge state, thus also for DIBs identification and consequently for dust formation theories and astrobiological hypotheses [201]. Rate coefficients used, however, in cited astrochemical models are based on experimentally measured values for two species only, benzene $\alpha = (1 \pm 0.3) \times 10^{-6}$ cm^{3}s^{-1} at 300 K, and naphthalene $\alpha = (3 \pm 1) \times 10^{-7}$ cm^{3}s^{-1} at 300 K [215], even though more experimental data are available (see results in refs. [216–219] measured on FALP-MS technique).

The extrapolation of the rate coefficient for heavier PAHs used in cited astrochemical models is based on the theory of recombination of grains [220, 221] which assumes that the recombination is proportional to the size of the grain and that Coulomb focussing enhances the rate coefficient. Due to the planar shape of a PAH molecule, a correction for disk shape is applied [206]. The recombination rate coefficient α can be expressed in the general form:

$$\alpha = C\sqrt{N_C/T}\, s(e) \tag{4.1}$$

where N_C is the number of carbon atoms in the PAH structure, T is the temperature, C the scaling constant derived from experiment and $s(e)$ is the so-called sticking coefficient arising from the theory of grain recombination. The sticking coefficient of a PAH greatly depends on its electron affinity [210] and it is generally assumed, that for larger PAHs ($N_C > 20$), it is unity [222]. For smaller PAHs, the value of $s(e)$ differs according to different authors. In some studies even a constant value of α for all PAHs without size dependence has been used [213].

Up to this time, recombination rates for aromatic molecules like benzene and its methylated derivatives [215, 217] or PAHs like naphthalene, phenanthrene [218] and fluoranthene [219] have been measured using the FALP-MS technique. This technique has been described extensively elsewhere [38], but has intrinsic limitations that are exposed in reference [218]. The main constraint is the amount of injected PAH neutrals. The concentration of PAHs has to be high enough to convert all precursor ions into PAH cations via charge transfer reactions. The vapor pressure of studied PAHs is too low, however, to produce sufficient

---

[5]Dense interstellar clouds have typical density $10^3 - 10^5$ cm^{-3}. At such concentration and typical cloud size most photons are captured and the cloud seems to be dark.

concentration at room temperature and thus heating of the PAH source was necessary. Hot molecules were found to condense on the walls of the apparatus and on the Langmuir probe. Even when a special, continuously heated probe was used [54], coating by a PAH layer significantly decreased the precision of the probe measurement. Moreover, many PAH display high electron attachment rates [59]. Thus with high concentrations of neutral PAHs in the flow, a significant concentration of PAH anions can be produced, as happens with pyrene and anthracene, and the Langmuir probe measurement is again unusable.

For these reasons another method had to be developed to continue the study of the recombination of PAH cations with electrons. We have developed a new technique named *Flowing Afterglow with Photo-Ions* (*FlAPI*) which involves producing PAH cations by photo-ionization instead of charge transfer with precursor ions.

4.2 Results

The results presented here have been obtained from measurements using the *FlAPI* apparatus, which is extensively described in section 2.3, along with the data analysis.

The first experiment and most additional tests on the *FlAPI* have been performed using anthracene as the studied PAH. In other experiments, pyrene, azulene and acenaphthene have been used as parent PAHs. The physical properties of the listed species are summarized in table 4.1.
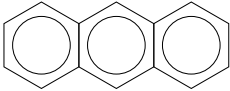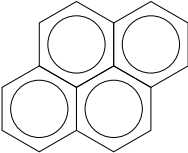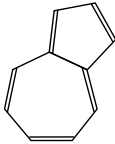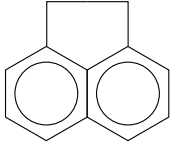
Name	ANTHRACENE	PYRENE	AZULENE	ACENAPHTHENE
Formula	$C_{14}H_{10}$	$C_{16}H_{10}$	$C_{10}H_8$	$C_{12}H_{10}$
Structure				
Mass [amu]	178.23	202.25	128.17	152.19
E_{iv} [eV]	7.42 ± 0.01	7.41 ± 0.005	7.43 ± 0.01	7.78 ± 0.03
State	solid	solid	solid	solid
E_A [eV]	0.530	0.500	0.694	unknown
σ_{PI} [$\times 0.1$ Å^2]	2.1 ± 0.7	2.1 ± 0.7	1.5 ± 0.5	1.8 ± 0.6

Table 4.1: Physical properties of measured PAHs. E_{iv} represents the vertical ionization potential and E_A the electron affinity. The *State* is given for $T = 300$ K and $p = 1$ Bar. The ionization cross-section σ_{PI} for the wavelength the laser $\lambda = 157$ nm is estimated from [62]. All other values are taken from the NIST database [223].

Anthracene and pyrene were introduced into the chamber by evaporation from a metal plate coated with a thin layer of the particular PAH, while azulene and acenaphthene have been evaporated from an external bottle flushed by helium and then injected into the flowtube at a controlled rate.

The best measurement conditions have been found during several tests using anthracene. All other measurements have then been performed with the same or very similar conditions:

Pressure: $p = 100$ Pa

Temperature: $T = 300$ K

Flow rate He: ~ 20 slpm

Flow rate Ar: ~ 1 slpm

Microwave discharge power: ~ 50 W

MCS dwell time (time resolution): 4 μs

Laser shots per data set: 20 000

Laser energy per 1 pulse: ~ 8 mJ

Electron concentration range used: 2×10^8 to 5×10^9 cm^{-3}, at higher values the recombination removes PAH$^+$ too quickly from the flow, however lower values are too low for measurement by Langmuir probe and also the ambipolar diffusion conditions may be disrupted.

Buffer gas velocity: 185 ± 15 m/s. The velocity has been measured several times and the range of values was within the presented error. The velocity is a crucial parameter for calibration and thus its considerable error greatly affects the total error.

Calibration of the Langmuir probe was performed after almost every experiment by measuring the recombination rate coefficient for O_2^+ in the basic FALP mode (see sections 2.3.2, 2.2.3 and appendix B). The correction factor so obtained ranged from 0.7 to 1.25. The variation may be caused by probe pollution by PAHs and by velocity fluctuations. An example of a calibration measurement is given in figure 4.2.

The error analysis shows that the main contribution to the total error of the measured recombination rate coefficient arises from the electron density determination by the Langmuir probe and from the flow velocity measurement[6], while statistical errors rising from MCS data are usually of minor significance. The typical overall error value is 30%.

Recombination rate coefficients obtained from using the *FlAPI* apparatus during this work are presented in the table 4.2 while appropriate analyzed data are plotted in figures 4.3, 4.4, 4.5 and 4.6.

PAH name	AZULENE	ACENAPHTHENE	ANTHRACENE	PYRENE
α [10^{-6} cm^{3}s^{-1}]	1.1 ± 0.3	0.5 ± 0.2	2.4 ± 0.8	4.1 ± 1.2
N_C	10	12	14	16

Table 4.2: Recombination rate coefficients of studied PAH$^+$ with electrons measured on the *FlAPI* apparatus. N_C is the number of carbon atoms in a particular ion.

---

[6]Both errors are combined in the precision of the calibration.
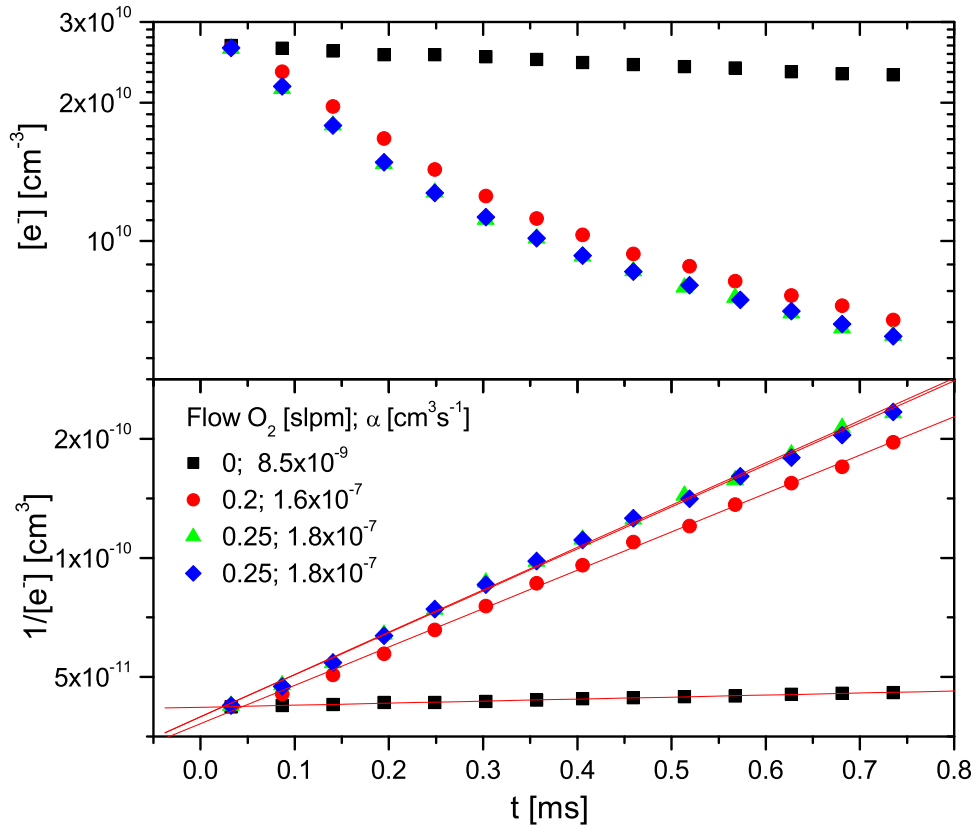
Figure 4.2: Calibration of the Langmuir probe. The recombination rate coefficient for O_2^+ with electrons has been measured using the basic FALP technique. The measurements have been performed for several flow rates of O_2, where at 0 slpm only diffusion and losses due to ion molecule reactions are observed. The upper panel shows the electron concentration $[e^-]$ vs time, while the lower panel shows the reciprocal value $1/[e^-]$ vs time, where the slope of the plot gives a first approximation to the recombination rate coefficient α (for details see section 2.3.2 or appendix B). The values of α so obtained are, in this case, very close to the literature value $\alpha(300 \text{ K}) = 1.8 \times 10^{-7}$ cm^{3}s^{-1} [55] and no correction factor has been used.

Figure 4.3: The data measured with ANTHRACENE as parent PAH. **Upper panel:** Decays of ion density in time measured by the QMS at several electron concentrations (different symbol types). Data used for the data analysis are highlighted by larger symbols. Particular data sets have been multiplied by different factors to distinguish them from each other. **Lower panel:** The plot of $y = \ln([\mathrm{PAH}^+]_{t_2}/[\mathrm{PAH}^+]_{t_1})/(t_2 - t_1)$ vs $x = -\frac{1}{v}\int_{z_1}^{z_2}[e^-]_0\, dz\,/\,(t_2 - t_1)$ gives the rate coefficient α as the slope of the linear fit. Each "group" of points represents a particular data set measured at different electron densities. The data-points with relative error higher than 200% are not displayed (but are used in the fit). For details of the analysis see sections 2.3.4 and 2.3.5.

Figure 4.4: The data analysis of data measured with PYRENE as parent PAH. **Upper panel:** Decays of ion density in time measured by the QMS at several electron concentrations (different symbol types). Data used for the data analysis are highlighted by larger symbols. Particular data sets have been multiplied by different factors to distinguish them from each other. **Lower panel:** The plot of $y = \ln([PAH^+]_{t_2}/[PAH^+]_{t_1})/(t_2 - t_1)$ vs $x = -\frac{1}{v}\int_{z_1}^{z_2}[e^-]_0\,dz\,/\,(t_2 - t_1)$ gives the rate coefficient α as the slope of the linear fit. Each "group" of points represents a particular data set measured at different electron densities. The data-points with relative error higher than 200% are not displayed (but are used in the fit). For details on the analysis see sections 2.3.4 and 2.3.5.
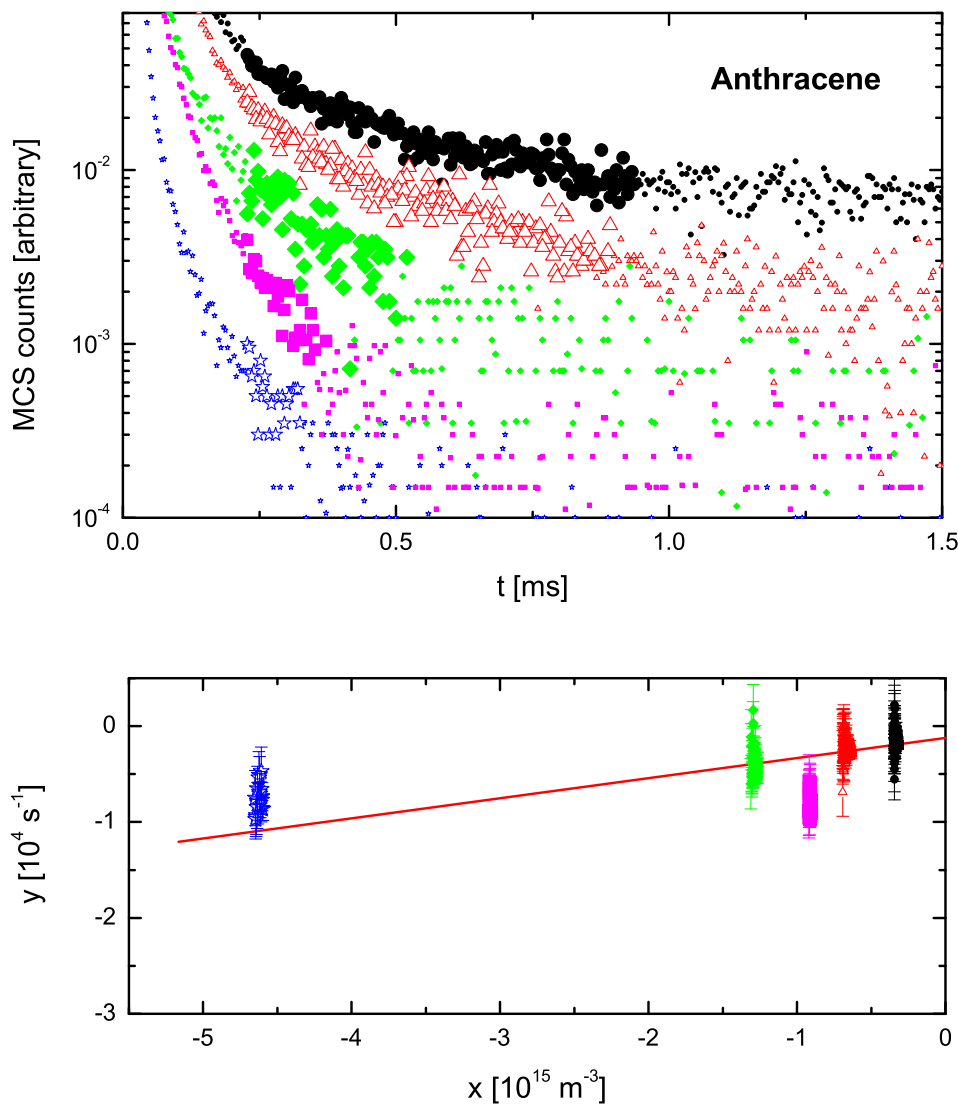
Figure 4.5: The data measured with AZULENE as parent PAH. **Upper panel:** Decays of ion density in time measured by the QMS at several electron concentrations (different symbol types). Data used for the data analysis are highlighted by larger symbols. Particular data sets have been multiplied by different factors to distinguish them from each other. **Lower panel:** The plot of $y = \ln([\mathrm{PAH}^+]_{t_2}/[\mathrm{PAH}^+]_{t_1})/(t_2 - t_1)$ vs $x = -\frac{1}{v}\int_{z_1}^{z_2}[e^-]_0\,dz/(t_2 - t_1)$ gives the rate coefficient α as the slope of the linear fit. Each "group" of points represents a particular data set measured at different electron densities. The data-points with relative error higher than 200% are not displayed (but are used in the fit). For details on the analysis see sections 2.3.4 and 2.3.5.
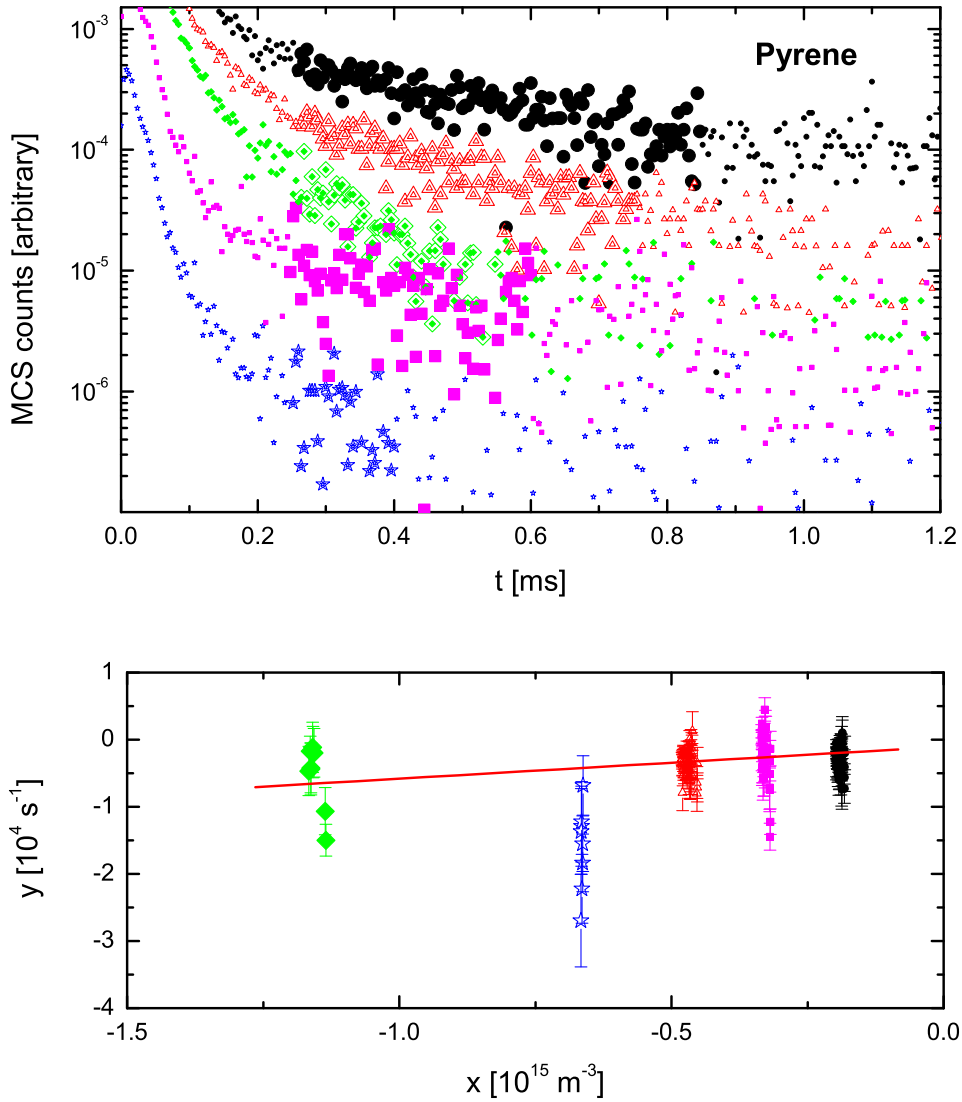
Figure 4.6: The data analysis of data measured with ACENAPHTHENE as parent PAH. **Upper panel:** Decays of ion density in time measured by the QMS at several electron concentrations (different symbol types). Data used for the data analysis are highlighted by larger symbols. Particular data sets have been multiplied by different factors to distinguish them from each other. **Lower panel:** The plot of $y = \ln([\text{PAH}^+]_{t_2}/[\text{PAH}^+]_{t_1})\,/\,(t_2 - t_1)$ vs $x = -\frac{1}{v}\int_{z_1}^{z_2}[e^-]_0\,dz\,/\,(t_2 - t_1)$ gives the rate coefficient α as the slope of the linear fit. Each "group" of points represents a particular data set measured at different electron densities. The data-points with relative error higher than 200% are not displayed (but are used in the fit). For details on the analysis see sections 2.3.4 and 2.3.5.
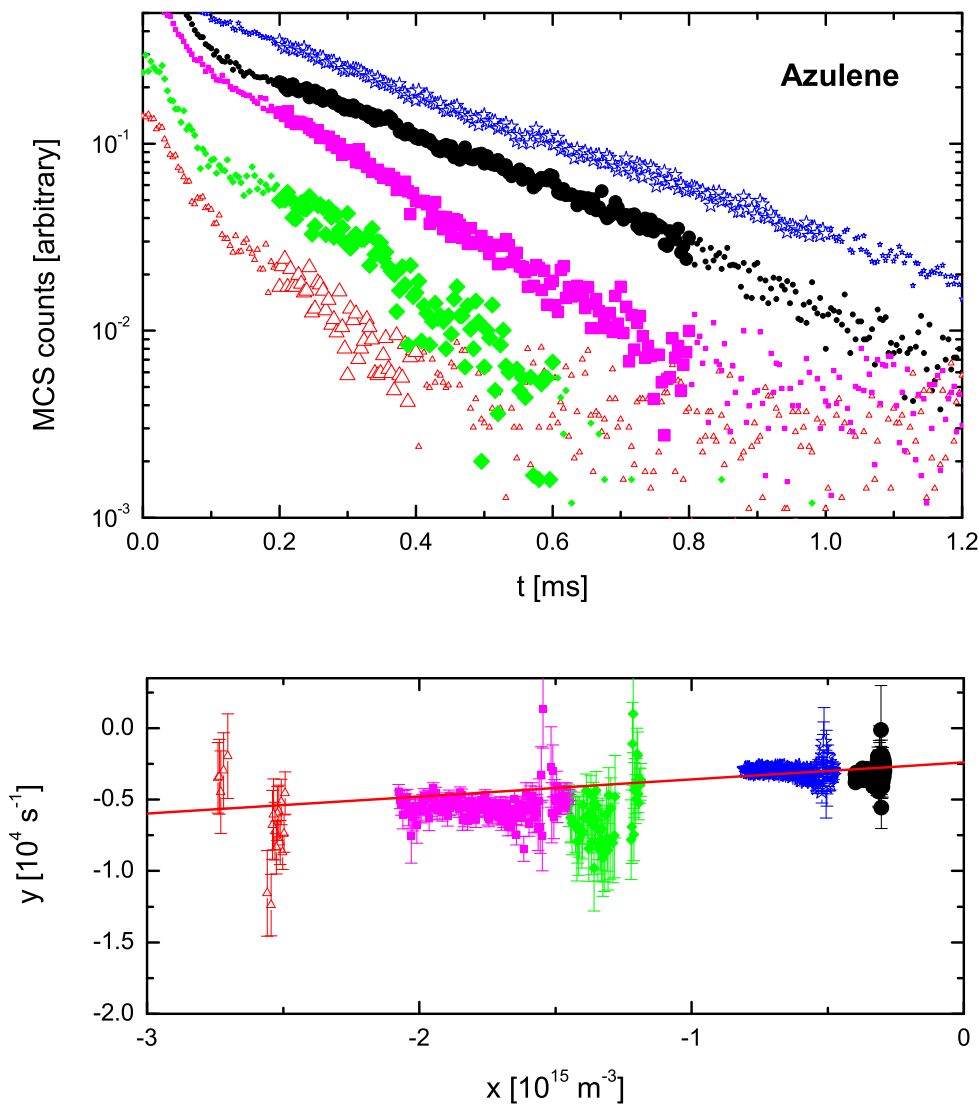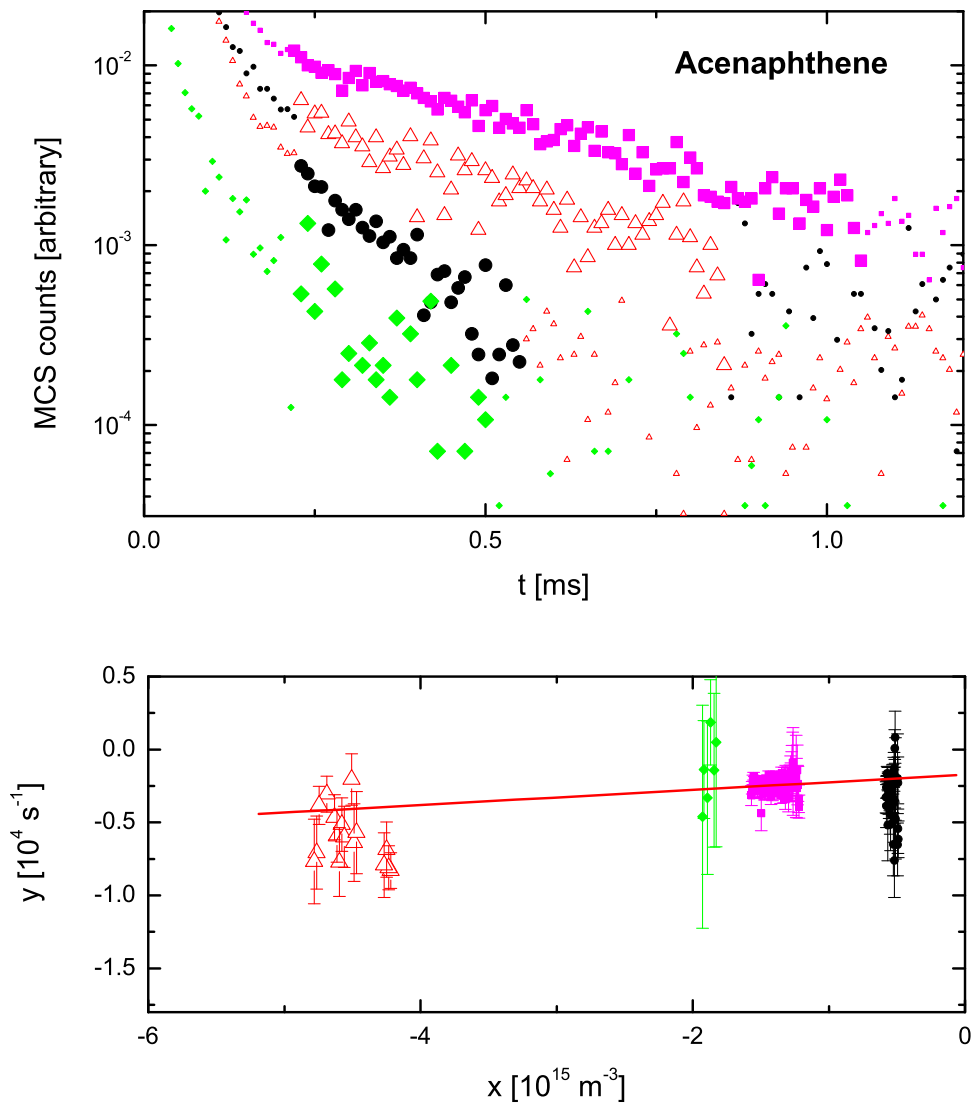
4.3 Conclusion

The new technique for the measurement of rate coefficients for PAH^+ recombination, *FlAPI*, has been developed and successfully tested in initial measurements. Previous problems involving pollution of the Langmuir probe and electron attachment in the FALP-MS apparatus have been resolved by decreasing the concentration of neutral PAHs, while PAH^+ are produced by photoionization.

Rate values obtained for the first four measured species (listed in table 4.2) are consistent with recombination rate coefficients of similar PAH^+ already studied [218]. Values for phenanthrene $\alpha = (1.7 \pm 0.5) \times 10^{-6}$ cm^{3}s^{-1} and fluoranthene $\alpha = (3.0 \pm 0.9) \times 10^{-6}$ cm^{3}s^{-1} can be directly compared with those for anthracene and pyrene as they are their geometric isomers. The recombination rate coefficient for acenaphthene, however, measured by the FALP-MS $\alpha = (1.5 \pm 0.45) \times 10^{-6}$ cm^{3}s^{-1} displays a large difference in comparison with the value measured with the *FlAPI*. The values of vapour pressure and photo-ionization cross-section were not available for this measurement and thus we do not have an estimation of the possible excess of photo-electron density, which can affect the data analysis by decreasing the final rate coefficient[7]. This experiment should be re-investigated using additional procedures suggested at the end of this section. The recombination rate of azulene has never been measured before because in the FALP-MS, azulene can isomerize to naphthalene when formed by ion-molecule reactions.

In table 4.3, recombination rate coefficients for PAHs measured using both the FALP-MS and *FlAPI* techniqes, are listed.

The data from table 4.3 are plotted in figure 4.7 as α vs number of carbon atoms N_C in the PAH^+. Comparison with values used in several astrochemical models[8] shows the same order of magnitude, but a significantly different trend. Despite this discrepancy, the measured data can still be described by the formula 4.1 because the behavior of the sticking coefficient $s(e)$ for $N_C < 20$ is not well understood. As already discussed above, it is known, that the sticking coefficient greatly depends upon the PAH's electron affinity [210] which can explain the differences in α for several PAHs of the same N_C, because different geometrical configurations can have significantly different electron affinities[9]. In FALP-MS experiments, the ions to be studied are formed via charge transfer reactions with primary ions. The excess energy in those reactions can in some cases induce isomerisation of the ions thus produced. In the *FlAPI*, however, the difference of ionization energy and the laser energy is low enough to neglect this effect and the results are thus more ion-specific.

---

[7]Data for lower electron densities are more affected by the possible high density of photo-electrons: for those data higher value of $x = -\frac{1}{v} \int_{z_1}^{z_2} [e^-]_0 \, dz \, / \, (t_2 - t_1)$ should be used and thus a higher value of the slope can be obtained.

[8]The "Spitzer limit" is derived from the theory of recombination of grains [220], which is modified for planar molecules by multiplying the rate coefficient by a factor 0.8: $\alpha = 1.58 \times 10^{-10} a^2 \sqrt{T} \times (1 + 1.665 \times 10^5/aT) \, s(e)$. Here a is the radius of the molecule in Å, for PAHs at $T = 300$ K estimated as $0.9\sqrt{N_C}$ [62,207]. Applied theory takes into account only Coloumb forces, which are in the case of electron-ion recombination always attractive. A full description, however, should also include repulsive forces at short distances dsetermined using quantum mechanical principles. For this, reason the values obtained are treated as a maximum limit of α. Moreover, in figure 4.7, the sticking coefficient is fixed at the maximum value $s(e) = 1$. *Allain et al* [204] applies the same model, but rescaled to fit experimental data, here the value for benzene [215]. *Salama et al* [208] and *Le Page et al* [213] use constant values for α in the displayed range of N_C again scaled to experimental value obtained for benzene.

[9]e.g. values of electron affinity for anthracene and phenanthrene (both $C_{14}H_{10}^+$) are 0.530 eV and 0.307 eV respectively [223]. The reason for such different behaviors of so similar molecules is not understood.

Parent molecule	Formula of PAH$^+$	N_C	α [10^{-6} cm^{3}s^{-1}]	Method	Reference
benzene	$C_6H_6^+$	6	1.0 ± 0.3	FALP-MS	[215]
naphthalene	$C_{10}H_8^+$	10	0.3 ± 0.1	FALP-MS	[215]
naphthalene	$C_{10}H_8^+$	10	0.8 ± 0.2	FALP-MS	[218]
azulene	$C_{10}H_8^+$	10	1.1 ± 0.3	*FlAPI*	this work
acenaphthene	$C_{12}H_9^+$	12	1.15 ± 0.35	FALP-MS	[218]
acenaphthene	$C_{12}H_{10}^+$	12	1.5 ± 0.45	FALP-MS	[218]
acenaphthene	$C_{12}H_{10}^+$	12	0.5 ± 0.2	*FlAPI*	this work
phenanthrene	$C_{14}H_{10}^+$	14	1.7 ± 0.5	FALP-MS	[218]
anthracene	$C_{14}H_{10}^+$	14	2.4 ± 0.8	*FlAPI*	this work, [266]
fluoranthene	$C_{16}H_{10}^+$	16	3.0 ± 0.9	FALP-MS	[218]
pyrene	$C_{16}H_{10}^+$	16	4.1 ± 1.2	*FlAPI*	this work, [266]

Table 4.3: List of measured recombination rate coefficients for PAHs. For FALP-MS experiments, the most recent results measured with modified apparatus have been chosen [218], which update results from [217] and [216]. All values have been measured at room temperature $T = 300$ K. The corresponding plot of rate coefficient α vs number of carbon atoms N_C is displayed in figure 4.7.

Unfortunately, most cited astrochemical models use a scaling factor derived from experimental values of α measured for very small PAHs: benzene ($N_C = 6$) and napthalene ($N_C = 10$). A scaling factor, however, taken from $N_C = 16$ gives α at least $2\times$ higher than previously used values, which can significantly affect the charge state of PAHs and thus also the final results of such calculations.

4.4   Outlook

In the ISM, the average mass of PAHs is expected to be much higher than the mass of PAHs yet studied. It was shown, that PAHs with number of carbons higher than 20 survive photoionization by energetic UV photons and therefore the distribution of PAHs in the ISM is centered around a mass corresponding to 40-50 carbon atoms [202, 212]. Thus it would be important to extend our measurements to higher PAH masses.

The current configuration of the *FlAPI* apparatus allows us to measure rate coefficients of PAHs with the following limits:

Maximum PAH mass is limited by the QMS used, currently 300 amu ($\sim$ 23 carbon atoms). For higher masses, a different QMS control unit has to be used.

Maximum vertical ionization energy is limited by the energy of laser, currently 7.9 eV. As the ionization potential of PAHs decreases with mass [223], PAHs with higher masses important for astrochemistry can be measured without changing the laser. In the case of too high difference between ionization energy and the laser energy, excited PAH$^+$ can be produced. Under the current configuration we are not able to control the population of such excited states.
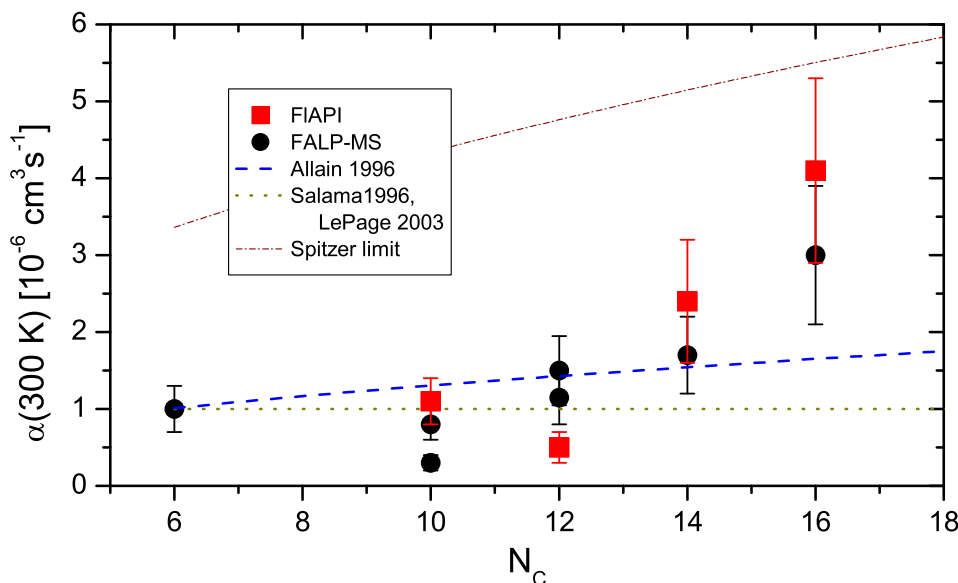
Figure 4.7: Recombination rate coefficients of PAH$^+$ measured with FALP-MS and FlAPI techniques - appropriate to table 4.3. The data are compared with values used in astrochemical models of *Allain et al* [204], *Salama et al* [208] and *Le Page et al* [213] rescaled for 300 K. The Spitzer limit [62, 207, 219, 220] shows the maximum value of the rate coefficient based on the theory of recombination of grains.

Minimal vapor pressure and photoionization cross-section: The combination of vapor pressure and photo-ionization cross-section of the PAH being studied determines the efficiency of PAH$^+$ production. The ionization cross section increases linearly with the number of carbon atoms in the PAH [62]. However, the vapor pressure decreases with mass much faster [224], which probably can not be compensated by increasing the laser pulse energy or the evaporation area. For this purpose we have searched for different ways of producing neutral PAHs. Preliminary studies suggest, that PAHs may be photo-desorbed by a secondary laser and then ionized by a primary laser in the same way as in the current configuration [225].

Although the *FlAPI* has proved its ability to measure recombination rate coefficients for large hydrocarbons, new improvements may help to control measurement conditions and the state of measured PAH$^+$. The following improvements of instrumental techniques are suggested:

Langmuir probe measurement: Currently the electron density measurement is performed only with the laser switched off in continuous mode and the electron concentration evolution after the laser shot (or the concentration of photo-PAH$^+$) is estimated indirectly. Probe measurements synchronized with the laser shot would simplify the adjustment of the laser energy to fulfill limits given by the data analysis, mainly the requirement of negligible concentration of photo-electrons in comparison with the concentration of electrons measured without the laser shot. This measurement can be implemented in the same way as has been done e.g. by *Plašil et al.* [108] at the stationary afterglow apparatus in Prague: probe current decay is measured during each plasma decay after

the laser shot (after stopping the microwave discharge in the case of the stationary afterglow) while the probe potential is fixed at a chosen value. The probe potential is then changed in steps between laser shots. Thus the 2-D evolution of the probe current with time and probe potential is acquired, which can be also interpreted as the evolution of the Langmuir probe characteristics in time. By analyzing those characteristics, the decay of electron density in time is obtained.

QMS measurement: The measurement of QMS spectra is currently not synchronized with the laser shot and thus we do not have direct information concerning the plasma composition after the laser shot. Nevertheless, the combination of MCS spectra measured for different ion masses will give the time evolution of the QMS spectra in a selected mass range. Measurement of time dependent QMS spectra may help us to understand possible photo-fragmentation or clustering of PAH^+ with PAHs.

QMS mass resolution and mass stability in time at high masses may be estimated as ± 1 amu. Improvement of mass selection would allow precise identification of the measured ion.

Identification of products of dissociative recombination: Currently, we do not have any information as to whether the recombination of PAH^+ with electrons is dissociative or not. Possible identification of product fragments can be performed by Residual Gas Analysis (RGA) with the QMS. Such measurement requires addition of a filament or an electron gun inside the QMS. Identification of neutral molecules from the RGA spectra could be complicated due to fragmentation. The electron density will be varied to differentiate products of recombination and products of photo-fragmentation.

A better method, but probably more demanding, would be spectroscopic identification of the neutral products.

Measurements at low temperatures: Recombination rate coefficients obtained with the *FlAPI* apparatus are not directly applicable to astrochemical models as they are acquired at room temperature. Transformation to the temperature of the diffuse clouds (typically ~ 100 K) is usually performed via equation 4.1, or simply as

$$\alpha(T) = \alpha(300 \ K)\sqrt{300/T}.$$

The $1/\sqrt{T}$ dependence, however, is based on the assumption of the direct mechanism of DR (see section 1.3.1) and this assumption has never been confirmed for PAHs. Thus it would be profitable to measure the DR of PAH^+ at lower temperatures to obtain recombination rate coefficient directly at low temperatures, or at least to obtain an experimental confirmation of the expected behavior with T.

Cooling of the flowtube in the current configuration of *FlAPI* would be technically complicated, but it should be possible to rebuild the main chamber in the same way as done in the case of the *FALP–VT* apparatus (see section 2.2). A feasible solution is also cooling of the studied plasma by means of a supersonic expansion. Such a technique is employed in the *CRESU (Cinétique de Réaction en Ecoulement Supersonique Uniforme)* apparatus [226], which is operated in the same laboratory as the *FlAPI*.

DISSOCIATIVE RECOMBINATION OF RARE GAS HYDRIDE IONS

5.1   Introduction

The dissociative recombination of rare gas hydride ions is of interest both from a fundamental and from an applied point of view.

HeH$^+$ is an ion of considerable astrophysical [227] and fusion-technological [228] significance. An experimental study by *Yousif and Mitchell* [15] showed that despite the lack of suitable curve crossings through which the direct mechanism can proceed [16] the recombination of HeH$^+$ exhibits a substantial recombination cross-section at low collision energies. This observation initiated a long series of experiments [17–23] and theoretical efforts [24, 25, 27–29] which led to the introduction of new ideas concerning recombination processes (see section 1.2).

KrH$^+$ and XeH$^+$ participate in the ion chemistry in krypton and xenon lasers. The recombination rate coefficients for these two ions have been examined in afterglow experiments [231, 232] and while a low value $< 10^{-8}$ cm^{3}s^{-1} was found for KrH$^+$, that for XeH$^+$ was quite large (8.3×10^{-8} cm^{3}s^{-1})since this ion has a suitable curve crossing and high rate coefficient due to the direct mechanism was expected.

The recombination of ArH$^+$ and NeH$^+$ ions have not been studied in afterglow experiments since they react rapidly with H$_2$ to form H$_3^+$ (see section 3.2) and prior to the present this study, there were no beam experiments performed concerning the recombination of these ions.

ArH$^+$ is a subject of considerable technological consequence as it is an important ion species in widely used argon-hydrogen plasmas such as those employed in the cleaning of carbon-containing contaminated films on vacuum vessel surfaces in fusion devices [233]. The chemistry of ArH$^+$ has been extensively modeled and it has been generally assumed that the recombination of ArH$^+$ is a rapid process that plays an important role at low hydrogen densities [234–237], when ArH$^+$ recombination dominates H$_3^+$ recombination. The value of the recombination rate coefficient that has been used in cited works is 10^{-7} cm^{3}s^{-1}, since this is typical of many diatomic molecular ions [238].

NeH$^+$ plays an important role in plasma experiments. In addition to its appearance in neon-containing afterglow plasmas, NeH$^+$ will be present in future thermonuclear reactors. It was shown that turbulence is dramatically reduced in the reactor core in response to the

injection of neon as an impurity into the reactor chamber [239]. Furthermore, neon will be used to cool the hot plasma in the divertor[1] region to avoid wall destruction [228, 229, 240]. Energy can be absorbed by neon ionization and excitation in the hot plasma followed by dielectronic recombination. Radiative electronic relaxation processes then release the energy to the walls of the divertor, which is a much less destructive process than bombardment by fast charged particles. Hydrogen molecules formed on the surface of the reactor are rapidly ionized and react with neon, producing NeH^+ ions. As vibrationally excited $H_2^+ (v > 0)$ reacts preferentially, the distribution of vibrational distribution of H_2^+ is significantly affected, which is important in context with subsequent hydrogen chemistry [229, 230]. It is also desirable to neutralize NeH^+ prior reaching the wall, releasing the recombination energy and possible wall destruction. The rate coefficient value for NeH^+ recombination with electrons is thus an important parameter in the design and operation of such systems.

In this work results for an experimental measurement of the cross-section for DR of ArH^+ and NeH^+ with electrons is presented.

5.2   Experimental method

The experiments on ArH^+ and NeH^+ were performed at the *ASTRID* heavy-ion storage ring. For a detailed description of the experimental procedure and data analysis see sections 2.4.

At *ASTRID*, the ions under study were produced in an electron impact source (see section 2.4.7) from a 50/50 mixture of hydrogen and argon or neon respectively, accelerated to 150 keV and injected into the storage ring where they were further accelerated to ~3.1 MeV. This process takes about 4 s to accomplish. In both cases the ion beam current was too small (below 200 nA) to be measured directly by a current transformer and an alternative method described in section 2.4.4 was used.

Due to the high mass ratios of H and ArH^+ (1/40) and NeH^+ (1/20) atoms respectively and due to limited energy resolution of the SBD detector used in those experiments, we were not able to differentiate between neutrals produced in a recombination process

$$e^- + XH^+ \rightarrow X + H \tag{5.1}$$

from those produced due to a dissociative excitation reaction:

$$e^- + XH^+ \rightarrow X + H^+ + e^- \tag{5.2}$$

(X represents ArH^+ or NeH^+ respectively) since we can not distinguish between the arrival of a single X atom and an X + H pair. The excitation process :

$$e^- + XH^+ \rightarrow X^+ + H + e^- \tag{5.3}$$

was not observed because the pulse height due to a single hydrogen atom is low compared to the full energy pulse height and fell within the electronic noise of the detection system.

As already discussed in section 2.4.1, the storage time is usually sufficiently long that all ions in higher vibrational states decay to the ground state. However, this is not always true for rotational states and thus calculations of the lifetimes of the ro-vibrational states of both ArH^+ and NeH^+ have been performed following the procedure of *Amitay et al.* [71]. These

---

[1]A magnetic field configuration affecting the edge of the confinement region, designed to divert impurities to a target chamber.

calculations confirmed that the vibrationally excited states are very short lived ($\tau < 6$ ms) and will decay shortly after beam injection into the ring, long before the recombination measurements begin. The rotational levels of the ground vibrational state on the other hand are very long lived ($\tau > 30$ s for $J < 15$) and will almost certainly be populated during the measurement. For exact lifetime values of ArH$^+$ and NeH$^+$ ro-vibrational states see ref. [178] and [242] respectively.

5.3 ArH$^+$

The measured rate coefficient for electron-ArH$^+$ collisions leading to the formation of argon atoms is shown in figure 5.1. The data are the sum of several experimental runs and have been smoothed using a moving average procedure with a step of 5 points. The statistical error due to the counting process is of the order of $\pm 20\%$. The main contribution to the total error arises from the ion beam current measurement. As already mentioned above, very low values of the ion beam current required an alternative normalization method which gives only an order of magnitude indication of the absolute value for the rate coefficient.

It can be seen that the rate at low energies is very small. While the signal detected in this region is comparable with the statistical error, the value of 1×10^{-9} cm^{3}s^{-1} is an upper limit. At higher collision energies, however, the process becomes more rapid and structured: three broad peaks appear centered around 7.5, 16 and 26 eV. Similar high-energy structures have been observed for HeH$^+$ [18, 22, 23] and for NeH$^+$ (see section 5.4).

Potential energy curves for the ground and first excited states of ArH$^+$ calculated by *Stolyarov and Child* [241] are shown in figure 5.3. The first set of excited states have Ar$^+$(^{2}P) + H($n = 1$) as their asymptote but we have not measured this channel as the arrival of lone H atoms produces signals that lie in the electronic noise of the detector.
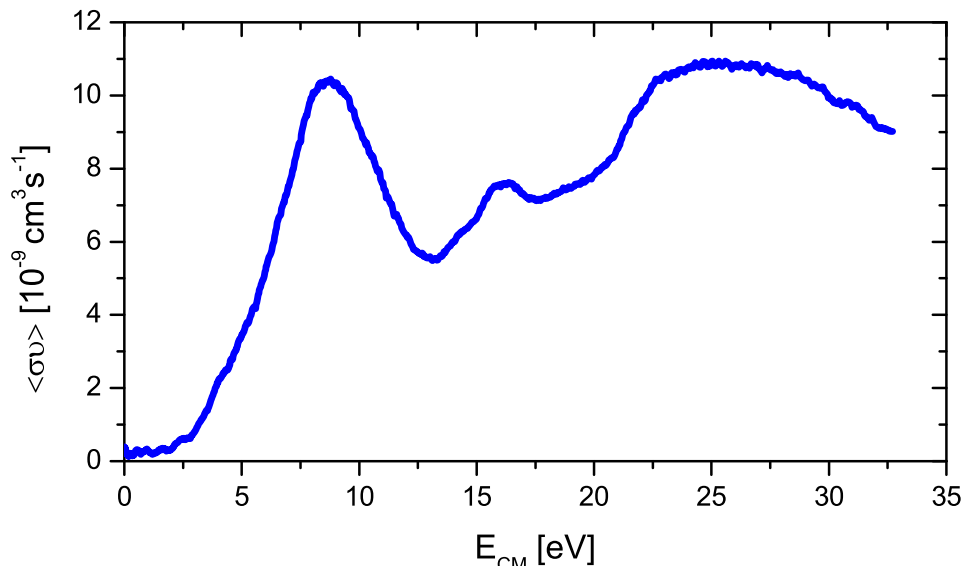

Figure 5.1: The measured rate coefficient $\langle \sigma\, v \rangle$ for the formation of argon atoms in electron collisions with ArH$^+$. The rate includes contribution from dissociative recombination and dissociative excitation channel.
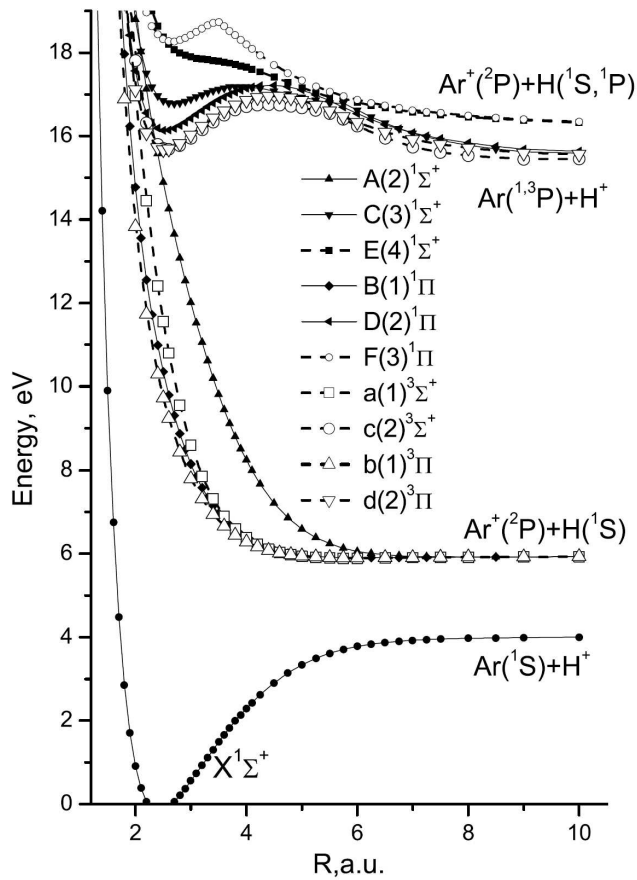
Figure 5.2: Calculated potential energy curves for the ground and first excited states of ArH$^+$ [241], reprinted from [178]. The internuclear distance is displayed in atomic units (1 a.u. = 1 Bohr radius $\approx 5.3 \times 10^{-11}$ m).

Recombination may occur due to a direct transition to a neutral Rydberg state lying underneath ionic excited states, with asymptotic limits Ar* + H($n = 1$). A similar recombination pathway has been shown for HeH$^+$ and NeH$^+$ by *Orel and coworkers* [27, 29, 242] and can explain the observed peak that has an onset at 3 eV and is centered around 7.5 eV.

The same type of recombination process is responsible for the second peak that is centered around 16 eV with the next set of excited states having an asymptote of Ar(^{1,3}P) + H$^+$ as the limit for its corresponding Rydberg states. The increase in the rate above 17.5 eV is due to dissociative excitation collisions to higher lying states, beginning with those shown in the figure that have Ar(^{1,3}P) + H$^+$ as asymptote. There are also perhaps contributions due to resonance-enhanced dissociation [243] via neutral Rydberg states lying below these states.

The present experiment was performed using vibrationally cold ions and given the lack of a suitable curve crossing near the minimum of the ion ground state, this is not unexpected. Calculations have shown that there is an indication of an existing curve crossing of the neutral repulsive state with the ion ground state at large internuclear distances [244]. This could be accessible for vibrationally excited ions and thus the recombination rate coefficient may significantly increase in that case. as for example is observed in case of vibrationally excited He$_2^+$ [245]. In plasma environments at higher temperatures higher ro-vibrational states could be populated, but given the short radiative lifetimes [178], however, rapid relaxation to the vibrational ground state will occur and thus no significant increase of the rate coefficient is expected.

5.4 NeH$^+$

The measured rate coefficient for electron-NeH$^+$ collisions leading to the formation of neon atoms is shown in figure 5.3. The data are the sum of several experimental runs and have been smoothed using a moving average procedure with a step of 11 points. Statistical errors due to counting are shown in the figure. The high statistical error around $E_{CM} = 1$ eV should be noted and so any structures seen in the rate coefficient in this region than should be considered with caution. The main contribution to the total error arises from the ion beam current measurement. As already mentioned in section 5.2, very low values of the ion beam current required an alternative normalization method which yields an order of magnitude indication of the absolute value for the rate coefficient.

As in case of HeH$^+$ [18], NeH$^+$ is seen to recombine at low centre-of-mass collision energies but above 0.3 eV the rate falls to a low value. High energy structures again appear above 7 eV. There are much fewer resonances, however, in the low energy region for NeH$^+$.

Despite the lack of a curve crossing between neutral and ion states of NeH and NeH$^+$ [242, 246] through which direct recombination could proceed, we observe a non-negligible recombination rate at low E$_{CM}$, similar to the case of HeH$^+$, where this was assigned to a new recombination mechanism, later entitled *tunelling recombination*. For references and further discussion of this mechanism, see section 5.1 and the theoretical description in chapter 1.

As mentioned in section 5.2, we cannot distinguish between products of dissociative recombination (eq. 5.1) and dissociative excitation (eq. 5.2) due to the high mass ratio of the products. Thus the rate coefficient in figure 5.3 can be a composition of both DR and DE channels. The potential energy curves of the singly and doubly excited resonant states of NeH calculated by *Florescu-Mitchell and Orel* [242] are plotted in figure 5.4. The threshold energy for dissociative excitation can be estimated as the sum of the dissociation energy of the neutral excited stated leading to Ne(3s) + H(1s) and the ionization energy of hydrogen (13.6 eV) thus giving a value of $\sim$16.5 eV. This process may be included with the peaks seen at high energies, in addition to recombination via transitions to exited neutral states.

5.5 Conclusion

The measured rate coefficient for the DR of ArH$^+$ contradicts the generally accepted idea that diatomic molecular ions display large recombination rates at thermal energies. It must be said that assumptions that have been made concerning the rapid recombination rate for these ions in plasmas [234] would appear to be erroneous. It can also be seen from our investigations that the recombination of NeH$^+$ with electrons exhibits a reasonably large rate coefficient over the energy range of interest to divertor plasmas in fusion devices, where the ions are expected to be rotationally excited at least at the same level as under our experimental conditions. Therefore NeH$^+$ has a good chance to be neutralized before collision with the wall and neon remains a good candidate for cooling divertor plasmas. However, a detailed study of the influence of dissociative excitation awaits future theoretical work.
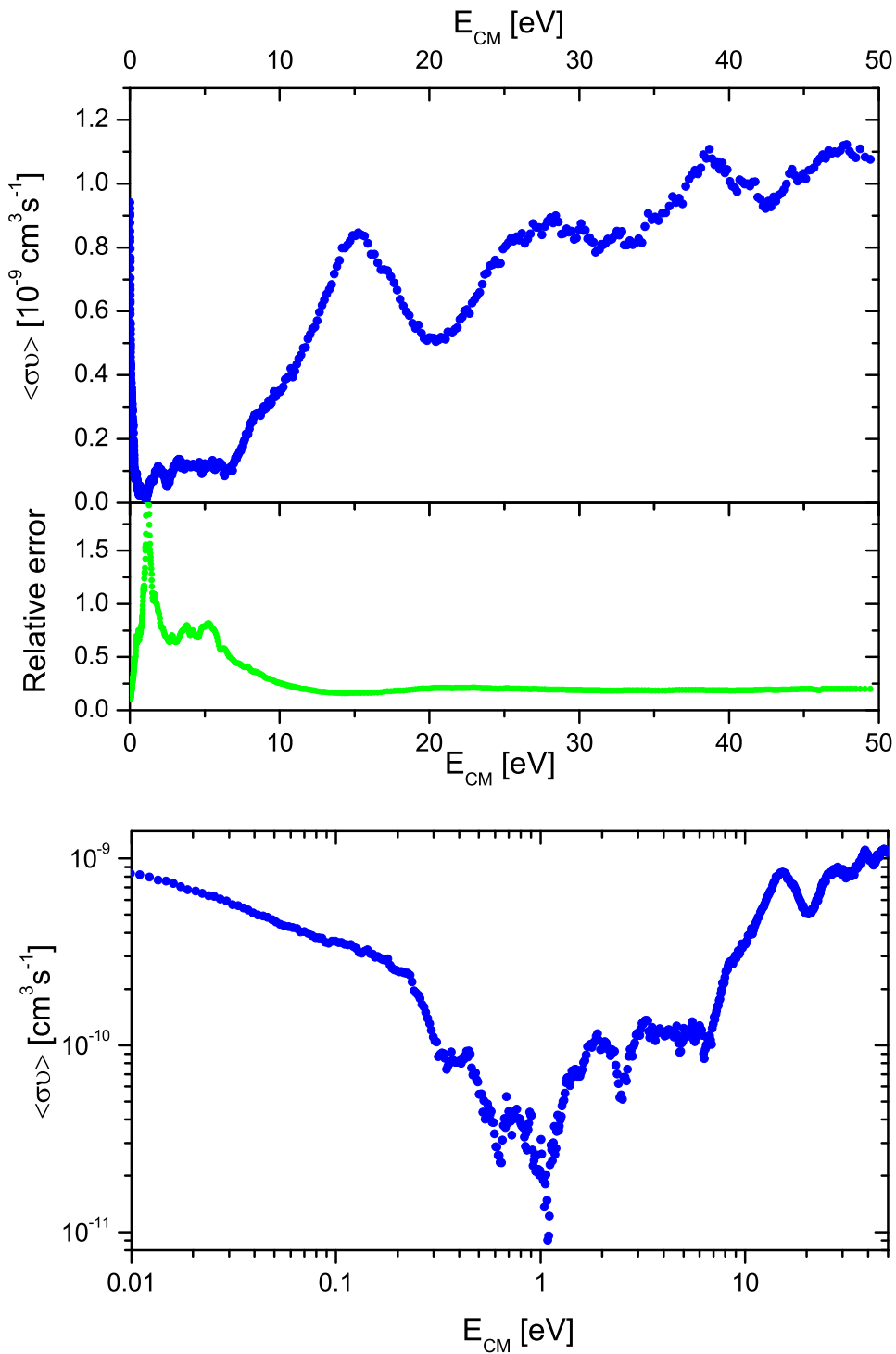
Figure 5.3: Measured rate coefficient $\langle \sigma v \rangle$ for the formation of argon atoms in electron collisions with NeH$^+$. Linear and log-log scale is used to highlight both low and high energy structures. A moving average procedure has been used to smooth several sets of the data with step of 11 points. Upper panel includes relative statistical error.
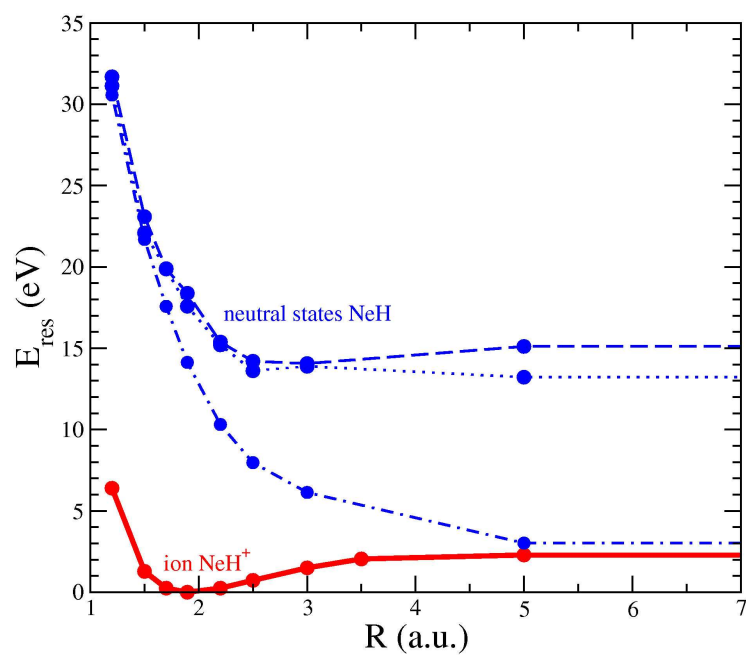
Figure 5.4: Potential energy curves of calculated singly and doubly excited NeH resonance states (blue) and the ground state of NeH$^+$ (red solid curve). The three resonance states have the following limits for $R \to \infty$: Ne(3s) + H(1s), dot-dash curve; Ne(3s) + H(2s), dotted curve; Ne(3s) + H(3s), dashed curve. Graph is reprinted from [242].

DISSOCIATIVE RECOMBINATION OF FLUOROCARBON IONS

6.1 Introduction

Fluorocarbon plasmas, with CF_4 as parent gas, are commonly employed in microelectronics processing to dry etch features into silicon due to their ability to preferentially etch SiO_2 over Si [247, 248]. Fluorocarbon layers deposited from plasmas have also been considered for use as dielectric interlayers [249]. Extensive research has probed the plasma conditions and components that contribute to the competing processes of deposition and etching in fluorocarbon plasmas [248, 250–253]. Also mathematical models of fluorocarbon plasmas have been developed to describe the etching process [254–258]. The ultimate goal of these studies is the optimization of the plasma etching process for the production of even smaller features in microelectronic circuits, produced from Si wafers of continually increasing diameters.

Fluorocarbon ions CF^+, CF_2^+ and mainly CF_3^+ are important species in CF_4 plasmas [259, 260] and their dissociative recombination with electrons is an important charge-loss channel. All the plasma models mentioned above have only included the recombination of CF_3^+ with the value of rate coefficient being $\alpha = 3.958 \times 10^{-9}/\sqrt{T_e}\,T_i$ cm^{3}s^{-1} which yields a rate coefficient at 300 K equilibrium conditions of $\alpha = 9.68 \times 10^{-7}$ cm^{3}s^{-1}. The origin of this value is actually unclear and the recent *FALP–MS* measurements [261] showed a rate coefficient which is significantly lower, $\alpha = 2.8 \times 10^{-7}$ cm^{3}s^{-1} at 300 K. Recombination rate coefficients of CF^+ and CF_2^+ are not included in plasma models and rate coefficient values were not available before this study at all.

We have therefore, used the heavy-ion storage rings method to perform merged beams studies of electron collisions with chosen fluorocarbon ions.

6.2 CF^+

Experimental method

The experiments on CF^+ were performed at the *ASTRID* and *CRYRING* heavy-ion storage rings. For a detailed description of the principle, experimental procedure and data analysis see sections 2.4 and 2.5. The main differences between the experimental facilities (note: mainly electron beam temperatures) are highlighted in section 2.5.

At *ASTRID*, the ions under study were produced from tetrafluoromethane (CF_4) in an electron impact source (see section 2.4.7), accelerated to 150 keV and injected into the storage ring where they were further accelerated to 2.5 MeV. This process takes about 4 s to accomplish.

At *CRYRING*, the ions were produced using the same type of ion source also using CF_4 as the source gas. Instead of using the filament, the plasma was created by an electrical discharge at 1 kV, at a pressure of about 0.1 Torr. The ions were extracted at 40 keV and injected into the ring where they were further accelerated to 3.1 MeV during 1 s. The beam lifetime was 1.2 s.

At *ASTRID* the ion beam current was too small to be measured directly and only a relative experimental rate was obtained. At *CRYRING* , however, the beam intensity was high enough to use a current transformer method for the ion current measurement (see section 2.4.4) and thus it was possible to determine the absolute rate coefficient.

The ion beam composition

Previous studies of CF^+ chemistry have indicated the possible presence of excited states in the ion beam. *Moris at al* [263] found a rapid reaction of CF_4 with CF^+ using the SIFT-VT technique. The plot of reactant ion signal versus neutral reactant concentration was curved, indicating the presence of at least two states of the ion with different reactivities toward the reactant neutral. Using several monitor gases with different ionization potentials, they were able to sort out the possibility that observed states are excited electronically. However *Langford et al* [264] have reported the observation of an electronically excited $a^3\Pi$ state that lies between 3.4 and 4.8 eV above the ground state of CF^+. In that study, the CF^+ ions were produced by electron impact on CF_4 while *Morris et al* used CF_3Br as the parent gas. In next study *Reid* [265] was even able to quantify the percentage of the $a^3\Pi$ state in a beam of CF^+: when produced from CF_4; as much as 32% of the CF^+ ions were in this excited metastable state. Since in the present study CF_4 was used as the parent gas, it must be assumed that the beam initially has a high proportion of the $a^3\Pi$ state.

The lifetime of the transition between $a^3\Pi$ state and $X^1\Sigma^+$ ground state was estimated [266] obtaining the value of 0.086 s. This time is long compared to typical measurement times in experiments cited above, but at storage rings the measurement commences several seconds after ion production and thus this state should have completely decayed.

As discussed in section 2.4.1, the storage time is usually not long enough to remove all rovibrational states. A calculation of the lifetimes of the rovibrational states for the $X^1\Sigma^+$ ground state and for the metastable $a^3\Pi$ state of CF^+ has been performed [266] and the values obtained show that the vibrationally excited levels should all radiate down to the $v = 0$ level during the storage of the ions in the ring prior to the recombination measurement. The $a^3\Pi$ state is also expected to have decayed as discussed in previous paragraph. Rotationally excited levels of the $v = 0$ state, however, have very long lifetimes and if present upon injection into the ring, should stay excited during the measurement.

Results and discusion

Figure 6.1 represents a typical pulse height spectrum accumulated during the experiment at *ASTRID* with the electron beam switched on and off, at a collision energy of $E_{CM} = 0$ eV. Particular peaks corresponds to C, F and C + F atoms reaching the SBD detector, where the latter appear at full ion beam energy as C and F atoms arriving simultaneously (the
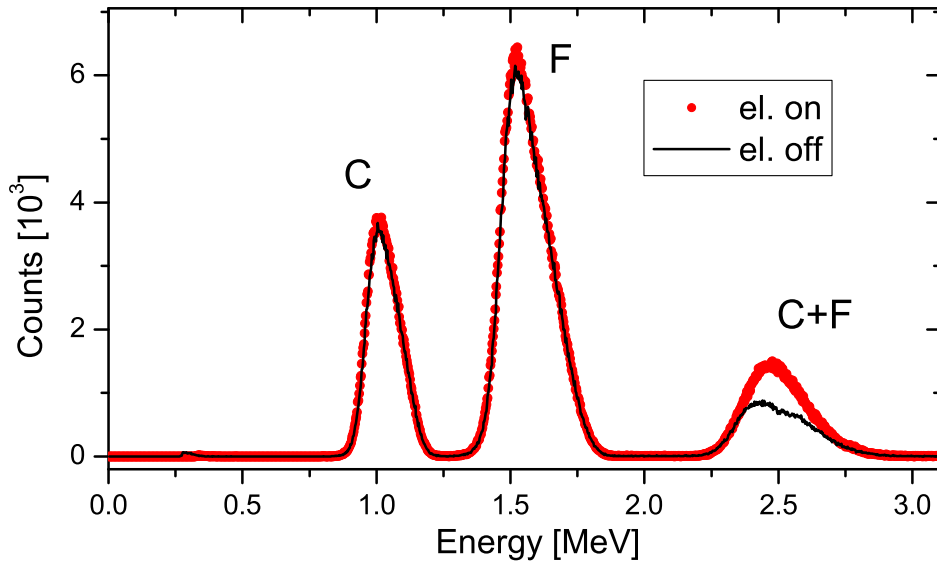
Figure 6.1: A pulse height spectrum of SBD detector signals at $E_{CM} = 0$ collected by MCA for electron beam in the electron cooler turned "on" (circles) and "off" respectively (line).

time difference is within the time resolution of the SBD detector). Pure data arising from ion-electron interactions is obtained by subtraction of both spectra, where data measured with the electron beam turned off originate from collisions with the residual gas in the ring. It can be seen, that at $E_{CM} = 0$, only a peak at the position of C+F is obtained, which corresponds to DR events.

The measured rate coefficient $\langle \sigma v \rangle$ for electron–CF$^+$ collisions is shown in figure 6.2. At *CRYRING* the absolute measurement was performed with higher energy resolution down to ~ 0.001 eV, while at *ASTRID* the data were measured separately in the C+F and F windows using longer integration times and higher collision energies up to $E_{CM} = 6$ eV. As the absolute values were measured only at *CRYRING*, the *ASTRID* data were normalized to the *CRYRING* data, using only data points above an energy of 2×10^{-2} eV to avoid the possible influence of higher electron temperatures at *ASTRID* to low energy points. Since the energy resolution of the electron beam is better at *CRYRING* than at *ASTRID* it was possible to extend the measurements to lower energies by combining the results. Thus the divergence between the two data sets below 0.01 eV reflects the different electron temperatures related to energy resolutions at the two machines. The main error is estimated to be $\pm 20\%$ due to the determination of the ion current. The statistical error due only to counting statistics is shown in the graph.

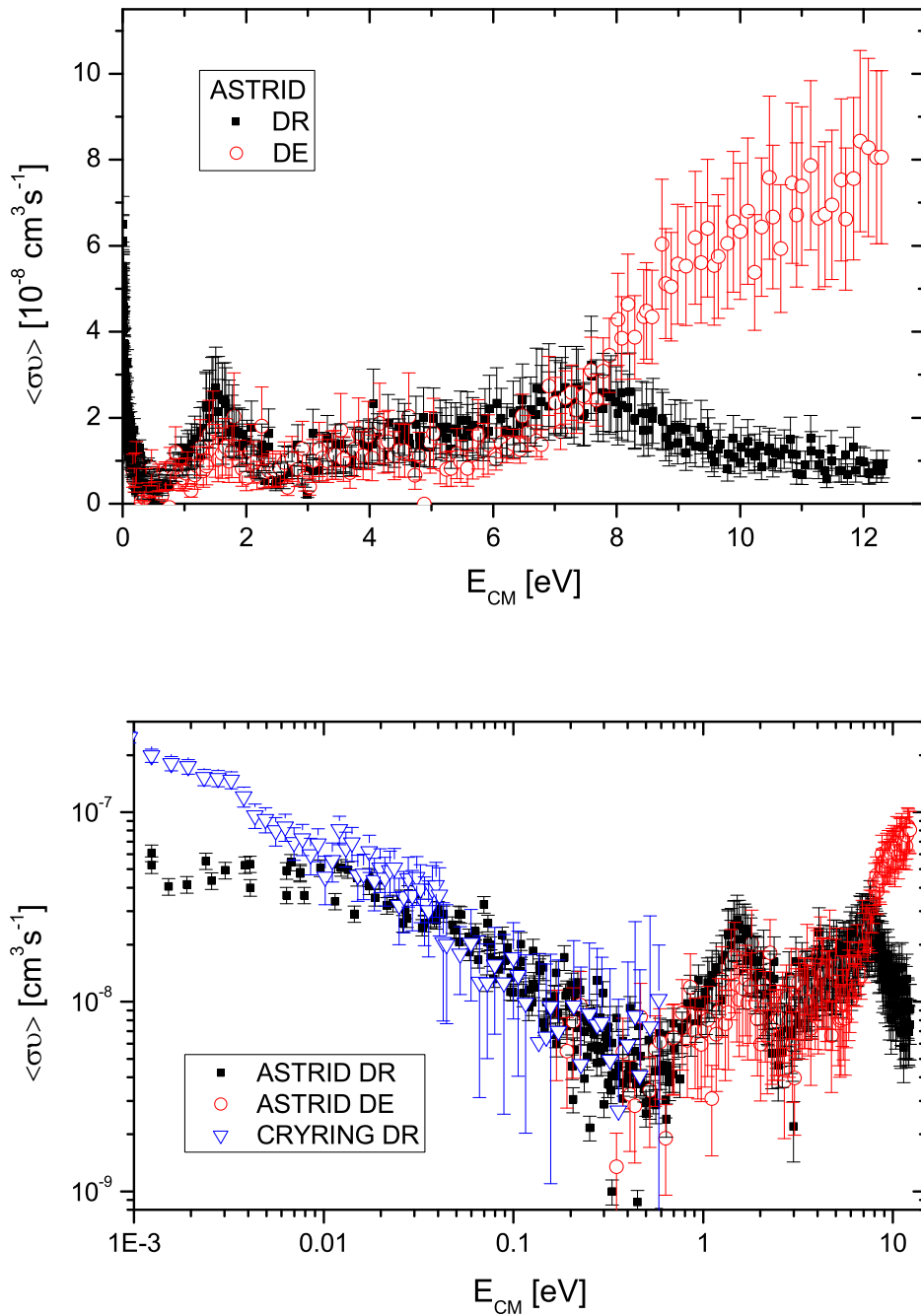Figure 6.2: The measured rate coefficient $\langle \sigma v \rangle$ for electron–CF^+ collisions versus center-of-mass energy E_{CM}. Data from both *CRYRING* and *ASTRID* are plotted, in latter case for both dissociative recombination (DR) and dissociative excitation (DE). Linear and log-log scale is used to highlight both structures at high energies and an overlap of data from both machines at low energies.

The data obtained from signals measured in the C+F window correspond to dissociative recombination

$$e^- + CF^+ \rightarrow C + F \tag{6.1}$$

and in the F window to the dissociative excitation reaction

$$e^- + CF^+ \rightarrow C^+ + F + e^-, \tag{6.2}$$

as the C$^+$ ion is deflected by the bending magnet and only neutral F atoms may reach the SBD detector. The energy threshold for this excitation reaction is 6.73 eV and 2.6 eV from the $v = 0$ levels of the ground X$^1\Sigma^+$ and metastable a$^3\Pi$ states respectively (see fig. 6.3 and discussion below in this section). In the energy range examined, no positive signals were found in the C window corresponding to the reaction

$$e^- + CF^+ \rightarrow C + F^+ + e^-. \tag{6.3}$$

The threshold for dissociation to this channel from the CF$^+$ ground vibrational state lies at 12.89 eV and 8.78 eV from the metastable state. The highest centre-of-mass energy used in this experiment was 12.3 eV for practical reasons and so one would not expect to have seen C atoms originating from the ground state. The fact that no C atoms at all were seen in this case indicates that there is no contribution from the a$^3\Pi$ state that would have decayed before our measurements were taken (see discussion in previous section).

It can be seen from the rate coefficient behavior that there is a low-energy peak in the recombination rate coefficient followed by a sharp distinct peak centered at about 1.5 eV and a broad diffuse peak centered at 7.5 eV. In the C$^+$ + F excitation channel, there is a sharp onset of a rising rate at about 7 eV.

In figure 6.3 we have reproduced the potential energy curves for CF$^+$ excited states calculated by *Petsalakis and Theodorakulos* [267] in order to interpret our observations. The zero point energy ($v = 0$) of the ground X$^1\Sigma^+$ state is 0.11 eV and that of a$^3\Pi$ state is 0.1 eV.

As the first excited state (a$^3\Pi$) lies at 4.83 eV above the $v = 0$ level of the CF$^+$ ground state, the peak in the rate coefficient lying at 1.5 eV must arise from the capture to neutral Rydberg states lying below this ion state. Such a process have been already observed for other molecular ions – mainly for HeH$^+$ [20, 21] and NeH$^+$ (see section 5.4) and have been described theoretically by *Orel and co-workers* [27, 29]. The next peak centered at 7.58 eV arises from the same process via capture to the next series of Rydberg states lying below the 1$^1\Pi$ ion state.

The dissociation limit of CF$^+$ lies 6.73 eV above the $v = 0$ level and thus the a$^3\Pi$ state does not contribute to the dissociative excitation process. However, the calculated vertical excitation energy of the 1$^1\Pi$ state is 8.35 eV above the $v = 0$ level of the ground state and this corresponds quite well with the observed onset of the dissociative excitation cross section.

Recombination cross-sections obtained by dividing the measured rate coefficient by the relative velocity (see section 2.4.5) are plotted in figure 6.4. Again data taken both at *ASTRID* and *CRYRING* are included. Both sets of data agreed very well with regard to the slope of the cross-section. The cross-section has been used to derive a thermal rate coefficient (using equation 2.35) and this is found to have a value of

$$\boldsymbol{\alpha = (5.2 \pm 1.0) \times 10^{-8} \ (T_e/300)^{-0.8} cm^3 s^{-1}.}$$

It was shown by *Petsalakis and Theodorakulos* [267] that there exists, several diabatic state curve crossings between the ion ground state and the neutral states, which would lead to
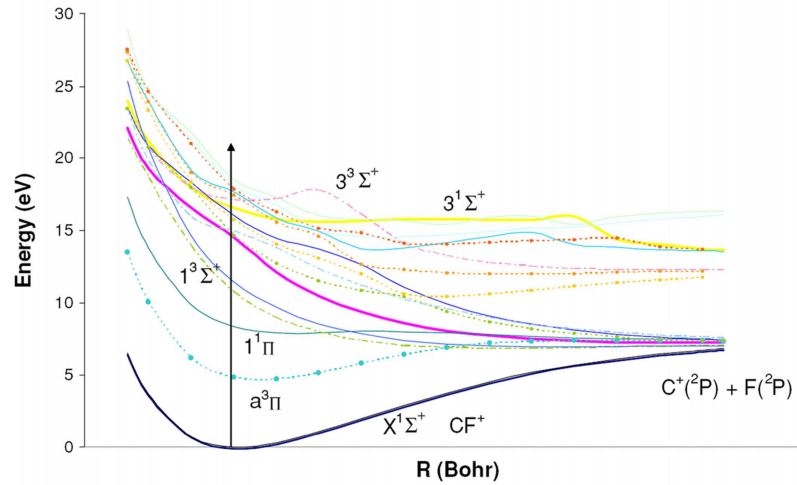
Figure 6.3: Potential energy curves for the ground and excited Σ and Π states of CF^+ [267], reprinted from [266]. Thick full curves: $^1\Sigma$ states; fine full curves: $^1\Pi$ states; dashed curves: $^3\Sigma$ states; dotted curves: $^3\Pi$ states.

a direct recombination process. Thus the thermal rate coefficient is rather small though a value around 10^{-7} cm^{-3}, which is more typical for a diatomic ions [238], might have been expected. This rather surprising observation should be an impulse for future theoretical studies.

6.3 CF_3^+

Experimental technique

The experiments on CF_3^+ were performed at the *ASTRID* heavy-ion storage ring. For detailed description of the principle, experimental procedure and data analysis see section 2.4. The ion were produced in the Nielsen electron impact ion source using CF_4 as parent gas. After initial acceleration by 150 kV, ions were injected to the storage ring and further accelerated to 1.95 MeV. The life time of the ion beam was 2 s where the decay of beam intensity is due to interaction with residual gas. The process of ion production, injection, acceleration and storing consumes about 4 s which is time long enough for complete infrared relaxation of ions to their vibrational ground state. However, higher rotational states may be presented in the ion beam. Such composition was observed also for CF^+, ArH^+ and NeH^+ and was also discussed in section 2.4.1. The ion beam current was too small (below 60 nA) to be measured directly by current transformer and alternative method described in section 2.4.4 have been used. At this experiment the rate coefficient and branching ratios were obtained.

Rate coefficient and cross-section

The measured recombination rate coefficient $\langle \sigma\, v \rangle$ and cross-section calculated as $\sigma = \langle \sigma\, v \rangle / v$ are plotted vs collision energy E_{CM} in figures 6.5 and 6.6. The statistical error arising from the counting is less than 20% for most of the data except for the region around $E_{CM} \approx 1$ eV, where
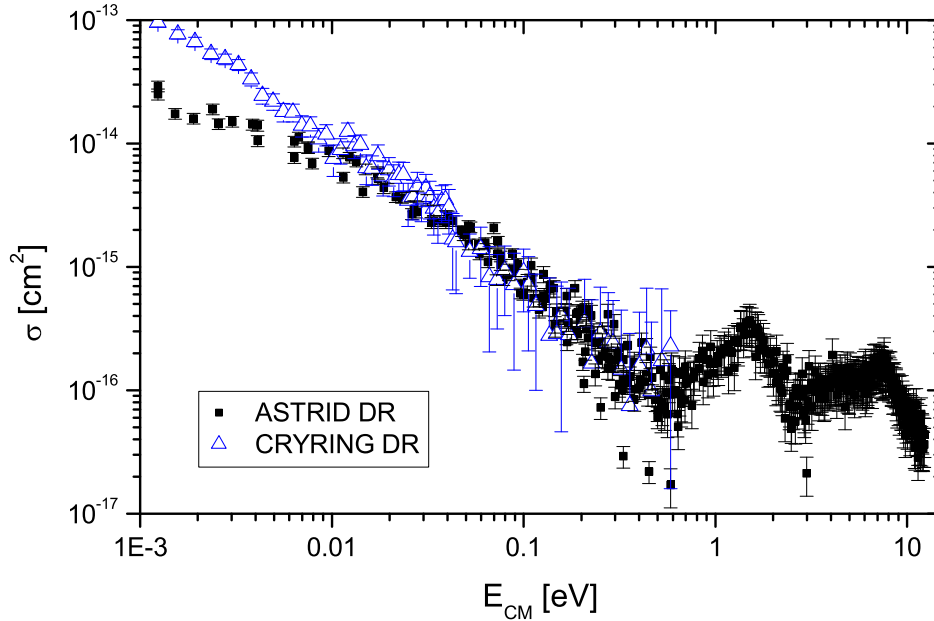
Figure 6.4: The cross-section for the recombination of CF^+ with electrons measured at *ASTRID* and *CRYRING*.

it may reach 70%. The absolute error is given mainly by the ion current measurement and as already mentioned, in this experiment an alternative method was used and thus a high error in the absolute value of the rate coefficient may be expected. Therefore the normalization to the other data set was performed using the striking similarity between the current set of measurements on fluorocarbon ions and measurements performed on ions derived from CH_4 a single pas merged beam technique [268]. All ions in the series CH_n^+ for $n = 2$–5 demonstrate almost indistinguishable rate coefficients below 0.1 eV. Above this energy, CH_3^+ exhibits a steeper energy dependence than CH_2^+, similar to the measured rate coefficient for CF_3^+ compared to the CF_2^+ rate coefficient obtained at the *CRYRING* facility [269]. As the ion beam current measurement at *CRYRING* was performed at higher precision, we followed this analogy and normalized the CF_3^+ rate coefficient (and so the cross-section as well) to the CF_2^+ data using the energy region $5 \times 10^{-2} - 1 \times 10^{-1}$ eV. It might be interesting to mention that recombination rate for CH^+ displays a lower rate coefficient than other ions in the series, in the same way as CF^+ in comparison to CF_2^+ and CF_3^+. Data points below 0.01 eV are not plotted as they lies below the resolution limit of the *ASTRID* apparatus.

The cross-section of CF_3^+ includes resonances, first starting at 2 eV, peaking around 8 eV, and then beginning to increase at 15 eV. Due to the lack of information concerning the excited states of CF_3^+, we cannot assign those peaks to specific states. However, the high energy of these structures indicates that the recombination may proceed by capture into doubly excited neutral Rydberg states. The incident electron excites one electron in the ion core and is itself captured to a Rydberg state lying below an excited ion state. Pre-dissociation then occurs by the same repulsive neutral state, which gives rise to the recombination at low energies. Similar process have been observed for other molecular ions (HeH^+, NeH^+ and CF^+) and have been described theoretically by *Orel and co-workers* [27, 29].
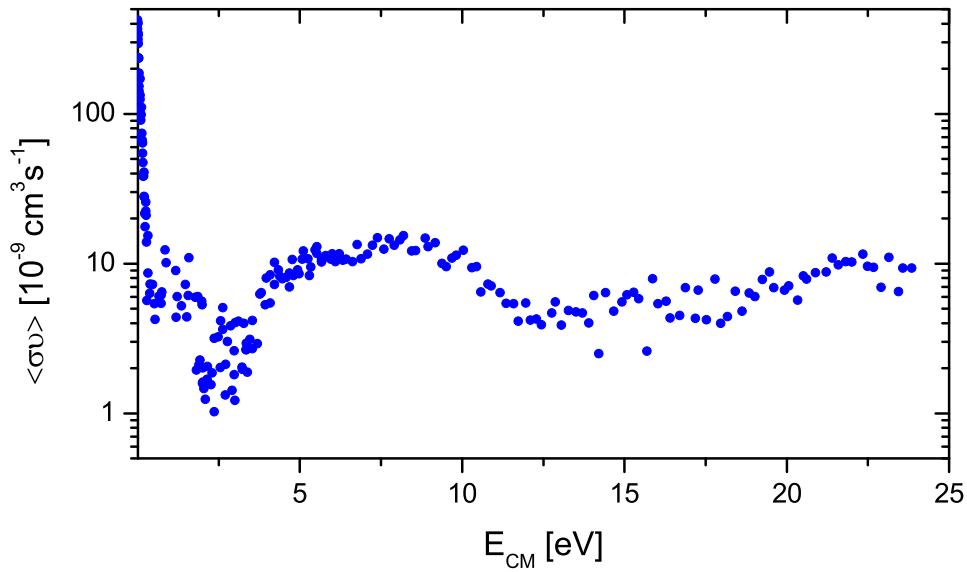
Figure 6.5: Measured rate coefficient $\langle \sigma\, v \rangle$ for electron–CF_3^+ recombination over centre-of-mass energy E_{CM}. No smoothing procedure have been used. The data were normalized to CF_2^+ rate coefficient, see details in the text.
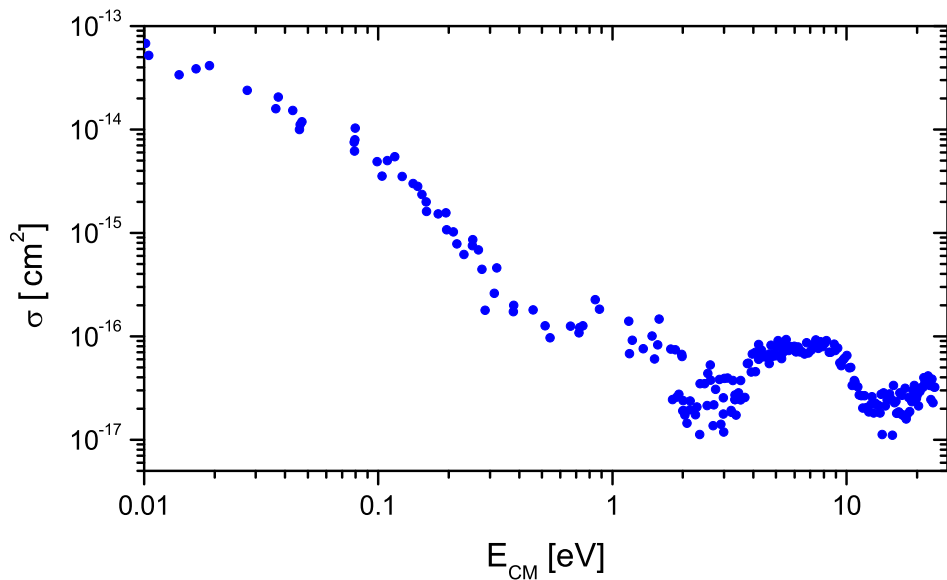

Figure 6.6: The cross-section σ for electron–CF_3^+ recombination vs center-of-mass energy E_{CM}. No smoothing procedure have been used. The absolute value have been normalized by CF_2^+ data, see details in the text.
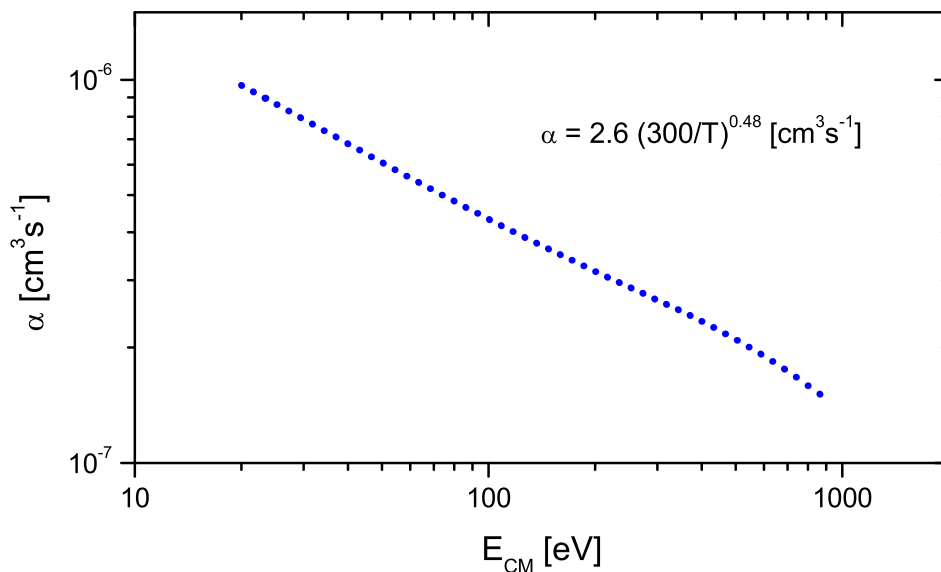
Figure 6.7: The thermal rate coefficient of CF$_3^+$ recombination with electrons based on a cross section plotted in figure 6.6.

The thermal rate coefficient for the Maxwellian velocity distribution has been calculated using equation 2.35. The curve thus obtained (see figure 6.7) yields the rate α to be

$$\alpha = \mathbf{2.6 \times 10^{-7}(300/T)^{0.48}} \text{ cm}^3\text{s}^{-1}$$

for $20 < T < 1000$ K.

That value is in very good agreement with the value obtained in the previous *FALP–MS* measurement namely 2.8×10^{-7} cm^{3}s^{-1} at 300 K [261], which vindicates the procedure of normalization to the CF$_2^+$ data. In this light, one could find interesting that thermal rate coefficient for CF$_2^+$ recombination ($\alpha = 3.7 \times 10^{-7}(300/T)^{0.76}$ cm^{3}s^{-1}, see ref. [269]) differs from that of CF$_3^+$. The origin of this discrepancy is in the different slopes of the cross-sections at low energies, as is also seen in case of CH$_2^+$ and CH$_3^+$.

Branching ratios

The dissociative recombination of CF$_3^+$ with electrons has 3 energetically allowed dissociation channels at zero collision energy $E_{CM} = 0$ eV. The kinetic energy release (KER) is calculated using data from the NIST database [223].

$$
\begin{array}{llll}
\text{CF}_3^+ + e^- & \longrightarrow \text{CF}_2 + \text{F} & +5.3 \text{ eV} & (A) \\
& \longrightarrow \text{CF} + \text{F}_2 & -0.3 \text{ eV} & (B) \qquad (6.4) \\
& \longrightarrow \text{CF} + \text{F} + \text{F} & +0.15 \text{ eV} & (C)
\end{array}
$$
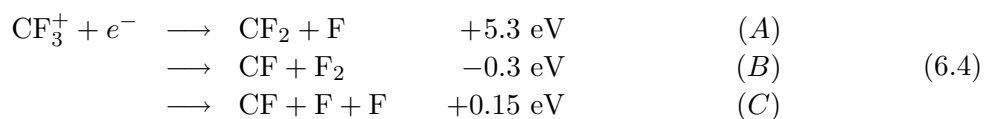
Channel (B) seems to be slightly endothermic, but due to the uncertainty of the input data for the KER calculation, we included this channel in the analysis as well.

Branching ratios were determined at $E_{CM} = 0$ eV using a transmission grid with $T = 0.235$ in front of the SBD detector to separate products in the pulse-height spectrum. A detailed description of this procedure is given in section 2.4.6. In figure 6.8, the pulse-height spectrum of product energies is plotted for both cases: electrons turned on and electrons turned off. As the pulses in the case without electrons in the electron cooler arises only from collisions with the residual gas, the spectrum with electrons turned off is subtracted from the spectrum with electrons turned on before further analysis.

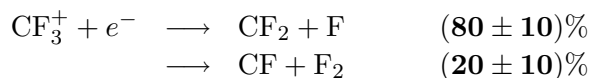Subtracted spectra have been fitted by a set of Gaussian curves representing peaks corresponding to energies (masses) of particular neutral products and their combinations (F, C+F, 2F, C+2F and C+3F), while the peak centers have been fixed at positions proportional to a particular mass. For the peak yields N_x, the following set of equations could be written:

$$
\begin{pmatrix} N_F \\ N_{C+F} \\ N_{2F} \\ N_{C+2F} \\ N_{C+3F} \end{pmatrix} = \begin{pmatrix} T(1-T) & 0 & 2T(1-T)^2 \\ 0 & T(1-T) & T(1-T)^2 \\ 0 & T(1-T) & T^2(1-T) \\ T(1-T) & 0 & 2T^2(1-T) \\ T^2 & T^2 & T^3 \end{pmatrix} \times \begin{pmatrix} M_A \\ M_B \\ M_C \end{pmatrix} \qquad (6.5)
$$

where M_x is the number of dissociation events in particular channel x. The T terms represent the probability of the fragment passing through the grid, the $(1-T)$ term, the probability of stopping the fragment on the grid. As positions of peaks arising from masses C+F and 2F lie close to each other (mass 35 and 38 at. u.) and the yield in both peaks is very low, only one equation for $N_{C+F} + N_{2F}$ has been used in the final calculation procedure. The set of linear equations 6.5 has been solved following the procedure described in section 2.4.6. The branching fractions have been obtained from the M_x by normalization to the total number of dissociation events.

Numerical treatment of the complete set of equations using all branching channels gives values of M_C close to 0 with very high statistical error. This confirms the expectation of it being a closed channel (C) as the re-association leading to F_2 is unprobable. For calculation of final results, only channels (A) and (B) have been used to achieve better precision. Overall, the MCA spectra with electrons turned on and off had nearly the same amplitude and their subtraction gives a very high statistical error leading to 10% error of final branching result:

$$
\begin{array}{lll} \mathrm{CF_3^+} + e^- & \longrightarrow \; \mathrm{CF_2 + F} & \mathbf{(80 \pm 10)}\% \\ & \longrightarrow \; \mathrm{CF + F_2} & \mathbf{(20 \pm 10)}\% \end{array}
$$

These branching ratios are very similar to values obtained for the dissociative recombination of $\mathrm{CF_2^+}$, where the loss of one and two fluorine atoms is represented by $(71\pm4)\%$ and $(29\pm4)\%$ of the dissociation events respectively.

6.4   Conclusion

The study of $\mathrm{CF^+}$ and $\mathrm{CF_3^+}$ interactions with electrons has led to an improvement of our knowledge of the chemistry in $\mathrm{CF_4}$ plasmas. The recombination rate coefficient for $\mathrm{CF_3^+}$ confirmed our previous measurement using the *FALP–MS* and thus has replaced a previously widely used value whose origin is obscure. The recombination of $\mathrm{CF^+}$ was studied experimentally for first time and thus rate coefficient values for both ions may enhance numerical plasma models.
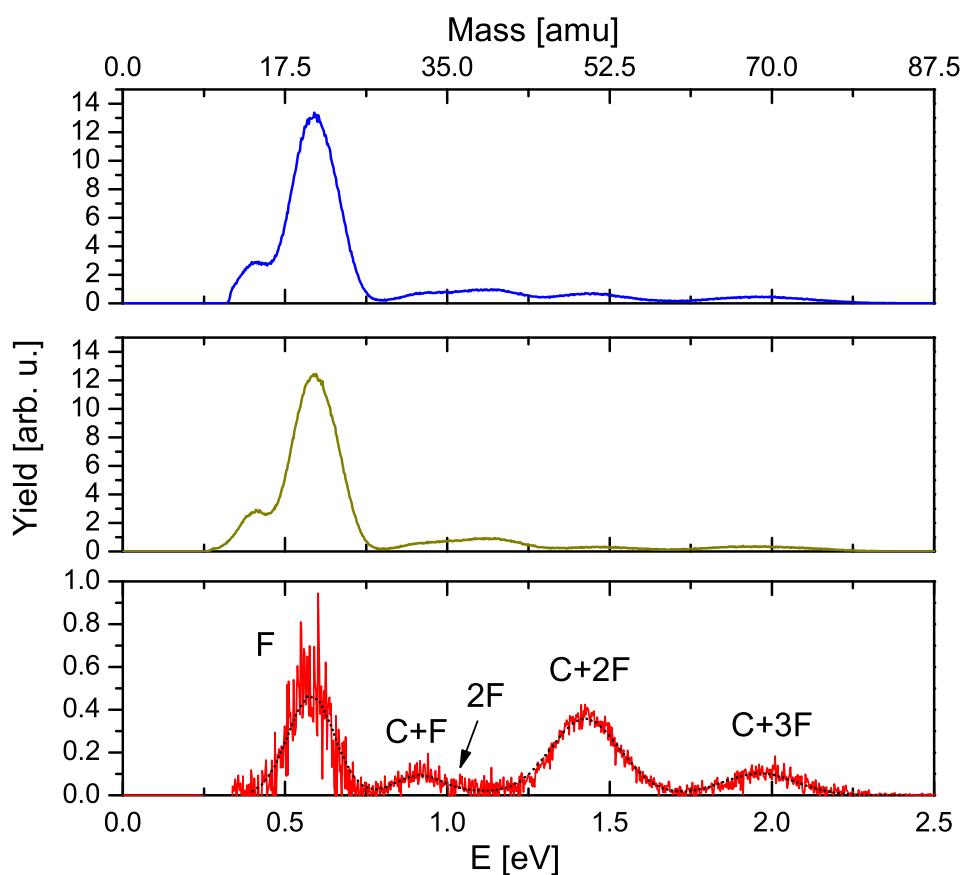
Figure 6.8: The pulse hight spectra of neutral products of CF_3^+ recombination recorded by MCA. The grid of transmission $T = 0.235$ have been placed in front of SBD detector. Spectra measured with electrons turned on (upper panel) and with electrons turned off (middle panel) have been subtracted to obtain pure signal arising from dissociative recombination process only (bottom panel). Dotted black line represents a fit by set of Gaussian curves.

Already a simple speculation shows that the recombination process is significant in CF_4 plasmas, especially for formation of CF radicals, which are in this environment the most important species participating in the etching process. The electron impact ionization of CF_4 produces mainly the CF_3^+ ion [270]. The reaction of CF_2^+ and CF^+ with CF_4 parent gas gives exclusively CF_3^+ as a product [263]. Fast recombination of CF_2^+ and CF_3^+ with electrons produces the CF radical in 71% and 20% cases respectively. As the cross-section for CF_4 electron impact dissociation does not exceed the cross-section for ionization of CF_4, its ionization folowed by recombination must be considered as the major route for the formation of CF radicals in etching plasmas.

The observed dissociative excitation and recombination through doubly-excited neutral states is a subject still poorly understood and should be an object of additional theoretical work.

SUMMARY

This thesis describes experimental investigations of electron-ion recombination. Several different ions have been studied using both afterglow and beam experiments.

A new *Flowing Afterglow with Langmuir Probe and Variable Temparature* (*FALP–VT*) apparatus has been designed and built. Very high purity over the whole system and the design of the flowtube has allowed us to study recombination with rates down to $\sim 2 \times 10^{-8}$ cm^{3}s^{-1} for time scales up to 60 ms. The *FALP–VT* has been used for two experiments:

The first study concentrated on the overall recombination rate coefficient α_{eff} in the plasma with deuterium as the reactant gas. The number density [D$_2$] was systematically increased from 2×10^{12} to 2×10^{15} cm^{-3} while the temperature ranged from 130 K to 300 K. The observed α_{eff} greatly depends upon [D$_2$] and temperature. For [D$_2$] $< 10^{14}$ cm^{-3} the plasma is dominated by D$_3^+$ while for higher [D$_2$], D$_5^+$ is also formed from D$_3^+$ in an association reaction with D$_2$ and destroyed by collision induced dissociation. The equilibrium characterized by the equilibrium constant K_C is established between D$_3^+$ and D$_5^+$ and therefore the measured effective recombination rate coefficient can be expressed as

$$\alpha_{\text{eff}} = (\alpha_3 + \alpha_5 K_C[\text{D}_2])/(1 + K_C[\text{D}_2]), \tag{7.1}$$

where α_3 and α_5 are the respective recombination rate coefficients for D$_3^+$ and D$_5^+$. The experimentally obtained α_{eff} ([D$_2$]) was fitted by equation 7.1 and values of $\alpha_3(T)$ and $K_C(T)$ have been obtained. The data are in good agreement with results from previous measurements using the *AISA* apparatus [112] and with thermodynamic data [174]. This experiment has confirmed that the very low values of α_{eff} measured in *AISA* for [D$_2$] $< 10^{12}$ cm^{-3} represents the recombination rate of D$_3^+$ only for at these concentrations of D$_2$ the formation of D$_5^+$ can be neglected.

In the second experiment the *FALP–VT* was employed for the investigation of the recombination of H$_3^+$. The measurement was performed over a wide range of [H$_2$]: from 2×10^{11} to 10^{15} cm^{-3} while the temperature was maintained at 250 K. We have obtained the overall recombination rate coefficient α_{eff} for H$_3^+$ from a very careful measurement. For $10^{12} <$ [H$_2$] $< 10^{14}$ cm^{-3} the data displays almost a constant recombination rate $\alpha_{\text{eff}} = 1.85 \times 10^{-7}$ cm^{3}s^{-1}. On the other hand, at lower concentrations α_{eff} exhibits a steep decreasing evolution with α_{eff} proportional to [H$_2$]. The lowest measured value was α_{eff} ([H$_2$] $= 1.5 \times 10^{11}$ cm^{-3}) $\approx 1.5 \times 10^{-8}$ cm^{3}s^{-1}. The observed dependence of α_{eff} agrees with recent measurements on *AISA* and *AISA-VT* [108, 111, 143]. The confirmation from flowing afterglow experiment suppressed any doubts due to the effects of the complicated H$_3^+$ formation and possible H$_2$ dissociation in *AISA*, because in the flowing afterglow technique,

the H_3^+ formation is much more straightforward and hydrogen is injected downstream of the discharge and cannot be dissociated. Results from both these techniques are in contrast however, with the value for the dissociative recombination rate coefficient for H_3^+ obtained at the Heavy Ion Storage Ring *CRYRING*: $\alpha_{DR}(250 \text{ K}) = 7.7 \times 10^{-8} \text{ cm}^3\text{s}^{-1}$. We have introduced a new schematic for H_3^+ recombination which includes the effects of collisions with He atoms at high pressures in afterglow experiments. Confirmation of the hypothesis requires further theoretical investigation.

The next very important result can be taken as the *FALP–VT* apparatus itself. The extreme lower limit for the mesurable recombination rate makes this apparatus suitable for studying the recombination of "exotic ions" with low recombination rates, e.g. KrH^+.

Next, the study of the recombination of Polycyclic Aromatic Hydrocarbons (PAHs) is presented. A new technique, the *Flowing Afterglow with Photo-Ions* (*FlAPI*), was developed to overcome technical problems which were raised during previous measurements of the recombination of PAHs using the *FALP–MS* apparatus. In the *FlAPI* apparatus, the majority of the electrons are produced in a standard way in the microwave discharge. Neutral PAHs are introduced at such a low concentration that there is no risk of pollution of the Langmuir probe or production of PAH anions via electron attachment. PAH cations are then produced by photoionzation using a pulsed laser beam oriented along the axis of the flowtube. The evolution of the concentration of the ion under study is measured with the QMS at a fixed position at the end of the flowtube. The electron density is measured along the flowtube in the standard way with a movable Langmuir probe. The excess of electrons over the photoproduced PAH ions allows us to measure the electron concentration independently of the laser emission. The *FlAPI* technique was used for recombination measurements of Azulene, Acenaphthene, Anthracene and Pyrene. The results obtained agree very well with recombination rates for similar species studied previously with the *FALP–MS* technique. The recombination rate for PAH cations is a very important parameter in astrochemical models of PAH populations in interstellar clouds. Our measurements have shown that rate coefficients often used in these models are highly underestimated. The *FlAPI* has proven to be a very promising technique for further recombination studies on ions of PAHs and other heavy species.

The last set of presented experiments have been performed at the *Aarhus STorage RIng Denmark* (*ASTRID*). The storage ring technique combined with the merged beams principle allowed us to study the recombination of simple polyatomic ions. The collision energy of the electrons and ions is tuned by changing the relative velocities of the electron and ion beams. In this way, the dependence of the recombination cross section on the interaction energy was studied. The thermal rate coefficient was also calculated by convolution with a Maxwell EEDF. In addition to the recombination rate for some ions, the branching ratio for dissociation channels was also determined using a grid of known transmission, inserted in front of the detector and analysis of the resulting pulse height spectrum. The low energy recombination cross section for the *DR* of ArH^+ contradicts the generally accepted idea that diatomic molecular ions display large recombination rates at thermal energies. This observation should considerably change assumptions made in some plasma experiments and models. The recombination of NeH^+, on the other hand, shows a reasonably large recombination cross section over the energy range of interest to divertor plasmas in fusion devices. NeH^+ has a good chance to be neutralized before collision with the wall and so neon therefore remains a good candidate for cooling in these regions. The study of the recombination of fluorocarbon ions CF^+ and CF_3^+ has shown recombination to be an important process for the formation of reactive radicals in CF_4 etching plasmas. The high recombination rate of CF_3^+,

$\alpha = 3.7 \times 10^{-7}(300/T)^{0.76}$ cm^{3}s^{-1}, and the fact that its main dissociation channel involves the formation of CF$_2$ demonstrates that such reactions are crucial processes in fluorocarbon plasma chemistry.

The results presented in the thesis have been published or are going to be published in papers and proceedings of conferences listed in appendix A.

LIST OF PUBLICATIONS

A.1 Papers related to this thesis

The list of author's papers discussing results presented in this thesis published in journals and in proceedings of conferences.

Chapter 3 - *DR* of Hydrogen and Deuterium Ions

I. **Recombination in deuterium plasma at cryogenic temperatures (down to 130 K)**
O. Novotny, J. Glosik, A. Pysanenko, P. Zakouril, R. Plasil, M. Tichy
12th *International Congress on Plasma Physics (ICPP)*, http://hal.ccsd.cnrs.fr/ccsd-00002040, CNRS ccsd, Nice (France), 25-29 October 2004

II. **The Recombination of D_3^+ and D_5^+ Ions with Electrons in a Deuterium Containing Plasma: Partial Pressure and Temperature Dependence**
O. Novotny, R. Plasil, A. Pysanenko, J. Glosik
WDS 2004, Proc. WDS'04, Ed. J. Šafránková, 401-406, Matfyzpress, Prague, 2004

III. **The recombination in deuterium containing plasma at temperatures 130 - 300 K**
O. Novotný, R. Plašil, P. Hlavenka, P. Macko, G. Bano, A. Pysanenko, J. Glosík
17th *International Symposium on Plasma Chemistry (ISPC)*, Abstracts and full-papers CD, Edited by J. Mostaghimi, T. W. Coyle, V. A. Pershin, H. R. Salami Jazi, paper Novot208.pdf, abstract p. 836, Toronto, Canada, August 2005

IV. **Recombination of H_3^+ in plasma - new type of recombination**
O. Novotný, I. Korolov, R. Plašil, T. Kotrik, J. Glosík
(2006), in preparation

V. **The recombination of D_3^+ and D_5^+ ions with electrons in deuterium containing plasma**
O. Novotný, R. Plašil, A. Pysanenko, J. Glosík
(2006), in preparation

Chapter 4 - Recombination of PAH ions

VI. **Recombination of polycyclic aromatic hydrocarbon photo-ions with electrons in a flowing afterglow plasma**
O. Novotný, B. Sivaraman, C. Rebrion-Rowe, D. Travers, L. Biennier, J. B. A. Mitchell and B. R. Rowe
J. Chem. Phys. **123** (2005), 104303

VII. **Measurement of the Recombination of Photoproduced PAH Ions**
O. Novotny, B. Sivaraman, C. Rebrion-Rowe, D. Travers, J. B. A. Mitchell and B. R. Rowe
Journal of Physics: Conference Series **4** (211-215), 2005

VIII. **Flowing Afterglow with Photo Ions - FLAPI**
O. Novotný, C. Rebrion-Rowe, D. Travers, L. Biennier, J. B. A. Mitchell, B. R. Rowe and B. Sivaraman
WDS 2005, Proc. WDS05, Ed. J. Šafránková, 377-382, Matfyzpress, Prague, 2005

IX. **Laboratory Measurements of the Recombination of PAH Ions with Electrons: Implications for the PAH Charge State in Interstellar Clouds**
L. Biennier, M. Alsayed-Ali, A. Foutel-Richard, O. Novotny, S. Carles, C. Rebrion-Rowe and B. Rowe
Faraday Discuss. (2005), submitted

Chapter 5 - DR of Rare Gas Hydride Ions

X. **Dissociative recombination of rare gas hydride ions: II. ArH$^+$**
J. B. A. Mitchell, O. Novotny, J. L. LeGarrec, A. Florescu-Mitchell, C. Rebrion-Rowe, A. V. Stolyarov, M. S. Child, A. Svendsen, M. A. El Ghazaly and L. H. Andersen
J. Phys. B: At. Mol. Opt. Phys. **38 No 10** (2005), L175-L181

XI. **Dissociative recombination of rare gas hydride ions: I. NeH$^+$**
J. B. A. Mitchell, O. Novotny, G. Angelova, J. L. LeGarrec, C. Rebrion-Rowe, A.Svendsen, L. H. Andersen, A. I. Florescu-Mitchell and A. E. Orel
J. Phys. B: At. Mol. Opt. Phys. **38 No 6** (2005), 693-703

Chapter 6 - DR of Fluorocarbon Ions

XII. **The Dissociative Recombination of Fluorocarbon Ions. II: CF$^+$**
O. Novotny, J. B. A. Mitchell, J. L. LeGarrec, A. I. Florescu-Mitchell, C. Rebrion-Rowe, A. Svendsen, M. A. El Ghazaly, L. H. Andersen, A. Ehlerding, A. A. Viggiano, F. Hellberg, R. D. Thomas, V. Zhaunerchyk, W. D. Geppert, H. Montaigne, M. Kaminska, F. Österdahl, and M. Larsson
J. Phys. B: At. Mol. Opt. Phys. **38 No 10** (2005), 1471-1482

XIII. **The dissociative recombination of fluorocarbon ions. III: CF$_2^+$ and CF$_3^+$**
A. Ehlerding, A. A. Viggiano, F. Hellberg, R. D. Thomas, V. Zhaunerchyk, W. D. Geppert, H. Montaigne, M. Kaminska, F. Österdahl, M. af Ugglas, M. Larsson, O. Novotny, J. B. A. Mitchell, J. L. LeGarrec, A. I. Florescu-Mitchell, C. Rebrion-Rowe, A. Svendsen, M. A. El Ghazaly and L. H. Andersen
J. Phys. B: At. Mol. Opt. Phys. (2005), submitted

A.2   Papers in journals

The full list of author's papers published in journals.

I. **Recombination of H_3^+ and H_5^+ ions with electrons in He-Ar-H_2 flowing afterglow plasma**
A. Pysanenko, O. Novotný, P. Zakouřil, R. Plašil, V. Poterya, J. Glosík
Czechoslovak J. Phys. **52** (2002), D681-694

II. **The recombination of H_3^+ and H_5^+ ions with electrons in hydrogen plasma: Dependence on temperature and on pressure of H_2**
J. Glosík, O. Novotný, A. Pysanenko, P. Zakouřil, R. Plašil, P. Kudrna, V. Poterya
Plasma Source Science & Technology **12** (2003), S117-S122

III. **An enhanced cosmic-ray flux towards ζ Persei inferred from a laboratory study of the $H_3^+- e^-$ recombination rate**
B. J. McCall , A. J. Huneycutt, R. J. Saykally, T. R. Geballe, N. Djuric, G. H. Dunn, J. Semaniak, O. Novotny, A. Al-Khalili, A. Ehlerding, F. Hellberg, S. Kalhori, A. Neau, R. Thomas, F. Österdahl, M. Larsson
NATURE **422: 6931** (2003), 500-502

IV. **Resonant ion-pair formation in electron collisions with rovibrationally cold H_3^+**
S. Kalhori, A. Al-Khalili, A. Neau, R. Thomas, A. Ehlerding, F. Hellberg, M. Larsson, A. Larson, A. J. Honeycutt, N. Djuric, G. H. Dunn, J. Semaniak, O. Novotny, A. Paal, F. Österdahl and A. E. Orel
Phys. Rev. A **69** (2004), 022713

V. **Branching Ratios for the Dissociative Recombination of Hydrocarbon Ions. III: The Cases of $C_3H_n^+$ (n=1-9)**
G. Angelova , O. Novotny, J. B. A. Mitchell, J.L. Le Garrec, C. Rebrion-Rowe, L. H. Andersen, H. Bluhme, A. Swendsen and L. H. Andersen
Int. J. Mass Spec. **235** (2004), 7-13

VI. **Branching Ratios for the Dissociative Recombination of Hydrocarbon Ions. II: The Cases of $C_4H_n^+$ (n=1-9)**
G. Angelova , O. Novotny, J. B. A. Mitchell, C. Rebrion-Rowe, J. L. Le Garrec, H. Bluhme, K. Seiersen and L.H. Andersen
Int. J. Mass Spec. **232** (2004), 195-203

VII. **First observation of four-body breakup in electron recombination: $C_2D_5^+$**
W. Geppert, A. Ehlerding, F. Hellberg, S. Kalhori, R. D. Thomas, O. Novotny, S. T. Arnold, T.M. Miller, A. A. Viggiano, M. Larsson
Phys. Rev. Lett. **93** (2004), 153201

VIII. **The dissociative recombination of CF_3^+**
G. Angelova, J. L. LeGarrec, C. Rebrion-Rowe, B. R. Rowe, O. Novotny, J. B. A. Mitchell
J. Phys. B: At. Mol. Opt. Phys. **37** (2004), 41354141

IX. **Dissociative recombination of rotationally cold H_3^+**
B. J. McCall, A. J. Huneycutt, R. J. Saykally, N. Djuric, G. H. Dunn, J. Semaniak, O. Novotny, A. Al-Khalili, A. Ehlerding, F. Hellberg, S. Kalhori, A. Neau, R. D. Thomas, A. Paal, F. Österdahl, M. Larsson
Phys. Rev. A **70** (2004), 052716

X. **Dissociative recombination of rare gas hydride ions: I. NeH^+**
J. B. A. Mitchell, O. Novotny, G. Angelova, J. L. LeGarrec, C. Rebrion-Rowe, A. Svendsen, L. H. Andersen, A. I. Florescu-Mitchell and A. E. Orel
J. Phys. B: At. Mol. Opt. Phys. **38 No 6** (2005), 693-703

XI. **Dissociative recombination of rare gas hydride ions: II. ArH$^+$**
J. B. A. Mitchell, O. Novotny, J. L. LeGarrec, A. Florescu-Mitchell, C. Rebrion-Rowe, A. V. Stolyarov, M. S. Child, A. Svendsen, M. A. El Ghazaly and L. H. Andersen
J. Phys. B: At. Mol. Opt. Phys. **38 No 10** (2005), L175-L181

XII. **The Dissociative Recombination of Fluorocarbon Ions. II: CF$^+$**
O. Novotny, J. B. A. Mitchell, J. L. LeGarrec, A. I. Florescu-Mitchell, C. Rebrion-Rowe, A. Svendsen, M. A. El Ghazaly, L. H. Andersen, A. Ehlerding, A. A. Viggiano, F. Hellberg, R. D. Thomas, V. Zhaunerchyk, W. D. Geppert, H. Montaigne, M. Kaminska, F. Österdahl, and M. Larsson
J. Phys. B: At. Mol. Opt. Phys. **38 No 10** (2005), 1471-1482

XIII. **Branching ratios for the dissociative recombination of hydrocarbon ions**
J. B. A. Mitchell, G. Angelova, C. Rebrion-Rowe, O. Novotny, J. L. Le Garrec, H. Bluhme, K. Seiersen, A. Svendsen and L. H. Andersen
Journal of Physics: Conference Series **4** (198-204), 2005

XIV. **Recombination studies in a He-Ar-H$_2$ plasma**
J. Glosík, R. Plašil, A. Pysanenko, O. Novotný, P. Hlavenka, P. Macko and G. Bánó
Journal of Physics: Conference Series **4** (104-110), 2005

XV. **Storage ring measurements of the dissociative recombination rate of rotationally cold H$_3^+$**
B. J. McCall, A. J. Huneycutt, R. J. Saykally, N. Djuric, G. H. Dunn, J. Semaniak, O. Novotny, A. Al-Khalili, A. Ehlerding, F. Hellberg, S. Kalhori, A. Neau, R. D. Thomas, A. Paal, F. Österdahl, M. Larsson
Journal of Physics: Conference Series **4** (92-97), 2005

XVI. **Measurement of the Recombination of Photoproduced PAH Ions**
O. Novotny, B. Sivaraman, C. Rebrion-Rowe, D. Travers, J.B.A. Mitchell and B.R. Rowe
Journal of Physics: Conference Series **4** (211-215), 2005

XVII. **Rate constants and branching ratios for the dissociative recombination of C$_3$D$_7^+$ and C$_4$D$_9^+$**
M. Larsson, A. Ehlerding, W. D. Geppert, F. Hellberg, S. Kalhori, R. D. Thomas, N. Djuric, F. Österdahl, G. Angelova, J. Semaniak, O. Novotny, S. T. Arnold and A. A. Viggiano
J. Chem. Phys. **122** (2005), 156101

XVIII. **Recombination of polycyclic aromatic hydrocarbon photo-ions with electrons in a flowing afterglow plasma**
O. Novotný, B. Sivaraman, C. Rebrion-Rowe, D. Travers, L. Biennier, J. B. A. Mitchell and B. R. Rowe
J. Chem. Phys. **123** (2005), 104303

XIX. **The dissociative recombination of fluorocarbon ions. III: CF$_2^+$ and CF$_3^+$**
A. Ehlerding, A. A. Viggiano, F. Hellberg, R. D. Thomas, V. Zhaunerchyk, W. D. Geppert, H. Montaigne, M. Kaminska, F. Österdahl, M. af Ugglas, M. Larsson, O. Novotny, J. B. A. Mitchell, J. L. LeGarrec, A. I. Florescu-Mitchell, C. Rebrion-Rowe, A. Svendsen, M. A. El Ghazaly and L. H. Andersen
J. Phys. B: At. Mol. Opt. Phys. (2005), submitted

XX. **Laboratory Measurements of the Recombination of PAH Ions with Electrons: Implications for the PAH Charge State in Interstellar Clouds**
L. Biennier, M. Alsayed-Ali, A. Foutel-Richard, O. Novotny, S. Carles, C. Rebrion-Rowe and B. Rowe
Faraday Discuss. (2005), submitted

XXI. **Branching Ratios for the Dissociative Recombination of (CH$_3$)$_3$N$^+$**
G. Angelova, O. Novotny, J. B. A. Mitchell, C. Rebrion-Rowe, J. L. Le Garrec, A. Svendsen and L. H. Andersen
(2005), in preparation

XXII. **Recombination of H_3^+ in plasma - new type of recombination**
O. Novotný, I. Korolov, R. Plašil, T. Kotrik, J. Glosík
(2006), in preparation

XXIII. **The recombination of D_3^+ and D_5^+ ions with electrons in deuterium containing plasma**
O. Novotný, R. Plašil, A. Pysanenko, J. Glosík
(2006), in preparation

A.3 Proceedings of conferences

The full list of author's papers published in proceedings of conferences with more than 2 pages of length.

I. **Study of the recombination of D_3^+ and D_5^+ ions with electrons in He-Ar-D_2 flowing afterglow plasma**
A. Pysanenko, P. Zakouřil, O. Novotný, V. Poterya, R. Plašil, J. Glosík
WDS 2002, Proc. WDS'02, Part II, Ed. J. Šafránková, pp. 407-411, Matfyzpress, Prague, 2002

II. **Application of Langmuir probe for study of recombination of D_3^+ ions with electrons in He-Ar-D_2 stationary and flowing afterglow plasma**
M. Tichý, V. Poterya, R. Plašil, A. Pysanenko, P. Kudrna, O. Novotny, P. Zakouril, J. Glosík
XI International Congress on Plasma Physics - ICPP 2002, AIP Conference Proceedings **669, Issue 1**, pp. 60-63, Sydney, Australia, June 11 2003

III. **The recombination of D_3^+ and D_5^+ - Dependence on partial pressure of D_2 and on temperature**
J. Glosik, A. Pysanenko, O. Novotny, P. Zakouril, R. Plasil, V. Poterya
16th International Symposium on Plasma Chemistry (ISPC), Abstracts and full-papers CD, CD - ISPC-253.pdf, abstract p93, pp.1-6, Taormina, Italy, June 22-27 2003

IV. **The study of ion recombination in a flowing afterglow - FALP**
O. Novotny, A. Pysanenko, R. Plasil, J. Glosik
WDS 2003, Proc. WDS'03, Ed. J. Šafránková, 446-451, Matfyzpress, Prague, 2003

V. **Study of recombination in a hydrogen dominated plasma**
A. Pysanenko, R. Plasil, O. Novotny, P. Hlavenka, P. Kudrna, J. Glosik
WDS 2003, Proc. WDS'03, Ed. J. Šafránková, 452-455, Matfyzpress, Prague, 2003

VI. **Recombination in deuterium plasma at cryogenic temperatures (down to 130 K)**
O. Novotny, J. Glosik, A. Pysanenko, P. Zakouril, R. Plasil, M. Tichy
12th International Congress on Plasma Physics (ICPP), http://hal.ccsd.cnrs.fr/ccsd-00002040, CNRS ccsd, Nice (France), 25-29 October 2004

VII. **The Recombination of D_3^+ and D_5^+ Ions with Electrons in a Deuterium Containing Plasma: Partial Pressure and Temperature Dependence**
O. Novotny, R. Plasil, A. Pysanenko, J. Glosik
WDS 2004, Proc. WDS'04, Ed. J. Šafránková, 401-406, Matfyzpress, Prague, 2004

VIII. **The recombination in deuterium containing plasma at temperatures 130 - 300 K**
O. Novotný, R. Plašil, P. Hlavenka, P. Macko, G. Bano, A. Pysanenko, J. Glosík
17th International Symposium on Plasma Chemistry (ISPC), Abstracts and full-papers CD, Edited by J. Mostaghimi, T. W. Coyle, V. A. Pershin, H. R. Salami Jazi, paper Novot208.pdf, abstract p. 836, Toronto, Canada, August 2005

IX. **Flowing Afterglow with Photo Ions - FLAPI**
O. Novotný, C. Rebrion-Rowe, D. Travers, L. Biennier, J. B. A. Mitchell, B. R. Rowe and B. Sivaraman
WDS 2005, Proc. WDS05, Ed. J. Šafránková, 377-382, Matfyzpress, Prague, 2005

X. **Recombination of HCNH$^+$. Calculation of Kinetics of HCNH$^+$ Formation in Flowing Afteglow**
I. Korolov, O. Novotny, P. Hlavenka, R.Plasil, and J. Glosik
WDS 2005, Proc. WDS05, Ed. J. Šafránková, 347-352, Matfyzpress, Prague, 2005

A.4 Presentations

The list of author's presentations: posters and talks.

I. **Storage ring study of DR of $C_2H_5^+$ and FALP studies of recombination of H_3^+ and D_3^+**
O. Novotny
3rd ETR meeting, Lovian la Neuve, Belgium, November 2002, *talk*

II. **The study of ion recombination in a flowing afterglow - FALP**
O. Novotny, A. Pysanenko, R. Plasil, J. Glosik:
WDS 2003, Prague, Czech Republic, June 2003, *talk*

III. **Branching ratios for the Dissociative Recombination of Hydrocarbon Ions**
G. Angelova, J. B. A. Mitchell, C. Rebrion-Rowe, J. L. Le Garrec, O. Novotny, H. Bluhme, K. Seiersen, and L.H. Andersen
4th ETR meeting, London, United Kingdom, September 2003, *poster*

IV. **The recombination of D_3^+ and D_5^+ ions with electrons in a deuterium containing plasma: Partial pressure and temperature dependence**
O. Novotny, R. Plasil, A. Pysanenko and J. Glosik
WDS 2004, Prague, Czech Republic, June 2004, *poster*

V. **Recombination in a deuterium containing plasma - Partial pressure and temperature dependence**
O. Novotný, R. Plašil, A. Pysanenko, J. Glosík
8th European Conference on Atomic and Molecular Physics (ECAMP VIII), Rennes, France, July 2004, *poster*

VI. **Measurement of the Recombination of Photoproduced PAH Ions**
O. Novotny, B. Sivaraman, C. Rebrion-Rowe, D. Travers, J.B.A. Mitchell and B.R. Rowe
6th International Conference on Dissociative Recombination: Theory, Experiments and Applications, Mosbach, Germany, July 2004, *poster*

VII. **The Recombination of D_3^+ and D_5^+ Ions with Electrons in Deuterium Containing Plasma**
O. Novotny, R. Plasil, A. Pysanenko, J. Glosik
15th Symposium on Applications of Plasma Processes, 3rd EU-Japan Joint Symposium on Plasma Processing (SAPP XV), Podbanské, Slovakia, January 15-20, 2005, *poster*

VIII. **Flowing Afterglow with Photo Ions - FLAPI**
O. Novotný, C. Rebrion-Rowe, D. Travers, L. Biennier, J. B. A. Mitchell, B. R. Rowe and B. Sivaraman
Week of Doctoral Students 2005 (WDS), Prague, Czech Republic, June 2005, *poster*

IX. **The recombination in deuterium containing plasma at temperatures 130 - 300 K**
O. Novotný, R. Plašil, P. Hlavenka, P. Macko, G. Bano, A. Pysanenko, J. Glosík
17th International Symposium on Plasma Chemistry (ISPC), Toronto, Canada, August 7-12 2005, *poster*

X. **The recombination of Polycyclic Aromatic Hydrocarbons with electrons**
O. Novotný
Seminar of Atomic and Molecular Physics at the MPI-K Test Storage Ring Group, Max-Planck-Institut fr Kernphysik, Heidelberg, Germany, 13th September 2005, *talk*

A.5   Other publications

I. **Studium elektron-iontové a iont-iontové rekombinace**
The study of electron-ion and ion-ion recombination
O. Novotný
Faculty of Mathematics and Physics, Charles University, Prague (2002), Diploma work

LANGMUIR PROBE

B.1 Theory

The *Langmuir probe* (LP) is the favored diagnostic tool for the determination of the concentration of charged particles in flowing afterglow techniques. Its popularity is given mainly by its local measurement range and by its simple realization. The probe (a tiny wire) is placed in a plasma and the voltage-current (IV) characteristic (also called the "probe characteristic") of the system probe–plasma–chamber yields information about several local plasma parameters including the concentration of charged particles. The basic theory linking the shape of the probe characteristic and the required plasma parameters was developed by *Irving Langmuir* [271–273] and later several other authors have improved the theory. An interesting overview of the technique is given in [274].

Generally speaking, the LP can be used for the determination of electron density as well as for ion density. In this work the LP was used only for electron density measurements and therefore further discussion concentrates on this parameter only.

In order to the determine accurately electron number density n_e, it is necessary that the presence of the probe does not perturb n_e at the distance of about one mean free path length l_e from the probe. It means that l_e must exceed the characteristic size of the probe r_p (the diameter in the case of a cylindrical probe). Another requirement is the "smallness" of the size of the space-charge layer, λ_D, in comparison with l_e. These quantities are given by

$$l_e = \frac{1}{N\sigma}, \tag{B.1}$$

$$\lambda_D = \sqrt{\frac{\epsilon_0 k_B T_e}{q^2 n_e}}, \tag{B.2}$$

where N is the concentration of neutrals, σ the cross section for electron-neutral collisions, ϵ_0 is dielectric permittivity of vacuum, k_B the Boltzmann constant, q the elementary charge and T_e the electron temperature.

When the potential V applied to the probe is equal to the plasma potential V_p, the current to the probe is formed mainly by electrons as their velocities are (in equilibrium) much higher than the velocities of heavy ions. The measured current I_p at $V = V_p$ is then proportional to the electron number concentration n_e, the probe surface area A and the mean velocity of the electrons $\overline{v}_e$:

$$I_p = A\,q\,n_e\,\overline{v}_e/4, \tag{B.3}$$

where

$$\overline{v}_e = \sqrt{\frac{8k_B T_e}{\pi m_e}}, \tag{B.4}$$

and m_e is the electron mass. In principle, formula B.3 can be directly used for the determination of n_e. The necessity however, of knowing T_e, possible influences of the ion current and the need to make a precise determination of the current at one point on the LP characteristics[1] may complicate the analysis.

More accurate values of n_e can be obtained from the slope of a linear plot of I^2 versus V in the accelerating region of the LP characteristic:

$$I^2 = \frac{2A^2 q^2 n_e^2}{\pi^2 m_e}[k_B T_e + q(V - V_p)] \tag{B.5}$$

n_e is then simply determined without the need for an accurate value of V_p and T_e as

$$n_e = \sqrt{\frac{\pi^2 m_e}{2A^2 q^3}} S, \tag{B.6}$$

where S is the slope of the linear plot of I^2 versus V. This method is often called the *i-squared* method.

LP is also often used to determine the electron energy distribution function $f(E)$. Collisionless theory predicts that the second derivative of the electron current to a probe in the retarding region[2] of the probe characteristic is proportional to $f(E)$:

$$\frac{d^2 I}{d(V - V_p)^2} = \frac{1}{4} A q^2 \sqrt{\frac{2q}{m_e(V - V_p)}} [f(E)], \tag{B.7}$$

where $E = -q(V - V_p)$. The general equation can be easily applied to the particular case of a Maxwellian distribution function, which is

$$\frac{d^2 I}{d(V - V_p)^2} = \frac{1}{4} A q^3 \sqrt{2\pi m_e} (k_B T_e)^{-3/2} \exp\left[-\frac{q(V - V_p)}{k_B T_e}\right]. \tag{B.8}$$

Thus, in a thermalised plasma, a plot of $\ln(d^2 I / dV^2)$ versus V will be linear and the slope of the line will provide a value for T_e.

Examples of LP characteristics and basic analysis are given in figures B.1 and B.2.

B.2 Implementation

Considering the l_e, λ_D, and r_p parameters we can check whether the above mentioned restrictions are valid for our experimental conditions in the FALP-VT and the *FlAPI* apparates. Table B.2 summarizes calculated parameters for typical experimental conditions in both experiments.

---

[1]Precise determination of V_p and I_p is difficult due to "surface effects": The surface properties (e.g. the thickness of the surface layer and contact potentials respectively) may change along the probe. Then measured probe characteristics can be interpreted as an integral of several characteristics with a shifted V_p due to different properties of the measurement loop. The characteristic so obtained is "smoothed" and the absolute value of I_p may in particular be affected.

[2]The region where V is negative in respect to V_p and electrons, which would normally hit the probe, are decelerated or deflected.

Experiment	r_p [mm]	N [cm^{-3}]	n_e [cm^{-3}]	l_e [mm]	λ_D [mm]
FALP-VT	0.014	4×10^{17}	10^{10}	0.040	0.012
FlAPI	0.025	2×10^{16}	10^9	0.8	0.038

Table B.1: Parameters of the measurement with the LP in the FALP-VT and FlAPI experiments. In both cases cylindrical probes are used and for the characteristic dimension r_p, the diameter of the probe is taken. In equations B.1 and B.2 the following parameters were used: $T_e = 300$ K, $\sigma = 6 \times 10^{-20}$ m^2 [275].

It can be seen, that in the case of the *FlAPI*, both conditions $l_e \gg r_p$ and $l_e \gg \lambda_D$ are fulfilled. In the case of the FALP-VT, however, the dominance of l_e is not so convincing and the probe probably works in the *transitional mode*[3] where Langmuir theory is not fully valid. There are other extended theories which cover the *collisional mode* of the LP [276–278]. It was shown several times, however, that the simple *i-squared* method gives acceptable results also for the *transitional mode* and most authors prefer its simplicity over the slightly higher precision of more complicated methods. For details see comparative studies [279–282].

The *i-squared* method is even more acceptable when calibrated. This is usually performed by comparison of the measured and a tabulated recombination rate coefficient for the studied ion. From equation 2.9, it is obvious that the analysed recombination rate coefficient α is proportional to the absolute measured value of n_e. O_2^+ is often used as a test ion as its recombination rate is stable over a wide range of pressures and is well known over a wide range of temperatures [55]:

$$\alpha(O_2^+) = 2.0 \times 10^{-7}(300/T^{0.65}) \text{ cm}^3\text{s}^{-1}. \tag{B.9}$$

From the ratio of the tabulated value and the measured value, a correction factor is obtained which is then applied to multiply the measured electron density values or could be used to directly correct the final rate coefficients.

In an afterglow, the LP surface often gets coated by species in the environment and this can significantly change parameters of its surface and thus also the final LP characteristic. In order to maintain the quality of the surface, the LP is cleaned by bombardment with positive ions: between individual measurements, the probe potential is set to ~ -60 V for ~ 100 ms where the current is limited by a safety resistor to 2 mA.

In the *FlAPI*, the deposition PAHs is extremely intensive. For this reason, a continuously heated probe [54] previously developed for measurement with PAHs in the FALP-MS, was employed. The probe in this case is not a single wire but a loop. The current in the loop is maintained at ~ 80 μA by an accumulator. The potential of the whole loop is then scanned over the required range of LP characteristics. The probe is moreover cleaned by ion bombardment between measurements.

---

[3]The transitional mode is defined between the collisionless mode, where electrons do not collide in the space charge layer close to the probe, and the collisional mode, where collisions close to the probe significantly affect the flux to the probe and the measured current differs from that predicted by Langmuir theory.
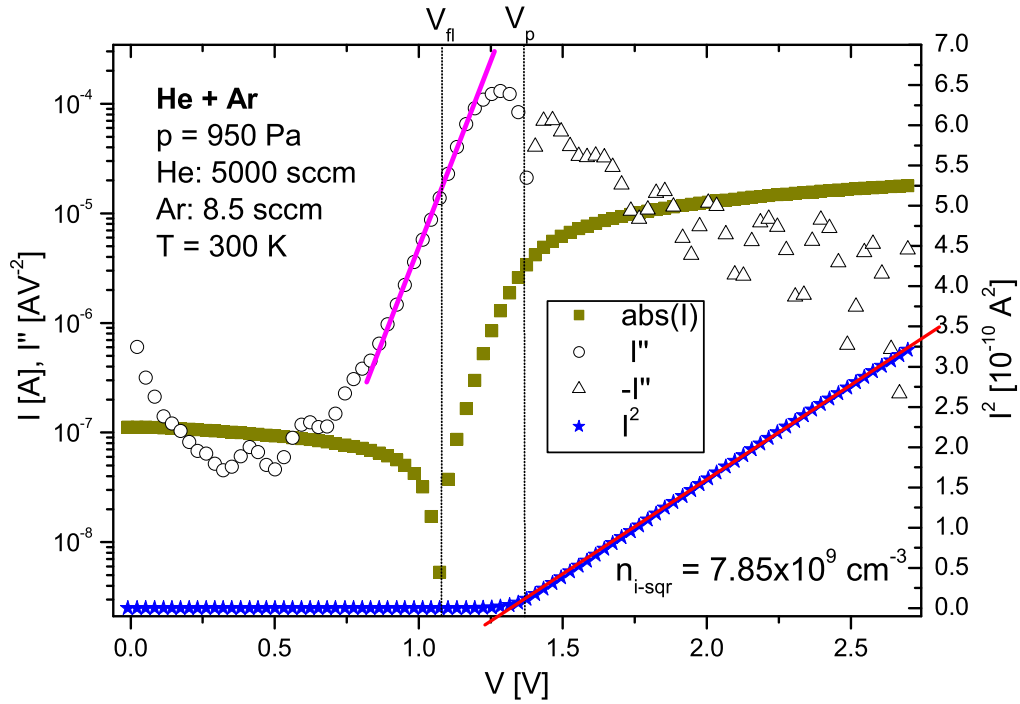
Figure B.1: An example of the LP characteristic in a He-Ar plasma. From the slope of I^2, n_e is obtained by applying equation B.6. The second derivative of I is marked by different symbols for its negative and positive parts where the exponential region gives information on the EEDF and T_e.
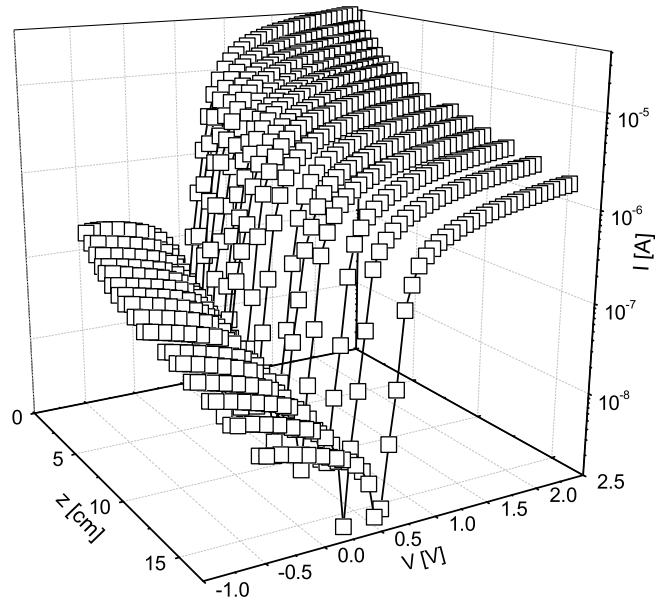

Figure B.2: An example of the evolution of the LP characteristic as a function of probe position z along the flowtube measured in a He-Ar-H_2 plasma.

BRANCHING RATIOS

C.1 Mathematical treatment and error analysis

This section is an extension of section 2.4.6.

The solution of the set of equations 2.38 is treated as a *General Linear Least Squares* fitting problem [168]. Equations 2.38 describe the physical model which is used for fitting the data points, obtained as peak areas from the pulse height spectrum. The method is based on minimizing the sum of squared differences between data points and model values weighted by errors in the data points.

$$n(p) = \sum_{c=1}^{C} m_c \, T_c(p) \tag{C.1}$$

represents the set of equations 2.38 (the model), where $n(p)$ is the number of counts in peak p calculated by the model, m_c is the number of events through dissociative channel c, C is the number of channels and $T_c(p)$ is the transmission probability factor for channel c contributing to peak p (e.g. $T(1-T)^2$). The minimized quantity is called χ^2 and is obtained as

$$\chi^2 = \sum_{i=1}^{P} \left[\frac{n_i - n(p_i)}{\sigma_i} \right]^2 = \sum_{i=1}^{P} \left[\frac{n_i - \sum_{c=1}^{C} m_c \, T_c(p_i)}{\sigma_i} \right]^2 , \tag{C.2}$$

where P is the number of data points (peaks), n_i are data points (peak areas) and σ_i are the errors for those data points. Normally, statistical errors arising from the counting nature of the measurement are used as input errors. The peak area error in the measured spectrum (background not yet subtracted) is obtained as the square root of the number of events in this peak[1].

As equation C.2 is linear[2] in parameters m_c, it can be solved analytically using the *Singular Value Decomposition* (SVD) method , which is not iterative and so there is no risk to obtain the local minimum only. For details see *Numerical Recipes* [168]. As a result, the vector m and appropriate covariance matrix $\mathbf{S}$ is extracted, where diagonal terms of $\mathbf{S}$ describes the variances σ^2 of vector m and non-diagonal terms give the linear correlation between particular m_i and m_j as $\mathbf{S}_{ij}/\sigma_i\sigma_j$. Correlation factors are important e.g. for the normalization of the number of events in a particular channel m_i to branching ratio via eq. 2.39. As m_i are usually not independent, the general formula for the error calculation of the

---

[1]This result comes from Poisson statistics, see [66].
[2]There are no terms with multiplication of different m_c.

result has to be used:

$$\sigma_f = \sqrt{\sum_{j=1}^{N} \sum_{i=1}^{N} \frac{\partial f}{\partial a_i} \frac{\partial f}{\partial a_j} \mathbf{S}_{ij}} \tag{C.3}$$

where σ_f is an error of quantity f described as $f = f(a_i)$ with parameters a_i.

In the case of more than one grid used in the branching ratio measurement, the calculation may be done at one jump putting equations 2.38 for particular grids together. However, this is possible only in the case of the same total number of dissociation events measured for each grid. In another words: the beam intensity has to be stable and the measurement time has to be constant for measurements on all grids. If it is not the case, the calculation is done first independently for each grid obtaining the total number of events for each measurement. Then the number of events in all peaks can be normalized to a chosen value (e.g. 1) and the final calculation is treated on the full set of equations using all data from measurements on all grids.

The error in the branching ratios arising from statistical errors of $n(p)$ only is directly obtained using the covariance matrix $\mathbf{S}$ and eq. C.3. However, the input error of n_i may be also of origins other than statistical error and the procedure does not take into account the uncertainty of the grid transmission T. The latter influence may be tested by using several values of T within the expected error and observing the effect on the final branching ratios.

Another possibility is to examine the minimized value of χ^2 calculated for final values of m. This value should follow the so-called χ^2-distribution (see e.g. [283]). The mean value of this distribution is equal to the number of degrees of freedom ν in the solved problem[3]. The so obtained value of χ^2 should be close to ν. Quantification of the fit quality is done by the so-called χ^2-test, which evaluates the probability, that any other set of data will have a worse fit (higher χ^2) than the current fit[4]. Generally the accepted value for a "good fit" is the value 0.1.

Obtaining a "bad fit" may have two reasons: the model used is not appropriate for the measured data or the input errors are not correct. Since we are usually not able to build a better model and we do not know the real behavior of the input errors, an alternative method of obtaining the "good fit" is employed: all input errors are increased by multiplying by the same factor, until the expected value of χ^2 is reached. This trick is frequently used in fitting procedures in commercial programs (e.g. Origin). It should be noted, that the described procedure works only for normally distributed data and should be applied to large data sets. However, at least certain information on the quality of the result is obtained.

---

[3]Number of data points minus number of parameters.
[4]Complementary incomplete gamma function gives χ^2-test value. See e.g. [168]

C.2   Calculation of maximal kinetic energy release

Let us consider the dissociative recombination reaction of ions A^+ with electrons giving products B and C:

$$A^+ + e^- = B + C + E_k \tag{C.4}$$

where E_k is the total kinetic energy of the fragments with respect to the center of mass. The maximum value of E_k is obtained as

$$E_k = E_{fr} - E_{fp} \tag{C.5}$$

where E_{fp} and E_{fr} are the enthalpies of formation of products and reactants respectively. A negative E_k shows that the reaction as impossible – the reaction will not proceed. However, a positive value does not guarantee the reaction will proceed because a significant amount of energy may be stored in internal states of the products. Particular enthalpies are calculated as

$$E_{fp} = E_f(B) + E_f(C) \tag{C.6}$$

where $E_f(B)$ and $E_f(C)$ are enthalpies of formation for particular products. For reactants E_{fr} is calculated from the enthalpy of formation of the neutral molecule $E_f(A)$ and it's ionization energy $E_i(A)$

$$E_{fr} = E_f(A) + E_i(A) \tag{C.7}$$

Required enthalpies was generally obtained from *NIST database* [223], where the enthalpy of formation is marked as $\Delta_f H^0$.

Useful conversion relation: 1 eV = 96.487 kJ/mol

BIBLIOGRAPHY

[1] J. E. Dyson and D. A. williams: *The physics of the interstellar medium*, Institute of Physics Publishing, 2nd edition 1997

[2] S. Kalhori, A. Al-Khalili, A. Neau, R. Thomas, A. Ehlerding, F. Hellberg, M. Larsson, A. Larson, A. J. Honeycutt, N. Djuric, G. H. Dunn, J. Semaniak, O. Novotny, A. Paal, F. Österdahl and A. E. Orel: *Phys. Rev. A* **69** (2004), 022713

[3] A. Neau: *PhD Thesis*, Molecular Physics Division, Dep. of Physics, Univ. of Stockholm, Sweden 2002

[4] J. Kaplan: *Phys. Rev.* **38(5)** (1931), 1048-1051

[5] H. S. W. Massey: *Proc. Roy. Soc. A* **163** (1937), 542-553

[6] E. V. Appleton: *Proc. Roy. Soc. A* **162** (1937), 451-479

[7] J. von Neumann and E. Wigner: *Physik Z.* **30** (1929), 467

[8] D. R. Bates: *Phys. Rev.* **78** (1950), 492

[9] D. R. Bates and H. S. W. Massey: *Proc. Roy. Soc. A* **187** (1947), 261

[10] J. N. Bardsley: *J. Phys. B* **1** (1968), 349

[11] A. J. Cunningham and R. M. Hobson: *Phys. Rev.* **185** (1969), 98

[12] J. N. Bardsley: *J. Phys. B* **1** (1968), 365

[13] T. F. O'Maley: *Adv. At. Mol. Phys.* **7** (1971), 223-249

[14] T. F. O'Maley: *Dissociative Recombination: Theory, Experiment and Applications*, ed. by J. B. A. Mitchell, S. L. Guberman, Singapore: World Scientific 1989, p. 25

[15] F. B. Yousif and J. B. A. Mitchell: *Phys. Rev. A* **40** (1989), 4318

[16] H. H. Michels: *Dissociative Recombination: Theory, Experiment and Applications*, ed. by J. B. A. Mitchell and S. L. Guberman, Singapore: World Scientific 1989, p 97

[17] F. B. Yousif, J. B. A. Mitchell, M. Rogelstad, A. LePadellec, A. Canosa A and M. I. Chibisov: *Phys. Rev. A* **49** (1994), 4610

[18] C. Strömholm, J. Semaniak, S. Rosen, H. Danared, S. Datz,W. van der Zande and M. Larsson: *Phys. Rev. A* **54** (1996), 3086

[19] A. Al-Khalili, H. Danared, M. Larsson, A. LePadellec, R. Peverall, S. Rosen, J. Semaniak, M. af Ugglas, L. Vikor and W. van der Zande: *Hyperfine Interact.* **114** (1998), 281

[20] G. Sundstrom, S. Datz, J. R. Mowat, S. Mannervik, L. Brostrom, M. Carlsson, H. Danared and M. Larsson: *Phys. Rev. A* **50** (1994), R2806

[21] T. Tanabe, I. Katayama, N. Inoue, K. Chida, Y. Arakaki, T. Watanabe, M. Yoshizawa, S. Ohtani and K. Noda: *Phys. Rev. Lett.* **70** (1993), 422

[22] T. Tanabe, I. Katayama, S. Ono, K. Chida, T. Watanabe, Y. Arakaki, Y. Haruyama, M. Saito, T. Odagiri, K. Hosono, K. Noda, T. Honma and H. Takagi: *J. Phys. B: At. Mol. Opt. Phys.* **31** (1998), L297-L303

[23] T. Tanabe, I. Katayama, S. Ono, K. Chida, T. Watanabe, Y. Arakaki, Y. Haruyama, M. Saito, T. Odagiri, K. Hosono, K. Noda, T. Honma and H. Takagi: *J. Phys. B: At. Mol. Opt. Phys.* **32** (1999), 5221 (corrigendum)

[24] S. L. Guberman: *Phys. Rev. A* **49** (1994), R4277

[25] B. K. Sarpal, J. tennyson and L. A. Morgan: *J. Phys. B* **27** (1994), 5943

[26] M. Born and R. Oppenheimer: *Ann. Phys.* **84** (1927), 457

[27] A. E. Orel, K. C. Kulander and T. N. Rescigno: *Phys. Rev. Lett.* **74** (1995), 4807

[28] H. Takagi: *Phys. Rev. A* **70** (2004), 022709

[29] Å. Larson and A. E. Orel: *Phys. Rev. A* **59** (1999), 3601

[30] J. B. A. Mitchell: *Atomic Processes in Electron-Ion and Ion-ion Collisions*, ed. by F. Brouillard, Plenum Press, New York 1986, p. 185

[31] D. R. Bates: *J. Phys. B* **24** (1991), 3267

[32] D. R. Bates: *J. Phys. B* **24** (1991), 703

[33] D. R. Bates: *J. Phys. B* **25** (1992), 3067

[34] J. B. A. Mitchell and C. Rebrion-Rowe: *Int. Rew. Phys. Chem.* **16 No. 2** (1997), 201-213

[35] N.G. Adams and D. Smith: *Int. J. Mass Spec. Ion Phys.* **21** (1976), 349

[36] R. Plašil, J. Glosík, V. Poterya, P. Kudrna, J. Rusz, M. Tichý, A. Pysanenko: *Int. J. Mass Spec.* **218** (2002), 105-130

[37] J. Glosík, O. Novotný, A. Pysanenko, P. Zakouřil, R. Plašil, P. Kudrna and V. Poterya: *Plasma Source Science & Technology* **12** (2003), S117-S122

[38] B. R. Rowe, J. C. Gomet, A. Canosa, C. Rebrion and J. B. A. Mitchell: *J. Chem. Phys.* **96 (2)** (1992), 15

[39] B. Peart, K. Dolder: *J. Phys. B* **7** (1974), 1948

[40] R. L. F. Boyd and G. W. Green: *Proc. Phys. Soc.* **71** (1958), 351

[41] D. Auerbach, R. Cacak, R. Caudano, T. D. Gaily, C. J. Keyser, J. Mc Gowan, J. B. A. Mitchell and S. F. J. Wilk: *J. Phys. B* **10** (1977), 3797

[42] S. M. Trujillo, R. H. Neynaber and E. W. Rothe: *Rev. Sci. Instrum.* **37** (1966), 1655

[43] F. L. Walls and G. H. Dunn: *J. Geophys. Res.* **79** (1974), pp. 1911-1915

[44] D. DeWitt, D. Schneider, M. H. Chen, M. B. Schneider, D. Church, G. Weinberg, M. Sakurai: *Phys. Rev. A* **47** (1993), R1597-R1600

[45] Q. Chen, J.M. Goodings: *Int. J. Mass Spec.* **176** (1998), 1

[46] E.E. Ferguson, F.C. Fehsenfeld and A.L. Schmeltekopf: *Adv. Atom. Mol. Phys.* **5** (1969), 1

[47] M.R. Mahdavi, J.B. Hasted, and M.M. Nakshbandi: *J. Phys. B: Atom. Molec. Phys.* **4** (1971), 1726

[48] D. Smith, N.G. Adams, A.G. Dean, and M.J. Church: *J. Phys. D.* **8** (1975), 141

[49] J. Glosík, O. Novotný, A. Pysanenko, P. Zakouřil, R. Plašil, P. Kudrna, V. Poterya: *Plasma Source Science & Technology* **12** (2003), S117-S122

[50] O. Novotný: *Studium elektron-iontové a iont-iontové rekombinace / The study of electron-ion and ion-ion recombination, Diploma work,* Faculty of Mathematics and Physics, Charles University, Prague 2002

[51] Francis F. Chen: *Introduction of Plasma Physics and Controlled Fusions - volume 1: Plasma Physics,* Plenum Press 1974

[52] W. Lindinger, A. L. Schmeltekopf, F. C. Fehsenfeld: *J. Chem. Phys.* **61** (1974), 2890

[53] Y. Ikezoe, S. Matsuoka, M. Takabe and A. A. Viggiano: *Gas Phase Ion-Molecule Reaction Rates through 1986,* Maruzen Co., Japan 1987

[54] S. Laubé, T. Mostefaoui, B. R. Rowe: *Rev. Sci. Instrum.* **71(2)** (2000), 519-521

[55] P. Spanel, L. Dittrichova, D. Smith: *Int. J. Mass Spectrom. Ion Phys.* **129** (1993), 183

[56] A. Mozumder: *J. Chem. Phys.* **72** (1980), 1657-64

[57] P. Langevin: *Ann. Chim. Phys.* **5** (1905), 245

[58] D.R. Lide: *Handbook of chemistry and physics, 74th Ed.,* CRC Press, Boca Raton 1993

[59] A. Canosa, S. Laubé, C. Rebrion, D. Pasquerault, J. C. Gomet, B. R. Rowe: *Chem. Phys. Lett.* **245** (1995), 407-414

[60] A. Léger, P. Boissel, F. X. Désert and L. d'Hendecourt: *Astron. Astrophys.* **213** (1989), 351-359

[61] K. Fujiwara, A. Harada and J. Aihara: *J. Mass Spectrom.* **31** (1996), 1216-1220

[62] L. Verstraete, A. Léger, L. d'Hendecourt, O. Dutuit, and D. Défourneau: *Astron. Astrophys.* **237** (1990), 436-444

[63] W. Paul and H. Steinwedel: *Zeitschrift fr Naturforschung* **8A** (1953), 448

[64] T. J. M. Boyd and J. J. Sanderson: *The physics of plasma*, Cambridge University Press 2003

[65] O. Novotný, B. Sivaraman, C. Rebrion-Rowe, D. Travers, L. Biennier, J. B. A. Mitchell and B. R. Rowe: *J. Chem. Phys.* **123** (2005), 104303

[66] W. R. Leo: *Techniques for Nuclear and Particle Physics Experiments*, Springer-Verlag Berlin Heilderberg 1987 1994

[67] S. P. Møller: *Proceedings of the 1991 IEEE particle accelerator conference*, San Francisco 1991, 2811

[68] J. S. Nielsen and S. P. Møller: *Proceedings from the 6th European particle acceletartor conference*, Stockholm 1998

[69] K. Seiersen: *PhD Thesis*, Dep. of Physics and Astronomy, Univ. of Aarhus, Denmark 2003

[70] H. Danared, G. Andler, L. Bagge, C. J. Herrlander, J. Hilke, J. Jeansson, A. Källberg, A. Nilsson, A. Paal, K. G. Rensfelt, U. Roséngård, J. Starker, M. af Ugglas: *Phys. Rev. Lett.* **72** (1994), 3775

[71] Z. Amitay, D. Zajfman, P. Forck: *Phys. Rev. A* **50** (1994), 2304

[72] L. Lammich, D. Strasser, H. Kreckel, M. Lange, H. B. Pedersen, S. Altevogt, V. Andrianarijaona, H. Buhr, O. Heber, P. Witte, D. Schwalm, A.Wolf, and D. Zajfman: *Phys. Rev. Lett.* **91** (2003), 143201

[73] H. Poth: *Phys. Rep.* **196** (1990), 135

[74] M. Sedlaček, H. Poth, D. Krämer, L. Tecchio, H. O. Meyer: *Phys. Script.* **T 22** (1988), 204

[75] H. Danared: *Nucl. Instrum. Meth.* **A 335** (1993), 397

[76] H. Danared: *Hyperfine Interactions* **115** (1998), 61

[77] A. Paál, A. Simonsson, A. Källberg, J. Dietrich nad I. Mohos: *Proc. EPAC 2004*, Luzerne 2004, p 2743

[78] A. Lampert, A. Wolf, D. Habs, J. Kenntner, G. Kultus, D. Schwalm, M. S. Pindzola, N. R. Badnell: *Phys. Rev.* **A53** (1996), 1413

[79] M. Larsson, R. Thomas: *Phys. Chem. Chem. Phys.* **3** (2003), 4471

[80] K. O. Nielsen: *Nucl. Instrum. Meth.* **1** (1957), 302

[81] H. Danared, A. Källberg, G. Andler, L. Bagge, F. Österdahl, A. Paál, K. G. Rensfelt, A. Simonsson, Ö. Skeppstedt, M. af Ugglas: *Nucl. Instr. Meth. A* **441** (2000), 123

[82] J. J. Thomson: *Phil. Mag.* **21** (1911), 225-249

[83] J. J. Thomson: *Phil. Mag.* **24** (1912), 209-253

[84] J. J. Thomson: *Recollections and reflections*, New York: Macmillan 1937

[85] A. J. Dempster: *Phil. Mag.* **31** (1916), 438-443

[86] T. R. Hogness and E. G. Lunn: *Phys. Rev.* **26** (1925), 44-55

[87] T. Oka: *In Molecular ions: spectroscopy, structure and chemistry*, ed. by T. A. Miller and V. E. Bondybey, Amsterdam: North Holland 1983, pp. 73-90

[88] J. Glosík: *Int. J. Mass Spectrom. Ion Process* **139** (1994), 15

[89] D. W. Martin, E. W. McDaniel and M. L. Meeks: *Astrophys. J.* **134** (1961), 1012

[90] W. D. Watson: *Astrophys. J. Lett.* **183** (1973), L17

[91] E. Herbst and W. Klemperer: *Astrophys. J.* **185** (1973), 505

[92] C. A. Coulson: *Proc. Camb. Phil. Soc.* **31** (1935), 244-259

[93] J. B. Andreson: *J. Chem. Phys.* **96** (1991), 3702

[94] T. Oka: *Phil. Trans. R. Soc. Lond. A* **303** (1981), 543-549

[95] L. Trafton, D. F. Lester and K. L. Thompson: *Astrophys. J.* **343** (1989), L73-L76

[96] P. Drossart, J.-P. Maillard, J. Caldwell, S. J. Kim, J. K. G. Watson, W. A. Majewski, J. Tennyson, S. Miller, S. K. Atreya, J. T. Clarke, J. H. Waite Jr and R. Wagener: *Nature* **340** (1989), 539-541

[97] S. Miller: *Phil. Trans. R. Soc. Lond. A* **358** (2000), 2485-2502

[98] T. R. Geballe and T. Oka: *Nature* **384** (1996), 334-335

[99] T. Oka.: *Dissociative Recombination: Theory, experiment and Applications*, ed. by S. L. Guberman, New York: Kluwer 2003, 209-220

[100] B. J. McCall, T. R. Geballe, K. H. Hinkle and T. Oka: *Astrophys. J.* **522** (1999), 338

[101] B. J. McCall, T. R. Geballe, K. H. Hinkle and T. Oka: *Science* **279** (1998), 1910

[102] B. J. McCall, A. J. Huneycutt, R. J. Saykally, N. Djuric, G. H. Dunn, J. Semaniak, O. Novotny, A. Al-Khalili, A. Ehlerding, F. Hellberg, S. Kalhori, A. Neau, R. D. Thomas, A. Paal, F. Österdahl, M. Larsson: *Sixth International Conference on Dissociative Recombination*, ed. by A. Wolf, L. Lammich, P. Schmeicher, Journal of Physics: Conference Series **4**, IOP Publishing, Mosbach, Germany 2005, 92-97

[103] D. Smith and P. Španěl: *Mass Spectrometry Reviews* **14** (1995), 255-278

[104] A. Pysanenko: *PhD Thesis*, Dep. of Electronics and Vacuum Physics, Faculty of Mathematics and Physics, Charles University, Prague, Czech Republic 2004

[105] T. J. Millar, H. Roberts, A. J. Markwick and S. B. Charnley: *Phil. Trans. R. Soc. Lond. A* **358** (2000), 2535-2547

[106] H. Roberts, E. Herbst and T. J. Millar: *Astron. Astrophys* **424** (2004), 905-917

[107] M. Larsson: *Philos. Trans. R. Soc. London A* **358** (2000), 2433

[108] R. Plašil, J. Glosík, V. Poterya, P. Kudrna, J. Rusz, M. Tichý, and A. Pysanenko: *Int. J. Mass. Spectrom.* **218** (2002), 105

[109] R. Johnsen: *Sixth International Conference on Dissociative Recombination*, ed. by A. Wolf, L. Lammich, P. Schmeicher, Journal of Physics: Conference Series **4**, IOP Publishing, Mosbach, Germany 2005, 83

[110] M. A. Biondy and S. C. Brown: *Phys. Rev.* **76** (1949), 1697

[111] J. Glosik, R. Plasil, V. Poterya, P. Kudrna, M. Tichy, A. Pysanenko: *J. Phys. B: Atomic, Mol. Opt. Phys.* **34** (L485-L494;2001),

[112] V. Poterya, J. Glosik, R. Plasil, M. Tichy, P. Kudrna, A. Pysanenko: *Phys. Rev. Lett.* **88** (2002), 044802-1

[113] A. Pysanenko, O. Novotny, P. Zakouril, R. Plasil, V. Poterya, J. Glosik: *Czech. J. Phys.* **52** (2002), D681-694

[114] R. Plasil, J. Glosik, V. Poterya, P. Kudrna, M. Vicher, A. Pysanenko: *Dissociative Recombination of Molecular Ions with Electrons*, ed. by S. L. Guberman, New York: Kluwer 2003, 249-263

[115] J. M. Richardson and R. Holt: *Phys. Rev.* **81** (1951), 153

[116] L. J. Varnerin, Jr.: *Phys. Rev* **84** (1951), 563

[117] K. B. Persson and C. S. Brown: *Phys. Rev.* **100** (1955), 729

[118] M. Leu, M. A. Biondi R. and Johnsen: *Phys. Rev. A* **413** (1973),

[119] D. Mathur, S. U. Khan and J. B. Hasted: *J. Phys. B* **11** (1978), 3615

[120] J. W. McGowan, P. Mul, V. S. D'Angelo, J. B. A. Mitchell, P. Defrance and H. Froelich: *Phys. Rev. Letters* **42** (1978), 373

[121] N. G. Adams, D. Smith and E. Alge: *J. Chem. Phys.* **81** (1984), 1778

[122] J. A. Mac Donald, M. A. Biondi and R. Johnsen: *Planet Space Sci.* **32** (1984), 651

[123] N. Adams and D. Smith: , ed. by Dissociative recombination: Theory, Experiment and Application, J. B. A. Mitchell, S. L. Guberman p., Singapore: World Scientific
29;1989

[124] H. Hus, F. Youssif, A. Sen and J. B. A. Mitchell: *Phys. Rev. A* **38** (1988), 658-663

[125] T. Amano: *J. Chem. Phys.* **92** (1990), 6492

[126] A. Canosa, B. R. Rowe, J. B. A. Mitchell, J. C. Gomet and C. Rebrion: *Astron. Astrophys.* **248** (1991), L19

[127] A. Canosa A., J. C. Gomet, B. R. Rowe, J. B. A. Mitchell and J. Queffelec: *Chem. Phys.* **97** (1992), 1028

[128] D. Smith and P. Španěl: *Int. J. Mass Spectrom. Ion Process* **129** (1993), 163

[129] D. Smith D. and P. Španěl: *Chem. Phys. Letters* **211** (1993), 454

[130] M. Larsson: *Int. J. Mass Spectrom. Ion Process* **149/150** (1995), 403

[131] M. Fehér, A. Rohrbacher and J. Maier: *Chem. Phys.* **185** (1994), 357

[132] T. Gougousi, R. Johnsen and M. Golde: *Int. J. Mass Spectrom. Ion Process* **149/150** (1995), 131

[133] S. Laubé, A. Le Padellec, O. Sidko, C. Rebrion-Rowe, J. B. A. Mitchell and B. R. Rowe: *J. Phys. B* **31** (1998), 2111-2128

[134] T. Tanabe, K. Chida, T. Watanabe, Y. Arakaki, H. Takagi, I. Katayama, Y. Haruyama, M. Saito, I. Nomura, T. Honma, K. Noda, K. Hoson: *Dissociative recombination, Theory, Experiment and Applications IV*, ed. by M. Larsson, J. B. A. Mitchell, I. F. Schneider, Singapore: World Scientific 2000

[135] T. I. F. Schneider, M. Larson, A. E. Orel and A. Suzor-Weiner: *Dissociative recombination, Theory, Experiment and Applications IV*, ed. by M. Larsson, J. B. A. Mitchell, I. F. Schneider, Singapore: World Scientific 2000, p. 131

[136] P. Kudrna, R. Plašil, J. Glosík, M. Tichý, V. Poteriya, J. Rusz: *Czech. J. Physics* **50/S3** (2000), 329

[137] J. Glosík, R. Plašil, V. Poterya, P. Kudrna, M. Tichý: *Chem. Phys. Lett.* **331** (2000;), 209

[138] M. J. Jehnsen, H. B. Pederson, C. P. Safvan, K. Seiersen, X. Urbain, L. H. Andersen: *Phys. Rev. A* **6305** (2001), 2701

[139] T. Mosbach: *Inauguraldissertation,* Universitat Essen, Cuvillier Verlag 2002, Gottingen

[140] B. J. McCall, A. J. Huneycutt, R. J. Saykally, T. R. Geballe, N. Djuric, G. H. Dunn, J. Semaniak, O. Novotny, A. Al-Khalili, A. Ehlerding, F. Hellberg, S. Kalhori, A. Neau, R. Thomas, F. Österdahl, M. Larsson: *NATURE* **422: 6931** (2003), 500-502

[141] B. J. McCall, A. J. Huneycutt, R. J. Saykally, N. Djuric, G. H. Dunn, J. Semaniak, O. Novotny, A. Al-Khalili, A. Ehlerding, F. Hellberg, S. Kalhori, A. Neau, R. D. Thomas, A. Paal, F. Österdahl, M. Larsson: *Phys. Rev. A* **70** (2004), 052716

[142] P. Macko, G. Bánó, P. Hlavenka, R. Plašil, V. Poterya, A. Pysanenko, O. Votava, R. Johnsen and J. Glosk: *Int. J. Mass Spectrom.* **233** (2004), 299-304

[143] J. Glosík, R. Plašil, A. Pysanenko, O. Novotný, P. Hlavenka, P. Macko and G. Bánó: *Sixth International Conference on Dissociative Recombination*, ed. by A. Wolf, L. Lammich, P. Schmeicher, Journal of Physics: Conference Series **4**, IOP Publishing, Mosbach, Germany 2005, 104-110

[144] M. Larsson, H. Danared, A. Larson, A. Le Padellec, J. R. Peterson, S. Rosen, J. Semeniak, C. Stromholm: *Phys. Rev. Lett.* **79** (1997), 395

[145] A. Le Padellec, M. Larsson, H. Danared, A. Larson, J. R. Peterson, S. Rosen, J. Semeniak, C. Stromholm: *Phys. Scripta* **57** (1998), 215

[146] M. R. Flannery: *Atomic and Molecular Physics*, ed. by I. Alvarez, C. Cisneros, T.J. Morgan, World Scientific, London 1995, p. 329

[147] I. F. Schneider, A. E. Orel, A. Suzur-Weiner: *Phys. Rev. Lett.* **85** (2000), 3785

[148] V. Kokoouline, C. H. Greene, B. D. Esry: *Nature* **412** (2001), 891

[149] V. Kokoouline and C. H. Greene: *Phys. Rev. Lett.* **90** (2003), 133201

[150] V. Kokoouline and C. H. Greene: *Phys. Rev. A* **68** (2003), 012703

[151] D. Romanini, A. A. Kachanov, F. Stoeckel: *Chem. Phys. Lett.* **270** (1997), 538

[152] D. Romanini, A. A. Kachanov, N. Sadeghi, F. Stoeckel: *Chem. Phys. Lett.* **264** (1997), 316

[153] A. V. Phelps: *Phys. Rev.* **82** (1955), 453

[154] M. J. Seaton: *Mon. Notes Astron. Roy. Soc.* **119** (1959), 81

[155] D. R. Bates, A. Dalgarno: *Electronic Recombination. Atomoc and Molecular Processes*, ed. by D. R. Bates, N. Y. Academic 1962

[156] R. Deloche, P. Monchicourt, M. Cheret and F. Lambert: *Phys. Rev. A* **13** (1976), 1140

[157] E. E. Ferguson, F. C. Fehsenfeld, and A. L. Schmeltekopf: *Phys. Rev.* **138** (1965), A381A385

[158] X. Urbain: *Dissociative Recombination, Theory, Experiment and Applications IV*, ed. by M. Larson, J.B.A. Mitchell, I.F. Schneider, World Scientific, Singapore 1999, p. 131.

[159] J. Glosík, G. Bánó, R. Plašil, A. Luca, P. Zakouřil: *Int. J. Mass Spectr.* **189** (1999), 103-113

[160] D. K. Bohme, D. B. Dunkin, F. C. Fehsenfeld, and E. E. Ferguson: *J. Chem. Phys.* **51** (1969), 863

[161] T. Okada, M. Sugawara: *J. Phys. D: Appl. Phys.* **26** (1993), 1680-1686

[162] I. Dotan, W. Lindinger: *J. Chem. Phys.* **76** (1982), 4972

[163] H. Villinger, J. H. Futrell, F. Howorka, N. Duric and W. Lindinger: *J. Chem. Phys.* **76** (1982), 3529

[164] B.M. Smirnov: *Complex Ions*, Nauka, Moscow 1984

[165] R. Johnsen, C.M. Huang, M.A. Biondi: *J. Chem. Phys.* **65** (1976), 1539

[166] W. Lindinger, D. L. Albritton: *J. Chem. Phys.* **62** (1975), 3517

[167] V. G. Anicich: *J. Phys. Chem. Ref. Data* **22** (1993), 1469

[168] W. H. Press, S. A. Teukolsky, W. T. Veterrling, B. P. Flannery: *Numerical Recipies in FOR-TRAN*, Cambridge university press 1992, chapter 15

[169] Z. Karpas, V. G. Anicich and W. T. Huntress, Jr.: *Chem. Phys. Lett.* **59** (1978), 84

[170] J. Glosík, V. Skalský and W. Lindinger: *Int. J. Mass .Spectr. Ion Proc.* **134** (1994), 67

[171] J. Glosík, V. Skalský, C. Praxmarer, D. Smith, W. Freysinger and W. Lindinger: *J. Chem. Phys.* **101** (1994), 3792

[172] P. W. Atkins: *Physical Chemistry*, Oxford University Press 1988

[173] J. Glosík, G. Bánó, E. E. Ferguson and W. Lindinger: *Int. J. Mass Spectrom. Ion Process.* **176** (1998), 177

[174] K. Hiraoka , T. Mori: *Chem. Phys. Letters* **157** (1989), 5

[175] Hiraoka K., Mori T.: *J. Chem. Phys.* **91** (4821–4826), 1989

[176] Johnsen R., Huang C., Biondi M. A.: *J. Chem. Phys.* **65** (1539–1540), 1976

[177] Hiraoka K., Kebarle P.: *The Journal of Chemical Physics* **62** (2267–2270), 1975

[178] J. B. A. Mitchell, O. Novotny, J. L. LeGarrec, A. Florescu-Mitchell, C. Rebrion-Rowe, A. V. Stolyarov, M. S. Child, A. Svendsen, M. A. El Ghazaly and L. H. Andersen: *J. Phys. B: At. Mol. Opt. Phys.* **38 No 10** (2005), L175-L181

[179] H. Kreckel, M. Motsch, J. Mikosch, J. Glosík, R. Plašil, S. Altevogt, V. Andrianarijaona, H. Buhr, J. Hoffmann, L. Lammich, M. Lestinsky, I. Nevo, S. Novotny, D. A. Orlov, H. B. Pedersen, F. Sprenger, A. S. Terekhov, J. Toker, R. Wester, D. Gerlich, D. Schwalm, A. Wolf, D. Zajfman: *Phys. Rev. Lett.* (2006), in print

[180] H. Richter, T. G. Benish, O. A. Mazyar, W. H. Green and J. B. Howard: *Proc. of the Combustion Institute* **28** (2000), pp. 2609-2618

[181] P. Weilmünster, A. Keller and K. H. Homann: *Combustion and Flame* **116** (1999), 62-83

[182] F. Cignoli, S. De Iuliis, G. Zizak: *Fuel* **80** (2001), 945

[183] U. Ghosh, J. W. Talley, R. G. Luthy,: *Environ. Sci. Technol.* **35(17)** (2001), 3468

[184] R.W. Macdonald, L.A. Barrie, T.F. Bidleman, M.L. Diamond, D.J. Gregor, R.G. Semkin, W.M.J. Strachan, Y.F. Li, F. Wania, M. Alaee, L.B. Alexeeva, S.M. Backus, R. Bailey, J.M. Bewers, C. Gobeil, C.J. Halsall, T. Harner, J.T. Hoff, L.M.M. Jantunen, W.L. Lockhart, D. Mackay, D.C.G. Muir, J. Pudykiewicz, K.J. Reimer, J.N. Smith, G.A Stern, W.H. Schroeder, R. Wagemann, M.B. Yunker: *Sci. Total Environment* **254** (2000), 93-234

[185] M. M. C. Ferreira: *Chemosphere* **44** (2001), 125

[186] A. Shihadeh, R. Saleh: *Food Chem. Toxicology* **43** (2005), 655-661

[187] M. D. Guillen, P. Sopelana: *Food safety*, ed. by D'Mello, JPF, CABI Publishing (Wallingford, UK) 2003, p.175

[188] S. Mollerup,S. Ovrebo, A. Haugen: *Int. J. Cancer* **92** (2001), 18

[189] M. A. Mehlman, M. M. Mumtaz, O. Faroon, C. T. DeRosa: *Advances in Modern Environmental Toxicology* **26** (2002), 201

[190] S. J. Clemett, C. R. Maechling, R. N. Zare, P. D. Swan, R. M. Walker: *Science* **262** (1993), 721725

[191] L. Becker, D. P. Glavin and J. L. Bada: *Geochimica et Cosmochimica Acta* **61** (1997), 475-481

[192] H. Naraoka, A. Shimoyama, K. Harada: *Earth Planet Sci. Let.* **184** (2000), 1

[193] S. P. Willner: *Galactic and Extragalactic infrared spectroscopy*, *Proceedings of the sixteenth ESLA Symposium*, Dordrecht, D. Reidel Publishing Co 1984, p35-57

[194] M. Cohen, A. G. G. M. Tielens, J. Bregman, F. C. Witteborn, D. Rank, L. J. Allamandola, D. H. Wooden and M. de Muizon: *Ap. J.* **341** (1989), 246

[195] A. Leger and J. L. Puget: *Astron. Astrophys.* **137** (1984), 5

[196] L. J. Allamandola, A. G. G. M. Tielens, J. R. Barker: *Ap. J.* **290** (1985), 25

[197] A. Leger and L. d'Hendecourt: *Astron. Astrophys.* **146** (1985), 81

[198] G. P. van der Zwet and L. J. Allamandola: *Astron. Astrophys.* **146** (1985), 76

[199] M. L. Heger: *Lick Observatory Bull.* **10(337)** (1922), 146

[200] T. P. Snow: *The Diffuse Interstellar Bands*, ed. by G. A. G. M. Tielens, T. P. Snow, Kluwer, Dordrecht 1995, p. 379

[201] L. J. Allamandola and D. M. Hudgins: *From Interstellar Polycyclic Aromatic Hydrocarbons and Ice to Astrobiology, Prodeedings of the NATO ASI entitled "Solid State Astrochemistry"*, ed. by V. Pirronello and J. Krelowski, Kluwer: Dordrecht 2003, 1-54

[202] R. Ruiterkamp, N. L. J. Cox, M. Spaans, L. Kaper, B. H. Foing, F. Salama and P. Ehrenfreund: *Astron. Astrophys.* **432** (2005), 515-529

[203] A. Leger: *The Diffuse Interstellar Bands*, ed. by G. A. G. M. Tielens, T. P. Snow, Kluwer, Dordrecht 1995, 363-368

[204] T. Allain, S. Leach, E. Sedlmayr: *Astron. Astrophys.* **305** (1996), 602

[205] P. Ehrenfereund and B. H. Foing: *Astron. Astrophys.* **307** (1996), 25

[206] E. Dartois and L. d'Hendecourt: *Astron. Astrophys.* **323** (1997), 534-540

[207] A. Omont: *Astron. Astrophys.* **164** (1986), 159

[208] F. Salama, E. L. O. Bakes, L. J. Allamandola and A. G. G. M. Tielens: *Astroph. J.* **458** (1996), 621

[209] M. H. Vuong and B. H. Foing: *Astron. Astrophys.* **363** (2000), L5

[210] L. J. Allamandola, A. G. G. M. Tielens and J. R. Barker: *Astrophys. J. S.* **71** (1989), 733

[211] T. Allain, S. Leach, E. Sedlmayr: *Astron. Astrophys.* **305** (1996), 616

[212] V. Le Page, T. P. Snow and V. M. Bierbaum: *Astrophys. J.* **132** (2001), 233-251

[213] V. Le Page, T. P. Snow and V. M. Bierbaum: *Astrophys. J.* **584(1)** (2003), 1

[214] G. Pineau des Forêts, D. R. Flower, A. Dalgarno: *Mon. Not. R. Astron. Soc.* **235** (1988), 621

[215] H. Abouelaziz, J. C. Gomet, D. Pasquerault, B. R. Rowe, J. B. A. Mitchell: *J. Chem. Phys.* **99** (1993), 237

[216] B. R. Rowe and C. Rebrion-Rowe: *Dissociative Recombination: Theory, Experiment and Applications III*, ed. by D. Zajfman, J. B. A. Mitchell, D. Schwalm and B. R. Rowe, Singapore: World Scientific 1996, p. 184

[217] C. Rebrion-Rowe, T. Mostefaoui, S. Laube and J. B. A. Mitchell: *J. Chem. Phys.* **113 (8)** (2000), 3039

[218] M. Hassouna, J.-L. Le Garrec, C. Rebrion-Rowe, D. Travers, B. R. Rowe: *Dissociative Recombination of Molecular Ions with Electrons V*, ed. by S. L. Guberman, Kluwer Academic / Plenum Publishers 2003, pp. 49-57

[219] C. Rebrion-Rowe, J.-L. Le Garrec, M. Hassouna, D. Travers, B. R. Rowe: *Int. J. Mass Spectrom.* **223-224** (2003), 237-251

[220] L. Spitzer: *Physical Processes in the Interstellar Medium*, New York: Wiley Interscience 1978

[221] B. T. Draine and B. Sutin: *Astroph. J.* **320** (1987), 803

[222] A. G. G. M. Tielens: *Dust and chemistry in astronomy*, ed. by T.J. Millar and D.A.Williams, 1993, 127

[223] NIST Standard Reference Database 69 - July 2005 Release: *http://webbook.nist.gov/chemistry/* (2005), National Institute of Standards and Technology

[224] V. Oja and E. M. Suuberg: *J. Chem. Eng. Data* **43** (1998), 486-492

[225] L. Biennier, M. Alsayed-Ali, A. Foutel-Richard, O. Novotny, S. Carles, C. Rebrion-Rowe and B. Rowe: *Faraday Discuss.* (2005), submitted

[226] J. L. le Garrec, O. Sidko, J. L. Queffelec, C. Rebrion-Rowe, J. B. A. Mitchell and B. R. Rowe: *J. Chem. Phys.* **107** (1997), 54

[227] A. Dalgarno: *Int. J. Mass Spectrom. Ion Proc.* **149/150** (1995), 429

[228] J. B. A. Mitchell: *Dissociative Recombination: Theory, Experiment and Applications III*, ed. by D. Zajfman, J. B. A. Mitchell, D. Schwalm and B. R. Rowe, Singapore: World Scientific 1996, p. 21

[229] R. K. Janev: *Atomic and molecular processes in fusion edge plasmas*, Plenum Publishing Press, New York 1995

[230] R. K. Janev: *Dissociative Recombination: Theory, Experiment and Applications IV*, ed. by M. Larsson, J. B. A. Mitchell, I. F. Schneider, Singapore: World Scientific 2000, p. 40

[231] M. Geoghegan, N. G. Adams and D. Smith: *J. Phys. B: At. Mol. Opt. Phys.* **24** (1991), 2589

[232] A. Le Padellec, S. Laubé, O. Sidko, C. Rebrion-Rowe, B. R. Rowe, B. Sarpal and J. B. A. Mitchell: *J. Phys. B: At. Mol. Opt. Phys.* **30** (1997), 963

[233] L. Yao, S. Sun, D. Yan, D. Xu, H. Zhang, L. Peng, Z. Cao, Q. Yang, S. Yang, W. Fu and B. Yang: *J. of Nucl. Mater.* **176-177** (1990), 654

[234] R. F. G. Muelenbroeks, A. J. van Beek, A. J. G. van Helvoort, M. C. M. van de Sande and D. C. Schraam: *Phys. Rev. E* **49** (1994), 4397

[235] A. Bogaerts and R. Gijbels: *J. Anal. At. Spectrom.* **15** (2000), 441

[236] A. Bogaerts and R. Gijbels: *Spectrochim. Acta B* **57** (2002), 1071

[237] A. Bogaerts: *J. Anal. At. Spectrom.* **17** (2002), 768

[238] J. B. A. Mitchell: *Phys. Rep.* **186** (1990), 215

[239] G. R. McKee, M. Murakami, J. A. Boedo, N. H. Brooks, K. H. Burrell, D. R. Ernst, R. J. Fonck, G. L. Jackson, M. Jakubowski, R. J. La Haye, A. M. Messiaen, J. Ongena, C. L. Rettig, B. W. Rice, C. Rost, G. M. Staebler, R. D. Sydora, D. M. Thomas, B. Unterberg, M. R. Wade, and W. P. West: *Phys. of Plasmas* **7** (2000), 1870

[240] J. B. A. Mitchell: *Atomic and Plasma-Material Interaction for Fusion vol 6*, Vienna: International Atomic Energy Agency 2001, p 97

[241] A. V. Stolyarov and M. S. Child: *Phys. Chem. Chem. Phys.* **7** (2005), 2259-2265

[242] J. B. A. Mitchell, O. Novotny, G. Angelova, J. L. LeGarrec, C. Rebrion-Rowe, A. Svendsen, L. H. Andersen, A. I. Florescu-Mitchell and A. E. Orel: *J. Phys. B: At. Mol. Opt. Phys.* **38 No 6** (2005), 693-703

[243] A. E. Orel, K. C. Kulander: *Phys. Rev. A* **54** (1996), 4992

[244] I. D. Petsalakis and G. Theodorokopoulos: *J. Phys. B: At. Mol. Opt. Phys.* **27** (1994), 4483

[245] X. Urbain, N. Djuric, C. P. Safvan, M. J. Jensen, H. P. Pedersen, L. Vejby Søgaard and L. H. Andersen: *J. Phys. B: At. Mol. Opt. Phys.* **38** (2005), 43

[246] I. D. Petsalakis, G. Theodorakopoulos, Y. Li, R. J. Buenker and M. S. Child: *J. Chem. Phys.* **108** (1998), 7607

[247] J. W. Coburn: *Appl. Phys. A* **59** (1994), 451

[248] G. S. Oehrlein: *Surf. Sci.* **386** (1997), 222

[249] J. A. Thiel: *J. Vac. Sci. Technol. B* **17** (1999), 2397

[250] K. Takahashi, M. Hori, and T. Goto: *J. Vac. Sci. Technol. A* **14** (1996), 2011

[251] C. F. Abrams and D. B. Graves: *J. Appl. Phys.* **86** (1999), 5938

[252] K. Teii, M. Hori, M. Ito, T. Goto, and N. Ishii: *J. Vac. Sci. Technol. A* **18** (2000), 1

[253] K. Yanai, K. Karahashi, K. Ishikawa, M. Nakamura: *J. Appl. Phys.* **97** (2005), 053302

[254] K. Denpoh and K. Nambu: *Japan. J. Appl. Phys.* **39** (2000), 2804

[255] T. Kimura and K. Ohe: *J. Appl. Phys.* **92** (2002), 1780

[256] N. V. Mantzaris, A. Boudouvis and E. Golides: *J. Appl. Phys.* **77** (1995), 6169

[257] D. Edelson and D. L. Flamm: *J. Appl. Phys.* **56** (1984), 1522

[258] V. Georgieva, A. Bogaerts, and R. Gijbels: *J. Appl. Phys.* **94** (2003), 3748

[259] K. Iwase, P. C. Selvin, G. Sato and T. Fujii: *J. Phys. D: Appl. Phys.* **35** (2002), 1934-1938

[260] B. L. Peko, I. V. Dyakov, R. L. Champion, M. V. V. S. Rao, J. K. Olthoff: *Phys. Rev. E* **60** (1999), 7449

[261] G. Angelova, J. L. LeGarrec, C. Rebrion-Rowe, B. R. Rowe, O. Novotny, J. B. A. Mitchell: *J. Phys. B: At. Mol. Opt. Phys.* **37** (2004), 4135-4141

[262] M. A. Biondi: *Principles of Laser Plasmas*, ed. by G. Bekerfi, Whiley, New York 1976, p. 125 ff.

[263] R. A. Morris, A. A. Viggiano, J. M. Van Doren and J. F. Paulson: *J. Phys. Chem.* **96** (1992), 2597

[264] M. L. Langford, M. Hamdan and F. M. Harris: *Int. J. Mass Spectrom. Ion Process.* **95** (1990), 243

[265] C. J. Reid: *Chem. Phys.* **210** (1996), 501

[266] O. Novotny, J. B. A. Mitchell, J. L. LeGarrec, A. I. Florescu-Mitchell, C. Rebrion-Rowe, A. Svendsen, M. A. El Ghazaly, L. H. Andersen, A. Ehlerding, A. A. Viggiano, F. Hellberg, R. D. Thomas, V. Zhaunerchyk, W. D. Geppert, H. Montaigne, M. Kaminska, F. Österdahl, and M. Larsson: *J. Phys. B: At. Mol. Opt. Phys.* **38 No 10** (2005), 1471-1482

[267] I. D. Petsalakis and G. Theodorakopoulos: *Chem. Phys.* **254** (2000), 181

[268] P. M. Mul, J. B. A. Mitchell, V. S. D'Angelo, P. Defrance, J. Wm. McGowan and H. R. Froelich: *J. Phys. B: At. Mol. Phys.* **14** (1981), 1353

[269] A. Ehlerding, A. A. Viggiano, F. Hellberg, R. D. Thomas, V. Zhaunerchyk, W. D. Geppert, H. Montaigne, M. Kaminska, F. Österdahl, M. af Ugglas, M. Larsson, O. Novotny, J. B. A. Mitchell, J. L. LeGarrec, A. I. Florescu-Mitchell, C. Rebrion-Rowe, A. Svendsen, M. A. El Ghazaly and L. H. Andersen: *J. Phys. B: At. Mol. Opt. Phys.* (2005), submitted

[270] L. G. Christophorou, J. K. Olthoff and M. V. V. S. Rao: *J. Phys. Chem. Ref. Data* **25** (1996), 1341

[271] I. Langmuir: *J. Frank. Inst.* **196** (1923), 751

[272] I. Langmuir and H. M. Mott-Smith: *Gen. Electr. Rev.* **27** (1924), 449

[273] H. M. Mott-Smith and I. Langmuir: *Phys. Rev.* **28** (1926), 727

[274] J. D. Swift and M. J. R. Schwar: *Electrical Probes for Plasma Diagnostics*, Iliffe, London 1970

[275] Earl W. McDaniel, J. B. A. Mitchell, M. Eugene Rudd: *Atomic Collisions, Heavy Particle Projectiles*, John Wiley & Sons, inc. 1970, 545

[276] Z. Zakrzewski and T. Kopiczinski: *Plasma Phys.* **16** (1974), 1195

[277] P. David, M. Šícha, M. Tichý, T. Kopiczinski, and Z. Zakrzewski: *Contrib. Plasma Phys.* **30** (1990), 167

[278] M. Tichý, M. Šícha, P. David, and T. David: *Contrib. Plasma Phys.* **34** (1994), 59

[279] I. D. Sudit and R. C. Woods: *J. Appl. Phys.* **76** (1994), 4488

[280] R. Johnsen, E. V. Shun'ko, T. Gougousi, and M. F. Golde: *Phys. Rev. E* **50** (1994), 3994

[281] P. Španěl: *Int. J. Mass Spec. Ion Proc.* **149/150** (1995), 299

[282] J. H. Rogers, J. S. De Groot and D. Q. Hwang: *Rev. Sci. Instrum.* **63** (1992), 31

[283] Leo W. R.: *Statistics and the treatment of experimental data*, http://nedwww.ipac.caltech.edu/level5/Leo/Stats_contents.html 2005